UNIVERSITY OF STRATHCLYDE

Department of Physics

Micro- and nano- soft lithography for the fabrication of photonic devices

By

Elliot John William Richardson

A thesis presented in fulfilment of the requirements
for the degree of Doctor of Philosophy

June 2016

Declaration of Authorship

This thesis is the result of the author's original research. It has been composed by the author and has not been previously submitted for examination which has led to the award of a degree

The copyright of this thesis belongs to the author under the terms of the United Kindom Copyright Acts as qualified by University of Strathclyde Regulation 3.50. Due acknowledgement must always be made of the use of any material contained in, or derived from, this thesis.

Signed:

Date:

Frontispiece

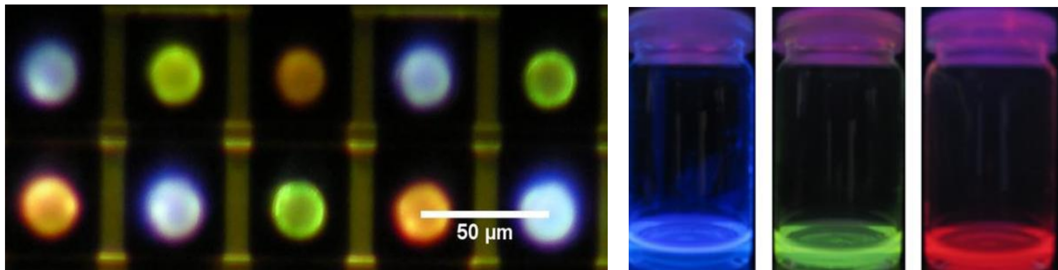

A multi-colour array being photopumped by underlying UV electrically driven micro-LED pixels.

Image of 3 light emitting polymers used in hybridisation work.

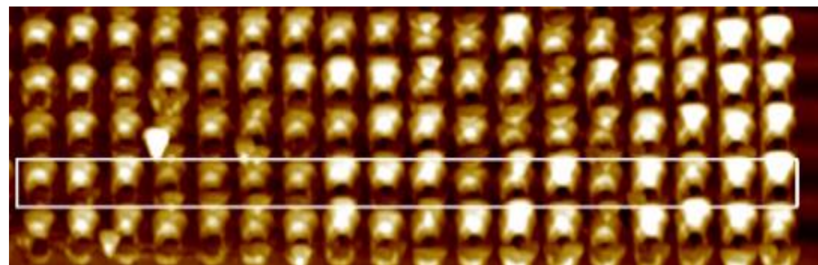

Plan image

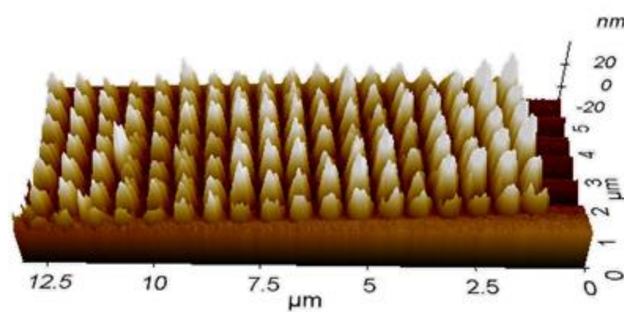

Oblique reconstruction

Atomic force microscope images of 700nm pitch imprint patterning of BBEHP-PPV spin coated film achieved via dip negative dip-pen nanolithography.

Abstract

This thesis presents the application of two soft lithographic tools for direct patterning of (soft) photonic materials at the micro- and nano-scale. Inkjet printing and Dip-Pen Nanolithography, respectively, have been used to pattern organic molecules, photoresists, and conductive inks to create optically active structures and devices. A series of light emitting polymers (LEPs), blended with a photo-curable host system, have been integrated as colour converters with an array of matrix-addressable gallium nitride (GaN) micro LEDs to form a red-green-blue (RGB) emitting array. Surface structure and conversion efficiency have been explored in detail with peak colour conversion efficiencies of 31.6% being obtained.

Inkjet printing of silver conductive inks has been used in conjunction with mask-free ultraviolet direct writing to generate an 8 x 8 GaN LED array. The smallest feature achieved with the mask-free writing set up is 1 μm and the conductive ink was used to form a contact with the n-GaN to enable wire-bonding and characterisation of the LED. This mask-free process is attractive as fabrication of conventional masks for photolithography is both costly and lengthy. Possessing the ability for define LED patterns “free form” on photoresist and subsequently producing a common n-contact with the silver ink allows for rapid prototyping for novel and experimental LED designs.

Two techniques were explored for utilising the potential of Dip-Pen Nanolithography; deposition of liquid inks (positive) and removal of dried material (negative). Photoresist inks were used to generate nanoscale features (560nm) on a planar LED structure. Subsequent exposure to a CHF_3 plasma treatment deactivated the Mg doped GaN which was not protected by the photoresist; LEDs with 3 μm diameter at full-width half-maximum were fabricated in this manner. Utilising dip-pen nanolithography for negative patterning allows for grating structures to be created via the displacement and removal of material. 1D and 2D structures were generated using a lasing polymer as the optically active gain medium. When optically pumped it was found that these structures lased and the grating structures acted as Distributed Bragg Reflectors (DBRs).

Key advantages for the techniques used throughout this thesis are that they allow the patterning of sensitive materials that otherwise would not survive classical lithography due to aggressive chemical treatment or high UV exposure. In addition all of the techniques used are readily programmable and require no masks to be fabricated thus allowing for rapid prototype production and experimental designs to be implemented without delays or incurring extra costs.

To my parents

Acknowledgements

Firstly I would thank my supervisor Prof. Martin Dawson as well as Dr. Nicolas Laurand and Dr. Erdan Gu for all their support, patience, and guidance. They helped me overcome the difficulties I faced throughout my PhD studies and I appreciate all the time they dedicated to helping me.

Many thanks go to Dr. Benoit Guilhabert for teaching me the laboratory procedures as well as the hours he patiently sat helping with micro-PL measurements. Our discussions on my work, and the advice that stemmed from them, was invaluable. Thanks also go to Dr. Min Wu for my initial training on the inkjet printer upon my arrival in Glasgow.

I am grateful to all my colleagues, past and present, for creating a friendly and supportive working atmosphere in the IOP. The minor ways which you helped in both the office and my personal life are innumerable.

Special note goes to my friends outside of the department; I have made some long lasting friends who helped me through the tough times.

Finally I want to express my deepest gratitude to my family. It cannot be over stated that without their unconditional love, support, and unending patience none of this would have been possible.

List of Figures

1.1.1	Schematic for photolithography through a mask with both positive and negative PR patterning……	3
1.1.2	Schematic of Nanoimprint Lithography, showing the transfer of a pattern by pressing a master grating into a soft polymeric resist……	7
1.2.1	Schematic of the micro-contact printing process……	9
2.1.1	Energy band diagram for Gallium Arsenide (GaAs) and Silicon (Si) semiconducting crystals. GaAs in a "direct" band gap material where there is no momentum change for electrons transitioning from the lowest energy in the conduction band to the highest energy of the valance band; Si is an "indirect" semiconductor where a change in momentum is necessary in transitioning from the conduction band to the valence band……	16
2.1.2	Illustration of the effect doping has in the energy-band structure in the creation of N-type (left) and P-type (right) extrinsic semiconductors……	17
2.1.3	Illustration of the alignment of Fermi levels, EF, in a PN junction. The energy levels re-align to create a depletion zone at the junction where electron-hole recombination occurs.	18
2.1.4	PN junction under forward bias (left) and reverse bias (right)……	19
2.1.5	Illustration of a homojunction pn-junction while operated under forward bias……	21
2.1.6	Example of double heterojunction structure that creates a quantum well. The energy levels corresponding to n and m are related to the width of the well (L) as well as the size of the energy barrier……	22
2.2.1	Bandgaps of group III-nitride alloys as a function of in-plane lattice constant……	23
2.2.2	Cross section of a typical InGaN/GaN quantum well LED structure used in this work (left). Image of disk geometry InGaN/GaN quantum well micro-LED array (right)……	24
2.2.3	Top-emitting (left) and Flip chip (right) modes of operation for a Gan-on-sapphire micro-LED device. The purple arrows denote light emission pathways and the red arrows are thermal dissipation pathways……	25
2.2.4	Schematic cross section of top-emission GaN micro LED with matrix-addressable contacting (left). Image of a section of the 64 x 64 micro-LED array with 50 µm pitch and 16 µm emission diameter (right). Also shown is the matrix of n- and p- contacts that allow for addressing individual pixels within the array……	26
2.2.5	Typical I-V characteristics (left) and output-power density (right) of a 368 nm device……	27
2.2.6	Cross section of planar LED device (left), Image of a planar LED with an 85 µm diameter, a Pd spreading layer and Ti/Au contact track……	28
2.3.1	Representation of arrangement of 4 basic copolymer types; 1) Statistical or "Random" copolymer, 2) Alternating copolymer, 3) Block copolymer, 4) Graft copolymer. A and B represent different monomer units……	29
2.3.2	CHDV monomer unit (top left), DAI-SbF6 photo acid generator (bottom left), Pholymerisation reaction of two monomer units of CHDV (right)……	30
2.3.3	Conjugated polymer chains with 2k carbon atoms and k double bonds……	32

2.3.4	Energy Level diagram for the HOMO and LUMO levels in a polymer showing vibrational energy levels 1-3 for each (Left). Example absorption and emission characteristics of a polymer; peaks in absorption or emission correspond to different vibrational energies (Right). The shift in energy for absorption and emission is known as the stokes shift...........	34
2.4.1	Skeletal structure for the three polymers used; each share a common backbone for absorption. The terminating polymer P1, P2 or P3 determines the emission wavelength of the polymer. Termination with P1 results in blue; P2 green; and P3 in red..........................	35
2.4.2	Images of the polymers P1-P3 integrated into CHDV with 368 nm illumination.................	36
2.4.3	Skeletal structure of BBEHP-PPV polymer (left), absorption and luminescence data (right)……………………………………………………………………………………	38
3.2.1	Left, photograph of inkjet printer with computer control. Right, image of the inkjet cartridge pre-assembled…………………………………………………………………………………………	44
3.2.2	Flow diagram depicting the “N” type MEMs ejection waveform for the inkjet nozzle at rest (a), drawing fluid from the well (b), initial droplet formation (c), droplet breakoff and return to standby (d). Image reproduced from the Dimatix DMP2800 manual.............................	46
3.2.3	High ejection voltage resulting in large tail formation, left. Tail separation resulting in secondary orbital droplets, middle. Optimal ejection of a droplet resulting in no tail or resultant orbital droplets, right…………………………………………………………………….	47
3.3.1	Top left: CHDV monomer unit, top right: the PAG used to initiate polymerisation, bottom: the polymerisation reaction that occurs when the PAG is stimulated to lose a H+ ion under UV stimulation…………………………………………………………………………………………	49
3.3.2	Normalised absorption and photoluminescence spectra for spin coated films of LEP in CHDV. Absorption spectra: P1: dashed line (blue), P2 dotted line (green), P3 Dot-dashed line (red). Photoluminescence spectra are solid lines marked respectively, P1-3.................	52
3.4.1	Diagram illustrating interaction energies that result in Young’s equation. This holds only for flat substrates rather than for roughened…………………………………………………………	53
3.4.2	Condensation reaction of PFODCS bonding onto a silica substrate......................................	55
3.4.3	Images of 5x5 printed array of 5 layers of 1 pl droplets of optical polymer CHDV with a 50µm centre-to-centre pitch deposited onto untreated glass (left) and silanised glass (Right). Droplet diameter ~10.5 µm untreated, ~8µm on treated glass...	56
3.4.4	Left, a graph of feature height change with increasing number of droplets with (insert) the respective profiles as measured by stylus profilometry. Right, an image demonstrating the increase in printed feature size with increasing volume. The pitch is 100 µm with the number of 1pL droplets ranging from 2 to 20 with 2 droplet increments from right to left................	57
3.4.5	Principle of layer-by-layer integration on an LED pixel, far left. SEM image of the two integration techniques each with 10 layers of 1pL droplets; bulk curing shown in the middle; layer-by-layer curing approach on the far right……………………………………………………….	58
3.5.1	Pixel integration of the three LEP inks on a glass slide (left) and on a test micro-LED device (right). The centre-to-centre pitch for each droplet is 50µm (right)…………………………….	59
3.5.2	Figure 3.5.2 Optical setup for micro photoluminescence measurement (left) with photo of the set-up (right). A 375nm laser diode used for optical excitation of samples and a camera for alignment with the UV-visible spectrometer……………………………………………	60
3.5.3	Photolumenescence of 5 layers of 1pl droplets for composite inks containing the colour converting polymers P1-P3. The narrow peak observed at 375nm is unconverted UV laser light. Insert is an optical micrograph of the printed features being laser pumped.................	62
3.5.4	Micro-photoluminescence spectra shown for colour converting LEP’s integrated onto and photo-pumped by micro-LED pixels. The peak at 370nm is unconverted UV light from the LED and the peaks at 413nm, 532nm and 610nm are that of down converted light from the blue, green and red material, respectively. The insert is an optical micrograph of the RGB array in operation; the integrated colour converter being photopumped by the underlying UV electrically driven micro-LED pixels……………………………………………………………….	63
3.5.5	Evolution of the emission profile for the green composite ink with increasing bias applied to the micro-pixel. Insert showing the change in ratio of the UV and converted peaks with increasing current…………………………………………………………………………………………	64

3.6.1	Schematic of LED-write setup (top), Optical micrograph of the entire LED patterned and etched 450-nm emitting 8×8 array (bottom left) and AFM scan profile of a representative gap between adjacent pixels of the array (bottom right)......	65
3.6.2	Image of printed common n-contact to a chequerboard LED array (left) and SEM image of dried sliver track (right)......	66
3.6.3	$I - V$ and $L - I$ characteristics of a typical pixel of the 8×8 array with, inset, an optical micrograph of several pixels individually addressed......	67
4.1.1	Illustration showing the deposition of SAMs via the formation of a meniscus between the tip and substrate, left. Deposition of inks as determined by fluid flow down the tip to contact the surface, right......	75
4.2.1	Image of the NLP 2000 Dip Pen system, left. Image of the substrate stage with probe holder and microscope optics, right......	77
4.2.2	Image of double-ended "M" type tip probes (left). Image of diving board frame probes with array geometry (middle). A-frame tips also shown alongside array geometry and spacing (Right)......	78
4.3.1	Top image showing the formation of solid "tails" of SU08 photoresist immediately after tip loading at the well. Bottom is a schematic to clarify the details of the photo taken......	80
4.3.2	Evolution of feature size with dwell time for NOA63 on an A-frame cantilever (Top left). Optical micrograph of a 4x6 array of NOA63 deposited onto GaN (Top Right). The centre to centre pitch is 15µm with a dwell time of 10s. AFM scan of array of deposited NOA63 on a GaN substrate (Bottom Left), gradient of white to black signifying tall to shallow topography. Profile taken along the white outline (Bottom Right) showing the profile and periodicity of the deposited features......	82
4.3.3	NOA 68T: evolution of deposited feature size with dwell time (Top Left). Red plot is the diameter along the y axis of the feature, blue plot the diameter along the x-axis. The dashed line gives the micron size scale. Image of NOA 68T deposited onto a SiO_2-topped GaN substrate with a 3µm pitch and 1s dwell (Top Right). AFM scan of an array deposited with 1s dwell and 2.5µm pitch (Bottom Left). 3D image of selected feature outlined in white (Bottom Right)......	83
4.3.4	AFM scan of NOA 68T features deposited onto SiO_2 topped GaN with a 0.5s dwell and a 1.5µm pitch (Top Left). 3D image of feature outlined in white (Top Right). Profile measurements taken for the width of the features taken across the dashed grey outline (x-axis) (Bottom Left). Profile measurements taken for the length of the features taken along the solid grey outline (y-axis) (Bottom Right)......	84
4.4.1	Image of RIE system (left) and the schematic (right) for an RIE chamber. Outlined in yellow is the processing chamber......	86
4.4.2	Image of ICP system (left) and the schematic for an ICP chamber (right). Outlined in yellow is the processing chamber......	87
4.4.3	I-V characteristics of co-planar Ti /Au metal electrodes deposited on the p-type GaN layers with different plasma treatments......	88
4.4.4	I-V (left) and L-I (right) characteristics of LEDs without and with a CHF3 plasma treatment......	89
4.4.5	Schematic cross-section of a GaN LED which has had protective photoresist deposited (left) and then given a plasma treatment to definite a specific area of emission (right)......	90
4.4.6	Test for NOA63 plasma protection for a GaN LED with emission at 520nm. NOA63 deposited onto an LED (left) the same LED turned on after 4 minutes plasma treatment (right)......	91
4.4.7	Schematic for imaging the LEDs and measurement of the emissive areas defined by the plasma treatment......	91
4.4.8	Deposition of NOA 63 onto a palladium-topped GaN LED with 520 nm emission wavelength, in a 3x3 array with 5s dwell and 10µm pitch (right). The same pixel turned on after having had a 4 minute plasma treatment (right)......	92
4.4.9	Wenzel wetting state (top left), Cassie-Baxter wetting (top right), Hemi-wicking across the roughened surface (bottom......	93

4.4.10 2x2 array of NOA 68Tdeposited on Pd topped GaN LED with emission at 450nm with a 1s dwell time and a 20μm pitch.......... 94

4.4.11 20x magnification of 2x2 array of emitters electrically pumped at 8V bias (left). 40X magnification of the largest emitter at 8V bias (middle). 40X magnification of the smallest emitter at 8V bias (right).......... 95

4.4.12 Intensity profile of the largest and smallest emitter defined by photoresist (left). Contour map of the emitters displaying near-circular emission (right).......... 96

5.1.1 SEM image and schematic of pyramid tip supplied by NanoInk Inc.......... 102

5.2.1 Top: basic schematic for laser design displaying the essential components of the mirrors for feedback and wavelength selection, the gain medium for light generation and the pump source for achieving population inversion in the gain medium. Bottom: schematic for DBR laser design illustrating the replacement of reflectors with DBR gratings.......... 105

5.2.2 Schematic and cross section of a distributed feedback reflector grating with materials of refractive index n_1 and n_2.......... 106

5.2.3 Cross section of a 2D photonic crystal structure of two materials with refractive indices of n_1 and n_2.......... 107

5.2.4 Schematic of in plane diffraction orders for coupled-wave model analysis. A and B are counter-propagating T=0 guided modes within the structure. The diffraction orders are K_1, K_2, K_3, and K_4.......... 108

5.2.5 Reflectivity of a DBR structure with 700 nm pitch and 10 periods. Two areas within the visible range are reflected, centred around wavelengths of 530 and 710 nm. As disorder is increased within the grating the reflectivity deceases, as is apparent when comparing the peak reflectivities with and without disorder.......... 110

5.3.1 Top left: AFM scan of scratched grating in BBEHP-PPV polymer, pitch 5 μm and writing speed 10μms-1. Bottom left is corresponding phase image of the AFM scan. Right is the profile scan of the segment outlined on the AFM scan.......... 112

5.3.2 Top left: AFM scan of 10 lines grating of 1μm pitch at 10μms-1 writing speed with 2 repeats. Bottom left: corresponding phase diagram. Right: measured profile along the white outline of the top left image.......... 113

5.3.3 Top Left: AFM scan of 1D grating of 40 lines at 350 nm pitch and 5 μms^{-1} writing speed. Top right: AFM scan of the final written edge displaying material displacement. Bottom is the modulation profile of the pattern, taken from the white outline of the top left AFM scan.......... 114

5.3.4 Top left: AFM scan of 30 lines written at 350nm pitch and $5\mu ms^{-1}$ writing speed and no repeats, pressed 300nm past surface contact. Bottom left: the phase diagram associated with the AFM. Right: the modulation profile taken from the white rectangle.......... 115

5.3.5 AFM example of polymer deformation under high tip pressure.......... 116

5.3.6 Top left: AFM scan of 2D imprint grating in BBEHP-PPV polymer, with a pitch of 2μm. Bottom left: corresponding phase image of the AFM scan. Right: the profile scan of the white outline on the top left AFM scan.......... 117

5.3.7 Left: AFM image of a 20x20 700nm pitch dot array conducted with the 33.6° half cone angle tip. Right: profile taken along the white rectangle.......... 117

5.3.8 Top left: AFM scan of a 5x20 700nm pitch patterning onto SU1805, Top right: AFM scan of a 5x20 500nm pitch patterning onto SU1805. Profiles for are shown below each respectively.......... 118

5.3.9 Top Left: AFM scan of a 10x20 700nm pitch imprint patterning onto a BBEHP-PPV spin coated film using 10° half-cone angle tip. Bottom left: 3D image of the AFM area. Right: the modulation profile shown in the white outline.......... 119

5.3.10 Fourier Transform of the modulation profile from figure 5.5.9. The one main peak at 1.5 μm^{-1} corresponds to an average periodicity of 666nm.......... 120

5.4.1 Three pattern designs, P1-P3, for the patterning of the DBR gratings on a polymer film to create DBR gain structures, giving the cavity length and periodicity of the DBR mirrors...... 121

5.4.2	Excitaation measurements of 1.5mm pump stripe on un-patterned BBEHP-PPV film. Top is one region with associated threshold curve on the right. The second region and associated threshold curve in on the bottom......	123
5.4.3	Spectral and threshold curves for P1 (Top) P2 (Middle) and P3 (Bottom) pumped with a 1.5mm x 50µm spot......	125
5.4.4	Spectral and threshold curves for P1 (Top) P2 (Middle) and P3 (Bottom) pumped with short excitation spot......	126
5.4.5	Normalised spectra of P1 pumped under varying energies......	128
5.4.6	Fourier Transform of the overlain spectra of figure 5.4.5. A spatial frequency of ~0.23 nm^{-1} is observed......	129
6.1.1	Illustration of a fusion of the techniques developed to achieve a high efficiency hybrid LED......	142

List of Tables

4.3.1 Fluid and physical properties of NOA 63 and NOA 68T optical adhesives. The refractive index, modulus and hardness are for cured material... 81

5.4.1 Comparison of ASE threshold values for the bare spin coated films and the patterned areas P1, P2 and P3 with both the long and short excitation spot sizes.. 127

Contents

Declaration of Authorship i

Frontispiece ii

Abstract iii

Acknowledgements v

List of Figures vi

List of Tables ix

Chapter 1 Introduction and Motivation……………………………………………………1
1.0 Introduction……………………………………………………………………1
1.1 Pattern Designation……………………………………………………………2
Photolithography…………………………………………………………………2
Mask-Free Lithography…………………………………………………………5
Nanoimprint Lithography………………………………………………………6
1.2 Pattern transfer…………………………………………………………………7
Micro-Contact Printing……………………………………………………………8
Wet Etching…………………………………………………………………………9
Dry Etching…………………………………………………………………………9
1.3 Conclusion……………………………………………………………………10
1.4 Thesis Outline…………………………………………………………………11
1.5 References……………………………………………………………………13
Chapter 2 Background on Materials and Devices……………………………………15
2.0 Introduction……………………………………………………………………15
2.1 Semiconductor Physics………………………………………………………15
The P-N Junction…………………………………………………………………18
Light Emitting Diodes……………………………………………………………20
2.2 GaN LEDs………………………………………………………………………22
GaN Micro-LEDs…………………………………………………………………24
Matrix-Addressable Micro-LEDs…………………………………………………26
Planar LEDs…………………………………………………………………………27
2.3 Polymers…………………………………………………………………………28
Organic Materials…………………………………………………………………28
Guest-Host System…………………………………………………………………30
Light Emission in Polymers………………………………………………………31
2.4 Light Emitting Polymers………………………………………………………34
Cross-Linkable LEPs………………………………………………………………35
Lasing Polymer……………………………………………………………………37
2.5 Conclusions……………………………………………………………………38
2.6 References……………………………………………………………………39
Chapter 3 Additive Lithography via Inkjet Printing…………………………………41
3.0 Introduction……………………………………………………………………41

3.1 Background……42
3.2 Inkjet Printing Technology……44
3.3 Ink Preparation and Design……48
3.4 Substrate Preparation……53
3.5 Red – Green – Blue (RGB) Integration……58
3.6 Mask – Less LED Fabrication……64
3.7 Conclusions……68
3.8 References……69
Chapter 4 Positive Patterning via Dip – Pen Nanolithography……73
4.0 Introduction……73
4.1 Principles and Models of Deposition……74
4.2 Dip Pen Operation……77
4.3 Photoresist Deposition……79
SU08 Deposition……79
Acrylate Deposition……80
4.4 Plasma Treatment of GaN LEDs……85
Photoresist Protection……91
4.5 Conclusions……96
4.6 References……98
Chapter 5 Negative Patterning via Dip – Pen Nanolithography……101
5.0 Introduction……101
5.1 DPN Operation and Tip Geometry……102
5.2 Distributed Feedback Structures……104
DBR Modelling……107
5.3 1D and 2D Grating Imprint Patterning……111
1D Gratings……111
2D Gratings……116
5.4 DBR Gain Structures……121
5.5 Conclusions……129
5.6 References……131
Chapter 6 Conclusion and Perspective……134
6.0 Conclusion……134
6.1 Future Work and Perspectives……139
6.2 References……143

Publications 144

Appendix A NLP 200 Datasheet 176

Appendix B Reflectivity calculation of a fourth-order in-plane grating 180

Chapter 1

Introduction and Motivation

1.0 Introduction

Photonic devices have become a cornerstone of modern society as they are present in the life of most people on a daily basis. The range of applications is ever increasing, from display technology, TV, phones, Smart glasses etc; to the emerging technology of visible light communications (VLC) [1-3]. The techniques currently used in the fabrication of most of these devices are well established and are able to achieve much in both an industrial and academic sense. Large scale patterning and processing of semiconductor materials with high resolution and reliability is what has permitted this industry to thrive. However there are some short comings to these techniques; as technology develops towards the hybridisation of inorganic semiconductors and organic materials [4-7] the current processes are ill-equipped to fully allow efficient integration of the two types of materials. Polymeric materials specifically fall between the gaps of the current lithographic techniques and various tricks must be employed when utilising them to achieve the desired result. Often the patterning methods used result in a large degree of wasted material, are expensive in setup and offer little flexibility for rapid prototyping necessary in research.

Classical lithography is used to define areas and patterns in the fabrication of semiconducting devices and, by its very nature, is often aggressive to the medium being patterned, whether that

be via high energy UV radiation or by exposure to etchant chemicals. In order to pattern materials that would be degraded by such steps, other techniques must be employed to preserve the desired design. In this chapter the specific motivations and necessity for new techniques will be explored as well as the current methodologies used in micro- and nano-scale fabrication. This thesis will focus on the development and applications of micro and nano lithographic techniques and their application in the fabrication of photonic devices and structures. It outlines how the two little-explored lithographic techniques of Inkjet Printing and Dip-Pen Nanolithography can be used in the fabrication of photonic structures, the hybridisation of inorganic light-emitting diodes (LEDs) and organic materials, and as a means of patterning soft polymeric materials.

1.1 Pattern Designation

The following section contains an overview of the techniques that are currently used in the micro- and nano-scale patterning of materials that are commonly used in the processing of semiconducting materials for fabrication of photonic devices and structures. The outline of a design pattern to enable further deposition or etching is often the key stage in the fabrication of photonic structures.

Photolithography

Photolithography is a common technique used for pattern definition on both the micro- and nano-scale. It is a patterning process which transfers the designed patterns from a photo-mask to photosensitive materials such as photoresist (PR), by light exposure; the basic process of photolithography is shown in figure 1.1.2. The sample is first coated with a PR layer, usually via spin-coating (step 1). This PR layer is then exposed to the light (usually ultraviolet) through

the photo-mask (step 2). The photo-mask contains a pattern consisting of clear and opaque regions, allowing the light to expose a specific design while leaving other areas unexposed. The chemical properties of the exposed PR are then be changed due to a photochemical reaction. In the subsequent development process, the sample is dipped into a suitable developer to remove unwanted PR and to form a desired PR pattern. Depending on the properties of PRs, the final PR patterns formed on the sample surface will be either the same as that on the photo-mask (positive PR) or a reversed pattern (negative PR) (step 3). The photolithography process can be divided into three main steps; PR coating, exposure, and PR development. In these steps, the operation of alignment and exposure plays a critical role in the photolithography process. This operation determines the success of transferring the designed patterns on the photo-mask to the PR layer. The wavelength of the exposure light source, used for pattern exposure, is an important parameter to decide the minimum resolution of final PR patterns.

The resolution (R) of an optical system is determined by the wavelength (λ) of the light source and the numerical aperture (NA) of the system. The equation for this is given by equation 1.1.1:

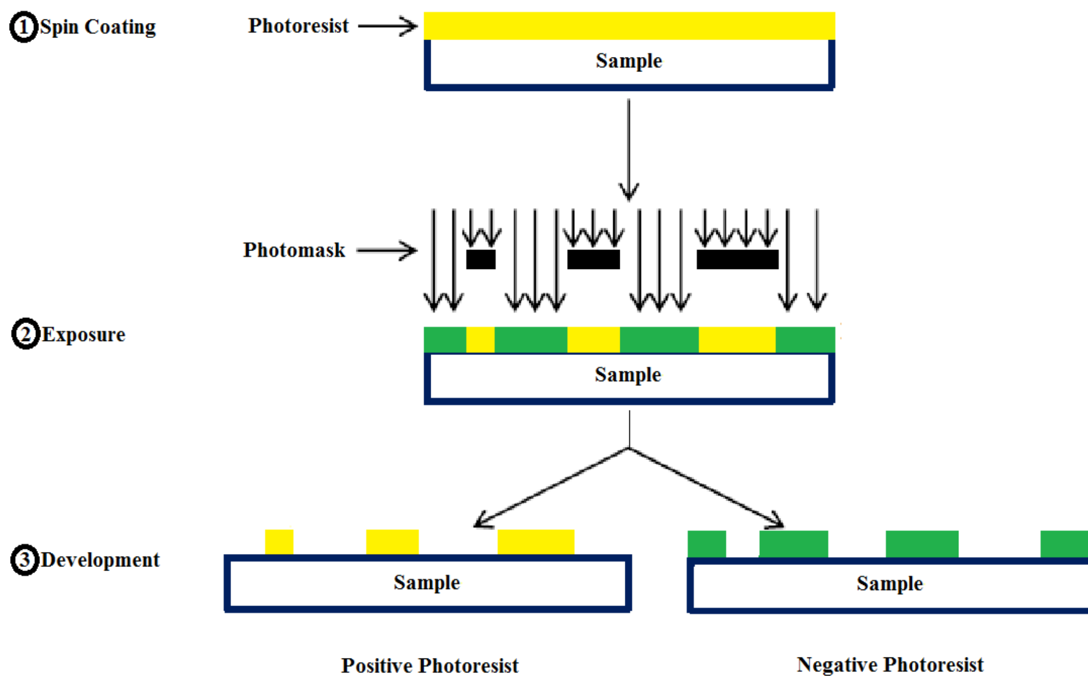

Figure 1.1.1 Schematic for photolithography through a mask for both positive and negative PR patterning.

1.1.1

$$R = \frac{\lambda}{2.NA}$$

From this equation it can be seen that to achieve smaller scale resolution a shorter wavelength of light and large numerical apertures must be used. There is however a trade-off between achieving small scale resolution and depth of focus (DOF). The DOF is the distance necessary to achieve a good focus for light leaving an aperture to project a pattern with a good resolution. The equation for the calculation of depth of focus is:

1.1.2

$$DOF = \frac{2\lambda}{(NA)^2}$$

with k_2 as a system constant. Re-arranging equation 1.1.1 for NA and inputting into 1.1.2 yields the relationship between the depth of focus and the optical resolution, given in equation 1.1.3:

1.1.3

$$DOF = \frac{8R^2}{\lambda}$$

It can be seen that as the resolved feature size is reduced to achieve a smaller scale, the position of the photo-mask must be closer to the substrate. The logical limit of this is where the mask is in contact with the PR, although this is often undesirable as there is possible damage to the

photo-mask or contamination of the mask with particulates so that the pattern is not true to the design. This, combined with optical diffraction of the wavelength used, are the limits for photolithography using a photo-mask to define the pattern.

The resolution limit is controlled by the wavelength of light used, which is why the UV region of the electromagnetic spectrum is commonly exploited. Typical wavelengths of UV light used for lithography lie between 400 nm and 200 nm, short enough to offer a good degree of resolution and with enough photon energy to initiate chemical change within the PR for subsequent development. While the high photon energy makes this process suitable for patterning of PR it is not suitable when attempting to pattern many other optically active materials. In the patterning of light emissive materials the harsh exposure to UV light can degrade or photobleach materials, reducing or eliminating the function for which they were designed. It is possible to use a negative PR style patterning to transfer a pattern using these soft materials; however that process is extremely wasteful and the whole process is costly and time consuming. Photolithography via mask exposure requires the fabrication of a high resolution mask; once the mask has been fabricated there is no flexibility and should the design need changing another mask needs to be made.

Mask-Free Lithography

Another method of defining a pattern in PR is to use focused irradiation and write the pattern directly [8]. This approach is used to varying degrees of success and depends on the ability to limit the spot size of the beam used. There are several different possibilities for the beam; UV laser, electron beam or ion beam, each having their own advantages and disadvantages. Direct laser writing is very common in optical lithography as it offers flexibility, ease of use, and cost effectiveness in rapid prototyping. Patterning at sub-micrometre resolutions is achievable and is a compromise between the high performance of the photo-masks and cost of fabricating said

masks. This technique is limited by the diffraction limit of light, permitting features of down to 200nm to be patterned but no smaller.

Electron beam lithography (e-beam lithography) is a means of achieving even smaller resolution, being able to transcend the diffraction limit associated with optical lithography, and permitting resolution down to the nanometre scale. While being able to offer extremely high resolution there are significant disadvantages to utilising this means of lithography; it does not scale for industrial processing, the time to complete a desired patterning can be multiple hours, and the machines themselves are costly in the extreme (millions of pounds). The common usage of e-beam lithography is in fabricating the photo-masks used in photolithography, being able to offer the high resolution in the master-mask so that defects in the mask are unlikely to occur and reproduce on any subsequent work.

Nanoimprint Lithography

Nanoimprint lithography (NIL), known as a "soft" lithographic technique, involves pressing a mould against a soft thermoplastic polymer or a liquid polymer precursor, as shown in figure 1.1.2. The solid state pattern is formed by either cooling (thermal NIL)[9,10] or UV-photocuring the precursor (UV-NIL)[11,12]. Both thermal and UV NIL can reach ~5nm resolution. There are a wide range of polymers that have been used for thermal NIL at temperatures above the polymer glass transition temperature, which is the temperature at which a polymer transitions from a hard material to a soft, molten one. The difficulty in thermal NIL is patterning the highly viscous polymers. Compared with the thermal NIL, UV-NIL has higher curing rates and intermediate viscosities. However, the high resolution patterns in UV-NIL are usually affected by oxygen sensitivity and polymer shrinkage in the photosetting.

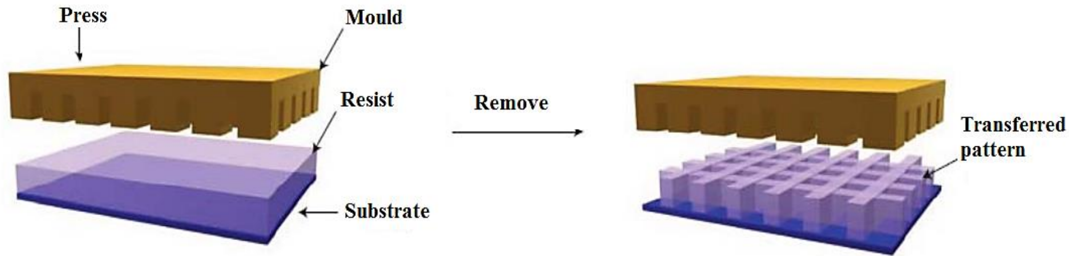

Figure 1.1.2 Schematic of Nanoimprint Lithography, showing the transfer of a pattern by pressing a master grating into a soft polymeric resist.

Therefore, ongoing developments on UV-NIL focus on new designs of photochemically sensitive polymers with oxygen inhibition, shrinkage suppression and easy mould release. This technique is highly attractive as the patterning area is limited only by the size of the master mould. However, the cost of this mould is OK compared to that of the photo-masks used in photolithography, if not more so as the moulds have to withstand physical contact with the resist material. Also, as with photolithography, this technique lacks flexibility that is essential in a research capacity. Once the mould is cast there is no altering it to accommodate changes in design or purpose.

1.2 Pattern Transfer

Described in this section will be the processes and techniques used to transfer the patterns designated by the methods described in section 1.1. These processes are widely utilised in the fabrication of inorganic semiconductor structures and devices.

Micro-Contact Printing

In micro-contact printing, an "ink" material is transferred to the substrate by close conformal contact with a rigid or elastic stamp with bas-relief features, as in the schematic shown in figure 1.2.1[13,14]. Micro-contact printing, which is efficient in large-area fabrication with sub-micrometre spatial resolution, is suitable for reel-to-reel or sheet-to-sheet production as it offers similar ability to pattern on a large scale to the NIL process mentioned in section 1.1. The control of contamination, deformation of the stamp and lateral diffusion of ink are main aspects influencing the quality of the micro-contact printing pattern. Micro-contact printing is subdivided in to two categories, namely direct and indirect printing. In direct micro-contact printing, the polymer solution is directly transferred from the stamp carrier to the substrate; while in indirect micro-contact printing, a polymer or a monomer is selectively deposited on a pre-patterned surface, with subsequent steps of surface-initiated polymerization, electropolymerisation or polymer multilayer deposition to complete the patterning process. Strong interaction between the polymer "ink" and the surface will result in high-resolution patterning; patterns with resolution of ~80nm can be achieved by electrostatic interaction between the ink and the substrate. Micro-contact printing is both a means of pattern transfer and also a soft lithographic technique in its own right, utilised in the patterning and processing of plastics in the fields of electronics, optics, biology and surface science. Once again, however, this is a technique that requires the formation of a master stamp; as such it offers no flexibility and new designs require the fabrication of a new stamp each time.

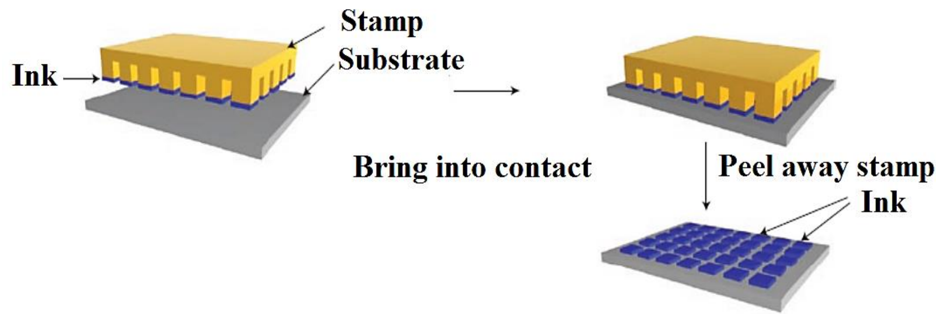

Figure 1.2.1 Schematic of the micro-contact printing process.

Wet Etching

Wet etching refers to a process which involves submersion of the substrate with a patterned PR layer, defined via one of the lithographic processes mentioned earlier, in a chemical solution to dissolve material, thus transferring a pattern into the substrate material. Etch selectivity between an etch mask and the etched materials is achieved in by careful control of the temperature and concentration of the chemical solution. However, wet etching normally produces an isotropic etching profile and the etching rate is strongly dependent on the crystallographic plane exposed. This preferential etching along certain crystal planes in inorganic semiconductors causes undercutting in any deposited sacrificial layer and is unsuitable for the fabrication of high resolution features. Due to the nature of the etchant chemicals this means of pattern transfer is unsuitable in the use of sensitive polymeric materials as the aggressive etchant is likely to attack the bonds within the material- rendering them inert or removing them completely from the substrate.

Dry Etching

Dry etching, so called in contrast to wet etching, is the process by where a material can be etched by bombardment with ions. There are two dry etch processes that are used in the

semiconductor industry and those are physical ion bombardment and pure chemical etching. Physical ion bombardment is where ions, formed by a plasma gas, are fired towards the substrate and physically dislodge material from the surface, achieving etching. The etch rate for this process is relatively low as the rate is related to the energy of the ions combined with the flux rate applied to the substrate. Pure chemical etching is where the surface is etched by chemical reaction, the surface being exposed to a gas of chemicals which react with the surface to create volatile by-products. These volatile by-products then remove themselves from the surface and the etching process continues. If the by-products are not volatile then they remain within the system and disrupt further etching. The etch rate of the chemical etch is strongly dependent on the chemical reaction of the gaseous etchants with the material to be etched. As with wet etching, dry etching is an aggressive means of pattern transfer, using high energy plasma ions or gaseous etchant chemicals to achieve the transfer. Either of these means is unsuitable in the patterning of soft polymeric materials as they would be destroyed in the process. Reactive ion etching (RIE) and inductively coupled plasma (ICP) etching techniques will be detailed in section 4.5

1.3 Conclusions

This chapter has highlighted and outlined the current techniques commonly used in the fabrication of inorganic and inorganic semiconducting materials and devices. This chapter has set the context of the work done in this thesis by allowing a contrast to the classical methods used in micro- and nano- scale fabrication. The techniques for pattern designation covered were photolithography, mask free photolithography, and nanoimprint lithography. These are used to fabricate devices with features below 200 nm but are costly to implement, requiring either an expensive photo-mask or high energy equipment to achieve those results. After the pattern

designation section the means of transferring those patterns into materials and devices were described. The methods discussed were micro-contact printing, wet etching and dry etching. Each have advantages, disadvantages, and areas of applicability. Micro contact printing is swift but requires a pre-made stamp for the pattern transfer, one that is fixed once fabricated. Wet and dry etching are suitable for patterning inorganic materials but the corrosive materials and high energy particles render them unsuitable for more sensitive organic materials. This thesis will explore 3 techniques that offer flexible means of patterning materials on the micro- and nano- scale. These techniques are deliverable via drop-on-demand inkjet printing technology, and dip pen nanolithography.

1.4 Thesis Outline

Several techniques were described in this chapter that are for either pattern designation, pattern transfer or both in one case (Micro-contact printing). Each of these processes has their advantages and disadvantages but there is room for further techniques to fill the gaps between them. In the patterning of soft materials only NIL and micro-contact printing are suitable for deposition and they offer no flexibility with the patterning process- they both require the fabrication of a new mould or stamp with each new design. Mask-free lithography has the potential for flexibility that is required in a research environment but the high energy irradiation beams used in the process have the same drawback that photolithography has; namely that the high energy ion/ electron/ photon beams used will often destroy any soft materials to be patterned. The work to follow in this thesis will explore the ability for inkjet printing and dip-pen nanolithography to provide micro and nanoscale patterning (patterning features down to

~200 nm full width half maximum (FWHM) reported in chapter 4) with a high degree of flexibility for rapid prototyping of soft, polymeric materials. Additionally the ability for these lithographic techniques to be suitable for additive lithography rather than negative lithography will be explored with the aims of demonstrating the hybridisation of inorganic micro-LEDs with organic colour converting polymers, patterning of nanoscale photonics structures, and the ability to pattern soft polymeric materials as a sacrificial mask in the fabrication of electrically addressable nano-LEDs.

Chapter 2 covers relevant semiconductor physics pertaining to photonic devices, beginning with band theory and leading into quantum wells and double heterojunction devices. Polymer physics and basic chemistry is also introduced with details on the theory behind light emitting polymers. Chapter 3 is the first of the results chapters and the Dimatix DMP 2800 inkjet system is detailed. Ink generation for this system is covered which is then shown in inorganic-organic hybridisation work as colour converting micro-LEDs are fabricated. Chapter 4 demonstrates the additive capabilities of dip-pen nanolithography (DPN) with a view to creating nano-scale LED emitters. The negative patterning potential of DPN is explored in chapter 5 where customisable optically active structures are demonstrated in a polymeric membrane. Chapter 6 gives perspectives and future work based on the applications developed throughout the work shown.

1.5 References

1. Kang-Il Ahn, Jae Kyun Kwon, "Color Intensity Modulation for Multicolored Visible Light Communications", IEEE Phot. Tech. Lett. Volume 24, Issue 24. 2254-57 (2012).
2. K. Cui, J. Quan, Z. Xu, "Performance of indoor optical femtocell by visible light communication", Optics Communications, Volumes 298-299, 59-66 (2013).
3. S. Zhang, Z. Gong, J. McKendry, S. Watson, A. Cogman, E. Xie, P. Tian, E. Gu, Z. Chen, G. Zhang, A. Kelly, R.K. Henderson, M.D. Dawson, "CMOS-Controlled Colour-Tunable Smart Display", IEEE Photonics Journal, Volume 4, Issue 5, 1639-46 (2012).
4. J. Clark and G. Lanzani, "Organic photonics for communications", Nature Photonics, Volume 4, 438-446 (2010).
5. M.Wu, Z. Gong, A.J.C. Kuehne, A.L. Kanibolotsky, Y.J. Chen, I.F. Perepichka, A.R. Mackintosh, E. Gu, P.J. Skabara, R.A. Pethrick, M.D. Dawson, "Hybrid GaN/organic microstructured light-emitting devices via ink-jet printing", Opt Express, Volume 17, Issue 19, 16436-43 (2009).
6. E. Gu, A. MackIntosh, A. Kuhne, R.A. Pethrick, C. Belton, D.D.C. Bradley, H.X. Zhang, M.D. Dawson, "Hybrid inorganic/organic micro-structured light-emitting diodes produced by self-aligned direct writing", 19th Annual Meeting of the IEEE-Lasers-and-Electro-Optics-Society (2006).
7. A. A. Damitha, T. Adikaari, D. M. Nanditha, M. Dissanayake, S. Ravi P. Silva, "Organic–Inorganic Solar Cells: Recent Developments and Outlook", IEEE Journal of selected topics in Quantum Electronics, Volume 16, Issue 6, 1595-1606 (2010).
8. B. Guilhabert, D. Massoubre, E. Richardson, J. J. D. McKendry, G. Valentine, R. K. Henderson, I. M. Watson, E. Gu, M. D. Dawson, "Sub-Micron Lithography Using InGaN Micro-LEDs: Mask-Free Fabrication of LED arrays", IEEE Photonics Tech. Letters, Volume 24, Issue 24, 221-24 (2012).
9. Chien-Li Wu, Po-Hung Yao, Chih-Hsien Lin, Cheng-Kuo Sung, Cheng-Huan Chen, "Fabrication of flexible metallic wire grid polarizer using thermal NIL and lift-off process", Microelectronic Engineering, Volume 98, 117-20 (2012).
10. JiHyeong Ryu, HyungJun Lim, Mira Jeong, JaeJong Lee, "A study of contact angles according to the resist thickness and imprint time effects during NIL", Microelectronic Engineering, Volume 98, 210-13 (2012).

11. L. Henrik D. Skjolding, G. T. Teixidor, J. Emnéus , L. Montelius, "Negative UV–NIL (NUV–NIL) – A mix-and-match NIL and UV strategy for realisation of nano- and micrometre structures", Microelectronic Engineering, Volume 86, Issues 4-6, 654-56 (2009).
12. G. Tsiminis, Y. Wang , A. L. Kanibolotsky, A. R. Inigo , P. J. Skabara , I. D. W. Samuel, G. A. Turnbull, "Nanoimprinted Organic Semiconductor Laser Pumped by a Light-Emitting Diode", Adv. Materials, Volume 25, Issue 20, 2826-30 (2013).
13. J. Yu, C. E. Packard, V. Bulovic, "Subtractive contact-patterning of molecular organic films, Organic Electronics", Volume 13, Issue 10, 1779-84 (2012).
14. T. Chen, R. Jordan, S. Zauscher, "Extending micro-contact printing for patterning complex polymer brush microstructures", Polymer, Volume 52, Issue 12, 2461-67 (2011).

Chapter 2

Background on Materials and Devices

2.0 Introduction

The field of application of this work is in the area of photonic devices: the fabrication of LEDs, photonic structures, and the hybridisation of polymeric materials with inorganic LEDs. This chapter will cover the physics behind the aspects of photonics utilised throughout the work, including the operation of LEDs and polymer science.

2.1 Semiconductor Physics

The general definition of a semiconductor is a substance that has an electrical conductivity that increases with temperature and is intermediate between that of a metal and an insulator [1]. The first documented observation of a semiconductor was noticed by Michael Faraday (1833), who discovered that the resistance of silver sulphide decreased with temperature [2], which was different to the dependence observed in metals. In a single atom, electrons occupy discrete energy levels; when more atoms are introduced into a system the number of electrons increases but, due to the Pauli Exclusion Principle, they cannot all occupy the lowest energy state [3]. This results in a splitting of the energy levels by a small amount to achieve discrete energies for the electrons to occupy. As the number of atoms in the system in increased to "N" a crystal lattice can be formed whereby the energy levels have spit to form a continuum and one arrives

at the model of energy bands within materials [4]. The periodic atomic arrangement in a semiconductor crystal results in an energy band structure of electrons creating conduction bands and valence bands, separated by the band gap. The band gap corresponds to the forbidden energy region between the valence and conduction bands. Its value, Eg, determines the wavelength of the light emitted from an LED and is given by equation 2.1.1 [5]:

$$E_g = E_c - E_v \tag{2.1.1}$$

where E_c is called the conduction band minimum and E_v is called the valence band maximum and E_g is normally given in electron-volts.

In the energy bands, the electrons are energetically located close to the minimum of the conduction band while the holes (positive charges corresponding to absence of electrons) are located to the maximum of the valence band.

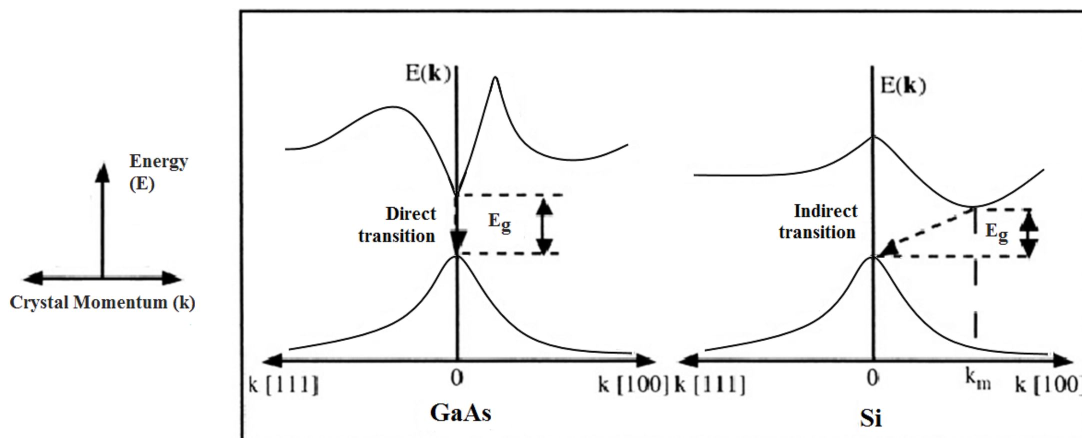

Figure 2.1.1 Energy band diagram for Gallium Arsenide (GaAs) and Silicon (Si) semiconducting crystals, respectively, GaAs in a "direct" band gap material where there is no momentum change for electrons transitioning from the lowest energy in the conduction band to the highest energy of the valance band; Si is an "indirect" semiconductor where a change in momentum is necessary in transitioning from the conduction band to the valence band.

There are two broad categories of semiconductors, namely direct-gap and indirect-gap. Figure 2.1.1 shows a schematic simplified band structure of GaAs and Si, direct-gap and indirect-gap semiconductors respectively, to illustrate these categories. The horizontal axis in the diagram is the crystal momentum, k, which depends on the crystal orientation in the band structure and is directly proportional to the wavenumber (cm^{-1}) [5]. Common representation for k is either in the form of a wave vector in reciprocal space or as crystal momentum, $p_{crystal}$, which is simply $p_{crystal} = \hbar k$.

Alongside the types of semiconductor based on direct and indirect transitions [6] there is also the classification of *intrinsic* and *extrinsic* semiconductors [7]. An intrinsic semiconductor is one whose properties derive from the crystalline material in a highly pure form; Si is one such material and exhibits semiconducting behaviour where there are a low number of defects and contaminants within the crystal. Extrinsic semiconductors have had dopant atoms incorporated into the crystal lattice as they are grown; for extrinsic semiconductors there are those doped to act as negative charge conductors (n-type) and those which are positive charge conductors (p-type). Whether a material is n-type or p-type is dependent on the dopant used during fabrication. The introduction of dopants in the creation of extrinsic semiconductors creates donor and acceptor levels within the band gap for n-type and p-type semiconductors respectively, as illustrated in figure 2.1.2 [8]. In n-type material the charge carriers are

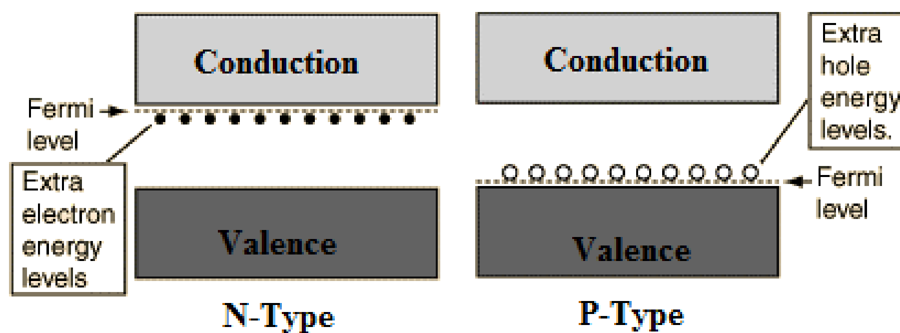

Figure 2.1.2 Illustration of the effect doping has on the energy-band structure in the creation of N-type (left) and P-type (right) extrinsic semiconductors.

electrons, being readily thermally excited from the donor levels to the conduction band. In p-type semiconductors positive "holes" are what carry charge through the valance band, the holes being effectively the absence of electrons. The Fermi level, E_F, is a hypothetical energy level representing the maximum energy of an electron within the material at 0K. Semiconductors and insulators have zero electrons within the conduction band at 0K and thus the Fermi level lies somewhere between E_c and E_v.

The P-N Junction

The fundamental basis of an LED is a p-n junction, where p-type and n-type semiconductors are brought into contact. In n-type materials, the Fermi energy level is close to the conduction band edge and in p-type materials it is near the valence band edge. If the structure is formed by two semiconductors of same material having the same band gap, the term 'homojunction' is used; if the structure is formed by two semiconductors with related structure but different band gap, the term 'heterojunction' is used. When the junction is under zero bias, it is in a thermal

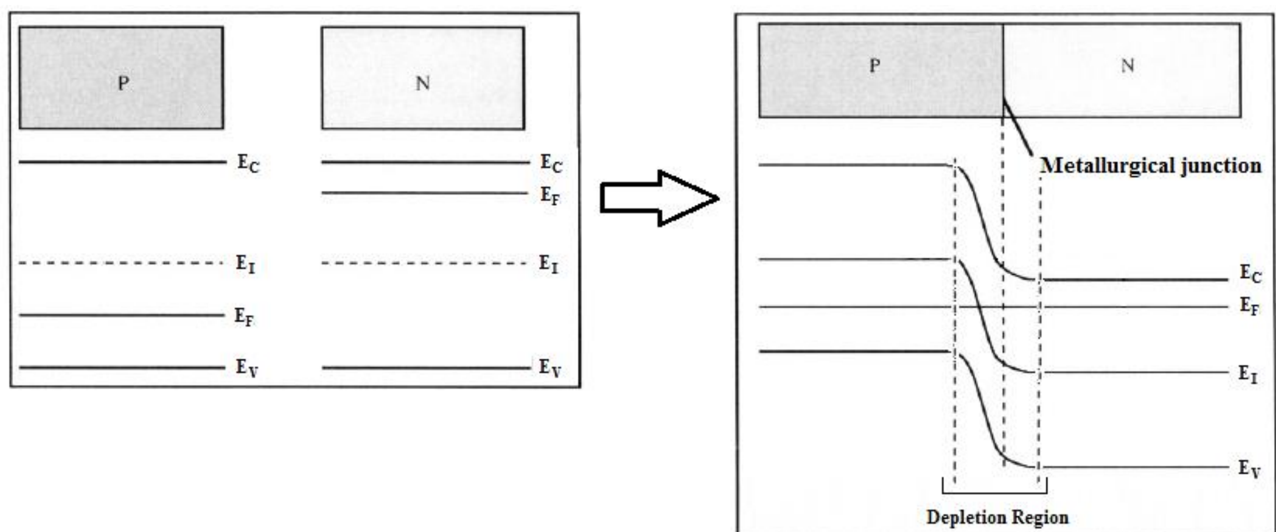

Figure 2.1.3 Illustration of the alignment of Fermi levels, E_F, in a PN junction. The energy levels re-align to create a depletion zone at the junction where electron-hole recombination occurs. Image taken from "Physics of Semiconductors" by J-P. Colinge and C.A Colinge.

equilibrium state and the conduction and valence bands have to bend to accommodate the Fermi energy (E_F) through the junction. The intrinsic energy level, E_i, is the energy level where the probability an energy state is occupied is 50%, when the material is under equilibrium conditions. This thermal equilibrium state is illustrated in figure 2.1.3 and the alignment of E_F causes a bending of the valence and conduction band energy levels in the depletion region.

Once created, a p-n junction can be given forward bias, where the positive electrode of a battery is connected to the p-type semiconductor and the negative electrode is connected to the n-type; or it can be placed in reverse bias, where the positive and negative electrodes are connected to the oppositely charged type semiconductor, as shown in figure 2.1.4.

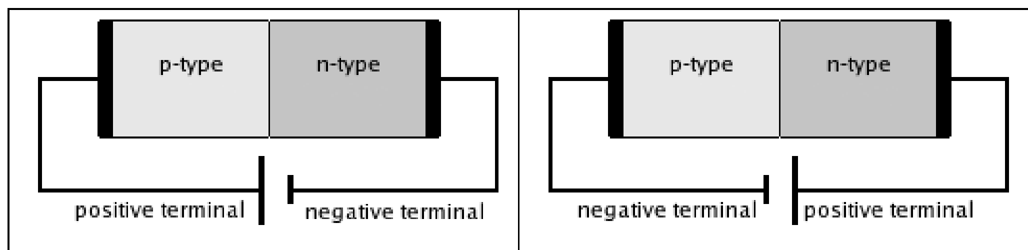

Figure 2.1.4 PN junction under forward bias (left) and reverse bias (right).

In forward bias holes in the P-type region and the electrons in the N-type region are driven towards the depletion zone, reducing its width in the process. The positive charge applied to the P-type material repels the holes, while the negative charge applied to the N-type material repels the electrons. The effect of reducing the width of the depletion zone and increasing the density of charge carriers also has the effect of lowering the barrier in potential. Increasing forward-bias voltage further, the depletion zone eventually becomes thin enough that the zone's electric field cannot counteract charge carrier motion across the p–n junction, as a consequence reducing electrical resistance and charge carriers flow across the junction.

In reverse bias the charge carriers are drawn away from the junction; widening the depletion zone. Under reverse bias the pn-junction prevents the flow of charge through the device. As

the reverse bias is increased there will be no current flow until the point where either Zener or avalanche breakdown occurs [9, 10]. In Zener breakdown the high electric field at the junction allows for tunnelling of charge carriers through the barrier, allowing electrons to tunnels from the valence band to the conduction band and visa versa. In avalanche breakdown the charge carriers are accelerated by the high field and generate electron-hole pairs by collisions with bound electrons. I-V curves for LEDs used here are in section 2.2.

Light Emitting Diodes

In LEDs, the pn–junction is connected in a forward bias configuration, achieving electron and hole flow to give electron-hole recombination at the depletion zone. The wavelength of the light emitted as a result is linked to the band gap of the materials used. Equation 2.1.1 gives the energy for the band gap, E_G and this determines the wavelength for photon emission according to equation 2.1.2;

2.1.2

$$E_G = \frac{hc}{\lambda}$$

Where h is Planck's constant, c is the speed of light and λ is the wavelength. The band diagram for an LED under forward bias is shown in figure 2.1.5 with the shift in the Fermi energy levels being given by the charge on an electron, q, multiplied by the applied external bias, V_a. In electron-hole recombination there are two possible outcomes; the energy can be released either by the emission of photons or as heat (phonons) by increasing the inter-atomic vibrations within the lattice. These two processes correspond to the radiative and nonradiative recombination in

a semiconductor and it is they that determine the internal efficiency of an LED device [11].

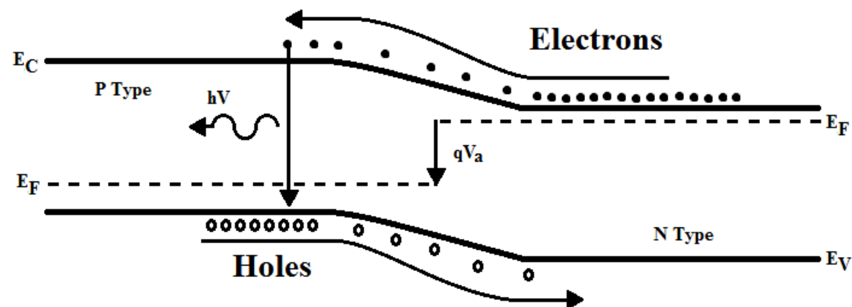

Figure 2.1.5 Illustration of a homojunction pn-junction while operated under forward bias. The vertical scale represents energy and the horizontal scale distance through the junction.

Commonly LEDs are fabricated with double heterojunction structures (DH), where a lower band gap material is confined either side by a higher band gap. The band diagram for such a structure under zero bias is shown in figure 2.1.6. When the lower bandgap material is thin enough ($\leq$ 10 nm, corresponding to the de Broglie wavelength of electrons in the material) the confinement of the electrons by the barrier material has the effect of creating discrete energy levels within the so-called quantum wells [12]. The energy levels present within such a quantum well are determined by the width of the quantum well structure and can (in the case of infinite potential barriers) be calculated by equation 2.1.3. In the equation E is the energy of the level, ħ is the Planck constant divided by 2π, n is a positive integer corresponding to the energy level (n=1 for level 1, etc,), m is effective mass of the charge carrier, and k is defined by equation 2.1.4.

$$E = \frac{\hbar^2 k^2}{2m_{e,h}} \quad (2.1.3)$$

$$k = \frac{n\pi}{L} \quad (2.1.4)$$

Here L is the width of the quantum well. LEDs usually comprise stacked quantum well structures and are referred to as multiple quantum well (MQW) devices. The total energy for photon emission or absorption is given by equation 2.1.5.

$$E = E_g + E_e + E_h \quad (2.1.5)$$

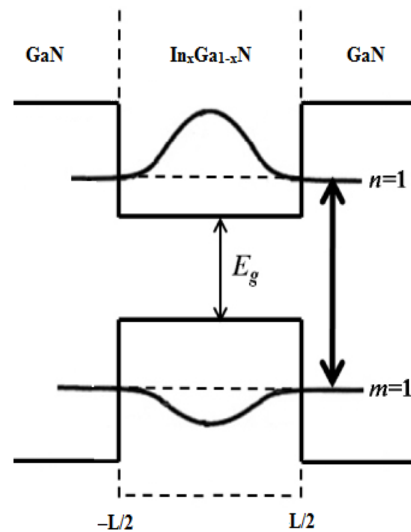

Figure 2.1.6 Example of double heterojunction structure that creates a quantum well, here based on indium gallium nitride between hallium nitride barriers. The energy levels corresponding to n and m are related to the width of the well (L) as well as the size of the energy barrier. Here L is typically 2 – 3 nm.

2.2 GaN LEDs

The devices used in this work were fabricated using gallium nitride (GaN) as the main semiconducting material. As can be seen from figure 2.2.1 indium gallium nitride $In_xGa_{1-x}N$ alloys can achieve emission wavelengths in principle spanning the visible spectrum (although achieving amber/red output is very challenging). In devices containing MQW structures for

emission in the visible region GaN is used as the barrier material with $In_xGa_{1-x}N$ as the lower bandgap well material.

A typical GaN LED device is formed by processing a multi-layer thin-film epitaxial structure, typically grown on a sapphire substrate. Electrical contacts for the n and p electrodes must be on the top surface of the device as the sapphire substrate is electrically non-conducting [13, 14]. The p-metal (Ni/Au) contact utilizes a transparent metal layer to help the spreading of the injected current and provides hole injection, while the n-metal (Ti/Al) contact injects electrons. When a forward bias is applied, electrons and holes are injected via the n-type and p-type GaN layers, respectively, and recombine in the InGaN quantum well active region for light generation. A cross section of a typical GaN LED device is shown in figure 2.2.2, the thickness of the wells and barriers in the MQW structures used in our work being 3nm thick $In_xGa_{1-x}N$ and 7-10nm thick GaN.

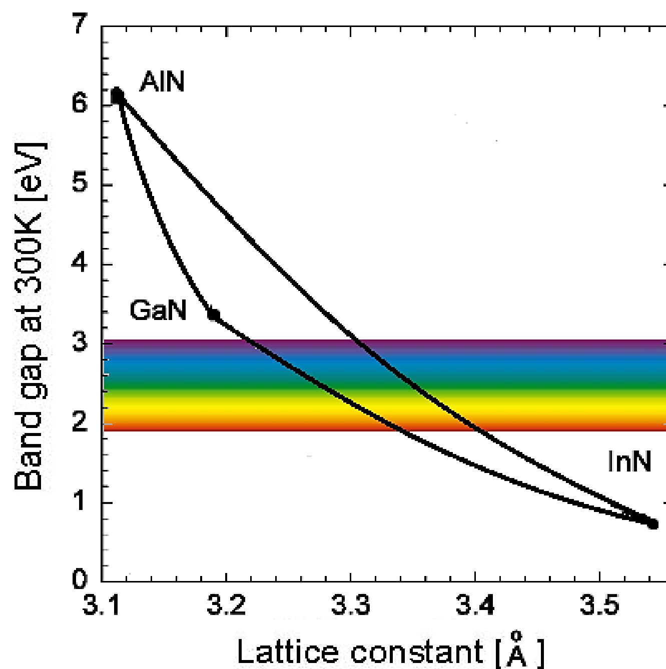

Figure 2.2.1 Bandgaps of group III-nitride alloys as a function of in-plane lattice constant.

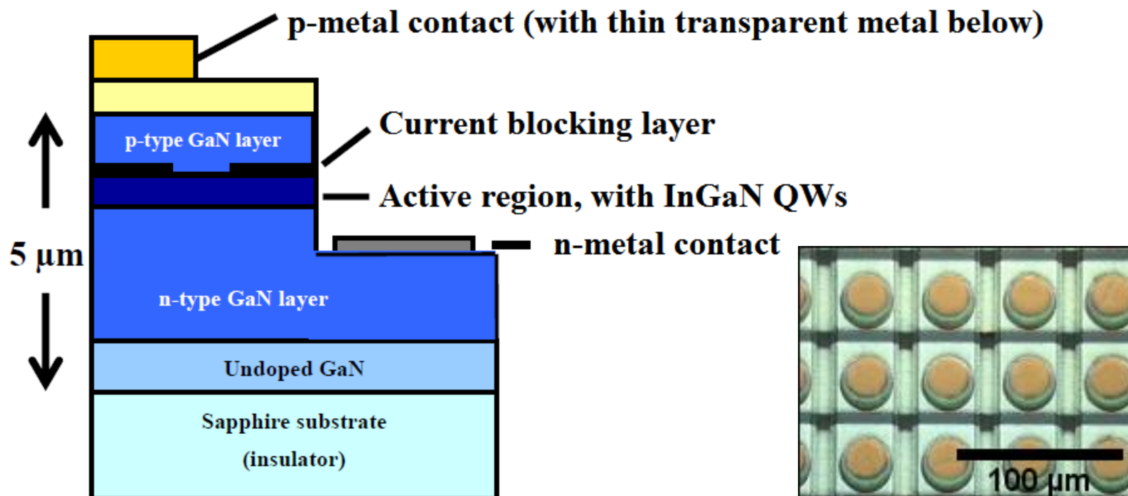

Figure 2.2.2 Cross section of a typical InGaN/GaN quantum well LED structure used in this work (left). Microscope image of disk geometry InGaN/GaN quantum well micro-LED array (right).

Fabrication of these devices is done using the techniques outlined in chapter 1; specifically conventional photolithography is used for the pattern designation combined with Inductively Coupled Plasma (ICP) dry etching which is the key process used in pattern transfer.

GaN Micro-LEDs

Micro-structured light emitting diodes, which form the basis of work described in chapter 3, are defined by shaping the surface of the conventional LED epitaxial layer into emitter pixels of a few tens of microns each in diameter. The individual emitting elements on the single chip are referred as 'micro-LEDs" formed into an array with the potential of assuming any configuration permitted by contacting and lithography including such shapes as disks, stripes and rings. In this work the devices used will be of disk emission geometry with a diameter of 16µm [15]. These micro-LED structures have been used in a variety of applications, including micro-displays, micro-optics and microfluidic systems, mask-free lithography (covered in

chapter 3), and most recently as an optical pumping source for the excitation of grating-patterned organic laser films.

There are two methods of emission for these disk geometry GaN-on-sapphire micro-LEDs, namely "top emission" and "flip-chip". In top emission the light is extracted through the p-side of the device whereas in flip-chip the light is extracted through the n-contact side, through the sapphire substrate. This is illustrated in figure 2.2.3, which shows the light extraction and heat dissipation pathways available for the two modes of operation.

In the top-emitting format, where the light is extracted from the p-side, the thickness of the metal contact layer needs to be as small as possible to prevent light absorption by the metal while maintaining an ohmic contact. However, in the flip-chip format, the metal layer may be made thick enough to also act as a mirror reflector on the p-side. There are different advantages for each configuration; flip-chip emission offers higher power density for extracted light but top-emitting can achieve a higher fill factor due to reduced bonding constraints.

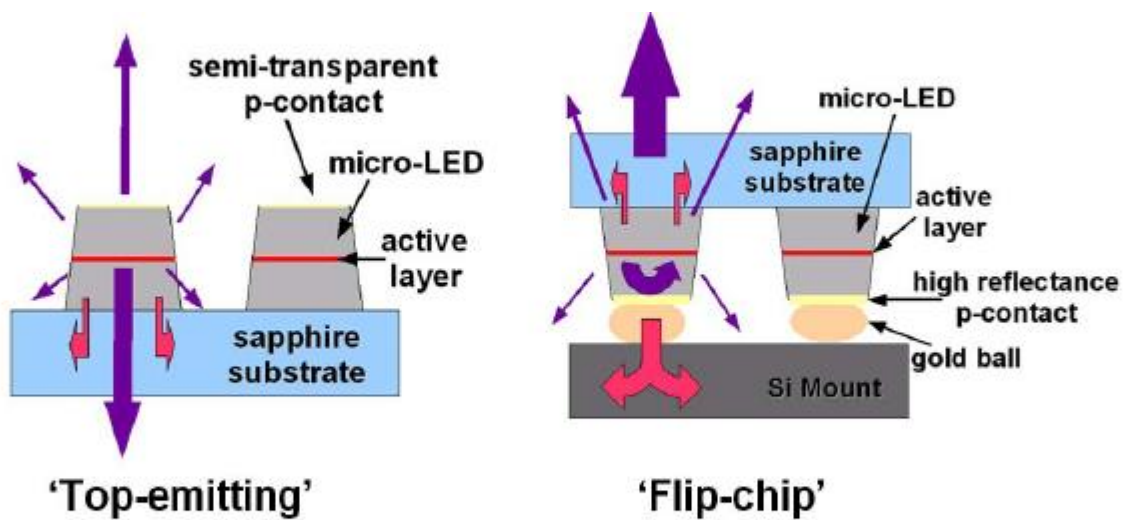

Figure 2.2.3 Top-emitting (left) and Flip chip (right) modes of operation for a GaN-on-sapphire micro-LED device. The purple arrows denote light emission pathways and the red arrows are thermal dissipation pathways.

Matrix-Addressable Micro-LED

One of the types of LED fabricated by our group is that of (row/ column) matrix-addressable top emitting micro LEDs. The work done in chapter 3 is conducted using 64x64 arrays of these micro-LEDs with disc geometry, having a 50 µm centre-to-centre pitch, a 16 µm diameter emissive area per LED, and being matrix addressable via orthogonal rows and columns of metal tracks. The matrix-addressing is completed by p-metal lines running down each column at right angles to the row and forming contacts for each micro-pillar element. The function for this matrix addressing system is that it allows control of individual pixels rather than addressing line by line. In display technology terms this approach with an emissive array provides a significant boost in device efficiency when compared to liquid crystal displays (LCDs) because when a pixel must be "dark" in an LCD the liquid crystal must polarise and prevent light from passing; it does not halt energy consumption in the initial photon generation. In the matrix-addressable LED arrays each pixels can be individually controlled so that only the pixels that are desired to be on are. Combined with control of which pixels are on there is also the potential to apply different bias voltages to different pixels so there can be variations in intensity as and

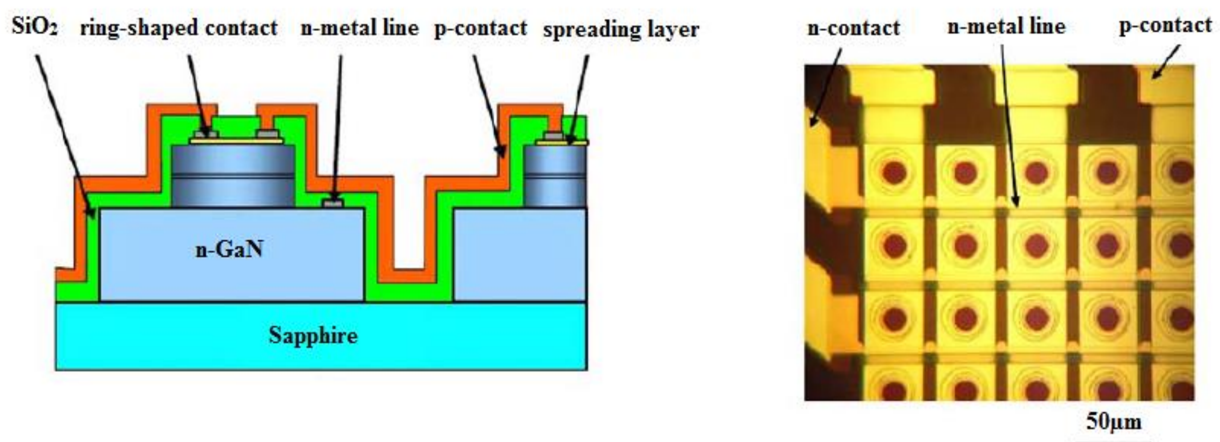

Figure 2.2.4 Schematic cross section of top-emission GaN micro LED with matrix-addressable contacting (left). Plan view microscope image of a section of the 64 x 64 micro-LED array with 50 µm pitch and 16 µm emission diameter (right). Also shown is the matrix of n- and p-contacts that allow for addressing individual pixels within the array.

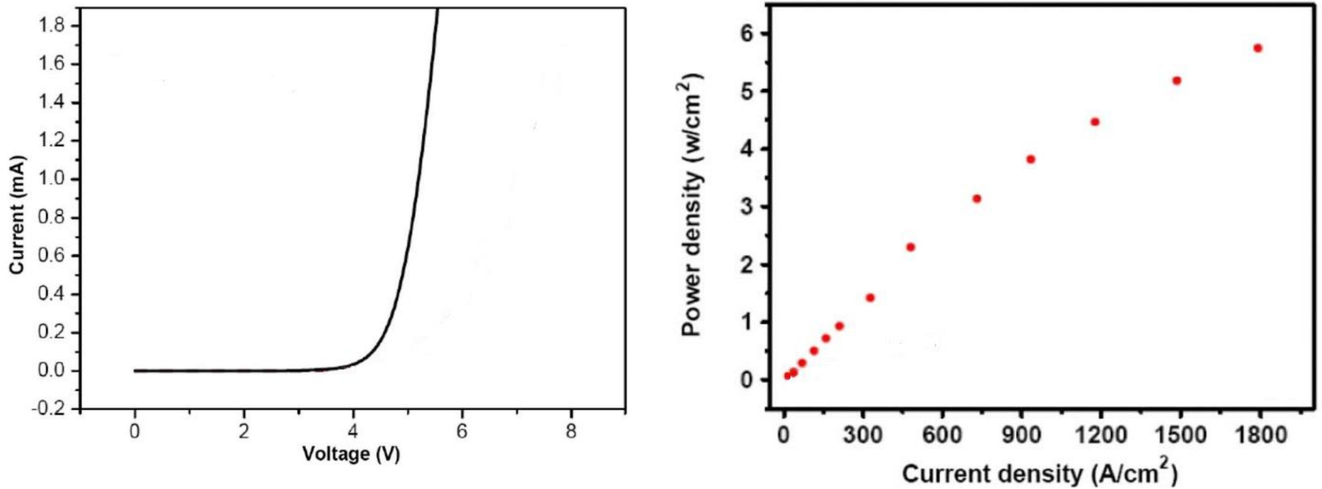

Figure 2.2.5 Typical I-V characteristics (left) and output-power density (right) of a 368 nm device.

when needed. Light- current and current-voltage curves are shown in figure 2.2.5 for a typical device.

Planar LEDs

Another style of device used in this work is that termed the "Planar LED", which differs from the matrix addressable LEDs mentioned earlier in that it is a mesa-free structure, rather than being mesa-etched [16]. The definition of the LED emissive area in this case is achieved by the selective passivation of the p-GaN via plasma treatment to create a current aperture; a photomask is used to protect the area that is to become the emissive area while the rest is exposed. This plasma treatment is applied using Inductively Coupled Plasma (ICP), resulting in electrical passivation of the p-GaN layer above the LED active region. This ICP process is detailed in section 4.5. This means that only the desired active area remains available to be electrically injected for light generation, avoiding mesa etching for pixel definition and dielectric deposition for electrical isolation. The cross sectioned structure of a planar device is shown in figure 2.2.6, alongside an image of a planar LED with an 85 µm diameter. For the

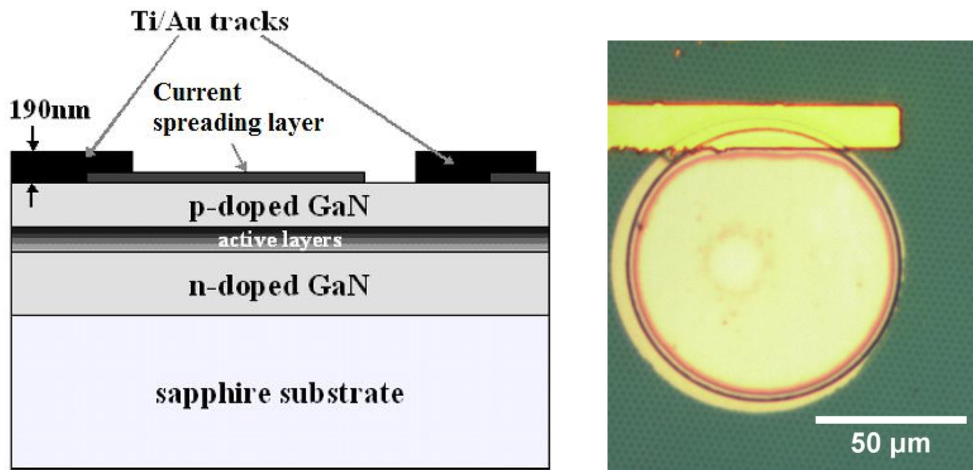

Figure 2.2.6 Cross section of planar LED device (left) and plan microscope image of a planar LED (right) with an 85 μm diameter, a Pd spreading layer and Ti/Au contact track.

devices fabricated by our group, the current spreading layer is either a nickel-gold blend (Ti/Au) or palladium, both acting as suitable current spreading layers but having slightly different electrical properties alongside their differing surface chemistry.

2.3 Polymers

As mentioned earlier, this work concerns the micro- and nano-scale patterning of polymeric materials with an aim of hybridisation with inorganic devices. This section will cover the fundamentals of polymeric materials pertaining to the work that will be covered in this thesis.

Organic Materials

A polymer is a substance that has a molecular structure built up from a large number of similar units bonded together; these similar units are known as monomers. The names "monomer" and "polymer" derive their names from Greek, "*mono*" being one or single, "*poly*" being many,

and *"mer"* meaning part or section. There are many different configurations that polymers can take and they can consist of multiple different monomer units.

① -A-B-B-A-A-B-A-B-A-A-A-A-B-A-B-B-A-B-B-A

② -A-B-A-B-A-B-A-B-A-B-A-B-A-B-A-B-A-B-A-B

③ -A-A-A-A-A-A-A-A-A-A-B-B-B-B-B-B-B-B-B-B

④ -A-A-A-A-A-A-A-A-A-A-A-A-A-A-A-A-A-A-A-A-A-A-A-A-A-

Figure 2.3.1 Representation of the arrangement of 4 basic copolymer types; 1) Statistical or "Random" copolymer, 2) Alternating copolymer, 3) Block copolymer, 4) Graft copolymer. A and B represent different monomer units.

A polymer that is comprised of two different monomers is known as an AB copolymer; the arrangement of the monomer units, dubbed "A" and "B", alters the properties of the polymer; figure 2.3.1 shows some of the basic forms these copolymers may take. In addition there are *"ter"* polymers where there are three monomer units and often there are many units present in a single polymeric structure. As polymers move from single chain to graft polymers there are further possible configurations: where the side chain group terminates with no connection we have a "branched" polymer, if the side chain terminates by linking with another of the backbone polymer then a cross-linked structure is formed. By control of the monomers used, the interaction chemistry and final structure it is possible to create polymers with widely varying properties. Tensile strength, elastic limit, electrical conductivity, light absorption and emission,

and longevity are all variable with careful selection of the monomer units in the polymer fabrication.

Guest-Host System

Widely throughout this work a "Guest-Host" system was employed. This entails loading a bulk material, which is readily processable, with an active material with desirable properties to exploit- in this work light emission that shall be covered later. The host material is one that can contain the guest material without undesired chemical reaction and has a combination of effects, primarily the ability to secure the guest material and fix it in place, secondarily the possibility of acting as barrier to oxygen and water. Denying entry of water and oxygen significantly reduces the rate at which oxidation of polymeric materials can occur and thus will have the effect of extending the lifetime of any air- and/or water- sensitive guest molecules contained within the host; this is known as encapsulation. An encapsulation material called 1,4-cyclohexanedimethanol divinyl ether (CHDV) is used extensively in chapter 3 [17]. The

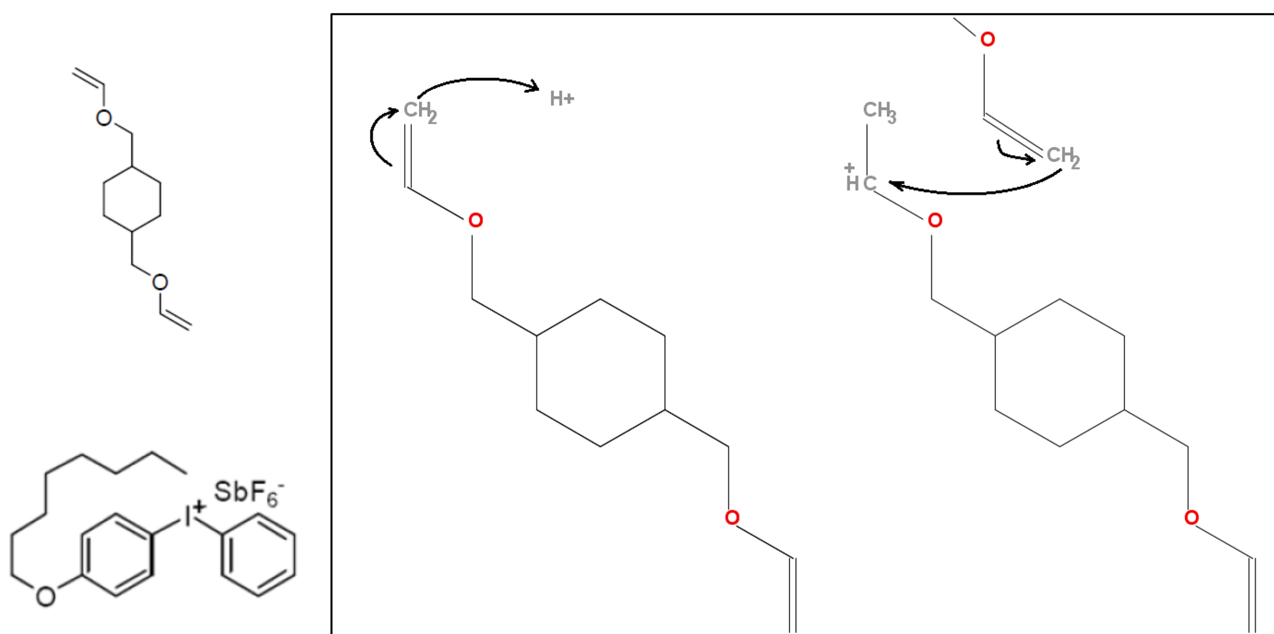

Figure 2.3.2 CHDV monomer unit (top left), DAI-SbF6 photo acid generator (bottom left), Pholymerisation reaction of two monomer units of CHDV (right).

chemical structure of the CHDV monomer units is shown in figure 2.3.2, where it can be seen to have divinyl ether functionalization at both ends, allowing polymerisation to occur at both ends. The CHDV monomer is unreactive in its base state; the polymerisation must be initiated with the addition of positive ions within the system. This is readily achieved by use of a photo-acid generator (PAG) which creates a positive ion when the activation wavelength of light is applied. The PAG used in conjunction with the CHDV is 4–octyloxy–diphenyliodonium hexafluoroantimonate (DAI-SbF6) and generates a positive ion under UV illumination.

The CHDV itself offers near 100% transmission through the visible spectrum and down to 300 nm in the UV range, meaning that when the CHDV is combined with the DAI-SbF6 there is no impedance of the polymerisation reaction due to undesired absorption of the UV light necessary to generate positive ions and initiate photo-polymerisation. Once polymerised the CHDV forms a fully cross-linked structure; being terminated by vinyl ether at each end means the both ends will be tethered and a hard 3D matrix will be formed. Having full transmission in the visible region of light means that the CHDV offers significant advantages as a host material in the region of light emission; allowing encapsulation of light-emissive molecules while showing no inherent re-absorption for the host.

Light Emission in Polymers

When a chain of carbon molecules is connected by alternating single and double bonds (conjugated bonds) the electrons within the bonds become delocalised over the length of the chain, for as long as there are alternating bonds. In light emitting polymers it is this delocalisation of electrons that creates energy levels that are similar in modelling to the "quantum wells" discussed in section 2.1 for inorganic semiconductors. In the case of polymers

the width of the quantum well is defined by the conjugation length. Figure 2.3.3 shows, for illustration, a simple polymer chain with progressively increasing number of double bonds.

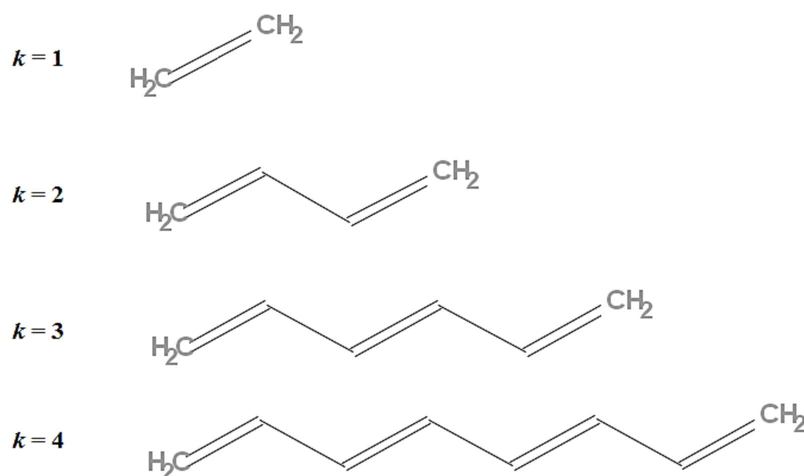

Figure 2.3.3 Conjugated polymer chains with 2k carbon atoms and k double bonds.

Increasing the conjugation length can be modelled as increasing the width of a quantum well, and estimation of the width of the well can be made through observation of the molecule. The average length of a C-C bond (D) is 1.54 Å, and the length of conjugation can be estimated according to equation 2.3.1:

2.3.1

$$L = (2k - 1)D$$

Here k is the number of double bonds and D is the length of the C-C bond. Rearranging equations 2.1.3 and 2.1.4 and substituting ħ as $(\frac{h}{2\pi})$ gives equation 2.3.2:

2.3.2

$$E = \frac{h^2 n^2}{8mL^2}$$

The band gap for such a semiconducting polymer is the difference in energy levels between the Highest Occupied Molecular Orbital (HOMO) and the Lowest Unoccupied Molecular Orbital (LUMO) [18]. This can be estimated by knowing that the free electrons along the conjugation length will fill up the lowest energy levels according to the Pauli Exclusion Principle and that electrons will band-fill up to the n=k state. The band gap is determined by determining the energy between the n = k state and the n = (k+1) state. This is given by equation 3.2.3

3.2.3

$$E_g = E_{(k+1)} - E_k = \frac{(2k+1)h^2}{8mL^2}$$

This model works as an estimation of the band gap energy, however there are several causes for deviation from this model; conjugation length will be reduced due to C-C-C bond angles, 3D twisting of long polymer chains reducing the conjugation length. A long chain polymer with delocalisation along the full length but physical twisting of the polymers is modelled as several smaller chains, each with a length defined by the distance between twists.

In addition to these deviations from the model there are vibrational energy states associated with the HOMO and LUMO levels [19]. These give a broadening of the absorption and emission characteristics as there is now no longer a single energy level for photon absorption or emission. Electrons that reside in a higher vibrational energy state swiftly, in the range of picoseconds, undergo mechanical relaxation to reach the ground state of the energy level they occupy. The additional possibilities are shown in figure 2.3.4 along with typical absorption/emission characteristics. The absorption and emission spectra of the polymer in question will often be close to a mirror image of each other, with the emission of course at

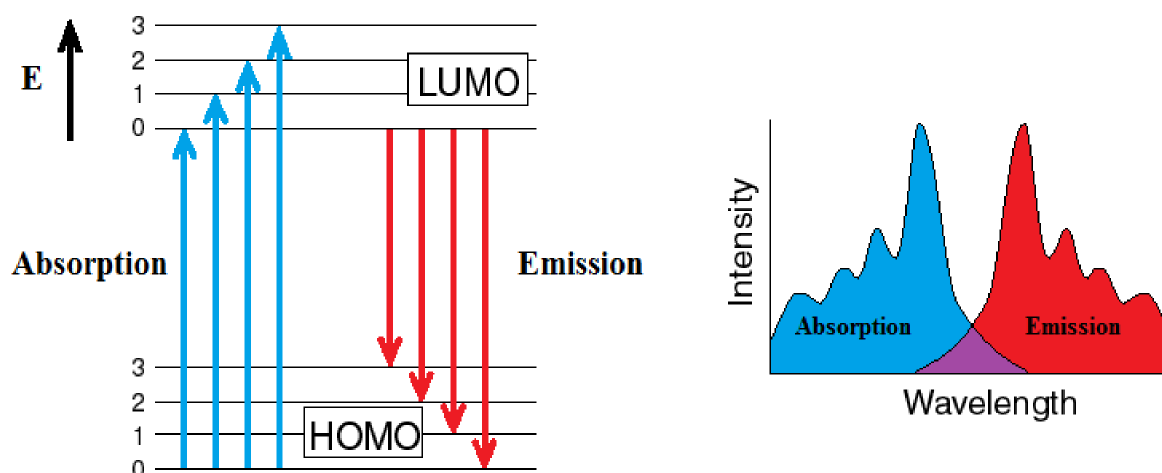

Figure 2.3.4 Energy level diagram for the HOMO and LUMO levels in a polymer showing vibrational energy levels 1-3 for each (Left). Representative absorption and emission characteristics of a polymer; peaks in absorption or emission correspond to different vibrational energies (Right). The shift in energy between absorption and emission is known as the Stokes shift.

lower energy than the absorption. This makes light emitting polymers a good candidate for colour conversion as they have the capability of strongly absorbing high energy photons, converting to a lower energy and efficiently re-emitting. These polymers were synthesised at the University of Cologne, Institut für Physikalische Chemie by Alexander Kuehne.

2.4 Light Emitting Polymers

As mentioned in section 2.0 the work done for this thesis will develop tools for patterning soft materials with aims for photonic applications. This section will detail the optically active light emitting polymer (LEP) materials used; chemical composition as well as the features that make them desirable for the roles they find within this work are presented.

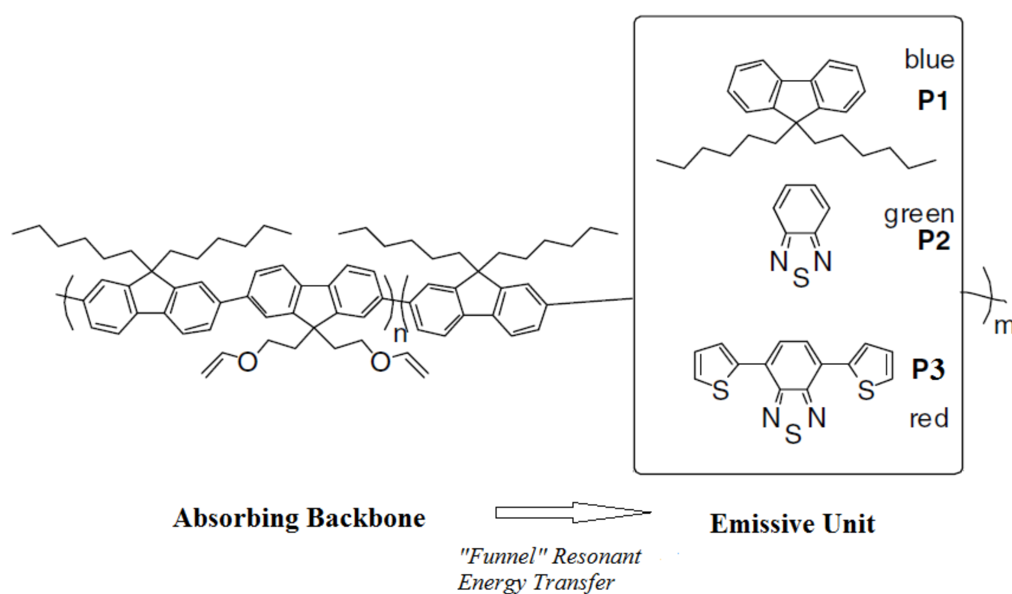

Figure 2.4.1 Skeletal structure for the three polymers used; each share a common backbone for absorption. The specific terminating polymer P1, P2 or P3 determines the emission wavelength of the polymer. Termination with P1 results in blue; P2 in green; and P3 in red. Image adapted from Alex Kuhne [20]

Cross-Linkable LEPs

Section 2.3 covered the mechanism for light emission in polymer materials; electron transitions from an excited HOMO to a LUMO, with photon emission as a result. Typically the absorption and emission spectra are tightly bound so that the absorption will be at an energy just higher than the observed emission. The group of materials used in Chapter 3 are a group of vinyl ether functionalised polymers that have a common absorbing backbone. The HOMO level can undergo a non-radiative energy transfer along the backbone to a separate emission molecule, thereby achieving emission at a wavelength greatly shifted from the original absorption energy [20]. This energy transfer method is known as “funnel resonance energy transfer” which is a specialised case of Förster-Resonance Energy Transfer (FRET). FRET is an energy transfer mechanism where a donor chromophore in the excited state can transfer energy to an acceptor

chromophore via nonradiative dipole – dipole coupling. The efficiency of this interaction is strongly dependent on distance, efficiency $\propto r^{-6}$. These polymers utilise funnel resonance transfer whereby the backbone of the molecule is a chain of conjugated electrons linking the donor and acceptor chromophores. Energy transfer occurs along this delocalised backbone. There are three such polymers used in Chapter 3 that share a common absorption wavelength while having different emission spectra. In these polymers, shown in figure 2.4.1, the monomer units are, respectively, 2,7-dibromo-9,9-(dihexyl)fluorene for the blue-emitter P1, 4,7-dibromo-2,1,3-benzothiadiazole for the green-emitter P2, and 4,7-bis(5-bromo-2-thienyl)-2,1,3-benzothiadiazole for the red emitter P3. The absorption peak for each of the three polymers is at a wavelength of ~370nm with peak emissions at 418nm for P1; 545nm for P2; and 645 for P3. Further details of the absorption and emission characteristics of these materials will be covered in chapter 3.3.

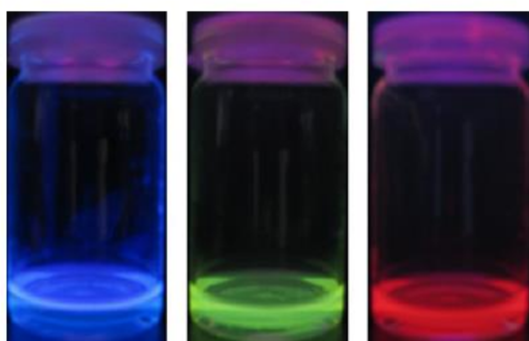

Figure 2.4.2 Images of the polymers P1-P3 integrated into CHDV with 368 nm UV illumination. Image courtesy of Alex Kuhne. [20]

An additional feature of these polymers is that they also have a vinyl ether functionalization, which is similar to that of CHDV discussed in section 2.3. These materials were designed to be integrated within the CHDV matrix and as such the vinyl ether functionalization is readily incorporated into the cross-linking polymerisation reaction. This means that rather than having the “host” material in the guest-host system merely hold the materials in place, the cross-linking LEP materials are actively part of the matrix structure that is formed. This permits ready

integration of the guest and host materials without issues of solubility inhibiting the process. As the CHDV is transparent in the visible spectrum there will be no issues of re-absorption of the light emitted from the LEP materials while cross-linked. Images of the LEPs integrated within the CHDV matrix with 368 nm UV illumination are shown in figure 2.4.2. With their common absorption wavelength and colour conversion to the red, green and blue these materials are used in Chapter 3 to demonstrate micron-scale fabrication of hybridised organic-inorganic photonic devices.

Lasing Polymer

In Chapter 5 a π-conjugated polymer is used in the creation of a polymer laser. The polymer, poly[2,5-bis(2',5"-bis(2"-ethylhexyl oxy)phenyl)-p-phenylene vinylene] (BBEHP-PPV), was originally designed for use in chemo-sensing applications [21]. Our samples of BBEHP-PPV were synthesised by Professor P. Skabara's group at the University of Strathclyde. BBEHP-PPV exhibits peak absorption at 431 nm and absorbs down into the UV and has emission peaks at 496 nm and 528 nm in the green. The skeletal structure is shown in figure 2.4.3 alongside the absorption and luminescence data. When transitioning to laser emission under increased optical pump intensity, the 528 nm peak becomes dominant and is the main peak. The usually low lasing threshold (40 nJ cm^{-2}) of this material when carefully prepared permits lasing when patterned with a distributed feedback grating structure. With a DBR structure this material is used in chapter 5 to demonstrate the nanoscale patterning potential of dip-pen nanolithography as a viable tool in the field of photonics.

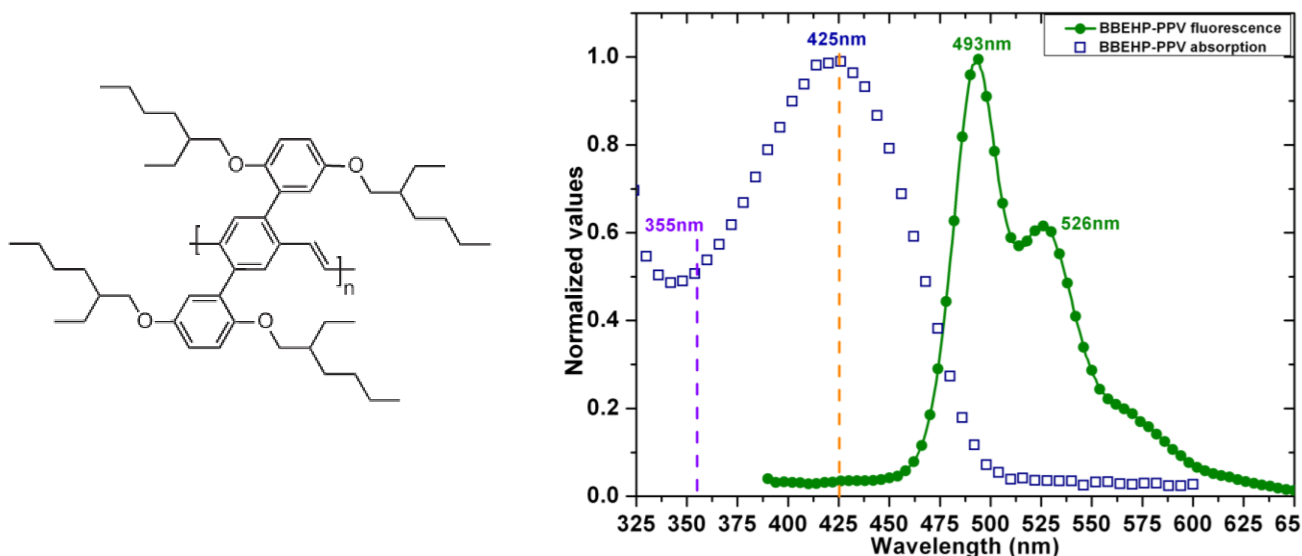

Figure 2.4.3 Skeletal structure of BBEHP-PPV polymer (left), absorption and luminescence data (right)

2.5 Conclusions

This chapter has covered the relevant basics of both inorganic and organic semiconductor physics. We have introduced the elements that are used to demonstrate the effectiveness of the patterning techniques covered in chapters 3-5. The top-emitting matrix addressable LEDs from section 2.2, emitting at 370 nm, are coupled with the guest-host system of CHDV and the LEPs, covered in section 2.3 and 2.4, to achieve hybridised colour conversion in chapter 3. The BBEHP-PPV lasing polymer is shown to be successfully patterned down to the nanoscale in chapter 5 with a Distributed Bragg Reflector (DBR) structure that lowers the threshold for stimulated emission. The planar LEDs from section 2.2 will be the basis for work covered in chapter 4 coupling the ability for dip-pen nanolithography to pattern photoresist and a novel room-temperature ICP plasma etch to define LEDs with a 3μm FWHM.

2.6 References

1. http://www.merriam-webster.com/dictionary/semiconductor
2. L. Łukasiak, A. Jakubowski, "History of Semiconductors", JTIT, Volume 1, Pages 3-9, 2010.
3. http://chemwiki.ucdavis.edu/Inorganic_Chemistry/Electronic_Configurations/Pauli_Exclusion_Principle
4. J-P Colinge, C.A Colinge, "Physics of Semiconductor devices", Page 7-8.
5. J-P Colinge, C.A Colinge, "Physics of Semiconductor devices", Page 2.
6. S. M. Sze, K. K. Ng, "Physics of Semiconductor Devices", Page 52.
7. http://www.doitpoms.ac.uk/tlplib/semiconductors/intrinsic.php
8. K. Rajagopal, "Textbook Of Engineering Physics, Part 2", Pages 37-38.
9. J-P Colinge, C.A Colinge, "Physics of Semiconductor devices", Pages 117-118.
10. M. C Jain, ""Textbook Of Engineering Physics, Part 2", Pages 181-182.
11. M. Fox, "Optical Properties of Solids", Pages 93-94.
12. M. Fox, "Optical Properties of Solids", Pages 119-123.
13. Xu Lin Nguyen, Thi Ngoc Nhien Nguyen, Vinh Thang Chau and Mau Chien Dang, "The fabrication of GaN-based light emitting diodes (LEDs) ", Advances in Natural Sciences: Nanoscience and Nanotechnology, Volume 1, Issue 2, (2010).
14. H. X. Zhang, D. Massoubre, J. McKendry, Z. Gong, B. Guilhabert, C. Griffin, E. Gu, P. E. Jessop, J. M. Girkin, and M. D. Dawson, "Individually-addressable flip-chip AlInGaN micropixelated light emitting diode arrays with high continuous and nanosecond output power", Optics Express, Volume 16, Issue 13, Page 9918 (2008).
15. Z. Gong, H. X. Zhang, E. Gu, C. Griffin, M.D. Dawson, V. Poher, G. Kennedy, P.M.W. French,M.A.A. Neil, "Matrix-addressable micropixellated InGaN light-emitting diodes

with uniform emission and increased light output" , IEEE Transactions on Electron Devices 54 , 2650-2658, 2007.

16. D. Massoubre, E. Xie, B. Guilhabert, J. Herrnsdorf, E. Gu, I. M Watson and M. D. Dawson, “Micro-structured light emission from planar InGaN light-emitting diodes”, Semiconductor Science and Technology, Volume 29, Number 1 (2014).
17. A. Hernandez-Santana, A. R. Mackintosh, B. Guilhabert, A. L. Kanibolotsky, M. D. Dawson, P. J. Skabara, D. Graham, “Dip-pen nanolithography of nanostructured oligofluorene truxenes in a photo-curable host matrix”, Journal of Materials Chemistry, Issue 37, Pages 14209-212 (2011).
18. A. Pron, P. Rannou, “Processible conjugated polymers: from organic semiconductors to organic metals and superconductors”, Progress in Polymer Science, Volume 27, Issue 1, Pages 135-190 (2002).
19. M. Fox, “Optical Properties of Solids”, Pages 167-173.
20. A. J. C. Kuehne, A. R. Mackintosh, R.A. Pethrick, B. Tieke, “Novel vinyl ether functionalized fluorene polymers for active incorporation into common photoresist matrices”, Tetrahedron Letters 49, 32, 4722-4724 (2008).
21. A. Rose, Z. Zhu, C. F. Madigan, T. M. Swager, V. Bulovic, “Sensitivity gains in chemosensing by lasing action in organic polymers”, Nature, Vol 434, Issue 7035 (2005).

Chapter 3

Additive Lithography via Inkjet Printing

3.0 Introduction

This chapter reports a means of additively patterning soft, transparent and photoactive compounds on the micron scale. Inkjet printing technology is used for its ability to deposit material only where desired, to generate patterns without requiring exposure to UV light in either positive or negative photoresist. In addition inkjet printing is a very swift process that offers high area scalability for large scale production. A Dimatix™ DMP 2800 inkjet printer was used as it offers droplet volumes down to 1pL, permitting the deposition of features down to below 10µm in diameter. This ability to deposit micron scale materials is utilised in the field of optoelectronics and the hybridisation of inorganic LEDs with organic materials. Two techniques for inkjet printing are demonstrated: deposition of optically active colour converters onto a micron sized 370 nm emitting LED (16µm diameter) to create red, green and blue emitting pixelated arrays with colour conversion efficiencies of up to 31%; also printing of silver metallic inks was used in the fabrication of high fill factor (99%) GaN LEDs that were fabricated entirely in the absence of lithographic stages involving hard masks.

3.1 Background

Micro-scale fabrication has a plethora of uses in modern-day society, including integrated circuits, lab-on-chip, micro-electro-mechanical systems (MEMS), and biosensors, to name but a few [1,2]. Techniques used towards these ends including optical lithography, micro-machining, chemical and ionic etching, as well as shadow masking, are commonplace in industry [3]. Most of these techniques are based on the removal of material to form a pattern, be that in “curing” an area to create/ preserve a structure or etching only the specified area. Additive lithography relies on these removal stages to expose the patterns where material is later to be added. In the last couple of decades so called “soft” techniques [4] have risen in popularity for their ability to pattern materials that are not compatible with the harsh ultraviolet exposure common in classical lithography. In particular inkjet printing has become a viable option [5,6] as the technology has developed to the point where the ejected volume per droplet is small enough to realistically permit patterning on a scale comparable to the more established methods. This technique offers some advantages such as the ability to specifically add material to a location without laborious stages of protection and removal. In the work described below the ability for the inkjet printer technology to aid in the field of photonics will be explored.

There are several methods that are commercially used for the generation of multi-colour displays including liquid crystal displays (LCD), plasma, and light emitting diode (LED) displays [7-9]. LCD displays use controlled polarisation filters to achieve red, green and blue (RGB) emission, the disadvantage of this being that the device must be backlit and every pixel must be on continuously. To achieve a “dark” pixel the polariser must filter all the light from that pixel which is both electrically and optically inefficient. Plasma technologies use charged electrodes to create an ionized gas which is electrically conductive, with collisions within the

gas resulting in emission of ultraviolent (UV) radiation. This UV light is colour converted into the visible spectrum by a phosphor coating within the pixel absorbing the UV, with the wavelength generated dependent on the phosphor used. The disadvantage of this methodology is that the electrical consumption is large, much larger than for an LCD, and the phosphor undergoes heat degradation [10] under extended operations resulting in a shadow image projected onto the screen. LED displays are highly efficient in their electrical to optical conversion but only for monochrome purposes. LED devices are manufactured using doped semiconducting wafers, and as covered in Chapter 2, a specific semiconductor alloy structure creating a specific band gap which defines the wavelength of light generated by that wafer. To achieve RGB displays it is therefore necessary to package many discrete LED emitters with different device structures to achieve multiple wavelength emission. This restricts the possible resolution of such a device and is costly both monetarily and in time to produce.

The following work utilises the capabilities of inkjet printing to pattern soft, transparent and photoactive compounds towards the fabrication of photonic devices. The process enables the combination of the high electrical-to-optical conversion efficiency of LEDs with colour converting media to realise multiple colour displays from one semiconductor wafer. Manufacture of micron-scale LED devices with the ability to individually address independent pixels is possible [11,12]; integration of colour converters which can convert the LED light in a low cost and high response speed manner would allow for multi-colour hybrid devices. Advantages would include high resolution; fast light emission modulation if required; individual pixel addressing permitting a higher degree of colour control by varying the bias applied to red, green and blue pixels; and increased energy efficiency as "dark" pixels would truly be unpowered rather than always active and having their emission blocked by filters. Inkjet printing offers attractive features for the integration of organic colour converters as it is

high speed and low cost, requiring no masking, and material efficient, allowing drop-on-demand (DoD) [13] functionality of materials to be deposited exclusively on the emissive area of the pixel.

3.2 Inkjet Printing Technology

Inkjet printing technology has demonstrated a wide range of applications including deposition of conductive materials, fabrication of organic transistors, 3D Electronics, deposition of monolayers and in LED fabrication. In the field of photonics, inkjet printing offers the ability to fabricate organic LEDs (OLEDs) [14], to hybridise materials with inorganic devices [15-18], to deposit metallic contacts for device interconnection [20,21], amongst other applications. The inkjet printer offers several attractive functions that are suited for soft additive lithography. A Dimatix DMP2800 research grade inkjet printer, shown in figure 3.2.1, was utilised for this work. This offers droplet-on-demand (DoD) technology permitting the deposition of ink only in the locations desired, rather than using a mask and later removing material by some other means. Thus several inks can be deposited in a variety of patterns relatively swiftly without intermediate steps to define the pattern.

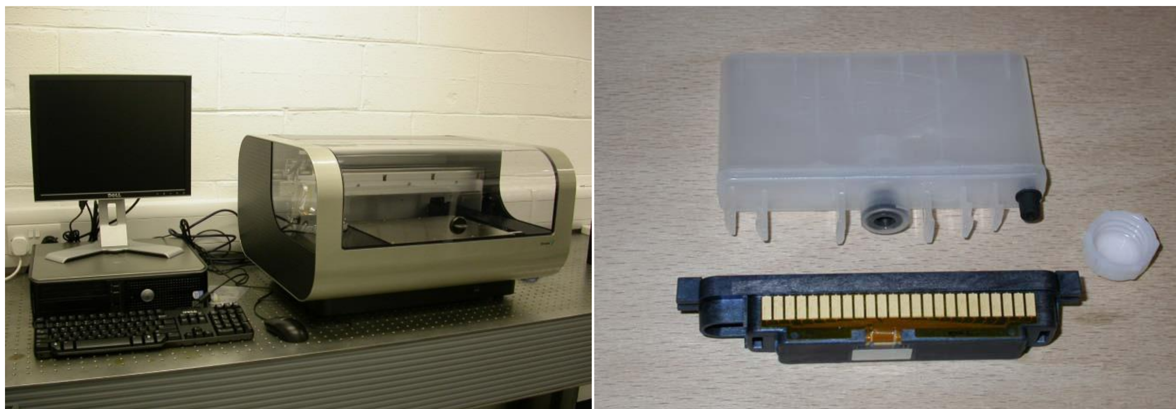

Figure 3.2.1 Left, photograph of inkjet printer with computer control. Right, image of the inkjet cartridge pre-assembled.

The ink cartridges used in this work are shown in figure 3.2.1 and eject either 1pL or 10pL droplets, determined by the diameter of the ejection nozzle. The droplet formation is controlled by a combination of factors including the viscosity and surface tension of the fluid, the presence of particulates, and the ejection parameters used with the actuator. Throughout the years that inkjet technology has been available, much work has been done in the field of droplet creation, specifically on the actuating electrical waveform that controls droplet formation. This waveform defines the voltage and deflection applied to the micro electromechanical (MEMS) actuator that controls droplet ejection. The cartridges for the DMP 2800 utilise an "N"-type profile as illustrated in figure 3.2.2, giving the best droplet formation. Secondary droplets, called orbital droplets, can be generated upon fluid ejection which have a dramatic effect on the accuracy and precision of deposition. Thus it is important to adjust the ejection profile to reduce the risk of this occuring. The Dimatix DMP2800 printer has an A4, 210mm x 260mm, xy substrate stage which is also a vacuum platen and hot plate operating up to 60°C. Depositing an ink involves tracking the printer cartridge across the substrate and moving the xy stage. The repeatability of this printer is ±25μm, meaning the ability to place a droplet on top of those previously deposited has some restrictions [22].

A key characteristic of the printer used in the work is the DoD printer cartridges. Inkjet printers utilise a constant stream of ink which is directed into an excess trough by electrically polarised plates. The patterning is controlled by either allowing the droplet to pass by the trough or to be caught. The inkjet printer heads in the DMP2800 use MEMS actuators that allow for droplet ejection only when desired. This results in a greatly increased efficiency in the printing technology, using a greatly reduced ink volume, beneficial in a reseach environment with the use of exotic materials in limited supply. In addition the reduced droplet volume enables micron scale patterning of materials. The process sequence diagram for fluid ejection is shown in

figure 3.2.2, showing the modulation of the MEMS actuator that achieves single droplet ejection. At the standby position the fluid chamber is slightly depressed. When jetting is to be initiated phase 1 begins and the firing pulse decreases the voltage to zero, bringing the piezo back to a neutral straight position with the chamber at its maximum volume and thus drawing fluid into the chamber through the inlet. In addition there is a draw on the meniscus at the nozzle, as shown in Figure 3.2.2 (b). The main drop ejection occurs in phase 2 where the chamber is compressed and pressure generated to eject a drop- see Figure 3.2.2 (c). The final phases are for recovery, where the piezo voltage is brought back down and the chamber decompresses, partially refilling in preparation for the next pulse (phases 3+4).

Once the droplet is formed and has detached from the nozzle the droplet shape becomes important; orbital droplet formation, droplet tail development and droplet accuracy are factors

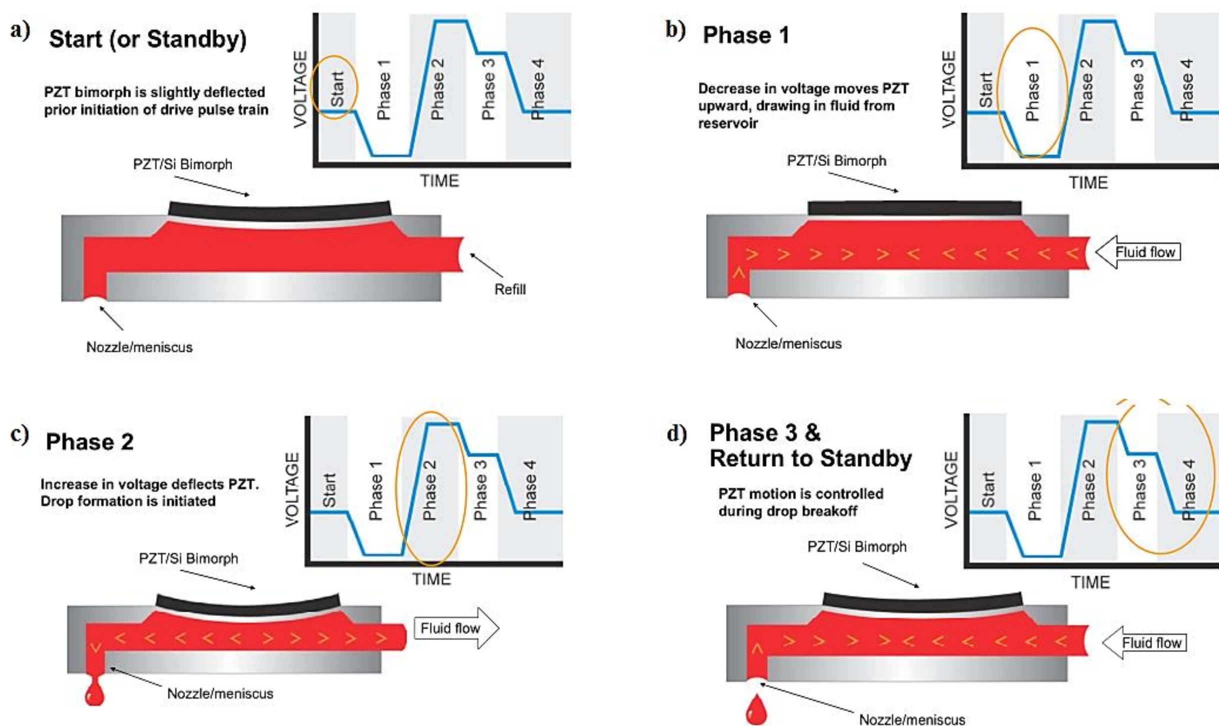

Figure 3.2.2 Flow diagram depicting the "N" type MEMs ejection waveform for the inkjet nozzle at rest (a), drawing fluid from the well (b), initial droplet formation (c), droplet breakoff and return to standby (d). Image reproduced from the Dimatix DMP2800 manual.

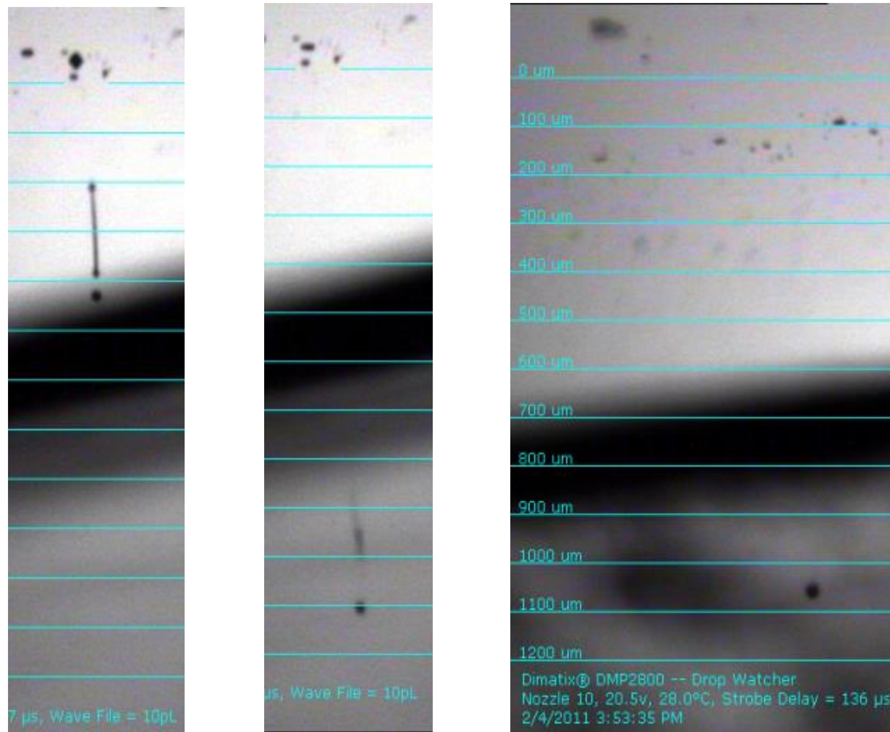

Figure 3.2.3 High ejection voltage resulting in large tail formation in ink-jetting, left. Tail separation resulting in secondary orbital droplets, middle. Optimal ejection of a droplet resulting in no tail or resultant orbital droplets, right.

contributing to the viability of the printing technology. Camera image examples of large tail formation and orbital droplet formation are compared to ideal droplet ejection in figure 3.2.3. Control of the fluid parameters as well as the ejection voltage and waveform contribute to the ultimate droplet formation. The fluid parameters [23] for ejection require the fluid viscosity to be between $1.0x10^{-2}$ - $1.2x10^{-2}$ Pa.s at the operating temperature. The printhead can be heated up to 70°C to lower the working viscosity if the fluid is viscous. Surface tension should be between 0.028 - 0.033 Nm^{-1}. Typically a surfactant is added to water-based fluids to achieve this surface tension range. High surface tension or viscosity fluids (up to 0.06 Nm^{-1} or $3.0x10^{-2}$ Pa.s) may be jetted with limited performance. Increasing the ejection voltage increases the droplet velocity and may allow for ejection of a fluid with non-ideal fluid properties, but there is a trade off with the formation of long tails and orbital droplet formation. To ensure accurate positioning the nozzle needs to remain clear of obstruction and particulates and to ensure this

the ink must be filtered prior to insertion into the cartridge. The fluid can be removed from its storage container, and a syringe filter is put on the end of the syringe in front of the needle used to load the cartridge. Any particles in the fluid should be ~1/100th the size of the nozzle. The effective diameter of the nozzle is 21.5μm, so any particle, polymer or aggregate should be less than 0.2μm.

3.3 Ink Preparation and Design

Design of the ink to be used in the integration of colour converters is a key part of realising hybridised LED multi-colour emitters. As mentioned in section 3.1 there are strict fluid parameters that can be jetted; the ink must be within these parameters yet give the functionality desired for optical conversion. A guest-host system, as introduced in section II, was utilised where a jettable host material can be loaded with colour converting material. The host matrix can serve multiple functions simultaneously, acting as the main jetting fluid, with the pre-requisite properties; as a means of fixing the deposited droplet in place, via polymerisation; and for oxidisation protection, shielding delicate compounds from oxygen or water that may degrade performance over time. Additionally the matrix serves to eliminate a "coffee stain" effect that is readily apparent in solvent-only inks. The solvent dries most rapidly at the edge of the deposited droplet and draws the load material away from the middle towards the edge. When completely dried the material is deposited in a ring shape dubbed a "coffee stain". When attempting to deposit material onto a circular LED emitter it is desirable to have colour converter spread over the whole emitter rather than adhered to the edge. This results in more colour converting material retained over the LED and thus to enhance the efficiency of the hybrid device. The host matrix used in this work is 1,4-cyclohexyldimethanol divinyl ether

(CHDV) introduced in Chapter 2 [26] which, when combined with a photo acid generator (PAG) molecule, undergoes a polymerisation reaction when illuminated by 254nm wavelength light. Figure 3.3.1 shows (c.f. also figure 2.3.2) the CHDV monomer unit; the PAG molecule, 4–octyloxy-diphenyliodonium hexafluoroantimonate; and the polymerisation reaction that occurs when the PAG undergoes UV stimulation. Upon exposure to 254nm UV light the PAG dissociates and produces an H^+ ion, causing cross-linking of the CHDV monomer and immobilising the colour converting material in a solid polymer matrix.

This host matrix system has the desired fluid properties for inkjet printing combined with a high transparency throughout the UV and visible spectrum. This transparency is crucial for the hybrisisation work to achieve high optical conversion efficiency by minimising absorption of light emitted both from the underlying LED and that converted into the visible spectrum. The

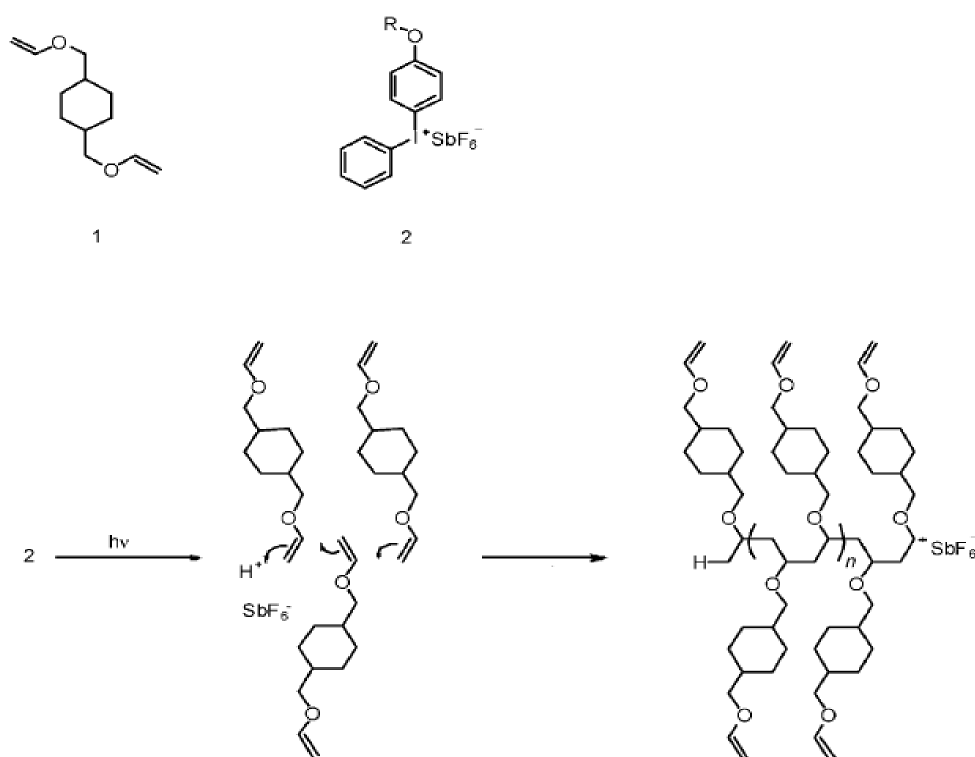

Figure 3.3.1 Top left: CHDV monomer unit, top right: the PAG used to initiate polymerisation, bottom: the polymerisation reaction that occurs when the PAG is stimulated to lose a H+ ion under UV stimulation.

light emitting polymer (LEP) materials used are co-polymers based on a polyfluorene backbone, all with a similar UV-blue absorption spectrum peaking at 370 nm (see figure 3.3.2). The emission characteristics however are tuned by selecting different emissive monomer units. As a reminder, these are respectively 2,7-dibromo-9,9-(dihexyl)fluorene for the blue-emitter **P1**, 4,7-dibromo-2,1,3-benzothiadiazole for the green-emitter **P2**, and 4,7-bis(5-bromo-2-thienyl)-2,1,3-benzothiadiazole for the red emitter **P3** [25].

Following excitation of these materials at 370 nm, resonant energy transfer 'funnels' the energy rapidly along the conjugated polymer backbone from the absorbing donor fluorene unit to the acceptor emissive unit (P1, P2 or P3). Reported characterisation for these materials [25] gives internal photo-luminescence quantum yield (PLQY) efficiencies of 63%, 45% and 31% for the blue, green and red materials, respectively, when excited at 370nm in toluene solution. The internal PLQY is solely the conversion efficiency of the colour converting unit and does not take into account the transfer efficiency to the converter or the efficiency of out-coupling the light. Once all these factors are taken into consideration you achieve the external quantum efficiency. The decrease in PLQY with increasing emission wavelength is due to a reduced spectral overlap between the emission of the polyfluorene backbone and the absorption of the emissive unit [18]. The conjugated polymers are functionalised with divinyl ether moieties (moiety- "a well-defined part of a larger molecule") to allow them to be incorporated into vinyl ether and glycidyl ether photoresist matrices (see figure 3.3.1). This increases the processability of the resulting materials. The LEPs are then incorporated into a solvent-less photocurable matrix suitable for ink-jet printing. The energy transfer process is highly distance dependent; in Förster resonant energy transfer (FRET) [26] the strength of the interaction between the donor and acceptor varies as $\propto \frac{1}{r^6}$ where r is the distance between the donor and acceptor. In these polyfluorene-based molecules, the donor and acceptor molecules are bound together via

a conjugated backbone permitting the energy transfer to occur much more efficiently than would otherwise be possible if the donor and acceptor molecules were not linked.

The following procedure was used to formulate photocurable composite inks from the LEPs. LEP powder was combined with the CHDV solution encapsulation material and the photo-acid generator. The latter promotes polymerisation, causing cross-linking of the CHDV monomer alongside the LEP divinyl ether and immobilising the LEP into a solid polymer matrix. Specifically, the composite inks were made by measuring out 30 mg of LEP powder using a high precision balance and then dissolving it in 200 μL of chloroform. This solution was then added to 1.5 mL of the CHDV monomer and 3 mg of the PAG, which was found to be adequate to ensure rapid polymerisation. The initial dissolution of LEP into a solvent aids the complete mixing of the LEP material within the CHDV monomer solution. The resulting solution underwent vacuum treatment for 30 s to fully evaporate any remaining chloroform solvent and was passed through a 0.2μm-pore size PTFE filter to remove any large particulates. Absorption measurements were taken to determine the absorption spectral characteristics once the LEPs were incorporated into the CHDV matrix. The absorption profiles as shown in figure 3.3.2 show good agreement to those reported by Kuhne *et al.* [25] and have absorption peaks at ~370nm for each polymer ink. Secondary absorption peaks in **P2** and **P3** are caused by the respective absorption of the different emissive units. The three materials in question have emission peaks centered on 418 nm, 545 nm and 645 nm for blue, green and red emission, respectively. Films of LEP in CHDV were created via spin coating, placing 100μL of LEP ink onto a cleaned glass cover slide and spin coating at 2000rpm for 60 s then photo-curing under 370nm illumination for 60s for a total exposure dose of 2.5 $J.cm^{-2}$. Emission spectra were also taken using photoluminescence measurements when pumped with a 375nm InGaN laser diode in continuous wave (CW) operation. Figure 3.3.2 also shows these spectra and it can be seen

that upon photo-pumping in the near UV that emission in the visible spectrum is obtained. The peaks shown for the respective LEP inks correspond to those obtained by Kuhne *et al.* [25]. Given that the three LEP inks share an absorption peak at ~370nm it is possible to use them together in the generation of triple-colour display units.

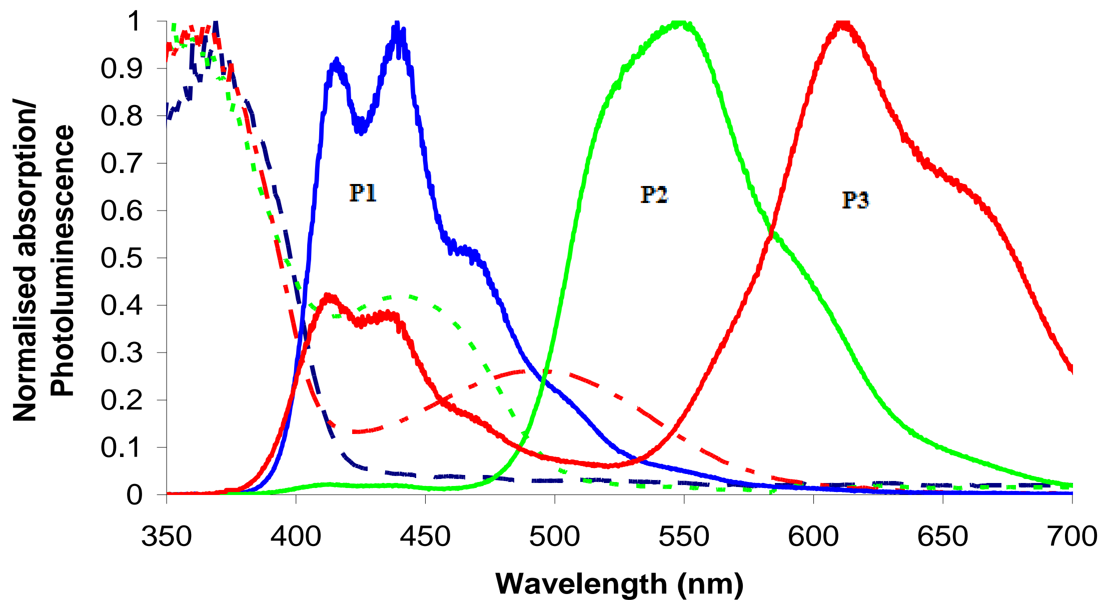

Fig 3.3.2 Normalised absorption and photoluminescence spectra for spin coated films of LEP in CHDV. Absorption spectra: P1: dashed line (blue), P2 dotted line (green), P3 Dot-dashed line (red). Photoluminescence spectra are solid lines marked respectively, P1-3.

Fabrication of AlInGaN LED arrays with 370nm emission is possible from appropriate epitaxial device wafers and they can be fabricated in arrays of 50μm pitch. Using a matrix electronic addressing scheme (Chapter 2) for these devices it is possible to individually address pixels as well as arrays of pixels. Therefore using this UV emitting micro-LED array and integrating the LEP polymers P1-P3 to form RGB pixel arrays it is possible to achieve RGB emission from a single nitride semiconducting wafer.

3.4 Substrate Preparation

The nanocomposite ink was designed and tested so that it had the fluid properties required for use in inkjet printing, and the optical qualities desired for use in colour conversion. The viability of printing and the deposition of material onto a substrate were then explored. Young's equation, given in equation 3.4.1, gives the equilibrium of forces that dictates the shape of a droplet resting on a surface; this equation stems from the interaction energies between the substrate and the gas, γ_{SL}, the substrate and the liquid, γ_{SL}, and the liquid and the gas, γ_{LG}. The contact angle between the substrate and the liquid is then given by θ_C:

$$\theta_C = \frac{\gamma_{SG} - \gamma_{SL}}{\gamma_{LG}} \quad (3.4.1)$$

The balance of these forces is illustrated in figure 3.4.1, which shows that the formation of a droplet on a surface is a trade-off of energies. The molecules within the liquid will have a potential energy, due to the effect of gravity. Without surface tension forces, a fluid would spread over a substrate to minimise this energy, however as there is such a force, energy must be expended to increase the surface area of the droplet.

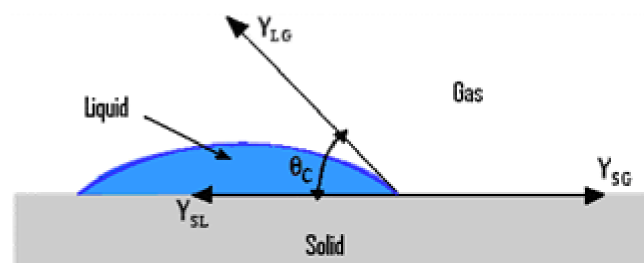

Figure 3.4.1 Diagram illustrating interaction energies that result in Young's equation. This holds only for flat substrates rather than for roughened.

This surface tension is a reflection of the surface interaction of the liquid with the environment within which it is present. Additionally there is an energy cost due to expansion across the substrate; the cost of such expansion is dependent on the energy cost of interacting with the substrate. The ultimate droplet shape will be determined by finding the equilibrium point for these energies, balancing the energy cost of increasing the surface area exposed to unfavourable interactions compared to the energy gained by increasing the number of favourable interactions. Examples of favourable and unfavourable interactions can be found readily upon examination of the interaction between oil and water. Water is a highly polar molecule; the electro-negative oxygen molecule draws charge away from the hydrogen molecule, resulting in a polar O-H bond. Overall H_2O exhibits a dipole due to the H-O-H bond angle being 104.5°. This dipole is a key reason for many of the extraordinary properties of water and undergoes high degrees of hydrogen bonding. The polar water molecules will bond favourably with other materials that have dipoles, allowing the water-to-hydrogen bond to have both slightly positively charged, $\delta+$, and slightly negatively charged, $\delta-$, areas. Conversely many long hydrocarbons are nonpolar, or have few areas to undergo hydrogen bonding, due to symmetrical positioning of carbon and hydrogen molecules around the chain. Thus non-polar and polar surfaces do not interact favourably and this can be used to control droplet shape on a substrate. A surface treatment can be applied to a substrate that enhances the interaction desired; either to a more polar or less polar medium depending on the liquid in question.

In this work the aim is to deposit the aforementioned composite ink onto the top of an LED to achieve colour conversion. This requires there to be a hydrophobic interaction between the ink and the substrate to prevent the ink from spreading unduly onto other pixels and away from the desired location. As the top surface the ink was deposited on was silica (the electrical isolation for the LEDs), a surface treatment of tridecafluoro-1,1,2,2-tetrahydrooctyl (1)

dimethylchlorosilane (PFODCS) [27] was used. The silane end of the molecule readily attaches to free oxygen at the surface of SiO_2 and a fluorinated carbon chain is presented to the environment. The condensation reaction that bonds the PFODCS to the silica substrate is shown in figure 3.4.2. This fluorinated carbon chain is non-polar; replacing the hydrogen typically present on hydrocarbon chains with electronegative fluorine atoms further reduces the polarisation potential from an already mainly non-polar molecule. The main constituent of the composite ink, CHDV, has several polar constituents; the C=C double bonds at both ends as well as the oxygen molecule further adding to the polarity.

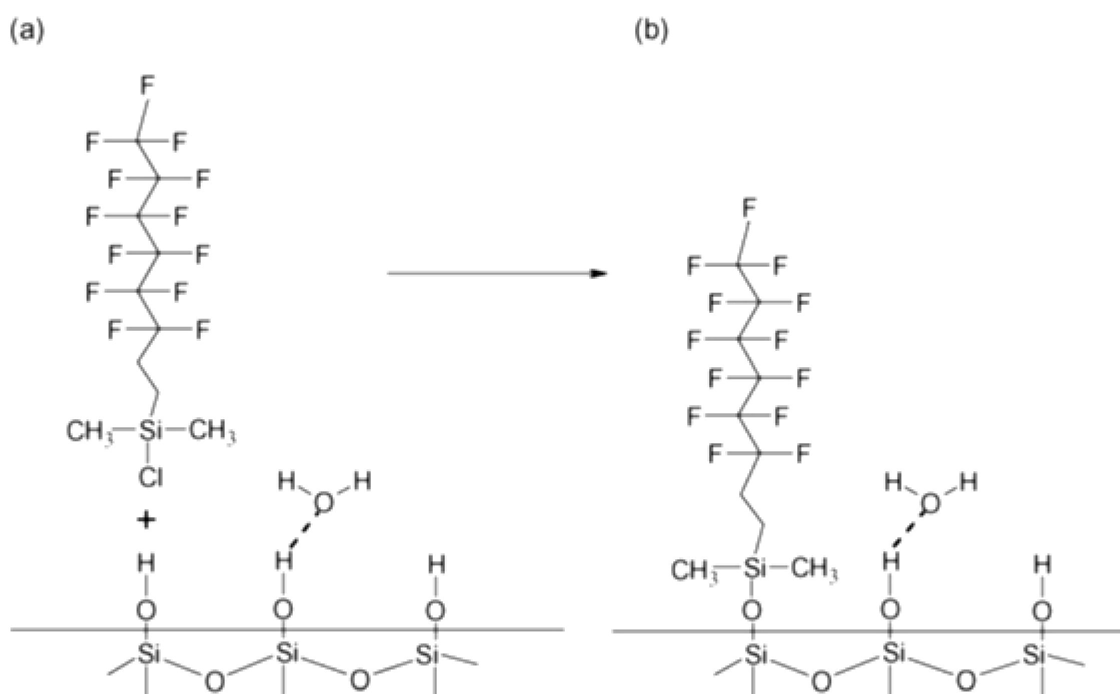

Figure 3.4.2 Condensation reaction of PFODCS bonding onto a silica substrate. [31]

This means that there will be unfavourable interactions between the ink and the treated surface, resulting in a larger contact angle in accordance with equation 3.4.1 and, by extension, droplets with a smaller diameter. Surface treatment of SiO_2 slides for testing this approach was conducted as follows. A glass slide was first cleaned of dust and various other particles that may adhere to the surface by being placed in an ultrasonic cleaner first in acetone for 5 minutes then in methanol for a further 5 minutes. The substrate was air-dried then placed on a raised

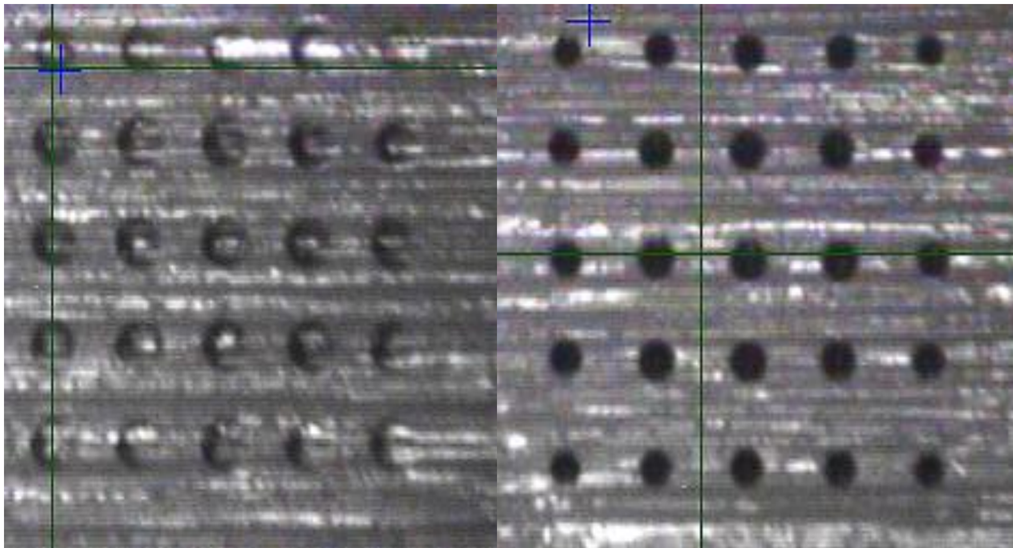

Figure 3.4.3 Images of 5x5 printed arrays of 5 layers of 1 pl droplets of optical polymer CHDV with a 50μm centre-to-centre pitch deposited onto untreated glass (left) and silanised glass (Right). Droplet diameter ~10.5 μm untreated, ~8μm on treated glass.

plate within an enclosed chamber containing the silane surface treatment around the base and left for 60 minutes at room temperature, giving the chamber environment time to saturate with silane vapour. Condensation occurs on the glass substrates where the silanisation treatment occurs and a monolayer of the silane surface treatment forms. If left for an extended period (>12hrs) then one cannot be assured of a monolayer as further condensation can occur and deposit an excess on the substrate. Print tests of CHDV with PAG only, i.e containing no LEP, have been conducted on both treated and untreated glass slides with the results shown in figure 3.4.3. There is a reduction from 10.5μm to 8μm in feature diameter when deposited upon the treated surface compared to that of an untreated substrate.

The volume of liquid deposited has an effect on the resulting droplet shape, with higher volume increasing the dimensions of the droplet. An investigation was conducted to determine the evolution of feature dimensions as 1 pL droplets are printed on top of each other because it was anticipated that thicker printed structures would be required for efficient colour conversion. Figure 3.4.4 shows this evolution with the measured profiles as an insert, the progress

demonstrating an approximately linear relationship at the volumes used. As the volume increases the effect of gravity would begin to be non-negligible and the relationship would become nonlinear.

Two deposition techniques were explored to ensure optimal containment of the ink on top of an LED pixel; one method was to deposit the number of droplets desired then cure the resultant volume; the second was a drop-by-drop (one at a time) curing technique to fix the deposited droplet in place and to reduce the degree of lateral spreading. The principle of such deposition on top of an LED pixel is shown in figure 3.4.5 alongside an SEM image of the result of integration using the two techniques. The bulk curing approach was photo-cured at 254nm for 5 minutes at an exposure dose of $10J.cm^{-2}$. In the layer-by-layer approach each droplet layer was photo cured for 60 seconds giving an exposure dose of $2.5J.cm^{-2}$ per layer.

Comparing the two techniques, as shown in the SEM images in figure 3.4.5, it can be seen that bulk curing creates a smoother structure than the layer-by-layer approach. This is most likely

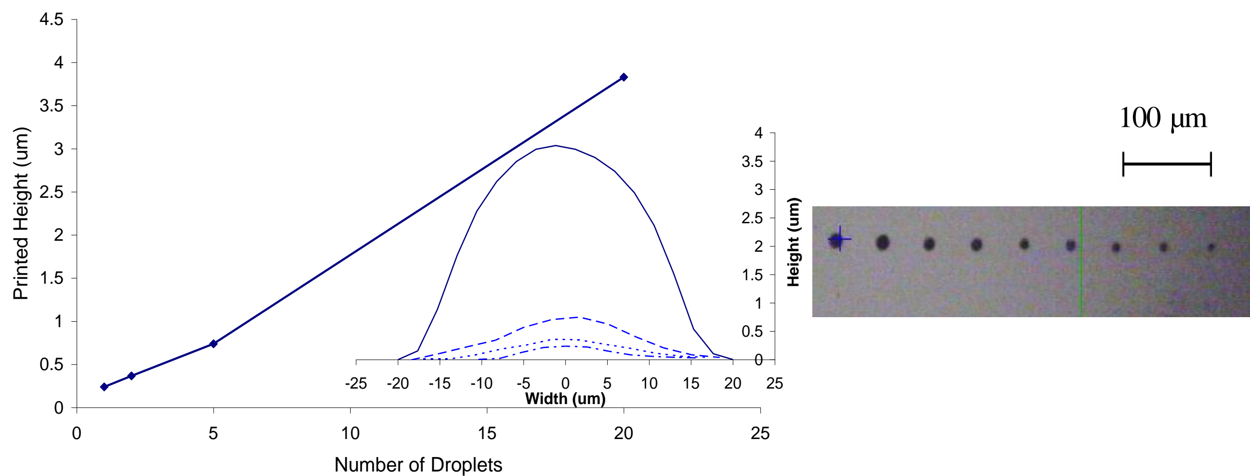

Figure 3.4.4 Left, a graph of feature height change with increasing number of sequential droplets with (insert) the respective profiles as measured by stylus profilometry. Right, an image demonstrating the increase in printed feature size with increasing volume. The pitch is 100 µm with the number of 1pL droplets ranging from 2 to 20 with 2 droplet increments from right to left.

due to a combination of effects: the bulk liquid will settle without any boundaries and in addition the layer-by-layer approach has significantly more UV exposure with increasing numbers of multi-layer curing stages. However, the layer-by-layer approach allowed the printed structure to be contained more fully on the pixel compared to the bulk cure technique. The overlap on the conductive track shown in figure 3.4.5 is due to small misalignment.

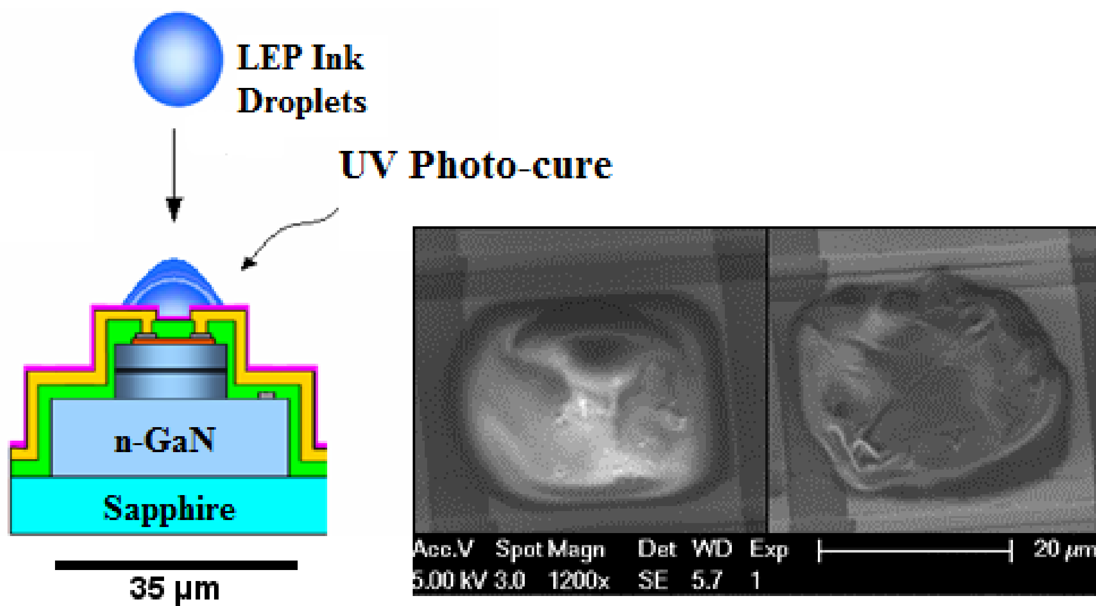

Figure 3.4.5 Principle of layer-by-layer integration on an LED pixel, far left. SEM image of the two integration techniques each with 10 layers of 1pL droplets; bulk curing shown in the middle; layer-by-layer curing approach on the far right.

3.5 Red-Green-Blue (RGB) Integration

Once the suitability of the substrates and inks for printing was demonstrated, creation of the colour converting inks as well as integration onto the micro-LED devices was explored. Arrays of the resulting printed RGB pixels are shown in figure 3.5.1, initial tests of resolution and

repeatability being conducted on clean, silanised glass substrates (left), leading to integration on a dummy (non-operational) micro-LED device (right). The printed features on glass and the dummy device were here illuminated with a 370nm UV handheld lamp, giving rise to the observed fluorescence, from the respective printed droplets.

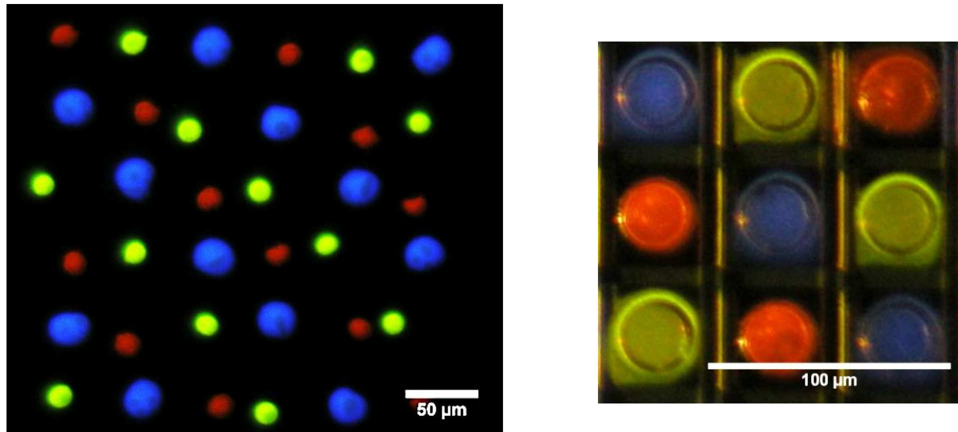

Figure 3.5.1 Pixel integration of the three LEP inks on a glass slide (left) and on a test micro-LED device (right). The centre-to-centre pitch for each droplet is 50μm (right).

Errors of alignment can be seen on both the glass slide and the test micro-LED device. Sources for misalignment can be large particles blocking the nozzle entrance, temperature variations altering the fluid properties (viscosity and surface tension), breakdown of the cartridge, and large distance between nozzle and target. Some of these can be eliminated – reducing the distance from the nozzle to the target, and having the lab and nozzle at a fixed temperature. Large particulates can be avoided by filtering the solution when first created but over time and low level UV exposure, aggregation occurs within the cartridge. Using fresh materials and new cartridges can mitigate this build up to have a reliably firing nozzle. The advantage of the layer-by-layer deposition technique is that it builds a taller feature and permitting more light to be absorbed by the colour converter.

Alignment errors in the blue and green integration on the test LED device are what stimulated the exploration of deposition build-up methods (bulk cure verses layer-by-layer). The blue ink was seen to have run into the groves between the pixels and the green ink has spilled over to cover the area surrounding the emission area of the LED. Integration on the two test substrates was done with 5 layers of 1pL volume droplets with the bulk cure methodology.

Measurement of the spectral emission of the printed colour converting droplets was done via use of micro-photoluminescence (μ-PL) with a pump laser spot diameter of 6μm. This technique, illustrated in figure 3.5.2, images the emitted light into a UV-vis spectrometer for spectral analysis. The setup houses a 375nm laser diode for optical excitation of materials, which are mounted on an xyz stage for focusing and locating micron-scaled samples. The optical camera aids in alignment of these samples and also helps alignment for signal being directed to the UV-visible spectrometer. It is then possible to photo excite individual printed droplets and to image their emission.

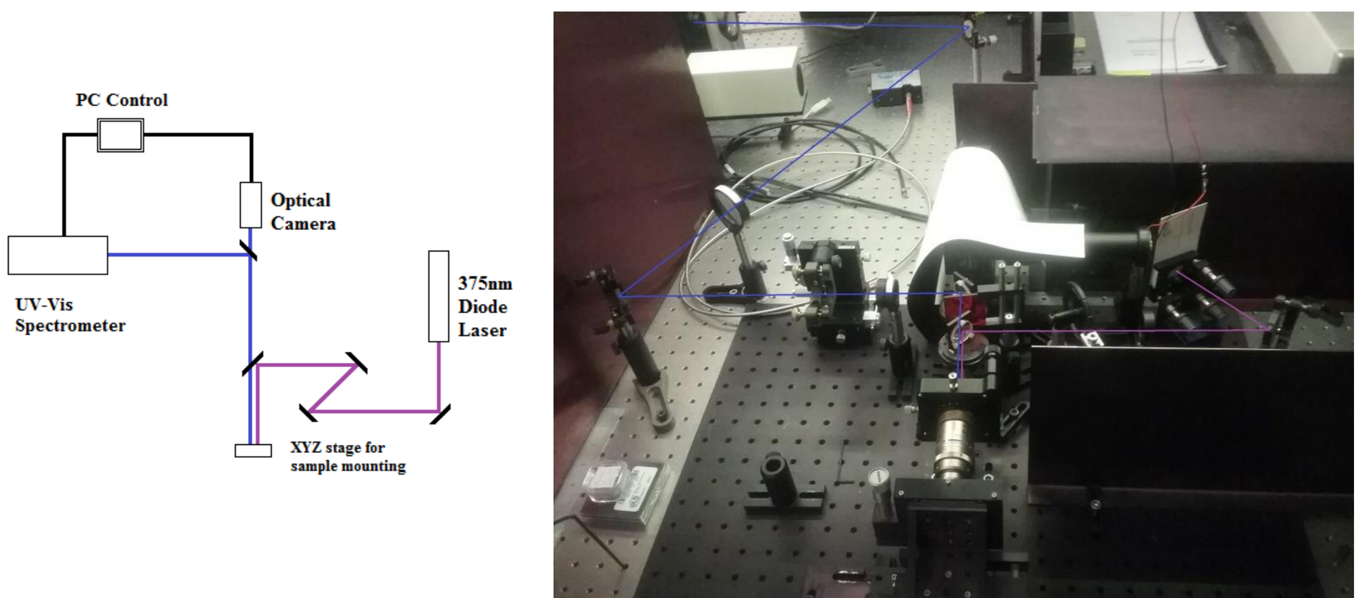

Figure 3.5.2 Optical setup for micro photoluminescence measurement (left) with photo of the set-up (right). A 375nm laser diode used for optical excitation of samples and a camera for alignment with the UV-visible spectrometer.

Spectra were taken for 5 pL printed structures when excited by the 375nm UV laser; the corresponding photoluminescence emission can be seen in figure 3.5.3. The main spectral peaks remain consistent with the spectra obtained for the reference LEP films and those reported in the literature. The blue emitter exhibits vibronic peaks at 418nm and 439nm, also observed in the printed green and red LEPs. The peak is at 545nm with a shoulder at 590nm for the green material; the shoulder is at 660nm for the red material. For both the green and red materials, in both the films and printed structures, emission at 410nm was seen, due to the energy transfer from 418nm to the higher wavelength emitter being less than 100% efficient. Optical micrographs of the printed structures being pumped by a 375nm laser are shown as an insert in figure 3.5.3. Each structure was pumped with the same optical power, 187W/cm^2 from the diode laser. The results of the μ-PL measurements show that integration onto an operational micro-LED device with emission at 368 nm should down-convert the light to the visible spectrum. The three LEP inks were therefore subsequently integrated onto an operational 368 nm emitting matrix addressable micro-LED array; each pixel was integrated with 20 layers of 1pL volume droplets. The larger deposited volume helped increase the amount of colour conversion achieved by increasing the number of chromophores available, increasing the chance of absorption of a UV photon. The absorbance for P1, P2, and P3 at 368nm was found to be 1.1, 0.8 and 0.6 for each, respectively. Photoluminescence spectra were taken for the three respective colour integrated structures and the conversion from the UV to visible is shown in figure 3.5.4. The peak at 368 nm seen here is unabsorbed/scattered light from the excitation LED micro pixel; longer wavelength peaks are of colour converted emission from the integrated LEP structures. Peak emissions of 413nm for P1, 532nm for P2, and 610nm with P3, respectively, corresponded to the photoluminescence characteristics of reference thin films of these materials.

The effect the printed structure has on the emission spectral profile and light extraction of the device was investigated. Optical power measurements were made with a Coherent Fieldmax power meter for a bare LED pixel and then repeated on the same pixel with 10 layers of pure CHDV matrix integrated. In addition the emission profile was determined by combination of a JVC TKC721EG charge-coupled device (CCD) camera and an Aerotech BM75 goniometer. The results showed negligible changes in both the power extraction and emission profile of the LED, implying there is no significant change in the efficiency measured for the colour conversion due to lensing in the polymer deposited onto the LED. The fraction of the light absorbed was calculated by comparing a reference LED, hybridised with the CHDV matrix with no LEP material, and an LED integrated with CHDV and colour converter. Having determined the proportion of light absorbed by the LEP the ratio of the converted light to the amount of absorbed light yields the efficiency for the integrated LEP structure. The efficiencies observed were 13.2%, 31.5% and 5% for structures of P1, P2 and P3 respectively. The enhanced colour conversion from the green printed pixel over the blue and red is thought to be

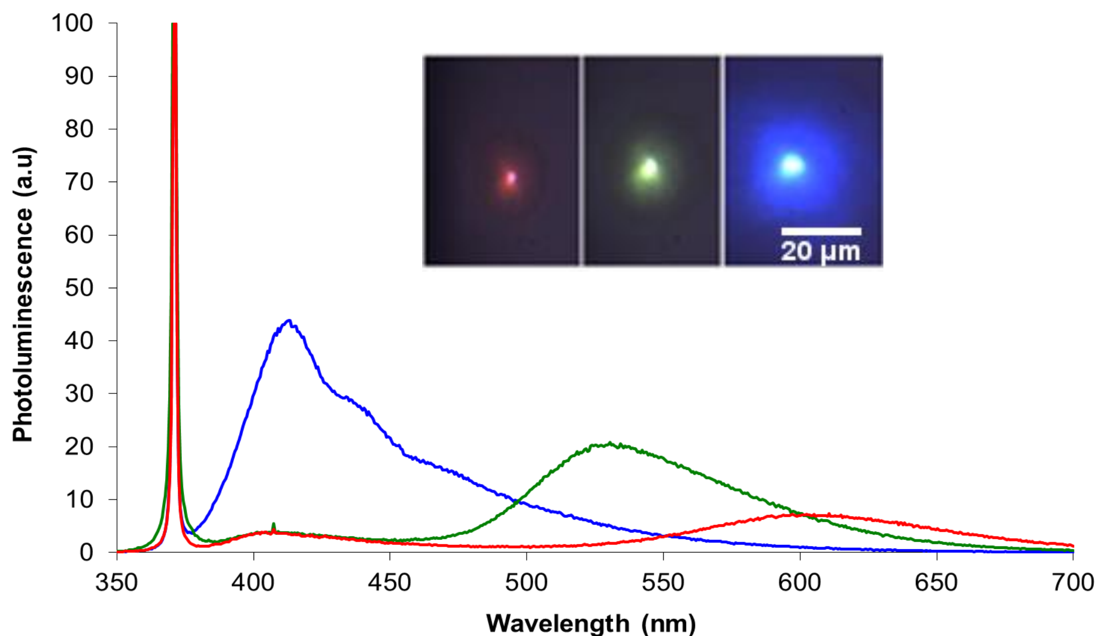

Figure 3.5.3 Photolumenescence of 5 layers of 1pl droplets for composite inks containing the colour converting polymers P1-P3. The narrow peak observed at 375nm is unconverted UV laser light. Insert is an optical micrograph of the printed features being laser pumped.

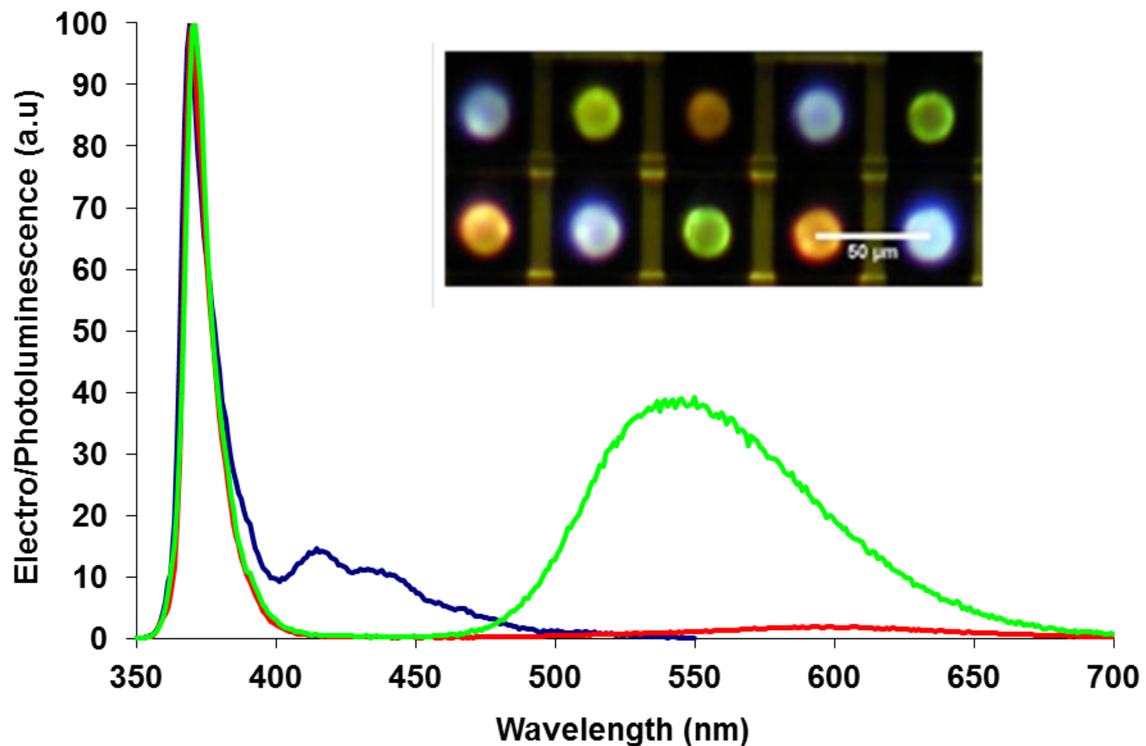

Figure 3.5.4 Micro-photoluminescence spectra shown for colour converting LEP's integrated onto and photo-pumped by micro-LED pixels. The peak at 370nm is unconverted UV light from the LED and the peaks at 413nm, 532nm and 610nm are those of down-converted light from the blue, green and red material, respectively. The insert is an optical micrograph of the RGB array in operation; the integrated colour converter being photopumped by the underlying UV electrically driven micro-LED pixels.

due to exceptional alignment when printing onto the pixel, improving the overall LED colour conversion efficiency. This shows the advantages of the layer-by-layer deposition technique in building a taller feature and permitting more light to be absorbed by the colour converter. Due to nozzle instabilities, the other pixels did not have such accurate confinement of the composite ink to the emissive area. This emphasises the importance of the layer-by-layer approach to increasing the efficiency as it aids in confinement to the emissive area of the pixel. An examination of how the light conversion changes with increasing bias applied to the LED was also conducted; figure 3.5.4 shows that initially the converted light dominates over the unabsorbed/scattered UV emitted, this ratio decreasing as the bias is increased to the point

where the un-absorbed/scattered UV signal dominates over the LEP emission. At this point the hybrid device enters a saturated state, where the LEP structure converts as much UV as permitted by the chromophore efficiency and concentration. This is characterised by deviation of the linear change in peak ratio with applied current, shown in the insert of figure 3.5.5, where S_{LEP}/S_{UV} is the ratio for the integrated area for the converted light to that of the LED light. By comparing the applied bias and the ratio of the converted light to the UV emission it can be seen that the hybrid device becomes saturated after 140µA of bias is applied.

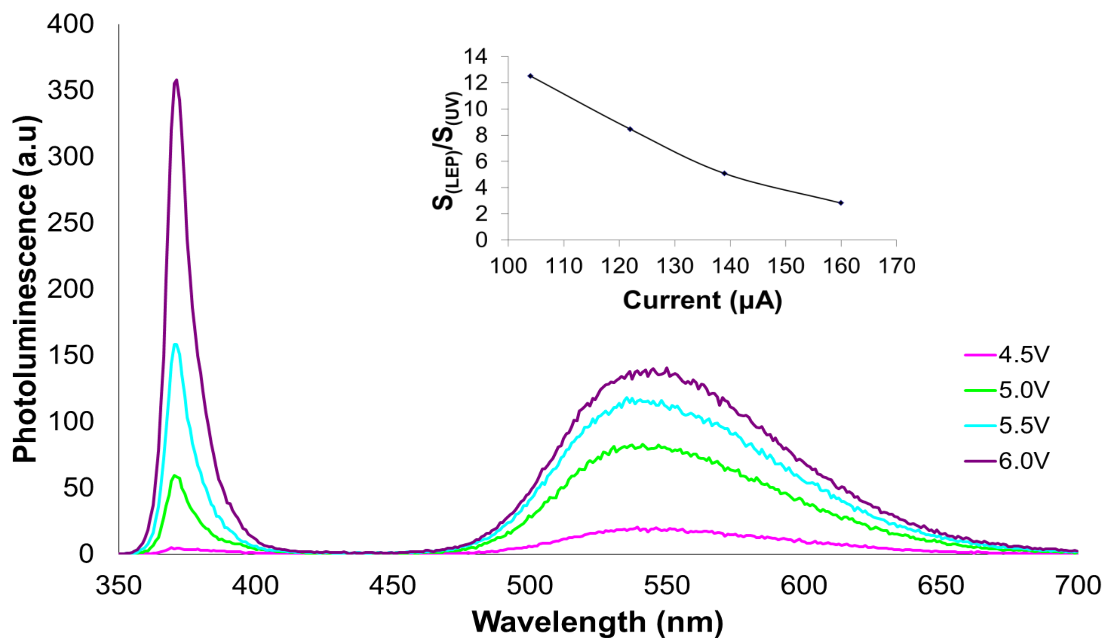

Figure 3.5.5 Evolution of the emission profile for the green composite ink with increasing bias applied to the micro-pixel. Insert showing the change in ratio of the UV and converted peaks with increasing LED drive current.

3.6 Mask-Less LED fabrication

The GaN LEDs reported above were all fabricated by standard optical lithography, where each stage of manufacture requires a dedicated photo-mask to be created. Such masks define the

areas of photoresist exposed to UV light to undergo selective etching or allow electrical contacts to be defined, but the process of mask design and creation is time consuming and expensive. We had previously constructed [29] a mask-free ultraviolet writing set-up using GaN micro-LEDs as the illumination source. It occurred to us that we could use this tool to pattern new LED structures in a mask-free manner and to utilise the ink-jet printing capability to apply conducting tracks/contacts to the device. Thus the whole process of LED production could be "mask free".

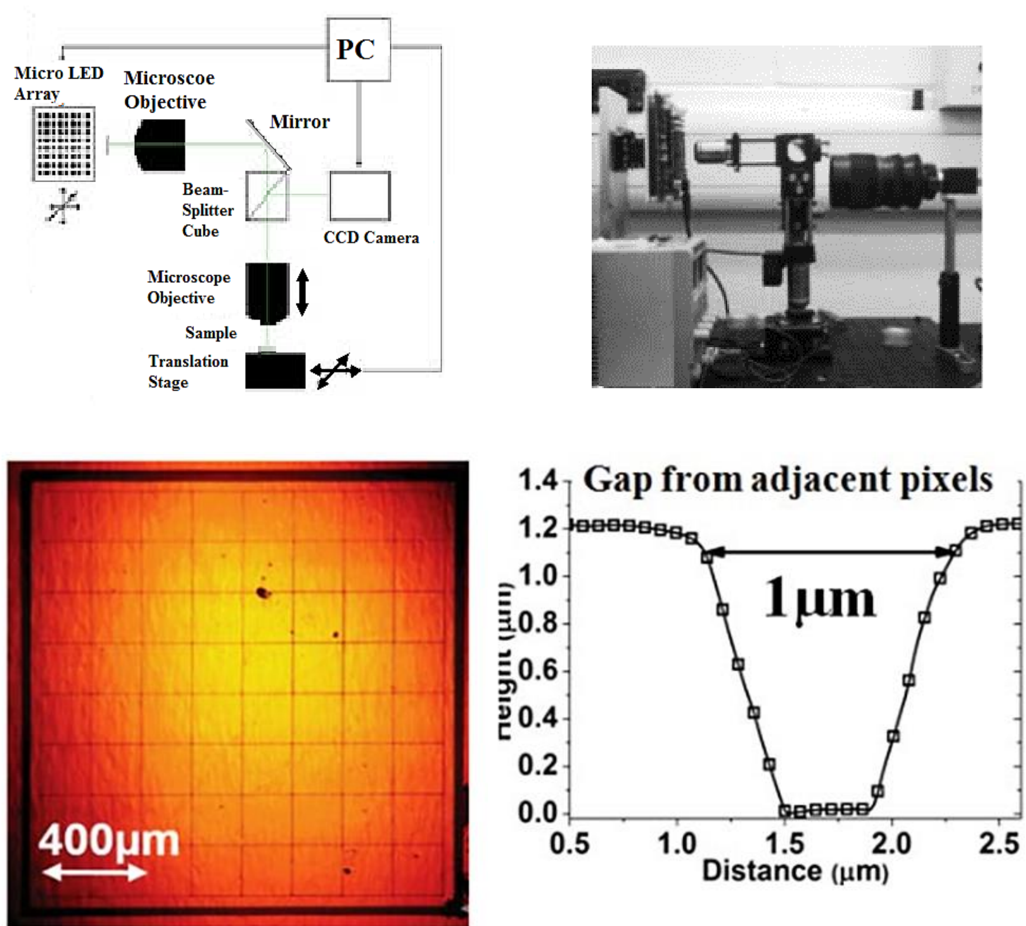

Figure 3.6.1 Schematic of LED direct-write setup (top left) with photograph of setup (top right), plan-view optical micrograph of the entire LED patterned and etched 450-nm emitting 8 × 8 array (bottom left) and AFM scan profile of a representative gap between adjacent pixels of the array (bottom right).

In the LED direct write system (figure 3.6.1) 8×8 micro-LED arrays, emitting at 368nm, with pixel sizes as small as 14μm-diameter in an imaging optical setup can pattern photoresist with features down to 500nm in order to process GaN-based LED hetero-structures [29]. First, a single direct-write 368nm pixel was used to "grid" pattern a sacrificial photoresist mask for a "chequerboard-type" array (see figure 3.6.1) to define individually addressable LEDs emitting at 450 nm. The checkerboard device was designed with a targeted 1μm gap between adjacent pixels, resulting in a 99% filling factor arrays in a suitable configuration for subsequent flip-chip bonding to custom complementary metal-oxide-semiconductor (CMOS).

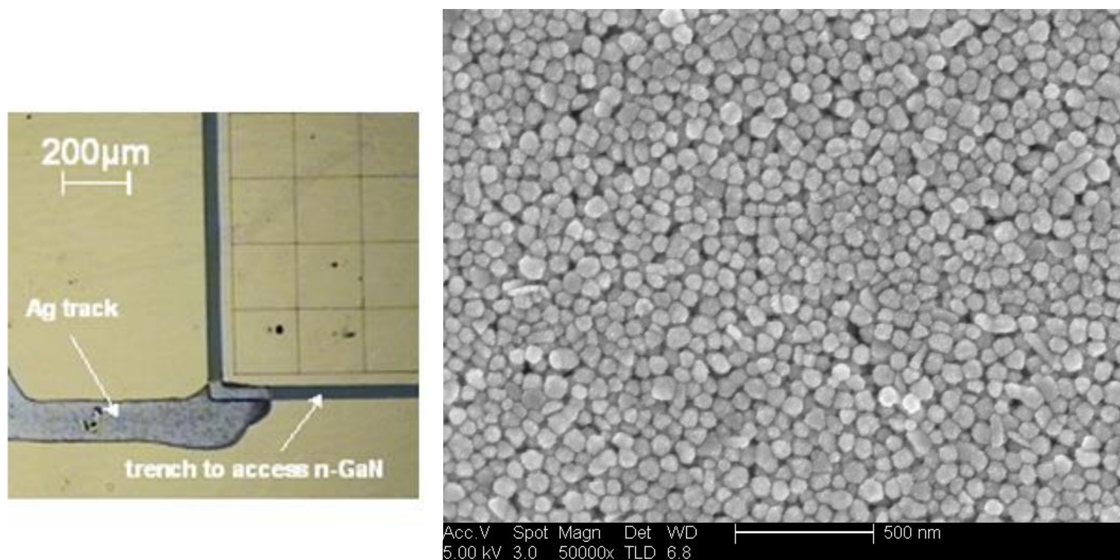

Figure 3.6.2 Image of printed common n-contact to a chequerboard LED array (left) and SEM image of dried sliver track (right).

Ink-jet printing of nano-metallic inks for the application of the conductive tracks was then carried out. An ink of silver nano-particles can be ink-jet printed in track form and, after sintering, was shown to be able to carry a current. The ink used is commercially available (Silver-jet DGP, 40% w/w) with silver particle sizes of 53.9 ± 8.3nm in a dried film. Once printed, the particles need to be heated, to remove solvent and dispersant molecules which prevent the metallic particles from coming into contact. Heating to 200°C for a period of 1 hour achieves this and decreases the resistivity of the silver track from $3.42 \times 10^{7} \mu\Omega \cdot cm$ to

15.4μΩ·cm. This reduced value of resistivity for the track [30] is only a factor of ten above that of bulk silver, 1.587μΩ·cm. The addition of the thus-produced common n-contact to the chequerboard device is shown in figure 3.6.2 alongside an SEM image of the sintered Ag particles. Each pixel was individually wire bonded to a printed circuit board for characterisation purposes. The inset of figure 3.6.3 shows an optical micrograph of the final checkerboard-LED array with several pixels turned on, demonstrating the individually-addressable capabilities of the device. Typical injection current versus forward bias voltage (I-V) and optical output power versus injection current (L-I) characteristics of a representative pixel are also shown in figure 3.6.3. The directed optical output was measured from the back side of the device (operation in flip-chip mode) using a power meter and a calibrated Si photodetector placed in close proximity.

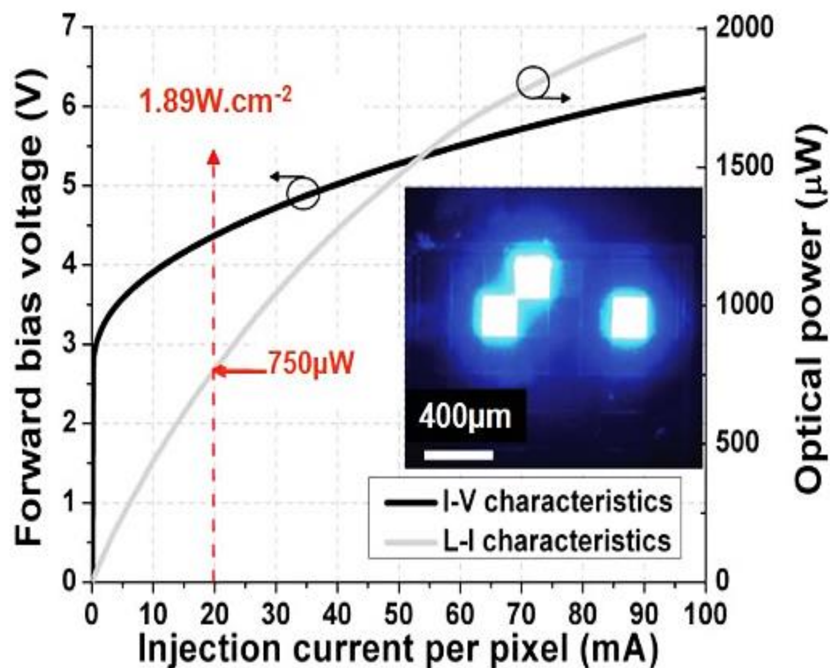

Figure 3.6.3 I − V and L − I characteristics of a typical pixel of the 8 × 8 array with, inset, an optical micrograph of several pixels individually addressed.

The device showed good electrical and optical performance with a maximum output optical power of 2 mW (5 W.cm^{-2}) at an injected current of 90 mA (750 μW or 2W.cm^{-2} at 20 mA injected current). A typical voltage of 4.3 V at 20 mA was measured, which is somewhat higher

than a typical GaN-based LED (usually around 3 V). This is likely due to the lower conductivity of the nanoparticle Ag ink and the higher potential barrier at the Ag/n-GaN interface compared with a more standard n-metal contact such as Ti/Au, but is illustrative of the potential for a fully mask-less LED fabrication process flow.

3.7 Conclusions

We reported a means of additively patterning soft, transparent and photoactive compounds on the micron scale. A Dimatix™ DMP 2800 inkjet printer was used with droplet volumes down to 1pL which offers deposition of features below 10µm in diameter. Exploration of this micron scale additive lithography has been conducted using the technique of inkjet printing. It has been shown to be able to pattern both inorganic and organic inks with feature sizes down to 8µm. This ability to deposit micron scale materials was used to create optoelectronic devices and hybridise inorganic LEDs with organic materials. Two techniques for inkjet printing are demonstrated: deposition of optically active colour converters onto a micron sized 370 nm emitting LED (16µm diameter) to create red, green and blue emitting pixelated arrays with colour conversion efficiencies of up to 31%; also printing of silver metallic inks was used in the fabrication of high fill factor (99%) GaN LEDs that were fabricated entirely in the absence of lithographic stages involving hard masks. This has been used for the successful creation of red, green and blue hybrid organic-inorganic micro-LEDs with conversion efficiencies as high as 31.5%. In addition, the ability for deposition of micron-scaled electrical contacts was realised in the mask-free fabrication of "chequerboard" GaN LED arrays. Various techniques for deposition of material were explored to allow accurate build-up of material on a desired area. The results of this work have been reported in the literature (see page 144).

3.8 References

1. Han, Arum; Hou, Huijie; Li, Lei; Kim, Hyun Soo; de Figueiredo, Paul, "Microfabricated devices in microbial bioenergy sciences", Trends in biotechnology, Volume 31, Issue 4, 225 – 232.

2. Yi Ou, Zhigang Li, Fengliang Dong, Dapeng Chen, Qingchuan Zhang, and Changqing Xie, "Design, Fabrication, and Characterization of a 240 ×240 MEMS Uncooled Infrared Focal Plane Array With 42μm Pitch Pixels", Journal of microelectromechanical systems, Volume 22, Issue 2, 452-62, 2013.

3. Lei-Jie Lai, Hang Zhou, Yu-Jie Du, Jie Zhang, Jing-Chun Jia, Li-Min Jiang, Li-Min Zhu, Zhao-Wu Tian, Zhong-Qun Tian, Dong-Ping Zhan, "High precision electrochemical micromachining based on confined etchant layer technique", Electrochemistry Communications, Volume 28, Pages 135–138, 2013.

4. Ravi S Kane, Shuichi Takayama, Emanuele Ostuni, Donald E Ingber, George M Whitesides, "Patterning proteins and cells using soft lithography", Biomaterials, Volume 20, Issues 23–24, 2363-2376, 1999.

5. M. Wu, Z. Gong, A. Kuehne, A. Kanibolotsky, Y. Chen, I. Perepichka, A. Mackintosh, E. Gu, P. Skabara, R. Pethrick, and M. Dawson, "Hybrid GaN/organic microstructured light-emitting devices via ink-jet printing", Opt. Express 17, 16436-16443, 2009.

6. Karl Crowley, Malcolm R. Smith, Anthony J Killard, Aoife Morrin, "Printing Polyanailine for sensor applications", Chemical Papers, Volume 67, 771-780, 2013.

7. Francis Nguyen, "Challenges in the design of a RGB LED display for indoor applications, Synthetic Metals", Volume 122, Issue 1, Pages 215-219, ISSN 0379-6779, http://dx.doi.org/10.1016/S0379-6779(00)01341-2, 2001.

8. Chen, J.; Sung-Jin Park; Zhifang Fan; Eden, J.G.; Chang Liu, "Development and characterization of micromachined hollow cathode plasma display devices," *Microelectromechanical Systems, Journal of*, vol.11, no.5, 536-43, 2002.

9. Inseok Choi; Hojun Shim; Naehyuck Chang, "Low-power color TFT LCD display for hand-held embedded systems," *Low Power Electronics and Design, 2002. ISLPED '02. Proceedings of the 2002 International Symposium on* , vol., no., pp.112,117, 2002.

10. G. Bizarri, B. Moine, "On phosphor degradation mechanism: thermal treatment effects, Journal of Luminescence", Volume 113, Issues 3–4, 199-213.536,543, Oct 2002.

11. H. Zhang, D. Massoubre, J. McKendry, Z. Gong, B. Guilhabert, C. Griffin, E. Gu, P. Jessop, J. Girkin, and M. Dawson, "Individually-addressable flip-chip AlInGaN micropixelated light emitting diode arrays with high continuous and nanosecond output power", Opt. Express 16, 9918-9926, 2008.

12. Z. Gong, H. X. Zhang, E. Gu, C. Griffin, M.D. Dawson, V. Poher, G. Kennedy, P.M.W. French,M.A.A. Neil, "Matrix-addressable micropixellated InGaN light-emitting diodes with uniform emission and increased light output" , IEEE Transactions on Electron Devices 54 , 2650-2658, 2007.

13. H. Dong, W. W. Carr, and J. F. Morris, "Visualization of drop-on-demand inkjet: Drop formation and deposition", Rev. Sci. Instrum. 77, 085101, 2006.

14. Shun-Chi Chang, Jie Liu, Jayesh Bharathan, Yang Yang, Jun Onohara, Junji Kido, "Multicolor Organic Light-Emitting Diodes Processed by Hybrid Inkjet Printing, Advanced materials", Volume 11, Issue 9, 734-7, 1999.

15. M. Achermann, M. A. Petruska, D. D. Koleske, M. H. Crawford and V. I. Klimov, "Nanocrystal-Based Light-Emitting Diodes Utilizing High-Efficiency Nonradiative Energy Transfer for Color Conversion", NANOLETTERS 6, 7, 1396-1400, 2006.

16. S. Chanyawadee, P. G. Lagoudakis, R. T. Harley, M. D. B. Charlton, D. V. Talapin, H. W. Huang, and C-H. Lin, "Increased Color-Conversion Efficiency in Hybrid Light-Emitting Diodes utilizing Non-Radiative Energy Transfer", Adv. Mater. 22, 602–606, 2010.

17. S. Nizamoglu and H. V. Demir, "Förster resonance energy transfer enhanced color-conversion using colloidal semiconductor quantum dots for solid state lighting", Applied Physics Letters 95, 151111, 2009.

18. G. Heliotis, G. Itskos, R. Murray, M. D. Dawson, I. M. Watson and D. D. C. Bradley, “Hybrid Inorganic/Organic Semiconductor Heterostructures with Efficient Non-Radiative Energy Transfer”, Adv. Mater. 18, 334-338, 2006.

19. S. Nizamoglu, E, Sari, J.H. Baek, I.H Lee, H.V. Demir, “White light generation by resonant nonradiative energy transfer from epitaxial InGaN/GaN quantum wells to colloidal CdSe/ZnS core/shell quantum dots”, New J. Phys. 10, 12300, 2008.

20. Veronica Sanchez-Romaguera, Marie-Beatrice Madec, Stephen G. Yeates, “Inkjet printing of 3D metal–insulator–metal crossovers, Reactive and Functional Polymers”, Volume 68, Issue 6, 1052-1058, 2008.

21. M. Wu, Z. Gong, D. Massoubre, Y. Zhang, E. Richardson, E. Gu, M. D. Dawson, “Inkjet-printed silver nanoparticle electrodes on GaN-based micro-structured light-emitting diodes, Applied Physics A, Volume 104, Issue 4, 1003-9, 2011.

22. Dimatix DMP2800 system information-
http://www.fujifilmusa.com/shared/bin/PDS00085-DMP2831.pdf

23. Dimatix Jettable Fluid Guidelines-
http://www.fujifilmusa.com/shared/bin/Dimatix_Materials_Printer_Jettable_Fluid_Formulation_Guidelines_05-13.pdf

24. A. J. C. Kuehne, D Elfström, A. R. Mackintosh, A. L. Kanibolotsky, B Guilhabert, E Gu, I. F. Perepichka, P. J. Skabara, M. D. Dawson, R. A. Pethrick, “Direct Laser Writing of Nanosized Oligofluorene Truxenes in UV-Transparent Photoresist Microstructures”, Advanced Materials 21, 7, 781–785, 2009.

25. A. J. C. Kuehne, A. R. Mackintosh, R.A. Pethrick, B. Tieke, “Novel vinyl ether functionalized fluorene polymers for active incorporation into common photoresist matrices”, Tetrahedron Letters 49, 32, 4722-4724, 2008.

26. Feron K, Belcher WJ, Fell CJ, Dastoor PC. “Organic Solar Cells: Understanding the Role of Förster Resonance Energy Transfer. International Journal of Molecular Sciences”, 2012.

27. Bico, José, Christian Marzolin, and David Quéré. "Pearl drops.", Europhysics Letters, Volume 47, Issue 2, (1999): 220-6, 1999.

28. Lei Zhai, Fevzi Ç. Cebeci, Robert E. Cohen, and Michael F. Rubner, "Stable Superhydrophobic Coatings from Polyelectrolyte Multilayers", Nano Letters 4 (7), 1349-1353, 2004.

29. B Guilhabert, D Massoubre, E Richardson, J J. D. McKendry, G Valentine, R. K. Henderson, I M. Watson, E. Gu, and M. D. Dawson, "Sub-Micron Lithography Using InGaN Micro-LEDs: Mask-Free Fabrication of LED Arrays", IEEE Photonics Technology Letters, Volume. 24, No. 24, 2012.

30. M. Wu, "Hybrid GaN/organic device fabrication by inkjet printing", PhD Thesis, University of Strathclyde, PhD thesis, University of Strathclyde, 2009.

Chapter 4

Positive Patterning via Dip-Pen Nanolithography

4.0 Introduction

As mentioned previously there are a multitude of methods available for lithographic patterning: photolithography, electron beam lithography and nanoimprinting, to name a few. Most of these processes involve a definition step and a washing with the developer to remove material not exposed, leaving a positive mask. However there are very few methods by which materials can be selectively added to the substrate, creating the pattern without the requirement of the process of exposure and development. Previously covered in Chapter 3 was the process of inkjet printing which allows for micron-scale patterning on selected areas via drop-on-demand technology. However the inkjet process is currently limited to feature sizes of ~10 μm. What processes are available for this form of positive lithography to pattern down to the nanoscale? When patterning with photonic devices and structures in mind then the feature size needs to be of a magnitude comparable to the wavelength of light to be manipulated, i.e. into the submicron regime for visible light. The technique of dip-pen nanolithography (DPN) has the capability to pattern materials into this regime. Originally designed for the patterning of organic peptides and self-assembled monolayers (SAMs) [1], the process utilises a nanoscale tip for deposition of structures down to a size of 10's of nanometres. The ability to pattern to such a scale is limited by the choice of ink selected for deposition: the smallest features achieved are with the

deposition of SAMs. Subsequently DPN has found many applications: fabrication of nanolens arrays [2], deposition of conductive polymers [3], and directed growth of carbon nanotubes [4] to name a few [5-7]. While the fine feature resolution is highly desirable there is a limit in its usefulness regarding photonic device fabrication and other such functions where feature height also plays a significant role. DPN has had only limited investigation as a deposition method for photonic applications; this chapter will cover the ability of this process to not only pattern photoresist material but to achieve this patterning into the submicron regime. The ability for DPN to pattern sacrificial photoresist as well as photoluminescent materials down to the nanoscale will open new possibilities in nanotechnology for both "bottom up" and "top down" fabrication of photonic devices [8,9].

4.1 Principles and Models of Deposition

The principle behind DPN is that a fine-scale quill or tip can be placed into a fluid ink and that ink can be deposited elsewhere. It was found that there were two types of ink that could be used in this system, namely "molecular" ink and "liquid" ink. Initially this technique was used to pattern alkane thiolates to imprint onto a gold surface and began to gain more use in the deposition of self-assembled monolayers (SAMs). The technique expanded and currently promises patterning of materials in the size range of 10 μm down to 50 nm. The size of features deposited is limited by the choice of ink as well as the length of time the tip touches the substrate, which is known as the "dwell time". The models for deposition of these two ink types are quite different. One describes deposition of molecular inks, i.e. materials such as silanes and alkynes in a "dry" state; and the other models liquid inks which do not dry onto the tip. In the patterning of dry organic molecules it is assumed that the molecules dry onto the tip itself

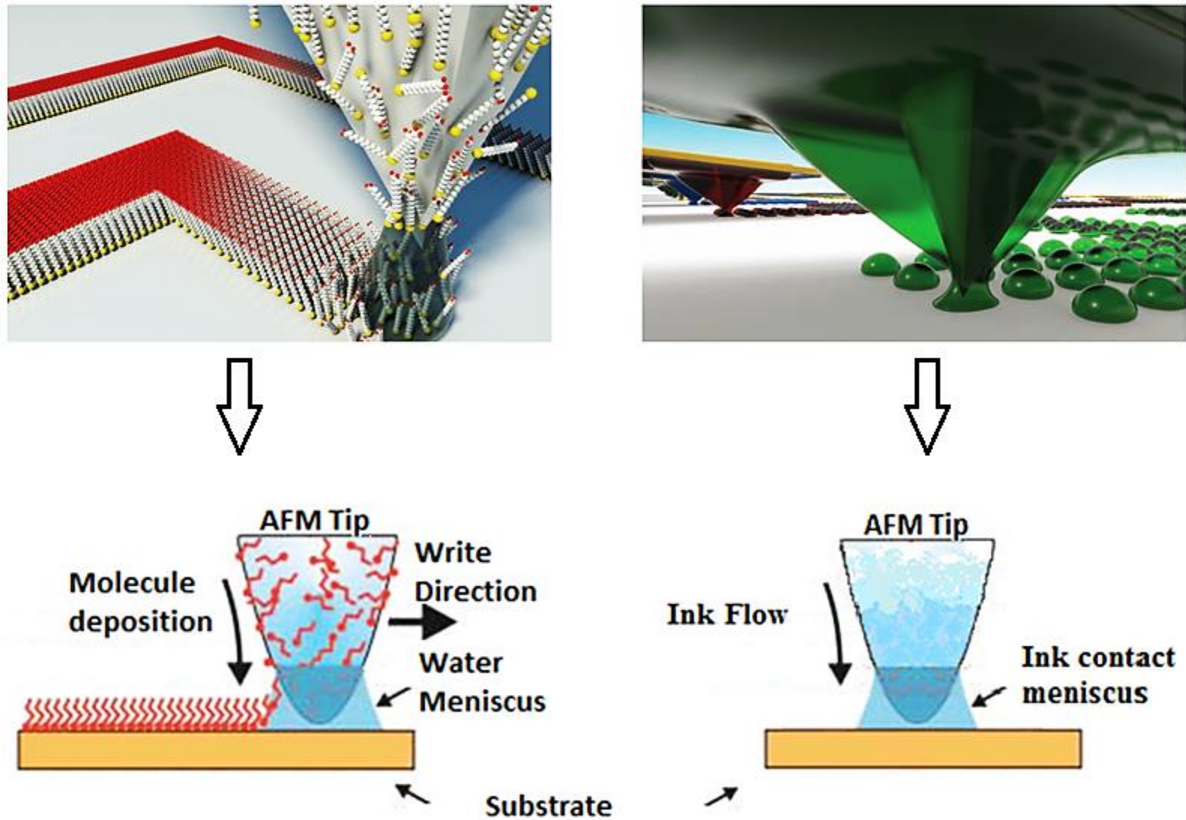

Figure 4.1.1 Illustration showing the deposition of SAMs via the formation of a meniscus between the tip and substrate, left. Deposition of inks as determined by fluid flow down the tip to contact the surface, right. Top images courtesy of NanoInk, lower adapted from National Physical Laboratory image.

through solvent evaporation. When brought into contact with the substrate a temporary water meniscus forms [10] between the atomic force microscope (AFM) tip and the substrate which allows diffusion-controlled [11] deposition of the materials as illustrated in figure 4.1.1. The second system models the liquid as might be present on a quill and ink; the tip is laden with material and deposition occurs as the fluid contacts the substrate rather than as part of a diffusion-controlled process [12]. The deposition is controlled by the surface tension of the ink to the substrate, the surface tension between the ink and the tip, and the viscosity of the ink [13]. For both these methods there are many factors affecting deposition; chemical composition (and purity) of both the ink and surface, the tip shape, composition, and surface chemistry, the

distribution and mobility of ink on the tip, as well as the temperature and humidity under which the experiment is carried out. The main difference between molecular and liquid ink deposition is the evolution of feature size with contact time; the SAM features undergo growth at a much reduced rate compared to the ink deposition, allowing for patterning down to 10's of nanometres. To achieve a balance of material properties and conditions that permit sub-micron patterning in the ink-based system requires careful selection of the ink to deposit as well as the conditions under which the deposition occurs. Our research group and colleagues have reported the deposition of UV-curing photoresist material, CHDV (this material was covered in chapter 3), laden with colour converting oligofluorene molecules [14]. The contact time was reduced to 0.25s and yet the minimum feature size achieved was just 4 μm; to achieve smaller features control of viscosity and surface interactions must be attained in addition to dwell time.

Operation of the dip pen system for deposition typically follows the process of moving the tips to where the well of the load material is and contacting to allow the tips to become laden with material. Immediately after the load phase the tip must be blotted by touching the laden tips to the surface of a clean glass slide. There is a great deal of material present on the tips directly after visiting the ink well and blotting removes this excess material. With the excess material removed from the tips, it becomes possible to deposit droplets of even size; without the blotting stage the size of features deposited deviates significantly from what should be obtained for a certain dwell time and will continue thus until the excess material is removed and stable features are generated.

4.2 Dip Pen Operation

The specific dip pen instrument used in our work was an NLP 2000 system [15] purchased from NanoInk, Inc. This machine has a large 40 mm x 40 mm XY stage with a positional repeatability of ± 25 nm in the XY plane and ±75nm in the Z plane when operated in high resolution mode. Control of the NLP 2000 stage is enabled by three encoded piezo-driven linear stages (XYZ) and 2 encoded goniometer (tilt) stages (Tx and Ty) making precise, rapid, large area patterning repeatable. The stage setup within the NLP 2000 system with the imaging microscope is shown in figure 4.2.1.

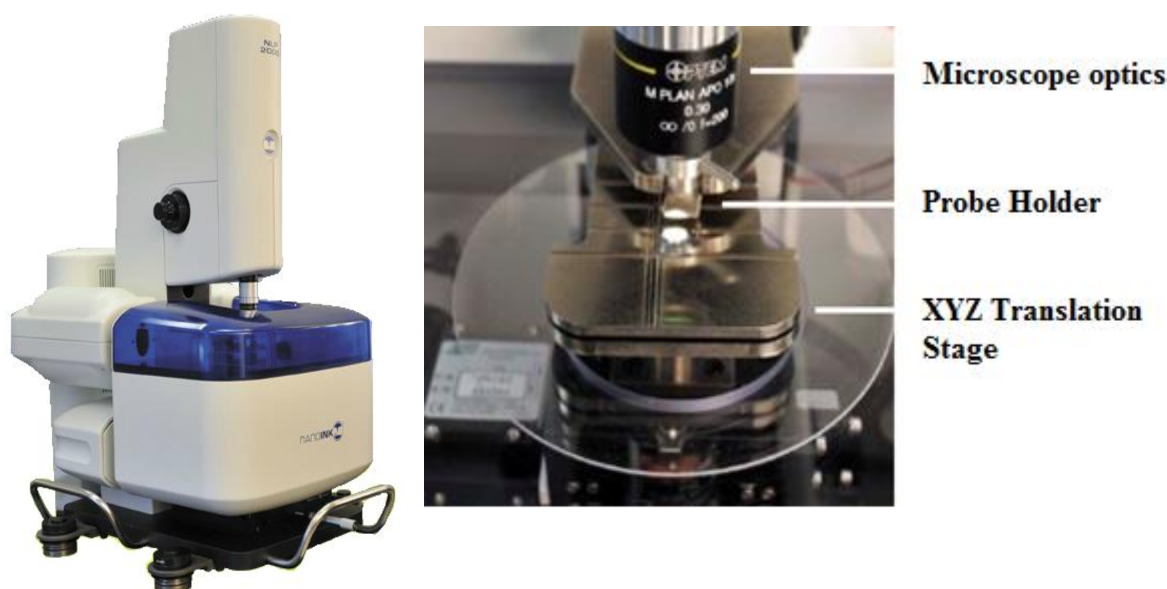

Figure 4.2.1 Image of the NLP 2000 Dip Pen system, left. Image of the substrate stage with probe holder and microscope optics, right.

The blue cover (figure 4.2.1) that is placed onto the translation area seals the environment, allowing for control and monitoring of the atmosphere within the deposition chamber. The system contains a water bath for adjusting the humidity, as well as the ability for connection to a nitrogen gas supply for completely replacing the atmosphere for handling air-sensitive

materials; these features were not used in this work. For applications which require the water meniscus for diffusion-based deposition, control of the atmosphere is critical to controlling feature size; obviously the higher the humidity the larger the meniscus will be which, in turn, will generate larger features. There are two styles of probe choices that are available for the NLP 2000 and were used in this work, one with a rectangular cantilever, dubbed a "diving board" frame, and another with a triangular cantilever, an "A-frame". These two cantilever types are shown in figure 4.2.2 along with the probe layout; there is the option of having either 12 or 48 tips in parallel allowing for large scale deposition should that be required. The functional difference between the two probes is that the A-frame has a higher spring constant than the diving board, $35Nm^{-1}$ compared to $20Nm^{-1}$. This makes the A-frame a more suitable choice for the patterning of more viscous inks and liquid inks. The diving board cantilever type

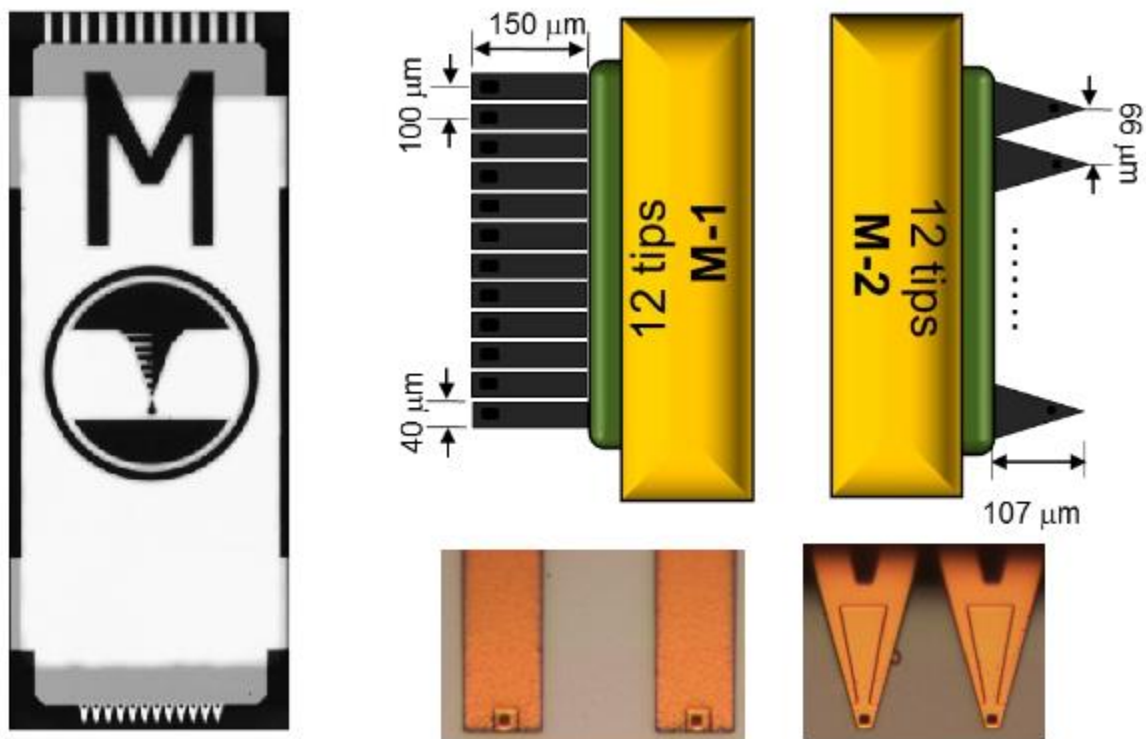

Figure 4.2.2 Image of double-ended "M" type tip probes (left). Image of diving board frame probes with array geometry (middle). A-frame tips also shown alongside array geometry and spacing (Right).

is more suitable for the deposition of molecular inks that require the formation of a water meniscus.

4.3 Photoresist Deposition

There are many photoresist materials that could be selected for work with the DPN for attempts to create masks suitable for LED fabrication. These include epoxy-based resists such as SU08 which is very viscous, solvent based and is frequently used in photolithography, and acrylate based photoresists such as the Norland family of optical adhesives, supplied with a range of fluid properties and solvent-less as it is a one part system.

SU08 Deposition

Initial tests were done with SU08 but it was found that this form of photoresist was incompatible with the dip pen deposition technique. As it is a solvent-based system evaporation can occur extremely rapidly at the small volumes that are taken when loading the tips. As the tips rise out of the ink well tails are formed as the material is drawn away, as shown in figure 4.3.1. The reason the image is blurry is to attempt to image the "tails" rather than the tips, the cause for the red shading is that the light from the imaging microscope needs to be filtered of any wavelengths that could cause premature curing of the photoresist.

Due to the rapid evaporation of the solvent attempts were made to try to extend the duration of the photoresist in its liquid state while on the tips. Dilutions of SU08 with varying amounts of toluene, having a boiling point of 110ºC, were each attempted. Dilution was found to extend the time of SU08 maintaining its liquid state but not significantly enough to permit writing of the SU08.

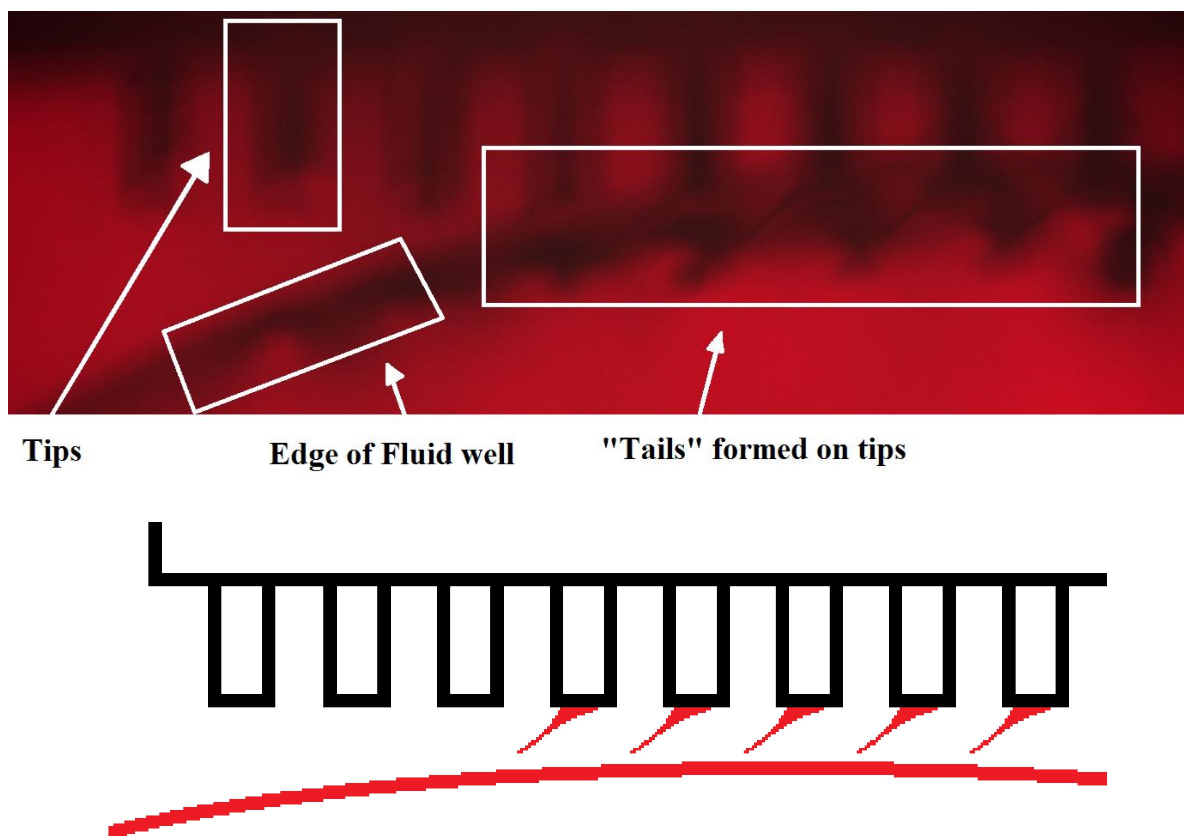

Figure 4.3.1 Top image showing the formation of solid "tails" of SU08 photoresist immediately after tip loading at the well. Bottom is a schematic to clarify the details of the photo taken.

Acrylate Deposition

These photoresist materials are a one-part system so there is no issue of solvent drying before deposition can occur. Two forms of acrylate photoresist were tested, namely NOA 63 and NOA 68T, both of which are commercially available from *Norland Products.* They are both optical adhesives that are often applied to bonding optical elements. They have optical transparency in the visible spectrum and are both cured by ultraviolet light with maximum absorption in the range of 350 nm to 380 nm. The recommended energy dosage required for full photocuring is 4.5 Jcm^{-2} in this wavelength range. The reasons they were selected is for their ability to photo-cure, the range of viscosities available, their transparency in the visible range and the potential

for their use as the host material in a guest-host system as discussed in section 2.3 and utilised in chapter 3.

	Viscosity at 25°C (cps)	Refractive index	Modulus (psi)	Hardness (Shore D)
NOA 63	2000	1.56	240,000	90
NOA 68T	20,000-25,000	1.54	12,400	50

Table 4.3.1 Fluid and physical properties of NOA 63 and NOA 68T optical adhesives. The refractive index, modulus and hardness are for cured material.

It was assumed that the key difference between the two materials selected is the viscosity when in the fluid state. Table 4.3.1 shows these values and NOA 68T has at least 10x the viscosity of the NOA 63. This higher viscosity was anticipated to limit the rate at which fluid could be transferred from the probe tip to the substrate, limiting material and reducing feature size as a result. The evolution of deposited feature size against time was measured for NOA63 on a GaN substrate. Depositions were made in varying steps from 10s down to 0.1s and then cured using a 370nm-wavelength hand lamp for 5 minutes. The size and shape of the feature size were determined with AFM measurements using an XE100 AFM instrument purchased from Park Systems. The diameter of the features was drastically reduced when the dwell time was halved from 10s to 5s, however further reductions in the size were much less dramatic upon further dwell time reduction. This size evolution for feature diameter against dwell time is shown in figure 4.3.2, alongside an image of larger such features deposited in an array.

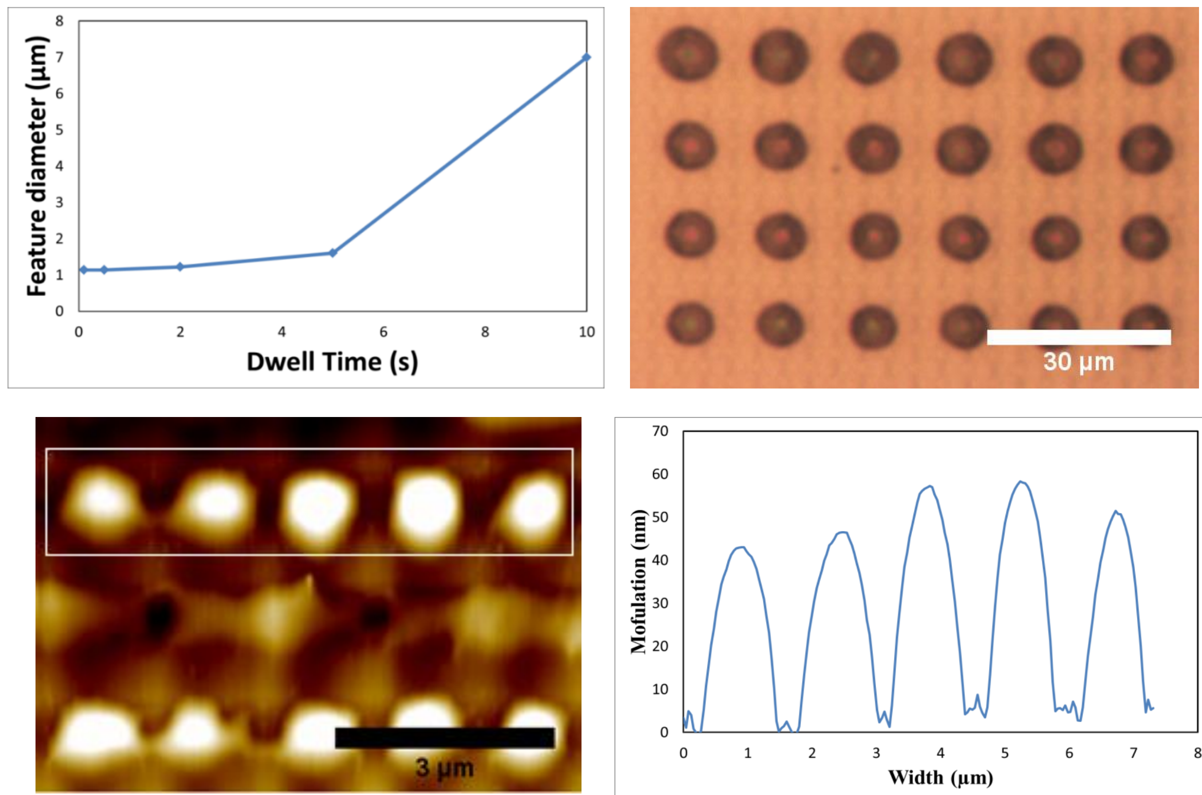

Figure 4.3.2 Evolution of feature size with dwell time for NOA63 on an A-frame cantilever (Top left). Optical micrograph of a 4x6 array of NOA63 microstructures deposited onto GaN (Top Right). The centre-to-centre pitch is 15µm with a dwell time of 10s. AFM scan of array of deposited NOA63 on a GaN substrate (Bottom Left), gradient of white to black signifying tall to shallow topography. Profile taken along the white outline (Bottom Right) showing the profile and periodicity of the deposited features.

The smallest features that the deposition of NOA 63 onto GaN achieved were 1.1µm at 0.1s dwell time; AFM scans of these features and the corresponding profile measurements are shown in figure 4.4.2. While the average size was found to be 1.1µm the shape was not always circular; it can be seen in the AFM image in figure 4.4.2 that several of the features deviate from circular deposition. This asymmetry can arise from a couple of factors – the angle of the tip as it contacts the surface and the viscosity of the photoresist. While calibrating the surface you are contacting you can see the point at which contact is made but you can't see if it is

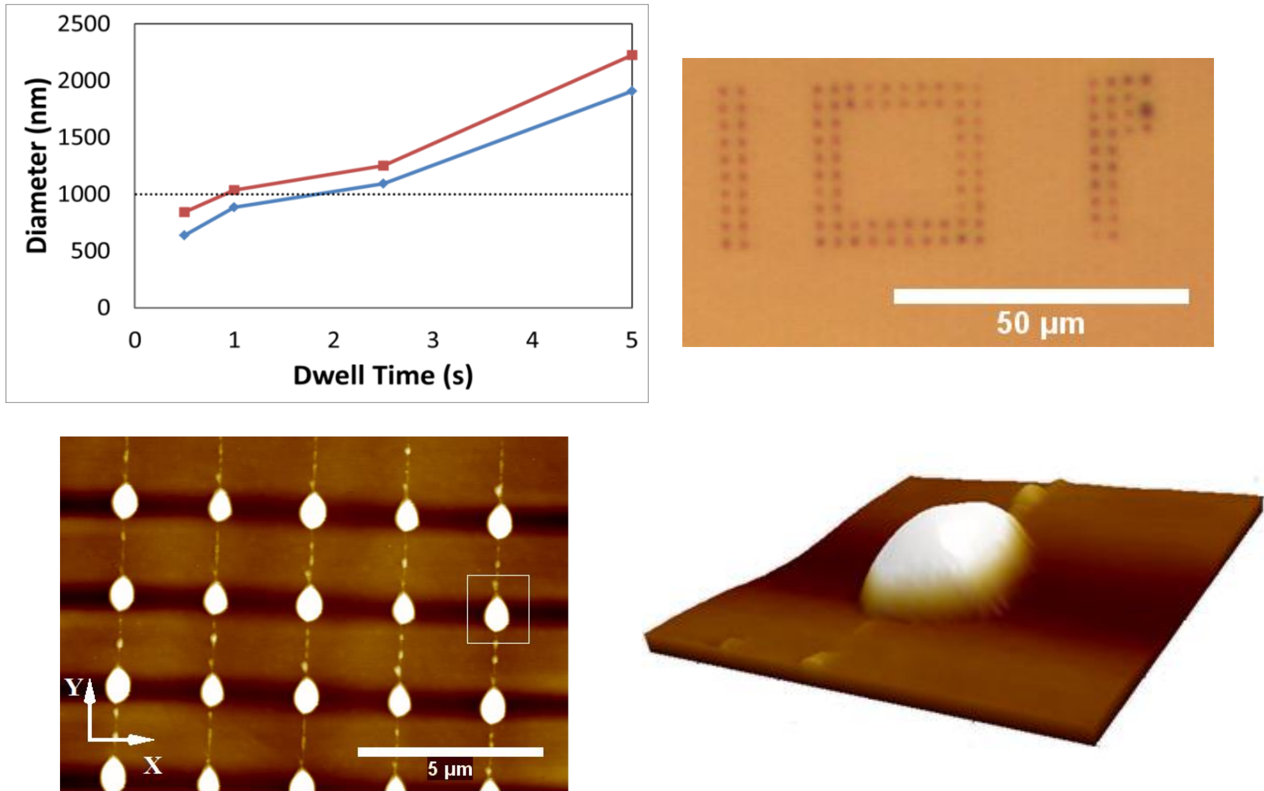

Figure 4.3.3 NOA 68T: evolution of deposited feature size with dwell time (Top Left). Red plot is the diameter along the y axis of the feature, blue plot the diameter along the x-axis. The dashed line gives the micron size scale. Image of NOA 68T deposited onto a SiO_2-topped GaN substrate with a 3µm pitch and 1s dwell (Top Right). AFM scan of an array deposited with 1s dwell and 2.5µm pitch (Bottom Left). 3D oblique image of selected feature outlined in white (Bottom Right)

perfectly perpendicular. Having an angle when contacting the substrate would mean that the droplet from the tip would flow in an asymmetric manner, generating the elongated shape observed. The viscosity of the material will also play a role, when the tip rises to relocate to the next drop a tail could form for higher viscosity materials. When the tip moved this tail could deposit additional material which again gives rise to the elongate shape. Ways to resolve this could be to introduce additional calibration steps to account for the tip tilt. Resolving the "tail" drips you could raise the tip higher before relocating, giving time for the excess material to drop onto the target on the substrate or return to the tip. In an attempt to pattern submicron features the more viscous NOA 68T material was tested with various dwell times. The

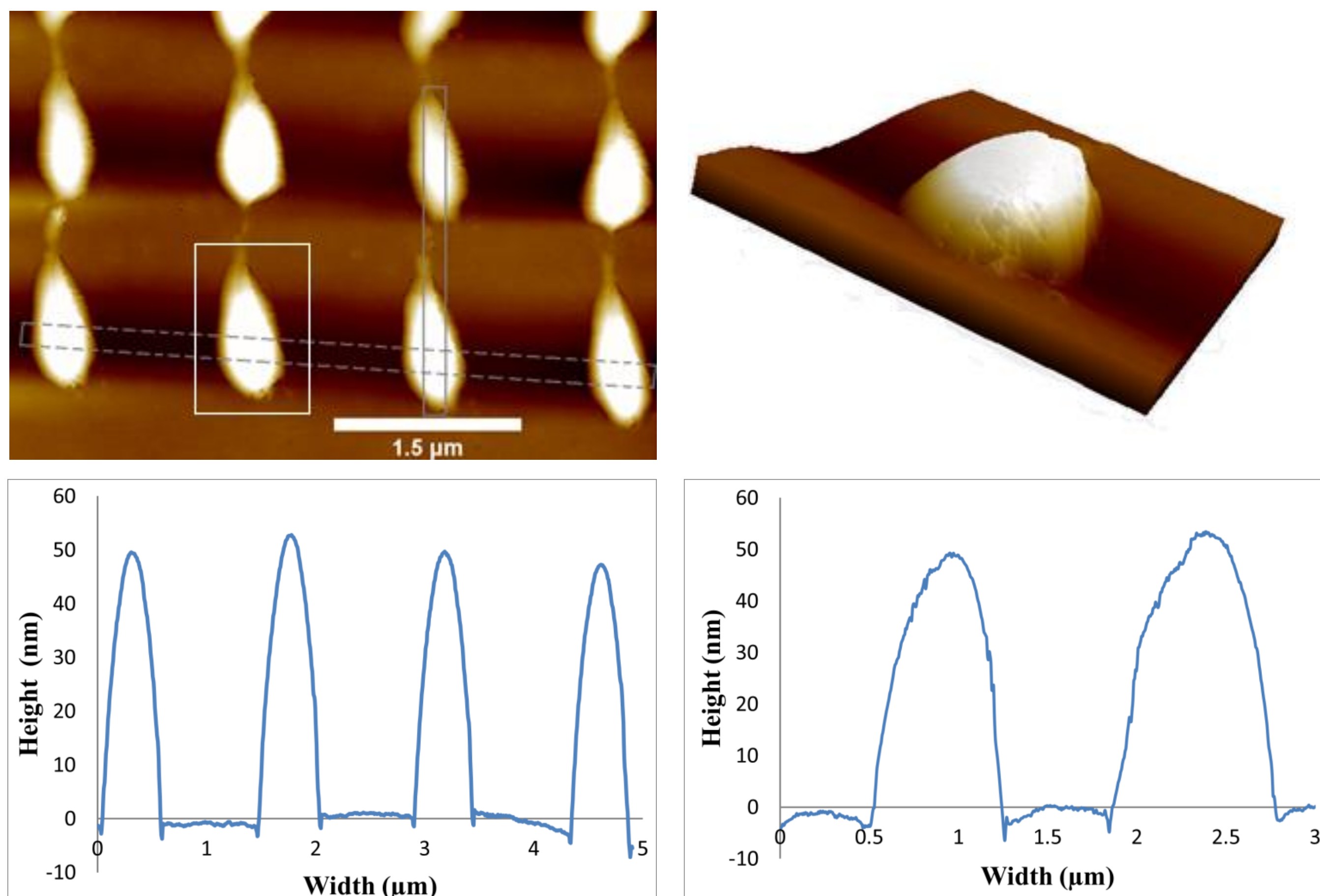

Figure 4.3.4 AFM scan of NOA 68T features deposited onto SiO_2 topped GaN with a 0.5s dwell and a 1.5µm pitch (Top Left). 3D image of feature outlined in white (Top Right). Profile measurements taken for the width of the features taken across the dashed grey outline (x-axis) (Bottom Left). Profile measurements taken for the length of the features taken along the solid grey outline (y-axis) (Bottom Right).

evolution of the feature diameter is shown in figure 4.3.3 and it can be seen that when using a 0.5s dwell time the deposited features are truly in the sub-micron scale. When depositing the more viscous NOA 68T ink it was observed that there was a "tail" formed in the writing direction, clearly shown in the AFM scans in figure 4.3.3. This gives rise to an asymmetry in the size in the direction of writing, the y-axis, and perpendicular to the writing direction, the x-axis. The trenches in the AFM scans (bottom left) running along the "x-axis" are artefacts of the data analysis and are not a physical phenomenon associated with the substrate. The presence of the tails is uniform but results in two different dimensions for the diameter; when the dwell

time was set to be 1s the x value for the size was sub-micron, 885nm, but the y value was still larger than a micron, 1035nm. The smallest features were achieved with the NOA68T material with a 0.5s dwell time and deposited onto SiO_2, where both the x and y dimensions for the features were in the sub-micron scale. The details of these features are shown in figure 4.3.4, displaying the asymmetry expected and having dimensions of 560nm and 840nm in the x and y directions, respectively. Comparing these values to those of other attempts to deposit photo-curable materials there is between a 4.8x and 1.2x size reduction for using liquid inks. When compared to the size of CHDV features deposited as in reference [14] there is a drastic improvement and the potential for nanophotonics is established. This size scale is state-of-the-art for this ink type and deposition methodology.

The ability to deposit these sub-micron features of photo-curable material opens a wide range of applications in top-down fabrication. For classical fabrication it eliminates several stages in patterning (the application of a photoresist film, UV exposure either through a high resolution mask or via time-intensive direct writing) and development is combined into one stage of deposition and 5 minutes of photo-curing. Once the nano-pattern is deposited it can be used as a sacrificial mask for etching, as a means of area selection for growth or further deposition.

4.4 Plasma Treatment of GaN LEDs

In the fabrication of LEDs, as covered in section 2.2, either a wet etch or a dry etch is used to transfer the photoresist pattern into the semiconductor for device definition. The wet etch process utilises corrosive chemical solutions that dissolve the wafer and photoresist material to transfer the pattern. The rate of etching of the semiconductor wafer to the etch mask is

controlled by the temperature and concentration of the chemical solution. One of the issues with the wet etch process is that it usually produces an isotropic etching profile. Achieving small features with high quality is thus very difficult. Furthermore, GaN materials are not readily compatible with wet etching.

The alternative to this is a dry etch process or plasma treatment, a common technique which can be used to embed ions into the crystal lattice of the semiconducting material, deposit material upon the surface for growth, or as a means of material etching (as covered in section 1.2) [16,17].

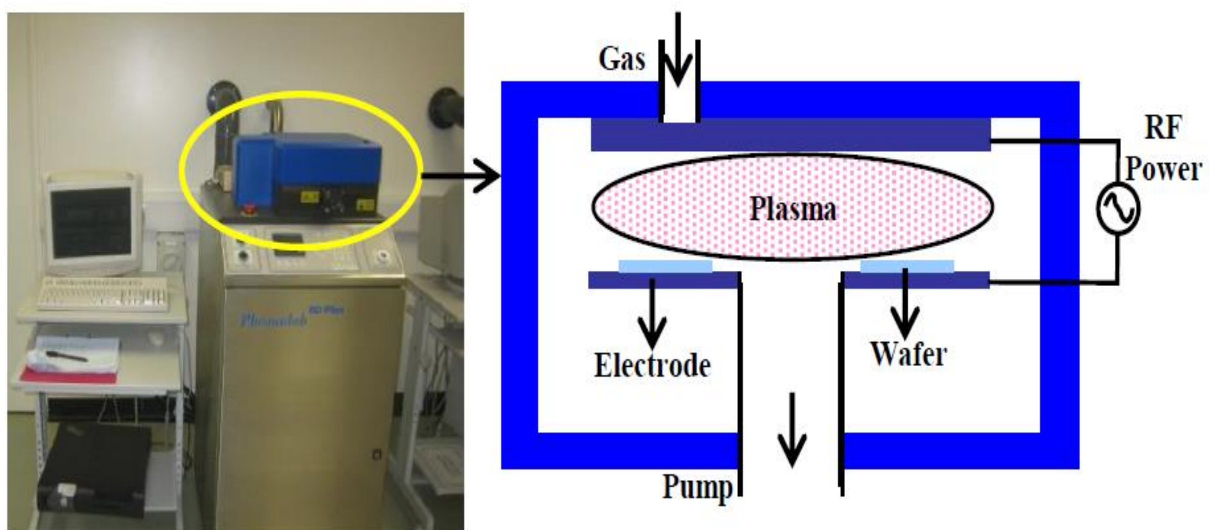

Figure 4.4.1 Image of RIE system (left) and the schematic (right) for an RIE chamber. Outlined in yellow is the processing chamber.

The rate of etching for physical bombardment in plasma etching is relatively low but has the advantage of being anisotropic, allowing high quality features of small size to be etched. Two dry etch tools are available to our group, namely reactive ion etch (RIE) and inductively coupled plasma (ICP) systems.

A schematic for the RIE chamber is shown in figure 4.4.1. Initiation of the plasma is achieved by applying a radio frequency (RF) electromagnetic field with a typical frequency of 13.56

MHz. The gases used to form the plasma are usually Ar and CHF_3 with the plasma formed having a density within the RIE chamber of around 1 to 5 x10^9 cm^{-3} with the processing pressure in the RIE chamber typically between 5 to 150 mTorr. The ion energy, which is directly related to the power of the electromagnetic field and processing pressure, ranges from 30 to 1000 eV.

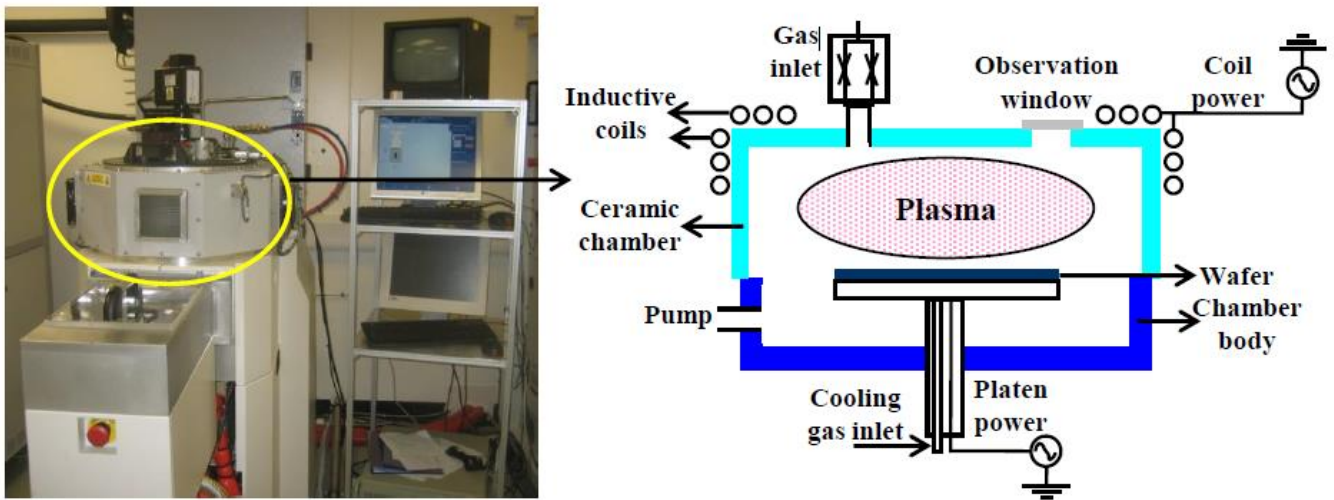

Figure 4.4.2 Image of ICP system (left) and the schematic for an ICP chamber (right). Outlined in yellow is the processing chamber.

The ICP, shown in figure 4.4.2, is a modified RIE system with an inductively coupled plasma source which incorporates a radial inductive coil design. This inductive coil can generate high density plasmas, compared with that of the RIE system, resulting in an increased etching rate. The power of the inductive coil mainly controls the plasma density, whilst the platen power strongly dictates the energy of ions for physical bombardment. The processing pressure in the ICP chamber is typically between 1 to 100 mTorr, with a plasma density being about 5 x 10^{11} cm^{-3}.

In this work passivation of Mg doped positive-type (p-type) GaN by means of H_2 plasma treatment via RIE system is explored. When high energy H ions combine they can easily form Mg-H complexes, which deactivate p-type material by reducing the "hole" defect density,

resulting in a greatly increased resistance of p-type GaN [18]. However, this treatment is not compatible with photoresist patterning, as the process requires temperatures above 300ºC, temperatures that would cause most photoresists to burn and degrade. Investigations were conducted into the use of fluorine in the plasma treatment gas [19]. Plasma mixes of CHF_3, CF_4 and H_2 were used in this investigation and it was found that not only did CHF_3 cause a passivation of the Mg doped GaN p-type contact but that a film of 500 nm thick photoresist could protect the underlying LED from this treatment.

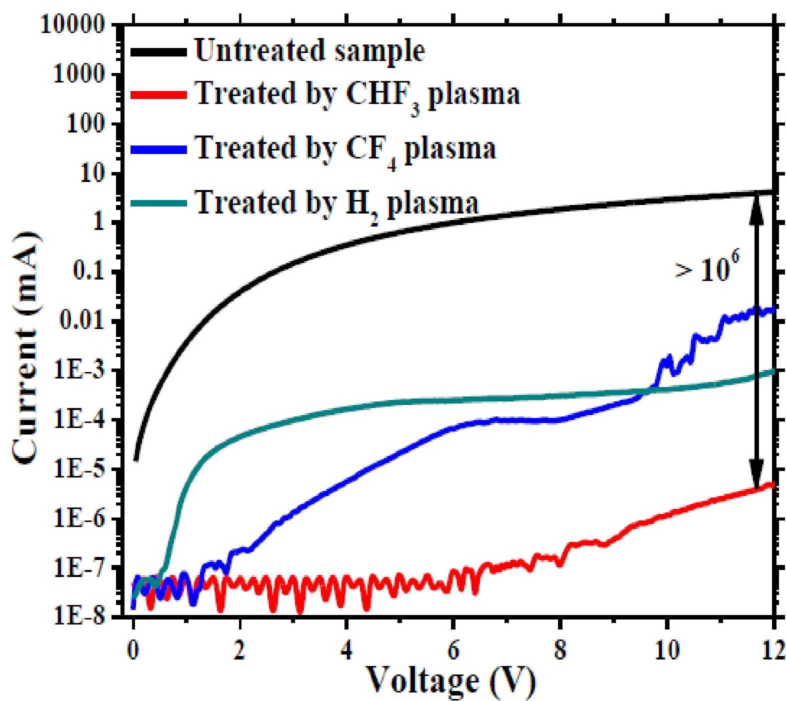

Figure 4.4.3 I-V characteristics of co-planar Ti /Au metal electrodes deposited on the p-type GaN layers with different plasma treatments. [19]

Three plasma-treated samples were prepared with CHF_3, CF_4 and H_2 used as the main plasma source for the respective treatments. The flow rates of these main plasma sources were set at 15 sccm. A small amount of Ar (5 sccm) was introduced in each test in order to stabilise the plasma density. The RIE power and chamber pressure were set at 200 W and 30 mTorr, the operation was at room temperature, and the total treatment time was 240s. Measurement of the conductivity was done by contacting the p-GaN with two conductive probes and measuring the

conductivity between them. A thick Ti/Au (40 nm/150 nm) metal bilayer was sputter coated on the plasma-treated areas of each sample in order to minimise the probe resistance during conductivity measurement. After metal lift-off the current-voltage (I-V) characteristic of each sample was measured by a semiconductor parameter analyser (HP 4155). Figure 4.4.3 shows the comparison of the I-V characteristics of the samples with plasma treatments to that without plasma treatment.

Compared with the untreated sample, a dramatic reduction of current by a factor exceeding 10^6 (at the voltages larger than 10 V) is observed for the sample treated by the CHF_3 plasma. The cause for this increase in resistivity is twofold. Firstly, there is the standard combination of H and Mg ions to reduce the carrier density within the p-type semiconductor. Secondly, the larger F ions dope the upper layers of semiconductor structure, causing a large negative charge build up at the metal-semiconductor interface. This causes an effect called "band banding" whereby the Shottky barrier is raised to inhibit electron injection. Combining these effects results in the exposed area having a greatly reduced conductivity, limiting the injection current to the multiple quantum wells (MQW) and passivation the p-GaN is possible.

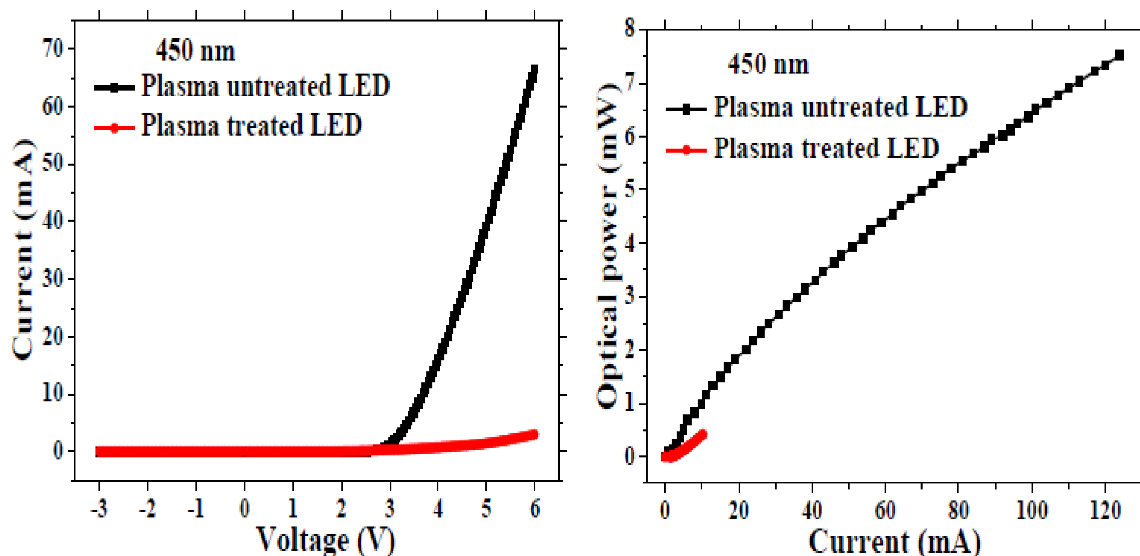

Figure 4.4.4 I-V (left) and L-I (right) characteristics of LEDs without and with a CHF_3 plasma treatment. [Personal communication]

Comparison of both the current-voltage (I-V) and output power-current (L-I) characteristics of two GaN LEDs, one which has been exposed to a CHF_3 plasma treatment and another which was untreated is shown in figure 4.4.4. It is obvious that the plasma treated LED performance is greatly reduced from the untreated; confirming that passivation of the p-GaN using the CHF_3 treatment, resulting in inefficient current injection into the LED active region for light emission.

The concept of protecting an area of an LED via photoresist and the subsequent plasma treatment is illustrated in figure 4.4.5. This concept is to fabricate a standard planar LED structure (as outlined in section 2.2), and protect a nanoscale sized area of the LED with resist via dip-pen patterning. We wished to investigate whether it would be feasible to deposit nanoscale photoresist onto a broad area GaN LED, apply plasma treatment, and then as a result have a nanoscale LED which is electrically pumped and individually addressable.

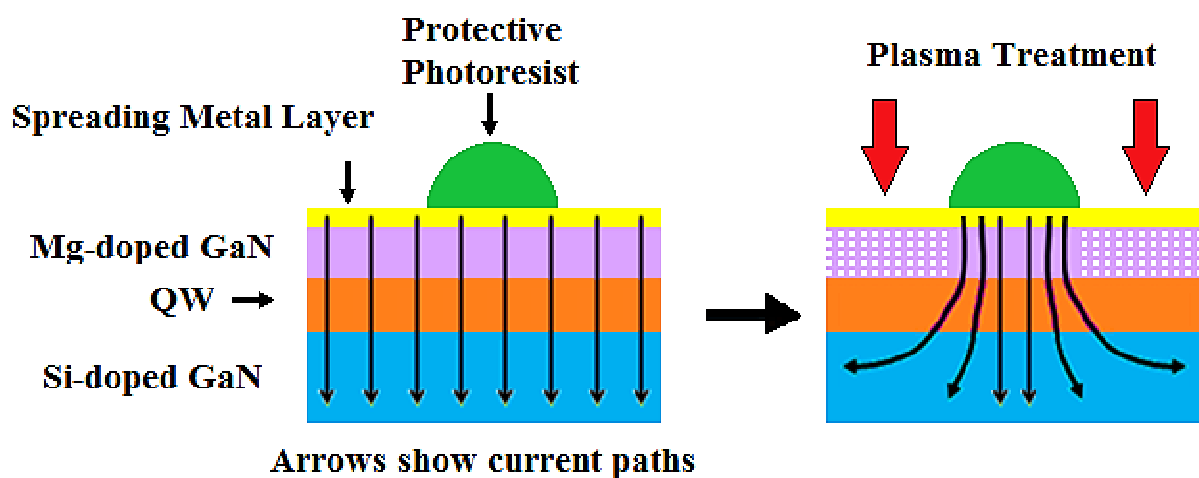

Figure 4.4.5 Schematic cross-section of a GaN LED which has had protective photoresist deposited (left) and then given a plasma treatment to definite a specific area of emission (right).

Photoresist Protection

Given the development of a plasma treatment for the passivation of p-GaN at room temperature it now became viable to use this in conjunction with photoresist materials to protect desired areas of the LED prior to treatment. With the capability of DPN to deposit nanoscale features in photoresist this opens the possibility of creating NanoLEDs in a fast and simple manner. Fabrication of nanoscale LEDs has been achieved by a number of methods previously. These include growth of nanorods, columns or wires from semiconducting material [20, 21]. However the means to achieve light generation from these structures is an issue; either the nanoscale emitting area is broadly addressed so electrical contacts can be applied, or each emitter is optically excited. Direct electrical excitation of a single nanoLED has thus not been demonstrated.

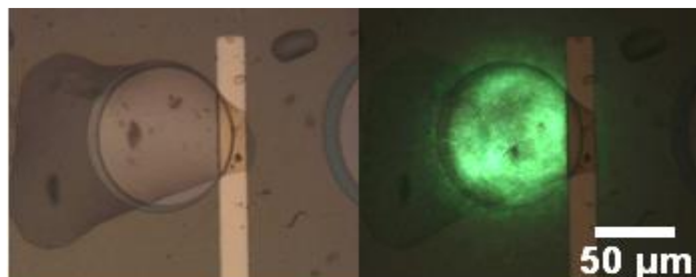

Figure 4.4.6 Test for NOA63 plasma protection for a GaN LED with emission at 520nm. NOA63 deposited onto an LED (left) the same LED turned on after 4 minutes plasma treatment (right)

To ensure that the Norland^{TM} range of optical adhesives are capable of acting as a protective layer for the GaN under plasma treatment, LED tests were conducted where 5pL of the low viscosity NOA63 was inkjet printed onto an LED and then given 4 minutes of CHF_3 plasma treatment. An example of the protected LED is shown in figure 4.4.6 and it can be seen that the protection was successful; the covered section of the LED remains active after a plasma

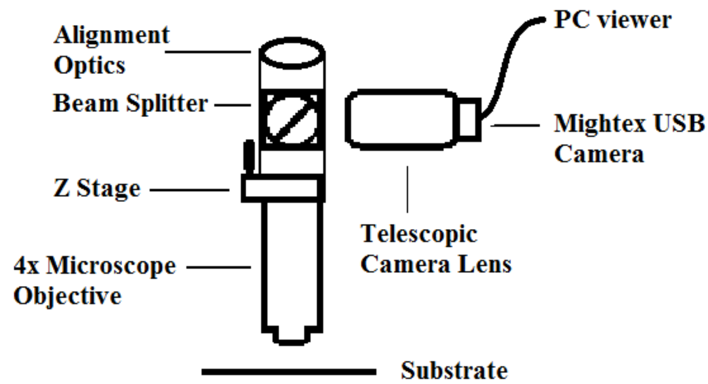

Figure 4.4.7 Schematic for imaging the LEDs and measurement of the emissive areas defined by the plasma treatment.

treatment, whereas the unprotected areas did not emit light (also shown in figure 4.4.8). Initial tests for the creation of LEDs defined by dip-pen and plasma treatment were made using NOA 63 as it has been confirmed as suitably protecting the LED in the inkjet testing.

Arrays of resist features were deposited onto LED areas to test the ability for thinner photoresist layers to protect the underlying p-GaN. The observation of the deposited features was made under either 20 x or 40 x magnification using the setup shown in figure 4.4.7. The LED substrates were placed on the substrate and aligned by eye using the alignment optics and then imaged via a USB-driven camera. The LEDs were electrically pumped by probing with

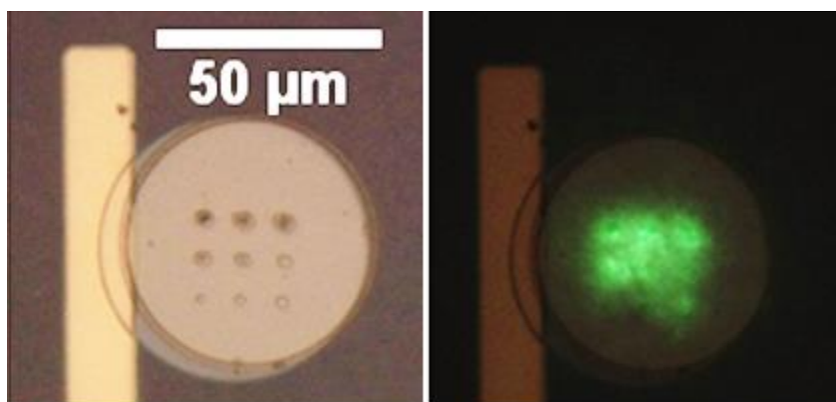

Figure 4.4.8 Deposition of NOA 63 onto a palladium-topped GaN LED with 520nm emission wavelength, in a 3x3 array with 5s dwell and 10µm pitch (right). The same pixel turned on after having had a 4 minute plasma treatment (right).

two signatone S-725 micropositioners connected to the electrical contacts. Figure 4.4.8 shows a 3x3 array of NOA63 deposited onto a palladium-topped GaN LED with an emission of 520nm, where the array had a photocure time of 5 minutes under a 370nm hand lamp.

When the dwell time was fixed to be 5s the deposited features had a size range of 5.5µm to 3.0µm. Comparing these values to those deposited previously on a GaN substrate they have nearly double the diameter at this dwell time. From this, it can be inferred that the palladium-topped surface is more hydrophilic to the NOA 63, resulting in the larger features. This would also explain the rapid depletion of material from the tips, giving the 2.5µm spread in feature size. As mentioned in section 4.2 the surface tensions involved play critical roles alongside the viscosity in determining the final feature size. When the LED emission was examined after plasma treatment it was found that the 3x3 array had protected the underlying LED but the emission was not confined to 9 distinct emitters, as shown on the right of figure 4.4.8. It is thought that, due to the hydrophobicity and roughness of the Pd surface, the NOA63 underwent further spreading than initially thought. The reason for the Pd roughness is that after deposition on the surface, a thermal annealing step is taken to increase the conductivity as a contact for the LED.

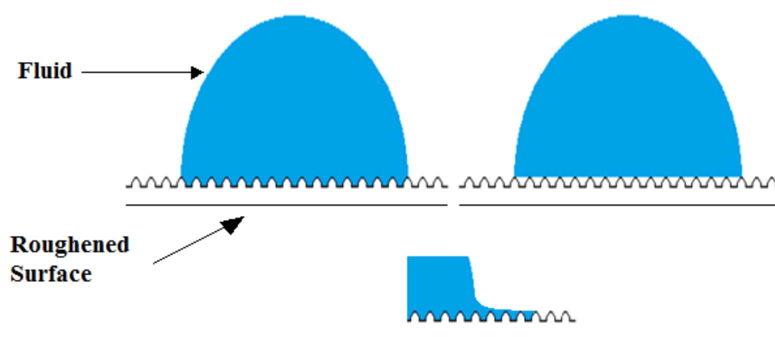

Figure 4.4.9 Wenzel wetting state (top left), Cassie-Baxter wetting (top right), Hemi-wicking across the roughened surface (bottom).

This annealing stage gives rise to an increased surface roughness as the palladium becomes granular during the atomic diffusion process. The means by which the surface can become "absorbent" is called Hemi-wicking [22, 23] and operates under a Wenzel model of wetting, illustrated in figure 4.4.9. This model involves the liquid penetrating the textured surface rather than trapping air beneath the droplet. Once upon the surface, the low viscosity NOA 63 would readily penetrate the textured Pd surface effectively creating another barrier for protection against the plasma treatment. This explains why much of the area surrounding NOA 63 deposited features remained active after the plasma treatment. The subsequent tests were conducted using the high viscosity NOA 68T in an attempt to reduce the amount of Hemi-wicking observed and generated distinct emitting areas. An array was deposited onto a 450nm emitting GaN LED using the NOA 68T with a dwell time of 1s and a 20µm pitch and a 5 minute cure time under a 370nm lamp, shown in figure 4.4.10.

There is, again, a change in feature size as the deposition progressed but it is far less prominent than observed for the NOA 63: 3.9µm diameter for the largest feature and 3.1µm for the smallest giving a 0.8µm variation rather than 2.5µm.The plasma treatment for the high

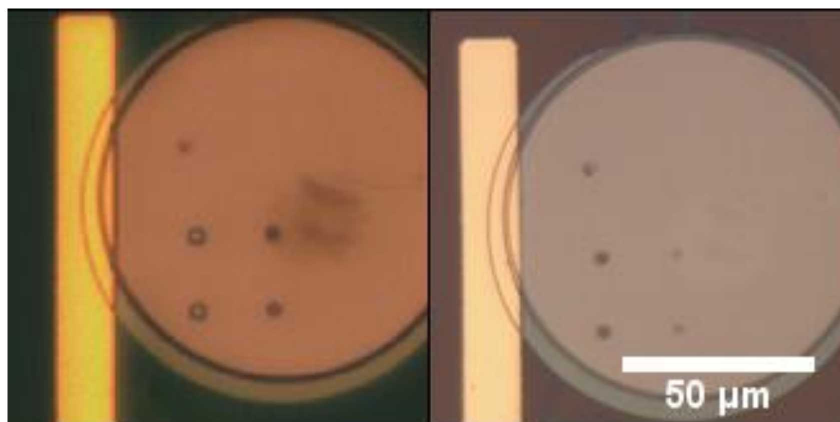

Figure 4.4.10 A 2x2 array of NOA 68Tdeposited on a Pd-topped GaN LED with emission at 450nm, with a 1s dwell time and a 20µm pitch.

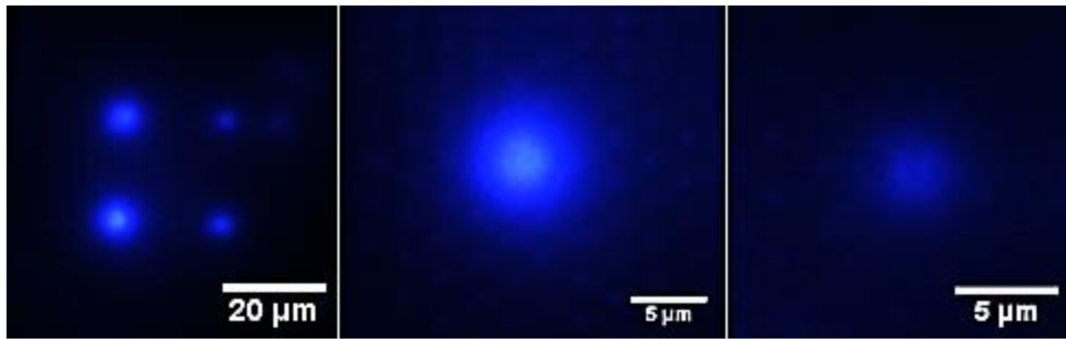

Figure 4.4.11 Plan view optical micrographs of 20x magnification of 2x2 array of emitters electrically pumped at 8V bias (left); 40X magnification of the largest emitter at 8V bias (middle); 40X magnification of the smallest emitter at 8V bias (right).

viscosity NOA 68T was successful in this instance, the deposited photoresist acting as a protective layer and 4 emitters being defined from one LED, as shown in figure 4.4.11. The blemish, seen to the centre of the LED prior to treatment, seemed to also provide some sporadic protection from the plasma treatment and there is still some light generation outside of the 4 defined areas. Shown alongside the image if the 2x2 array are images of the largest and smallest emitter defined, these images being under 40x magnification and with an 8V bias.

The size of the emitters was estimated by examining their intensity profiles. An intensity cross-section was taken for the largest and smallest emitter created; the comparison of the profiles for each of these is given in figure 4.4.12. At the FWHM the largest feature had a diameter of 6.5µm while the smallest had a diameter of 3µm. The contour map of emission at the FWHM is also shown for each of the emitters, showing that they have approximately circular emission. While this has given an estimation of the size of the emitters it is possible that near-field measurement would provide a more accurate means of determining the emitter size. Distortion of the light by epoxy remaining on the LED after plasma treatment could give an inaccurate estimation as well as natural divergence of the light from the emitter. Smaller emitters have yet to be achieved with this technique but as a proof of concept it has been successfully

demonstrated that the nano and micro-scale patterning offered by dip pen can be used in the fabrication of micro- and possibly nano-scale emitters.

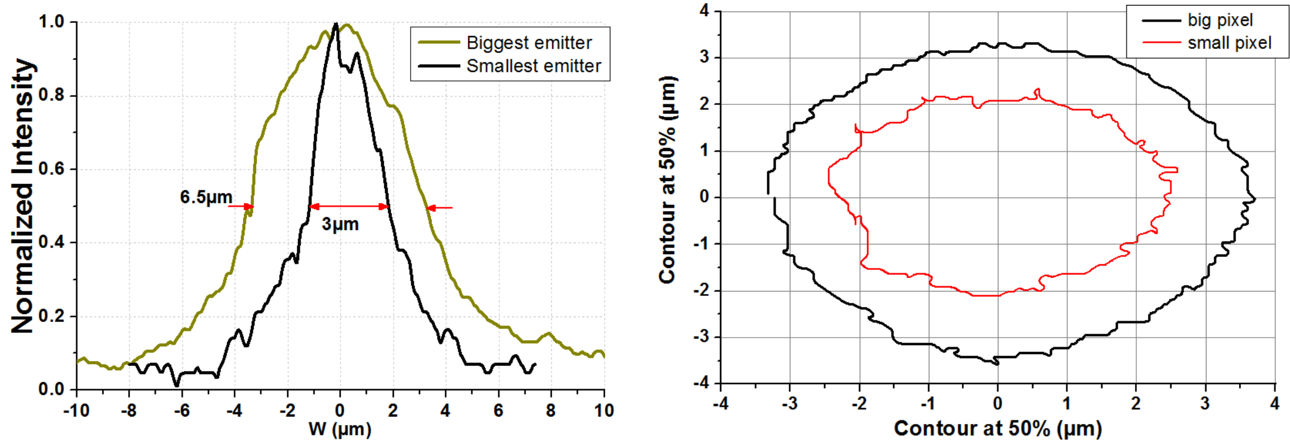

Figure 4.4.12 Intensity profile section of the largest and smallest planar LED emitter defined by photoresist (left). Contour intensity map of the emitters displaying near-circular emission (right).

4.5 Conclusions

This chapter covered the "additive" potential of dip-pen nanolithography for the fabrication of photonic devices. Investigations into photoresist materials, dwell time and tip geometry were explored with the aim of submicron patterning in mind. Features of 560 nm at full width half maximum (FWHM) have been reported, these representing a marked improvement on the ~4 μm structures reported elsewhere using similar materials and believed to be the smallest yet with relevant materials using the dip-pen technique. The ability to pattern into the nano-scale regime was coupled with a novel room temperature dry etch plasma treatment to attempt to define nano-scale LED emitters similar to the planar LEDs discussed in chapter 2. The theory and deposition model for dip-pen nanolithography, investigations into the choice of photoresist and tip type to achieve submicron features, and the application of this deposition method in the fabrication of a photonic device were also detailed. The dip-pen patterning of three UV-curable

photoresist materials was tested with the goal of achieving features of dimensions within the nanoscale regime. This was most successful when using the Norland optical adhesive NOA 68T; features with dimensions of 560nm in the x-direction and 840nm and y-directions were deposited onto GaN with a dwell time of 0.5s. This material was then tested as a mask for the fabrication of nano-emitters via a novel room temperature plasma treatment of planar LED structures. The material was shown to have a masking effect and emitters with a 3 μm diameter at FWHM were fabricated. Nanoscale emitters were not achieved in the early tests either due to a "hemi-wicking" process of the NOA 68T into the annealed palladium surface or the change in surface interactions creating larger features on Pd over GaN. Nonetheless, the approach looks very promising for future development.

4.6 References

1. D. Ginger, H. Zhang, C. A. Mirkin, "The Evolution of Dip-Pen Nanolithography", Angewandte Chemie International Edition, Volume 43, Issue 1, 30-45 (2003).
2. J-W. Jang, Z. Zheng, O-S. Lee, W. Shim, G. Zheng, G. C. Schatz, C. A. Mirkin, "Arrays of Nanoscale Lenses for Subwavelength Optical Lithography", Nano Letters, Volume. 10, Issue 11, 4399-4404 (2010).
3. H. Nakashima, M. J. Higgins, C.l O'Connell, K. Torimitsu, G. G. Wallace, "Liquid Deposition Patterning of Conducting Polymer Ink onto Hard and Soft Flexible Substrates via Dip-Pen Nanolithography", Langmuir, Volume 28, Issue 1, 804-11 (2012).
4. A. Smetana, S. Pacley, J. Boeckl, P. Adamczyk, S. Nettikadan, "Directed/Localized growth of Multiwalled Carbon Nanotubes Catalyzed by Cobalt Nanoclusters", Journal. Materials Chemistry C. Issue 9, 1798-1803 (2013).
5. L. Gonzalez-Macia, A. Morrin, M. R. Smyth, A. J. Killard," Advanced printing and deposition methodologies for the fabrication of biosensors and biodevices" , Analyst, Col 135, Issue 5, 845-67 (2010).
6. S. Hung, O. A. Nafday, J. R. Haaheim, F. Ren, G. C. Chi, S. J. Pearton, "Dip Pen Nanolithography of Conductive Silver Traces", The Journal of Physical Chemistry C, Volume 114, Issue 21, 9672-9677 (2010).
7. Nelly Durand, David Mariot, Bruno Améduri, Bernard Boutevin, and François Ganachaud, "Tailored Covalent Grafting of Hexafluoropropylene Oxide Oligomers onto Silica Nanoparticles: Toward Thermally Stable, Hydrophobic, and Oleophobic Nanocomposites", Langmuir, Volume 27, Issue 7, 4057-4067 (2011).

8. D. Lin, C. Lee, C. Liu, H. Han, Y. Lan, C. Lin, G. Chi, H. Kuo, "Efficiency and droop improvement in green InGaN/GaN light-emitting diodes on GaN nanorods template with SiO_2 nanomasks", Appl. Phys. Lett. Volume 101, Issue 23, 233104 (2012).
9. Y. Wang, F. Hu, Y. Kanamori, T. Wu, and K. Hane, "Large area, freestanding GaN nanocolumn membrane with bottom subwavelength nanostructure", Opt. Express, Volume 18, Issue 6, 5504-11 (2010).
10. O. A. Nafday, M. W. Vaughn, B. L. Weeks, "Evidence of meniscus interface transport in dip-pen nanolithography: An annular diffusion model", J. Chem. Phys. Volume 125, Issue 14, 144703 (2006).
11. J. Jang, S. Hong, G. C. Schatz, M. A. Ratner, "Self-assembly of ink molecules in dip-pen nanolithography: A diffusion model", J. Chem Phys, Volume 115, Issue 6, 2721-29 (2001).
12. S. K. Saha, M. L. Culpepper," An Ink Transport Model for Prediction of Feature Size in Dip Pen Nanolithography", The Journal of Physical Chemistry C, Volume *114, Issue* 36, 15364-69 (2010).
13. G. Liu, Y. Zhou, R. S. Banga, R. Boya, K. A. Brown, A. J. Chipre, S. T. Nguyen, C. A. Mirkin, "The role of viscosity on polymer ink transport in dip-pen nanolithography", Chem. Sci., Volume 4, Issue 5, 2093-99 (2013).
14. A. Hernandez-Santana, A. R. Mackintosh, B. Guilhabert, A. L. Kanibolotsky, M. D. Dawson, P. J. Skabara, D. Graham, "Dip-pen nanolithography of nanostructured oligofluorene truxenes in a photo-curable host matrix", *J. Mater.* Chem, Volume 21, Issue 37, 14209-12 (2011).
15. NLP 2000 system Specifications http://www.nanoink.net/pdf/DataSheets/Instruments/DS_System_NLP2000.pdf

16. D.S. Kuo, K.T. Lam, K.H. Wen, S.J. Chang, T.K. Ko, S.J. Hon, "GaN-based LEDs with Ar plasma treatment", Materials Science in Semiconductor Processing, Volume 15, Issue 1, 52-55 (2012).
17. F. F. Chen," Industrial applications of low-temperature plasma physics", Phys. Plasmas, Volume 2, Issue 6, 2164-8 (1995).
18. T.W. Kuo, S.X. Lin, P.K. Hung, K.K. Chong, C.I. Hung, and M.P. Houng, "Formation of Selective High Barrier Region by Inductively Coupled Plasma Treatment on GaN-Based Light-Emitting Diodes", Japanese Journal of Applied Physics, Volume 49, Issue 11, 6504-8 (2010).
19. D. Massoubre, E. Xie, B. Guilhabert, J. Herrnsdorf, E. Gu, I. M Watson and M. D. Dawson, "Micro-structured light emission from planar InGaN light-emitting diodes", Semiconductor Science and Technology, Volume 29, Number 1 (2014).
20. Y. D. Zhuang, C. J. Lewins, S. Lis, P. A. Shields, and D. W. E. Allsopp, "Fabrication and characterization of light-emitting diodes comprising highly ordered arrays of emissive InGaN/GaN nanorods", IEEE Photonics Technology Letters, Volume 25, Issue 11, pp. 1047-49 (2013).
21. A. Kikuchi, M. Kawai, M. Tada and K. Kishino, "InGaN/GaN Multiple Quantum Disk Nanocolumn Light-Emitting Diodes Grown on (111) Si Substrate", Japanese Journal of Applied Physics, Volume 43, Part 2, Number 12A (2004).
22. J. Bico, U. Thiele, D. Quéré, "Wetting of textured surfaces", Colloids and Surfaces A: Physicochemical and Engineering Aspects, Volume 206, Issues 1–3, 41-46 (2002.)
23. D. Quere, "Wetting and roughness", Annual review of materials research, Vol.38, 71 - 99 (2008).

Chapter 5

Negative Patterning via Dip Pen Nanolithography

5.0 Introduction

When attempting to generate nanoscale patterns there exist several established top down methods with optical lithography, electron beam lithography (e-beam) and nanoimprint lithography being amongst the most common. For applications where the removal (rather than the addition) of material is desired these methods can swiftly become complex and costly, as described in chapter 1. It is difficult to negatively pattern an active material without first having a master structure, created using the methods described, and imprinting the pattern using pressure. This is how nanoimprint lithography (NIL) operates and it is possible to have high pattern fidelity, feature fabrication down to 10 nm, with large area imprinting to permit high volume throughput [1,2]. Disadvantages of this technique are that a master imprint template is required, generated via either e-beam or optical lithography; the templates are prone to wear and cannot be altered once designed. In a research environment swift, small scale prototyping may be desirable over the more costly approach of nanoimprint lithography. Some related use of atomic force microscopy (AFM) technology has been explored such as dynamic ploughing and local oxidisation techniques [3-6], however there are issues there of patterning polymers to any depth that would allow for stand-alone films for either masking or as an active structure, without further processing. The work reported here expands on the abilities of the DPN tool as

a means of material removal and achieving sub-micron scale patterning to create active structures for lasing purposes [7,8]. This approach allows for interesting new structures to be realised swiftly and with complete flexibility, without the need for fabrication of a mask. In addition there is no exposure to high energy radiation or electron beams, so there is also the possibility of patterning sensitive materials that might not endure other means of patterning.

5.1 DPN Operation and Tip Geometry

The DPN system used in this work is an NLP 2000 series desktop instrument. The theory behind DPN and the operation of the NLP 2000 system are covered in chapter 4 sections 2 and 3. The tips supplied are pyramidal with a base of 4μm x 4μm and a height of 1.33 μm with a half-cone angle of 33.6°, as shown in figure 5.1.1. These tips are mounted on one of two types of cantilever, A-frame and diving board, as described in section 4.3. The A-frame cantilever exhibits a much larger stiffness constant than the rectangular diving board and is more suited to tasks with higher viscosity fluids. The tips are mounted on cantilevers either singly or as a tip array for parallel writing. The tips are held on a magnetic mount and maintain a fixed position throughout the nanolithography platform operation. The NLP 2000 has an optical microscope/imaging setup situated above these tips which is computer controlled to allow

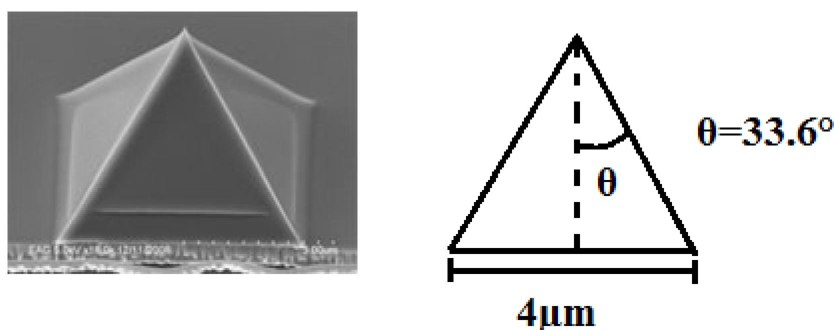

Figure 5.1.1 SEM image and schematic of pyramid tip supplied by NanoInk Inc.

imaging of the substrate and tips whilst in operation. Both focus and zoom functions are included for fine resolution of tips and substrate.

The NLP 2000 also has a computer-controlled motion stage for mounting the substrate on, having xyz control as well as x and y tilt control. Substrates and inkwells alike are positioned on this stage and it is control of their position relative to the fixed position of the tips that permits the writing of patterns. There is the capability of saving position parameters in the software, recording the xyz coordinate and the respective tilts, which can then be rapidly found and zoomed to at a later time. The use of three coordinates permits a plane to be defined; this plane allows the substrate to be raised to the tips at any point rather than having to have saved at each location individually. Coupled with the capability to save multiple positions of the stage, there is the ability to define several planes as you pattern, opening the possibility of patterning onto 3D shapes rather than flat substrates.

In order to find the correct position where the tips touch the substrate without excessive force the substrate must be gradually raised until it can be seen underneath the imaged tips. Using steps of 1 or 2 μm one raises the stage until the tips touch the substrate and then saves the position. It can be easily determined when the tips are in contact as the cantilever deforms and there is a change in the reflection observed. Once the plane has been defined by using the three saved coordinates the substrate can be contacted rapidly by using the "approach to plane" function. A defined plane is also necessary in the use of programmable patterns, of which arrays of lines and dots are possible.

5.2 Planar Distributed Bragg Reflectors

As mentioned earlier, the work in this chapter is focused on the ability of the DPN tips to negatively pattern a film rather than engage in additive lithography. The demonstration of this technique will be to pattern a DBR-based optical cavity structure and observe the effect it has on the stimulated emission in a lasing polymer.

Design of DBR lasers bears many similarities to other laser structures. On the most basic level the structure must have two mirrors to form the optical cavity, (one of which is for output coupling), a gain medium and a pump source. The schematic for such a laser is shown in figure 5.3.1. With DBR lasers the two mirrors are created with DBRs. They consist of features with a periodic modulation of the refractive index, the number of periods determining their reflectivity (see further). In our demonstration, the polymer film is the laser gain medium. This film also acts as an optical waveguide for the amplified light, which can then travel back and forth between the two DBRs as schematised in figure 5.2.1. The thickness of the film dictates the number of transverse modes that can be guided (transverse representing the vertical direction in figure 5.2.1). The thickness is chosen here so that only the fundamental transverse mode (TE_0, TE for transverse electric) is efficiently guided. The light-emitting polymer used for this gain medium is poly[2,5-bis(2',5"-bis(2"-ethylhexyloxy)phenyl)-p-pheylene vinylene], known as BBEHP-PPV [9], covered in section 2.4. A spin coated film of this material can be pumped optically with an excitation wavelength in the near UV to correspond with the absorption of the polymer. This polymer has previously been used to demonstrate

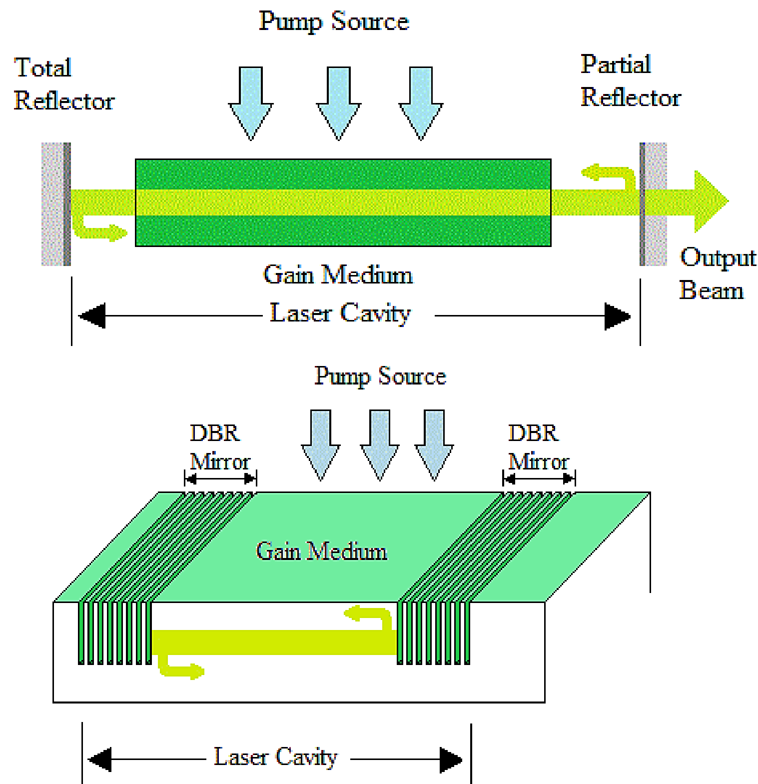

Figure 5.2.1 Top: basic schematic for laser design displaying the essential components of the mirrors for feedback and wavelength selection, the gain medium for light generation and the pump source for achieving population inversion in the gain medium. Bottom: schematic for DBR laser design illustrating the replacement of reflectors with DBR gratings.

"random lasing" [10, 11] action with no pre-defined laser cavity [12] and has been investigated for lasing in distributed feedback (DFB) cavities defined by imprinting techniques [13].

The DBR structures operate by periodic changes of refractive index causing reflection and therefore optical feedback for light guided in the film. Using the DPN removal of material on the polymer film can create periodic arrays of high and low refractive index regions via both lines and dot arrays, thereby leading to 1D and 2D grating structures. Such photonic structures have been demonstrated using the nanoimprint technique, as discussed earlier, but the flexibility of the DPN should allow the fabrication of photonic gratings alongside more exotic

photonic structures [14, 15]. A simple 1D grating design is shown in figure 5.2.2, variation of the periodicity within the DBR mirror allowing selection of wavelength for reflection.

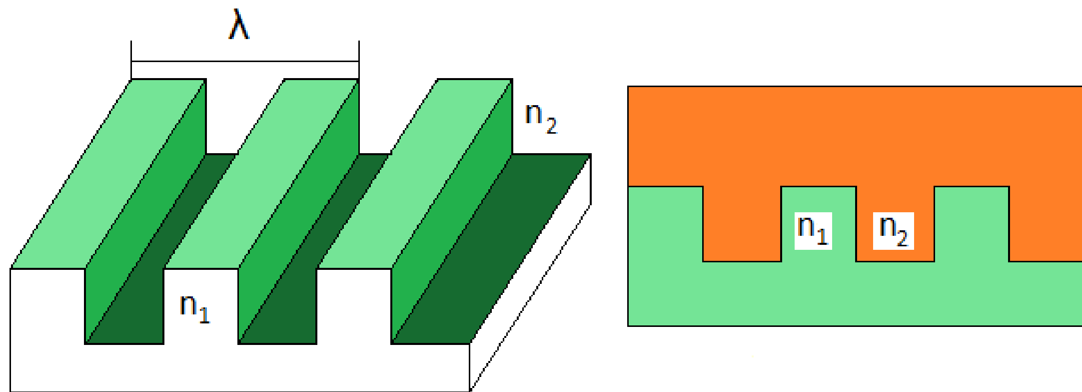

Figure 5.2.2 Schematic and cross section of a distributed Bragg reflector grating with materials of refractive index n_1 and n_2.

Here we consider light that is guided in the plane of the grating (plane of the page), and whose incidence is perpendicular to the refractive index periodicity, as the green arrows illustrate in the bottom of figure 5.2.1. In this case, the basic form of Bragg's law is given by equation 5.2.1 and governs the diffraction of electromagnetic radiation by such a periodic structure.

$$m\lambda_B = 2\Lambda n_{eff} \tag{5.2.1}$$

In equation (5.2.1) m is an integer, λ_B is the Bragg wavelength, Λ is the periodicity of the structure, n_{eff} is the effective refractive index of the guided mode. The reflectance of the whole structure is dependent on the magnitude of the difference in refractive indices of n_1 and n_2, the number of periods, and the modulation depth; a higher difference in index will yield a higher reflectivity for a given number of periods [16-18]. These 1D interference gratings can be used in laser structures, using the Bragg scattering to create the optical feedback necessary and making either material n_1 or n_2 the gain medium. Another term for these periodic corrugated

structures is a “photonic crystal”, with the type shown in figure 5.2.1 being a 1D photonic crystal. When increasing the dimensionality of a grating to that of 2D one must form shapes such as pillars or cylinders of different refractive indices. The change in design is shown in figure 5.2.3 and it can be seen that there are now islands of material n_1 contained by material n_2.

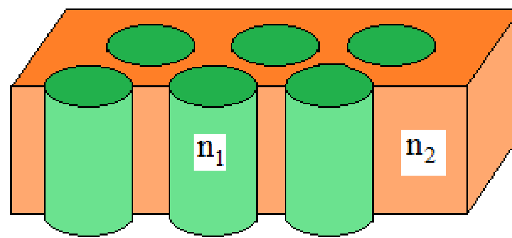

Figure 5.2.3 Cross section of a 2D photonic crystal structure of two materials with refractive indices of n_1 and n_2.

Photonic crystals both of 1D and 2D design can act as optical feedback structures and a means of light management within photonic systems [19, 20]. Using both the “dot array” and “line scribing” functions of the NLP2000 DPN apparatus, production of these two types of gratings was investigated. As explained in the following section, the two types of gratings can be, for simplification and in the case of the experiments carried out in this work, considered as 1D periodic structure for light propagating perpendicularly to the plane of periodic refractive index modulation (as obtained with holes as shown in figure 5.3.9)

DBR Modelling

To qualitatively understand the DBR fabricated in this work and to gain some insight when considering results of section 5.3, a matrix model was implemented by Dr N. Laurand (Appendix B). Parameters considered for the model are taken from experimental measurements

of the fabricated structure (see following sections for fabrication results). The model is used to estimate the expected reflectivity spectrum of the DBR fabricated in this work and is briefly explained below.

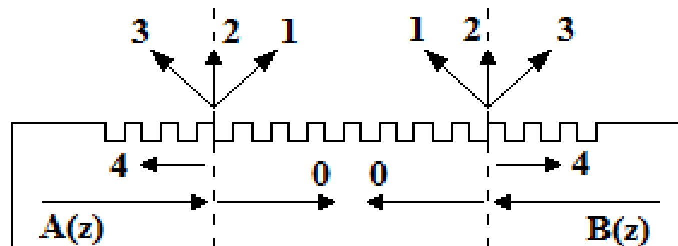

Figure 5.2.4 Schematic of in plane diffraction orders for coupled-wave model analysis. A and B are counter-propagating T=0 guided modes within the structure. The diffraction orders are κ_1, κ_2, κ_3, and κ_4.

The model considers a mode interacting with a one-dimensional grating but as said before, even our 2D problem can be approximated to such an equivalent 1D pattern if we consider light travelling perpendicularly to the periodic structure. The reflectivity calculated is for the TE_0 mode of the equivalent slab-waveguide, formed by the thin film of organic on glass, propagating perpendicularly to the grating (i.e. within the film). A typical value for the effective refractive index, n_{eff} (1.56), for the TE_0 mode at a wavelength of 530 nm for a BBEHP-PPV film of 200nm is considered.

The DBR in the experiment is made by a modulation of the thickness of the film obtained by indentation at the film surface. A small fraction of the guided light is reflected back at each of the interfaces created by these indentations. As will be seen in following sections, the periodicity of the fabricated DBRs is higher than one wavelength, therefore losses due to light diffracted out of the gain film needs to be considered. The different parameters can be obtained through a couple mode analysis [See appendix B]. A schematic for the problem is shown in

figure 5.2.4 for m=4, corresponding to the structures fabricated (see section 5.3). The field equation for the situation described in figure 5.2.4 is shown in equation 5.2.2.

$$E(x,z) = [A(z) + B(z)].E_T(x) \tag{5.2.2}$$

$E_T(x)$ is the transverse spatial profile of the TE_0 mode and $A(z)$ and $B(z)$ are the propagating and counter propagating mode amplitude (longitudinal direction, z), respectively. They couple through a coupling coefficient, basically representing the reflecting light over a periodicity of the grating, κ_4. The κ_1, κ_2, and κ_3 diffraction coefficients are considered as losses for the system as they represent the diffraction outside of the plane of the film. The couple-mode approach was used to determine values for the losses and the coupling coefficients. A simple planar waveguide analysis was first used to determine the average effective refractive index of the mode and the overlap of the modal field with the indentation region. The latter is a parameter for calculation of the coupled coefficients (see Appendix B).

Once the coupled coefficients of the structure are obtained, the model calculates the DBR reflection spectrum by a matrix approach. The matrix for one period is the product of a propagation matrix, P, and an 'interface' matrix, T. The propagation matrix takes into account the spectral gain of the material and the modal effective refractive index. The interface matrix accounts for losses (via K_1, K_2, and K_3) and the feedback from the coupling coefficient K_4. The product matrix is for a single period of the structure; it is taken to the Nth power to calculate the matrix of a DBR of N periods.

The reflectivity of such a grating structure was modelled and the results are shown in figure 5.2.5. The details of the programme and equations used to model this are, again, in appendix B. In the production of gratings deviation from the ideal can arise from variations of material

thickness and minor fabrication errors leading to disorder in the periodic features. This disorder gives random phase changes that can also be included qualitatively in the model. The modelled grating, whose reflection spectrum is shown in figure 5.2.5, comprises 10 periods with a pitch of 700 nm and a modulation depth of 40 nm. The reflectivity as a function of wavelength is shown alongside the change as disorder is included in the model. It can be seen that disorder reduces the reflectivity, but the latter is expected to be above 10% for 10 periods, at least if disorders and defects can be minimised.

Note that the DBR laser structure of Fig 5.2.1, can be simply considered as a Fabry-Perot cavity made of a gain material of effective refractive index n_{eff} enclosed between two mirrors whose reflectivity can be estimated by the model explained above. It is important to note though that

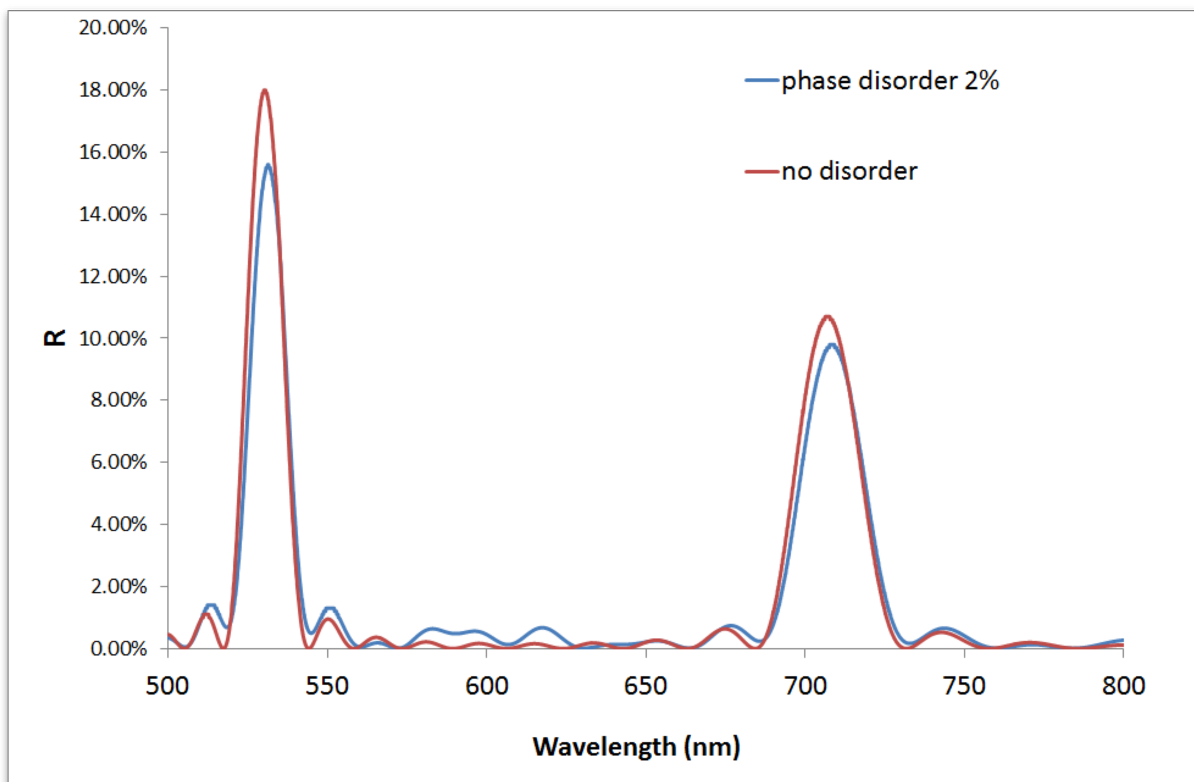

Figure 5.2.5 Calculated reflectivity of a DBR structure with 700nm pitch and 10 periods. Two areas within the visible range are reflected, centred around wavelengths of 530 and 710nm. As disorder is increased within the grating the reflectivity deceases, as is apparent when comparing the peak reflectivities with and without disorder. Analysis courtesy of Nicolas Laurand in Appendix B.

a field entering a DBR structure will have a penetration depth, L_{depth}, which corresponds to how far into the reflector the field penetrates before being mostly reflected. The total cavity length for the simple Fabry-Perot model is therefore the sum of the separation between the two DBRs and the penetration depths in both DBRs.

5.3 1D and 2D Grating Imprint Patterning

Initial tests for achieving 1D and 2D grating structures by DPN were carried out on an optically active gain medium spin-coated onto glass. The polymer used was the green-emitting π-conjugated polymer, (BBEHP-PPV), of refractive index $n=1.7$ at 530nm, which can be optically excited in the UV-blue range of the spectrum (see characteristics given in chapter 2). The methodology used for creating the spin-coated samples was to use a solution of BBEHP-PPV dissolved in toluene, drop-coat a cleaned glass slide with this solution and spin at 2.0krpm. The solution of BBEHP-PPV was created by weighing out 2.5-3mg of BBEHP-PPV powder and dissolving it in toluene to generate a 20mg/mL solution. The glass slide was cleaned using a cycle of washing by placing it in a beaker firstly in acetone, then in methanol and finally deionised water. Each wash step was given a 5 minute period in an ultrasonic bath, to remove all inorganic and organic contaminants. The glass slide was air dried and left on a hot plate at 60° for 10 minutes to ensure complete evaporation of the cleaning solvents.

1D Gratings

Initial tests for DPN-generated scratched gratings were conducted with the 33.6° half-cone-angle tips on the A-frame. Atomic force microscope (AFM) images, phase diagrams and profile measurements of the first patterns produced for 1D grating structures are shown in figure 5.3.1.

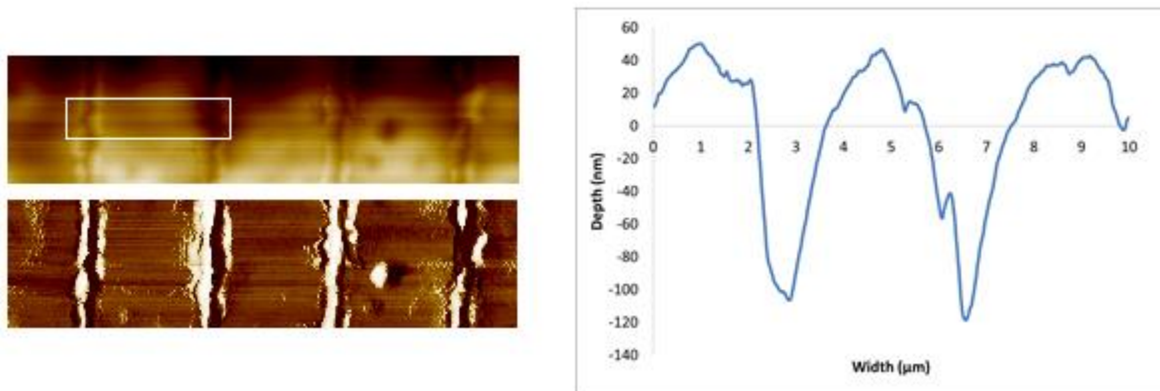

Figure 5.4.1 Top left: AFM scan of scratched grating in BBEHP-PPV polymer, pitch 5µm and writing speed 10µms^{-1}. Bottom left is corresponding phase image of the AFM scan. Right is the profile scan of the segment outlined on the AFM scan.

The patterns generated are clear to see but in this case however the scratched grating did not maintain correct fidelity to the desired pattern. The lines scored upon the film exhibit significant defects that would ultimately have had a detrimental effect on attempts to scale the patterns down to that of an optically active grating.

After preliminary tests on pattern designs were conducted, efforts were made to scale the process to the point where an optically active grating would be feasible. The requirements for such gratings (as determined by the Bragg equation) would be for the centre-to-centre feature pitch to be 350nm, 550nm or 700nm for a 2nd, 3rd or 4th order grating, respectively.

Subsequent attempts to achieve 1D grating structures used two methods for controlling the patterning; either changing the writing speed or including repeat scratch steps to ensure the correct grating formation. Figure 5.3.2 displays the results from increasing the number of repeats to two, as well as a decrease in pitch from 5µm to 1µm. The AFM of the scratched gratings again makes the transfer of the pattern obvious; this and the profile measurement

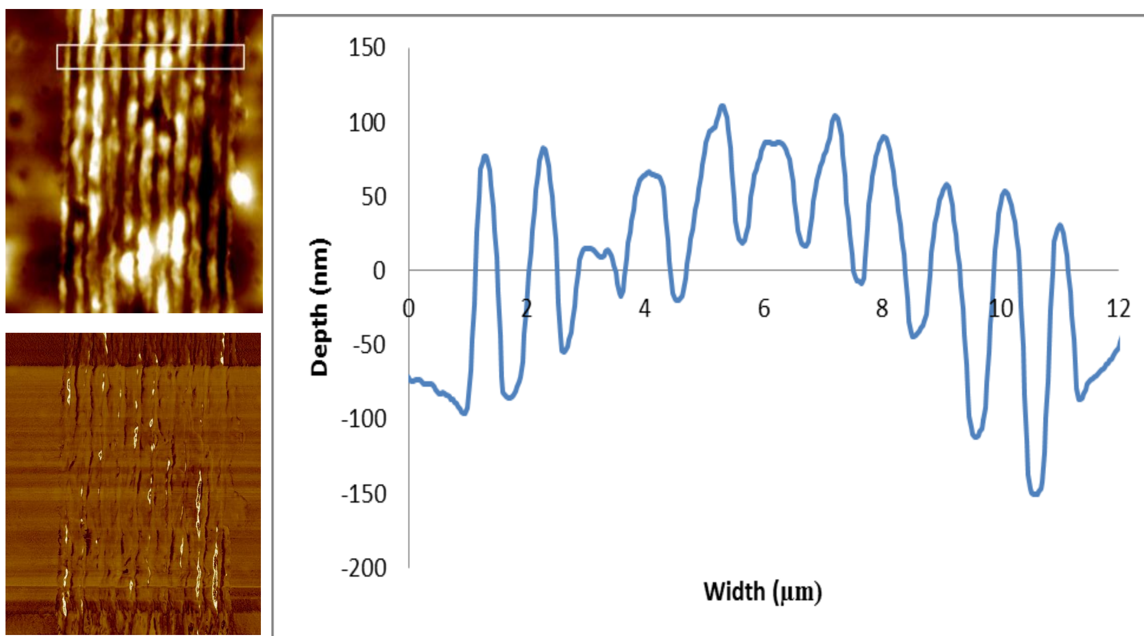

Figure 5.3.2 Top left: AFM scan of 10 lines grating of 1µm pitch at 10µms^{-1} writing speed with 2 repeats. Bottom left: corresponding phase diagram. Right: measured profile along the white outline of the top left image.

shows there is a clear grating structure present. The average full width half maximum, FWHM, of each ridge is 500-600nm but there is a widely varying modulation depth of 80-160nm. From the AFM results it can also be seen that there are breaks in the written structures, uneven ridges and some distortions in the film. Part of this will be due to inhomogeneity in the film and some will be due to the act of writing, with the tip distorting the film rather than removing material. To enhance the removal of material, tests were made of having a well of toluene to dip the tips into before writing commenced, with the hope of locally dissolving the film. This technique was found to have little to no effect however. Due to the high volatility of the solvent and the small volume retained on the DPN tip, any amount of toluene that may achieve the desired result evaporates before contact with the BBEHP-PPV film.

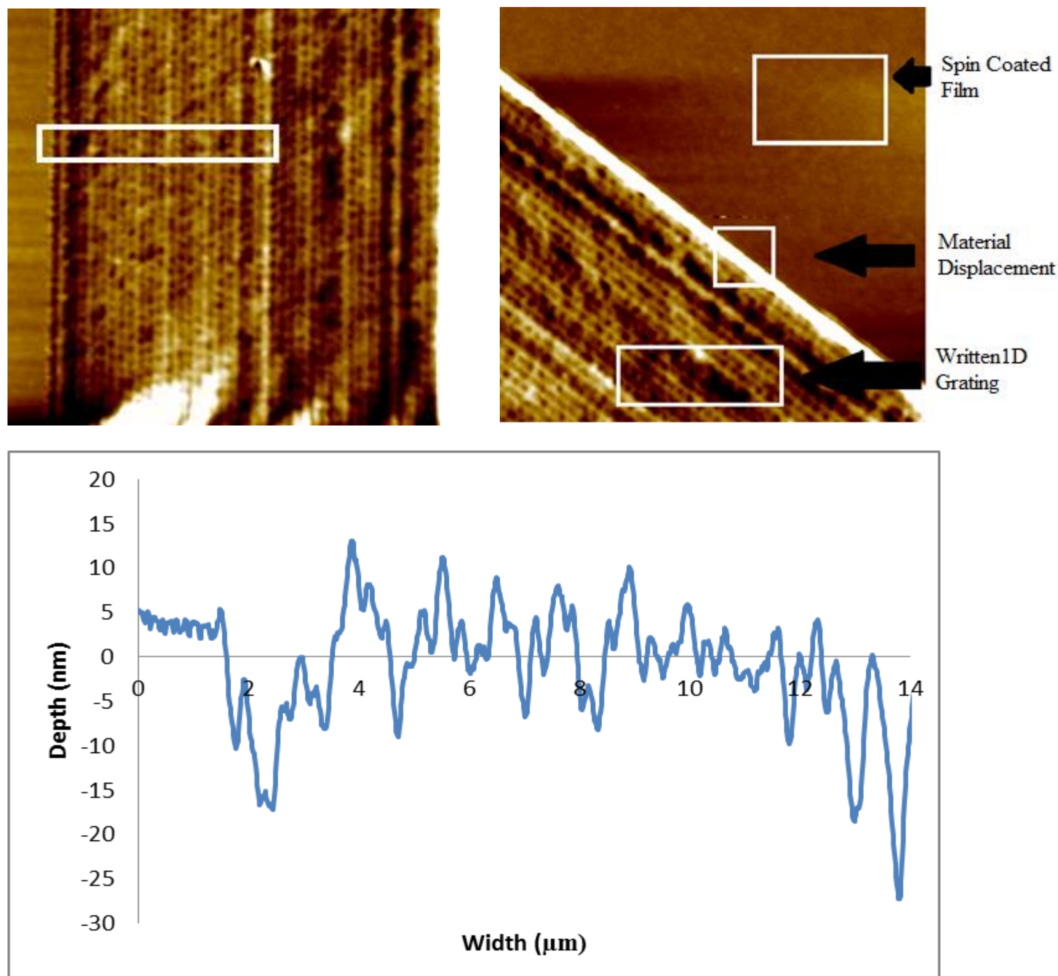

Figure 5.3.3 Top Left: AFM scan of 1D grating of 40 lines at 350nm pitch and 5µms^{-1} writing speed. Top right: AFM scan of the final written edge displaying material displacement. Bottom is the modulation profile of the pattern, taken from the white outline of the top left AFM scan.

The second means of altering the writing parameters, increasing or decreasing the writing speed, yielded more favourable results. The writing speed was decreased to 5µms^{-1} and pattern writing conducted; figure 5.3.3 shows these initial results. There is no longer the film distortion seen with previous findings, having a root mean squared surface roughness (R_q) of ~1nm. This result means that the maximum deviation of the surface for peaks and troughs will be 1nm from the mean line. The only material bunching is displaced to the edge of the patterned area and the pattern is again visible. There is similar height variation in the pattern as observed before, however, the addition of the undesired pits appearing along the writing length.

The average modulation depth and ridge FWHM are hard to estimate in this sample as the modulation depth is widely varying due to the pitting. The scale of the written features is now in the range where they could be considered useful for optical feedback, however the modulation depth would ideally be higher and the variation means that such a structure would exhibit very large losses as well as smear out any distributed reflection effect. A solution to this is to press the tips harder onto the surface, acting to increase the modulation depth as well as reducing or eliminating the effect the observed pits have. The pitting could be either due to the tip "skipping" on the surface as it is drawn across or is an artefact of the motion control system the DPN system uses.

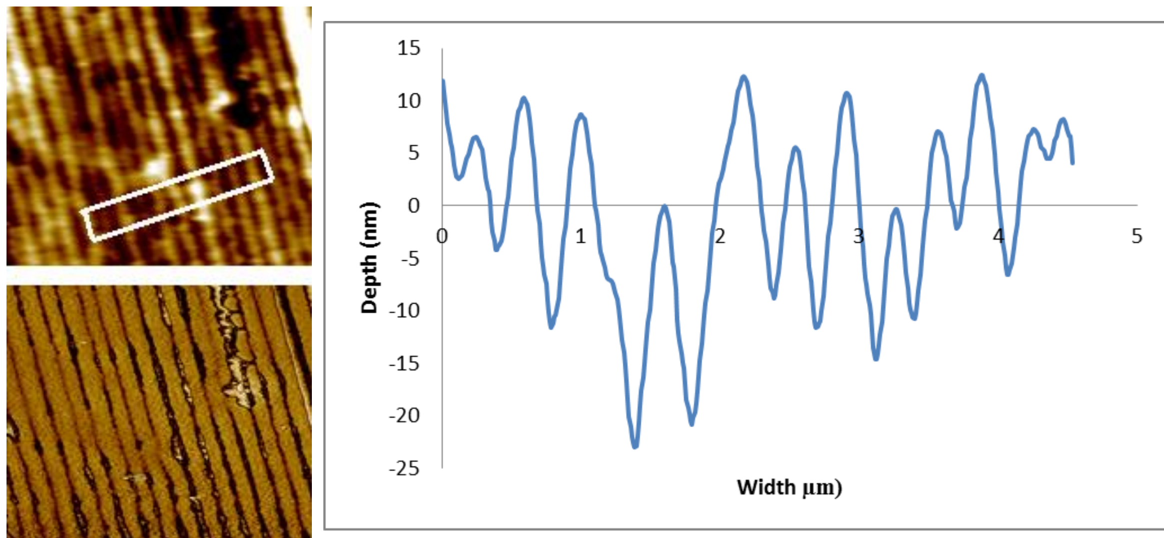

Figure 5.3.4 Top left: AFM scan of 30 lines written at 350nm pitch and 5µms^{-1} writing speed and no repeats, pressed 300nm past surface contact. Bottom left: the phase diagram associated with the AFM. Right: the modulation profile taken from the white rectangle.

The final results for achieving 1D grating structures maintained the same writing speed and pitch as previously used but the tips were pressed more firmly into the surface to prevent the pits being formed. This was accomplished by bringing the tips into contact with the surface of the BBEHP-PPV film then continuing to press the tips down by a further 300 nm. This has the effect of exerting more force on the film but, as can be seen from figure 5.3.4, does not correlate directly to modulation depth. The reason for this is that while the tips are pressed more firmly

onto the surface there is an associated stiffness of the cantilever the tips are attached to and the tip will not push 300 nm further into the film.

The final patterns produced with this technique showed great improvement when compared to when the tips were not pressed further into the film. The average modulation depth is more uniform, at 25nm, and the FWHM is at 200nm. Despite these improvements there are still variations in the scratched gratings, as can be observed in the AFM scan data in figure 5.3.4, where the film fractures and breaks off. In addition the modulation depth needs to be increased for efficient feedback. Inhomogeneities would also introduce significant losses into any optically active structures. There is an upper limit on the force that can be exerted by the tips on the film, so blunting and breaking the tips has to be considered as well as the risk of deforming the film. An example of the results of pressing the tips onto the surface with excessive force can be seen in figure 5.3.5; the film deforms severely upon contact and it is not possible to generate coherent patterns while at this pressure.

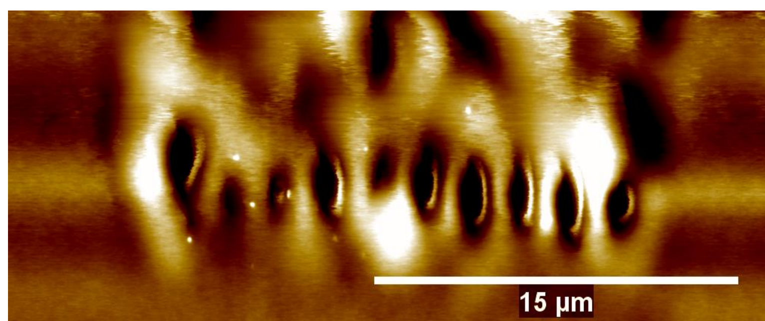

Figure 5.3.5 AFM example of polymer deformation under high tip pressure.

2D Gratings

2D gratings are created by generating periodic indentations as opposed to the parallel lines which characterise 1D gratings. For 2D gratings, the initial challenge was to realise a pattern with a pitch in the sub-micron regime. Figure 5.3.6 shows that the rectangular pattern was clear

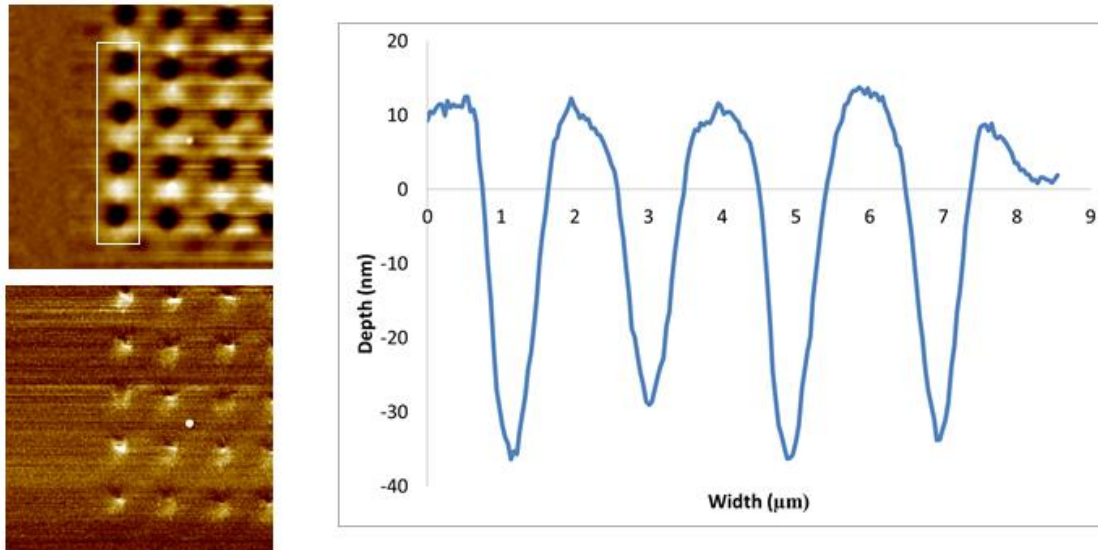

Figure 5.3.6 Top left: AFM scan of 2D imprint grating in BBEHP-PPV polymer, with a pitch of 2μm. Bottom left: corresponding phase image of the AFM scan. Right: the profile scan of the white outline on the top left AFM scan.

and could be maintained for a pitch of 2μm but it was expected that material displacement issues would have a larger effect the more the pitch was reduced. The average modulation depth of the features here is 50μm and each indented 'well' has a FWHM of 800nm.

The attempt to reduce the centre-to-centre pitch of the dot array was only partially successful; the AFM image shown in figure 5.3.7 shows that while it is possible to achieve holes there is material displacement which swiftly causes a large number of defects to be present on the film. The average modulation depth has dropped to 13nm here with a feature FWHM of 280nm. It

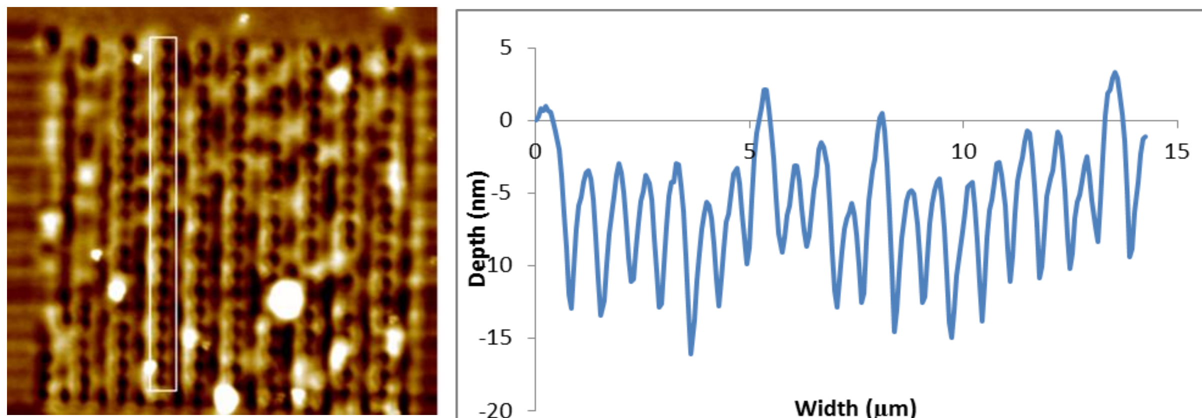

Figure 5.3.7 Left: AFM image of a 20x20 700nm pitch dot array conducted with the 33.6° half cone angle tip. Right: profile taken along the white rectangle.

can be seen that some of the holes have been closed up or improperly formed and there is a large amount of debris on the surface. This is most likely due to material build up on the tip being deposited at sporadic intervals while pattern writing is occurring. In order to achieve this pattern, it was found that pressing the tip less firmly upon the surface allowed for a reduction in pitch while sacrificing pattern depth. This was to be expected due to the tip morphology and half cone-angle.

A smaller tip was employed to realise patterning with sub-micron pitch, the tips being purchased commercially from Team Nanotec. The product used was ISC (125C40 - R) with a half-cone angle of 10° and radius of 10nm at the tip. The spring constant used for the cantilever arm was $40Nm^{-1}$ as the higher stiffness was assumed to aid in marking the polymer surface. With higher aspect ratio tips it becomes possible to achieve higher resolution in feature pitch while simultaneously realising deeper features and displacing less material. In addition to altering the tip type the spin coated material was changed to being photoresist material SU1805. The change was to conserve BBEHP-PPV (due to limited supply) and to continue testing on a material which can be marked and cured for measurement. The results of using this new tip are

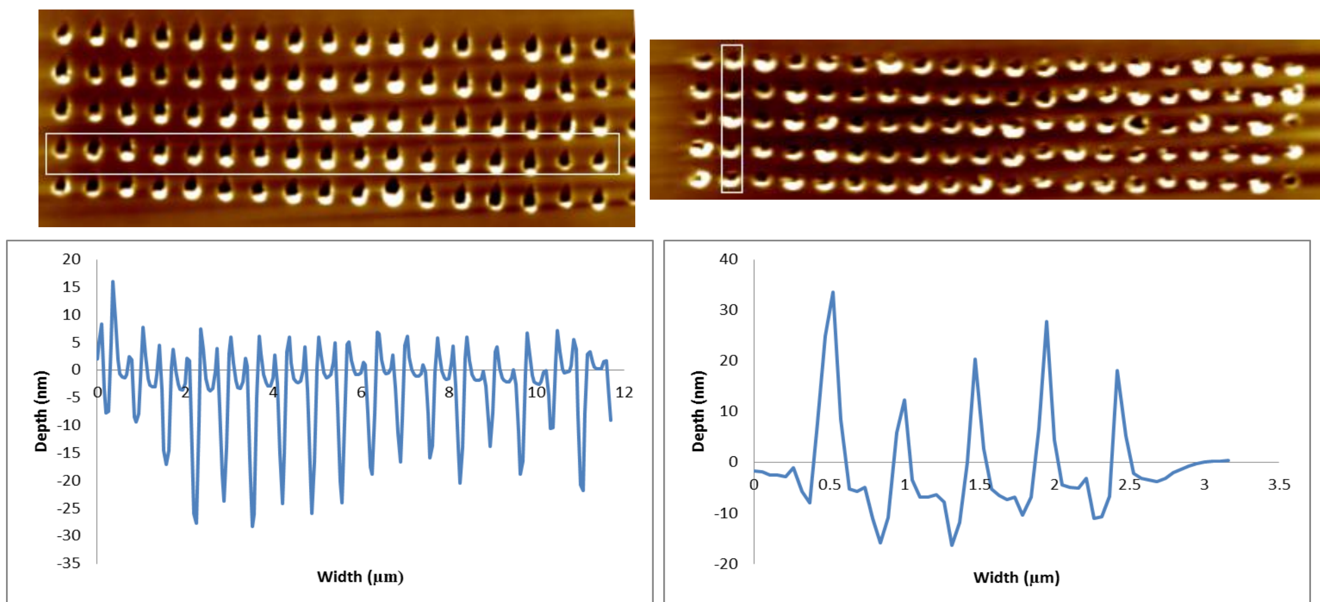

Figure 5.3.8 Top left: AFM scan of a 5x20 700nm pitch patterning onto SU1805, Top right: AFM scan of a 5x20 500nm pitch patterning onto SU1805. Profiles for are shown below each respectively.

shown in figure 5.3.8, exhibiting a marked improvement in pattern fidelity at 700nm pitch and displaying capability of patterning down to 500nm. For the 700nm pitch patterning the average modulation depth was 25nm with feature FWHM 160nm at 500nm the pitch average modulation depth was 15nm with a feature FWHM of 160nm. Calculation of the modulation depth as well as the FWHM here is for the imprinted holes only, discounting material displacement; including such displacement raises to 30-40nm in both cases.

The new tip has enabled nanopatterning via DPN on a scale where DBR structures can be considered for implementation. The displacement of material around the edge of the imprinted holes can also be seen in figure 5.3.9; the side bunching is due to non-perpendicular alignment of the tips to the plane of the polymer film. This enhances the modulation depth of the pattern and such an enhancement is favourable when designing optically active patterns. Increased modulation depth means that there will be a stronger interaction with the light of the in-plane guided modes. If the modulation depth is too shallow then the guided modes will not interact strongly, will not have a high effective refractive index difference, and will likely not be reflected back strongly enough to enhance the onset of ASE.

Having demonstrated the capability of the DPN to generate periodic structures in photoresist it was sought to achieve similar results in a BBEHP-PPV film to proceed to DBR structures. The

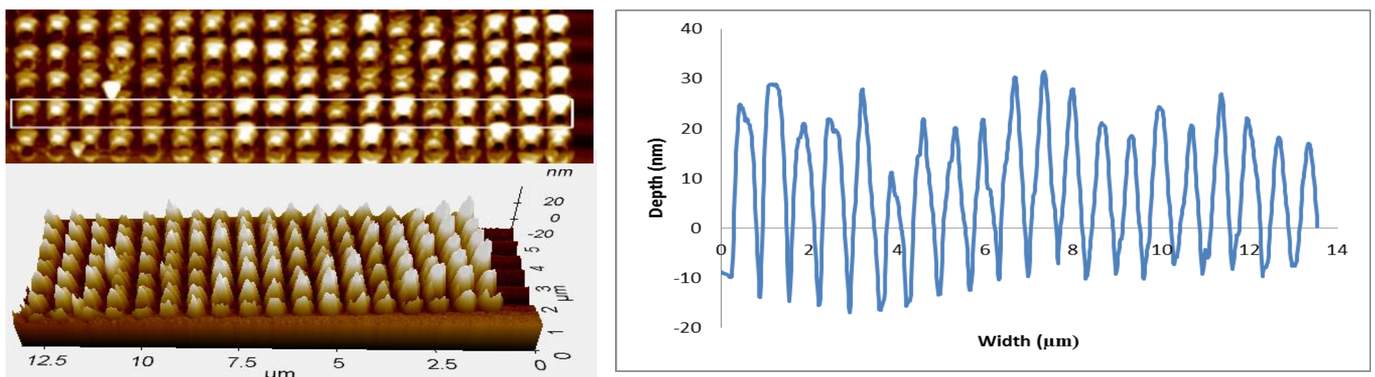

Figure 5.4.9 Top Left: AFM scan of a 10x20 700nm pitch imprint patterning onto a BBEHP-PPV spin coated film using 10° half-cone angle tip. Bottom left: 3D image of the AFM area. Right: the modulation profile shown in the white outline.

700nm pitch pattern was reproduced successfully and the material bunching has increased the effective modulation depth of the pattern. Without the raising of a side wall the modulation depths would average 15nm, maybe too small to realise lasing or ASE, but the addition of this effect increases the average modulation depth to 50nm with a FWHM of 205nm.

To assess the variation present within the patterns, Fourier transforms were determined for these 700nm pitch patterned grating structures. The Fourier transform on the AFM scan data in figure 5.3.9 allows the average modulation pitch to be determined. The results of this, shown in figure 5.3.10, display a peak at 1.5 μm^{-1} corresponding to an average periodicity of 666nm; close to the goal of 700nm. As there are no other major peaks the grating design remains simple with one periodicity rather than several; the reflectivity of such a grating was modelled in figure 5.2.4.

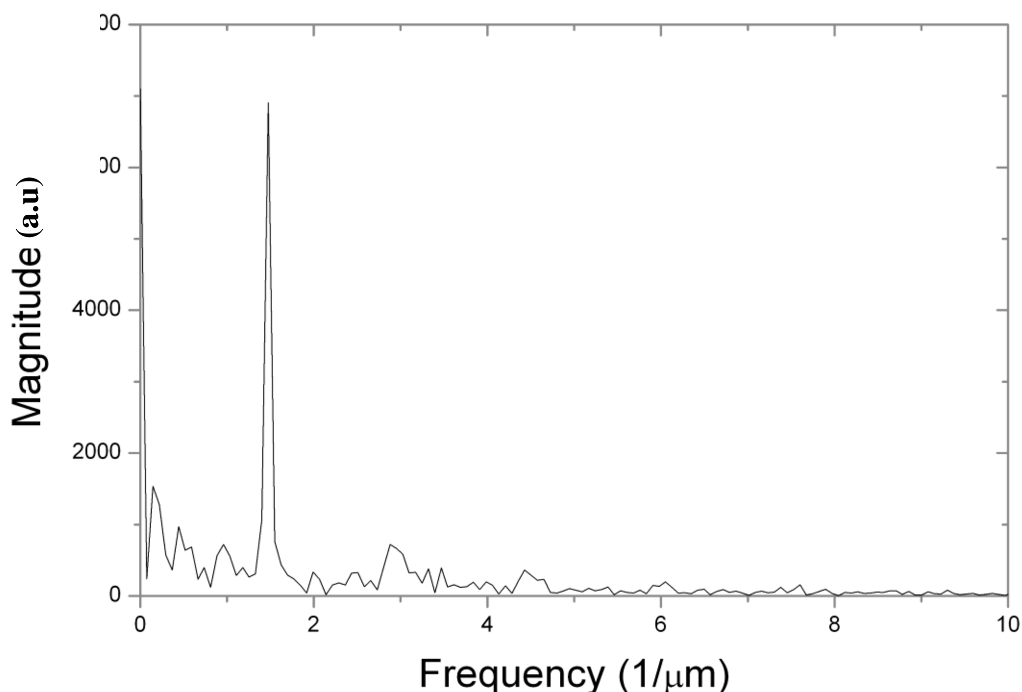

Figure 5.3.10 Fourier Transform of the modulation profile from figure 5.4.9. The one main peak at 1.5 μm^{-1} corresponds to an average periodicity of 666nm.

5.4 DBR Gain Structures

Three DBR cavity structures were manufactured via DPN and tested for ASE, the designs of which are shown in figure 5.4.1. They follow the design for a laser outlined in figure 5.2.1, with two DBR gratings acting as the mirrors defining the cavity length and the unpatterned BBEHP-PPV as the active gain medium. The period spacing for each pattern is 700 nm and 50 periods in width. P1 was designed with two symmetrical reflectors 10 periods deep with a cavity of 15 µm. P2 had asymmetric reflectors, one with 10 periods and another with 2 periods with a cavity of 15 µm . P3 also had symmetrical reflectors of 10 periods but a greatly increased cavity length of 100 µm. With the DBR gratings defining the cavity length, the polymer film is the gain medium and the BBEHP-PPV film can be pumped optically via a laser with an excitation wavelength at 355 nm within the absorption spectrum of the polymer.

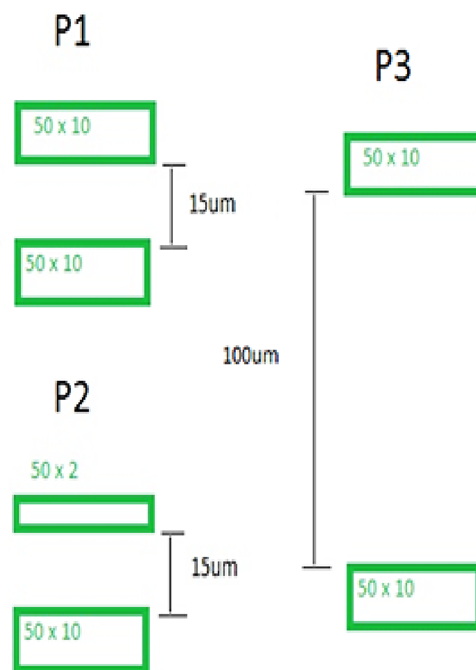

Figure 5.4.1 Three pattern designs, P1-P3, for the patterning of the DBR gratings on a polymer film to create DBR gain structures, giving the cavity length and periodicity of the DBR mirrors.

The patterns were generated on a glass slide, cleaned as per the previous samples, and spin coated with a 20mg/mL solution of BBEHP-PPV with a spin-coating speed of 2krpm. Upon spin coating there is an edge effect, where the thickness of the film is non-uniform and much thicker at the edge than in the majority of the film. This area must be avoided when creating the DBR structures as the non-uniformity will give rise to erratic results. The sample was pumped by a 355nm laser perpendicular to the film and emission from the structures was detected from the sample edge. The stripe length of the excitation beam was initially 1.5mm with a width of 50μm, much larger than the length of the patterns produced. ASE occurs when spontaneous emission in a gain medium is amplified as it propagates. If the gain and/or the propagation length is high enough, then the signature of ASE, a spectral redistribution of photons around the peak gain wavelength, can be detected in the stripe edge emission. Monitoring the intensity at the wavelength of maximum gain as a function of the excitation energy, it is possible to determine a threshold for ASE, at which point the slope of the intensity increase changes (and increases), as can be seen for example in Fig. 5.4.2. The ASE peak linewidth is typically smaller (<10nm) than spontaneous emission.

Firstly typical threshold values for ASE were determined for the film by pumping in two separate areas where there is no pattern, the results of which are displayed in figure 5.5.2.

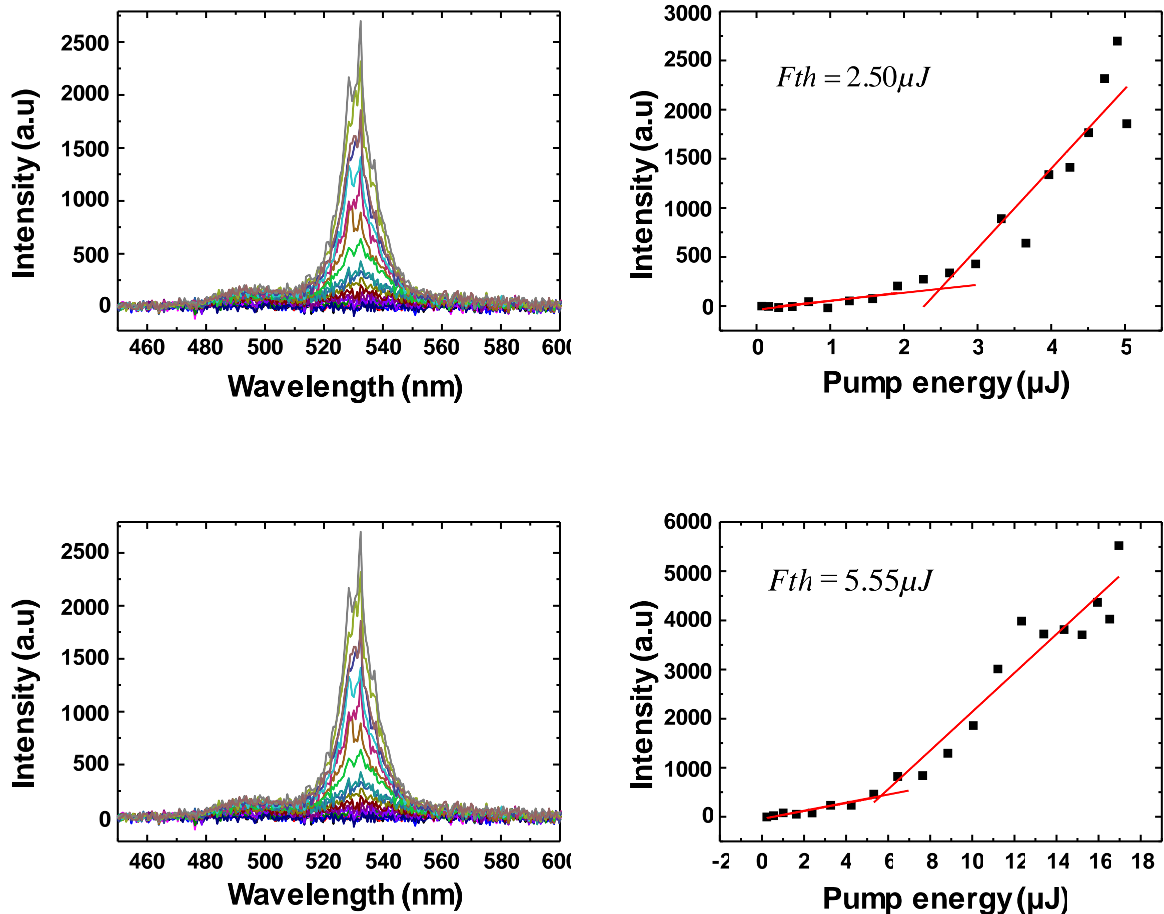

Figure 5.4.2 Excitation measurements of 1.5mm pump stripe on un-patterned BBEHP-PPV film. Top is one region with associated threshold curve on the right. The second region and associated threshold curve in on the bottom.

The peak at 532nm, shown in figure 5.4.2, is the main gain wavelength for BBEHP-PPV. This peak rises at a threshold value for pump energy while the secondary peak and shoulder from 480nm-510nm exhibits no such behaviour. The threshold values for ASE in the film thus measured was found to be 2.5 μJ and 5.5 μJ for each area, respectively, this variation being ascribed to possible inhomogeneity in the film as well as error in the positioning of the sample surface with respect to the pump focus position. Alignment of the sample/focus was done using

a camera to image the sample surface. The estimation of the sample ASE threshold with this size of pump stripe is estimated at 4+/- 2μJ.

Figure 5.4.3 displays the results for pumping the patterns P1-P3 with a 1.5mm x 50μm spot, the distance from the sample edge and the patterns being 2.5mm, 250μm and 250μm respectively. The results are varied, exhibiting ASE on P1, P2, and P3. The threshold values for P1 is lower than observed for the unpatterned film but similar, although on the low end, for P1 and P3. The spectra for P2 and P3 are most striking, with a multitude of narrow peaks that are simply not observed in an unpatterned film. These stable peaks are attributed to the DBR cavities and are detailed in figure 5.4.5.

The spectrum of P1 is akin to ASE but this ASE peak is at 500nm. Such behaviour is sometimes seen in very thin film of BBEHP-PPV and usually has a higher threshold. It is not possible to say if the DBR structures have any effect from this data in the case of P1.

However, the long stripe gives rise to a complicated analysis, a lasing cavity coupled to an amplifying region, without considering cm-scale film inhomogeneities. Thus the patterns were again measured but with a smaller excitation spot length, equal to the length of the patterns. We note that under the same pumping conditions, no ASE could be detected when probing an unpatterned area of the film. The results for structures P1, P2 and P3 are shown in figure 5.4.4, where the spectrometer resolution was lower than previously (2.5nm).

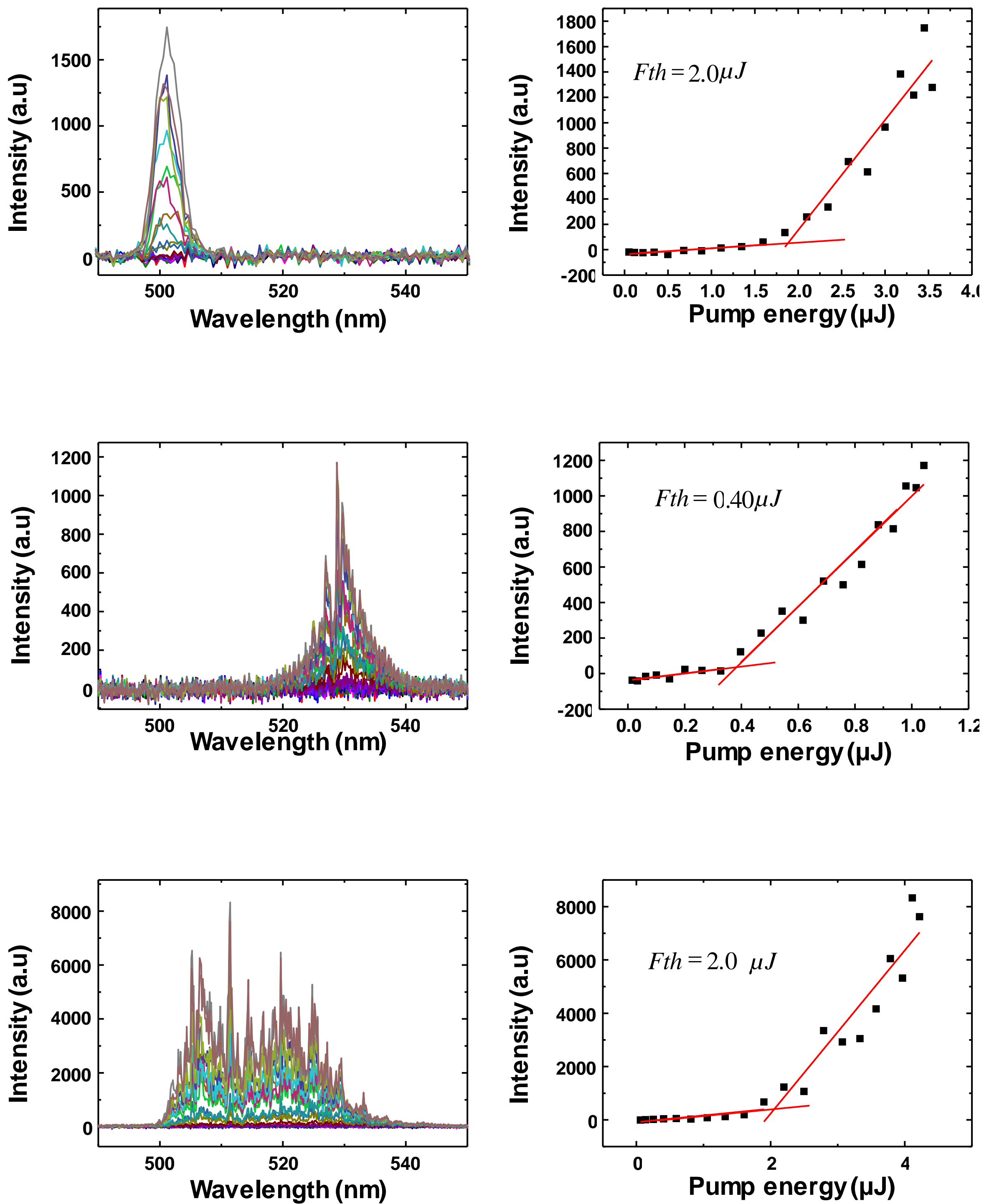

Figure 5.4.3 Spectral and threshold curves for P1 (Top) P2 (Middle) and P3 (Bottom) pumped with a 1.5mm x 50µm spot.

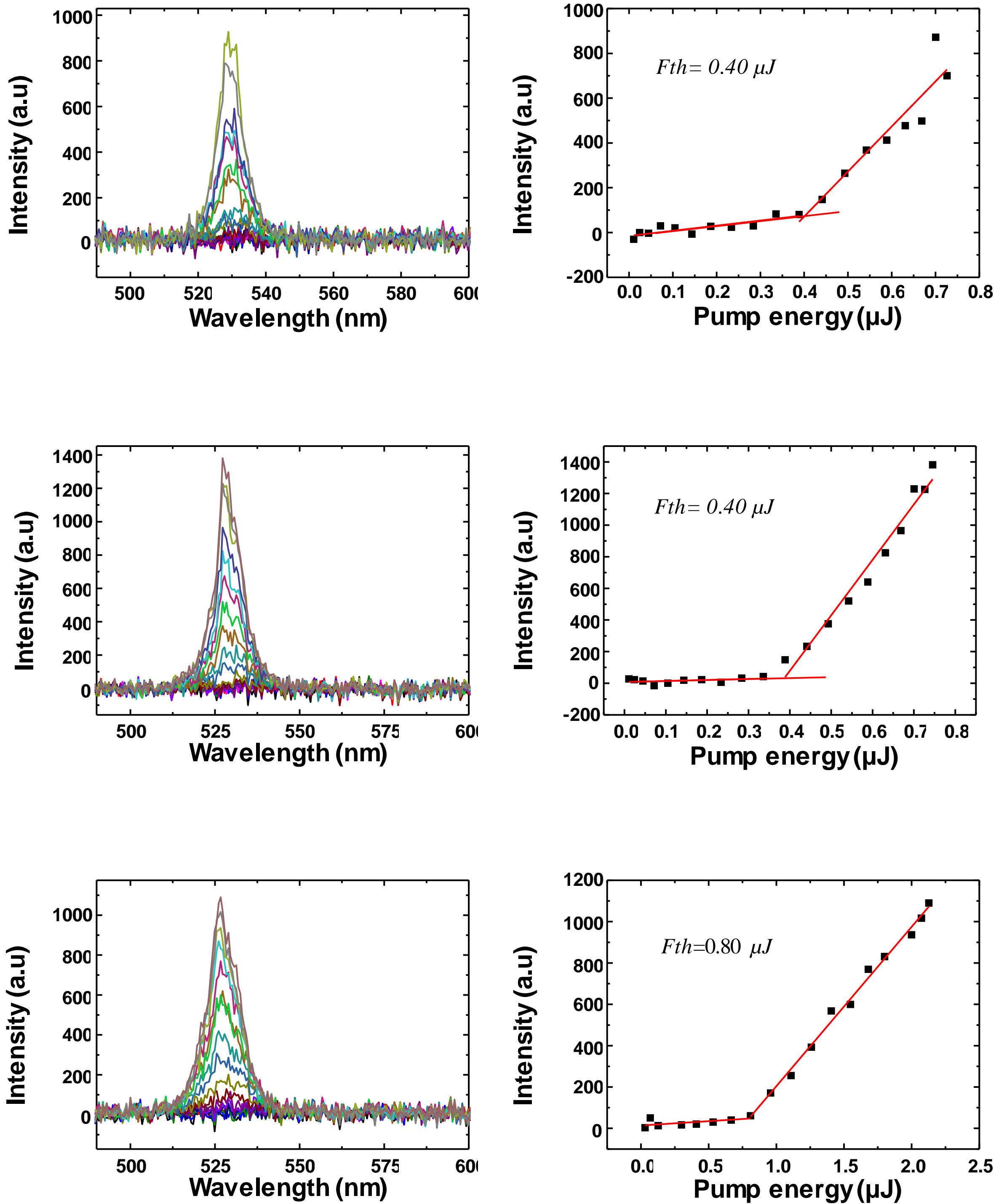

Figure 5.4.4 Spectral and threshold curves for P1 (Top) P2 (Middle) and P3 (Bottom) pumped with short excitation spot

Each structure exhibits ASE and the thresholds for each are comparable and even lower than before, an average of 0.5 μJ compared to 4 μJ for the unpatterned areas. Again, we reiterate here that no ASE could be seen for the unpatterned BBEHP-PPV film with the short stripe yet each DBR cavity exhibits ASE. This indicates that the structures are successfully acting as DBR resonators and increase the optical feedback. The wavelength gain occurs at 530 nm and the threshold values for each pumping conditions are summarised in table 5.4.1.

Pattern	Peak wavelength Long Stripe (nm)	Excitation threshold Long Stripe (μJ)	Peak wavelength Short Stripe (nm)	Excitation Threshold Short Stripe (μJ)
Bare 1	532	2.5	-	-
Bare 2	532	5.5	-	-
P1	505	2.0	532	0.4
P2	532	0.4	532	0.4
P3	500-540	2.0	532	0.8

Table 5.4.1 Comparison of ASE threshold values for the bare spin coated films and the patterned areas P1, P2 and P3 with both the long and short excitation spot sizes.

The results summarised in table 5.4.1 show that when there is no patterning present the excitation threshold is overall higher, thus the patterning itself has a beneficial effect on lowering the threshold by increasing feedback within the film. For the long stripe, with a higher spectrometer resolution, narrow peaks could be seen. Pumping the lasing structures with a stripe spot significantly longer than the structure itself, makes interpretation of the data and extraction of physical parameters from the spectra complicated. When pumping with a stripe that is matched to the cavity size there is a clear reduction in the ASE threshold (in fact, as said, no ASE is seen when pumping unpatterned regions). By looking at the details of the spectra with higher resolution, one can attempt to relate features to physical parameters of the DBR

structures. This was done for the P1 structure as the spectrum. It is possible to see a degree of effect that the 2D photonic crystal DBR mirrors have upon the emission spectrum, generating subsidiary peaks around the main emission of what would be expected from a truly 1D Fabry-Perot. Figure 5.4.5 shows the excitation of pattern P1 at varying pump energies with the resulting spectra normalised. This permitted examination for common peaks with fixed wavelength deviation from the main peak. It shows that above the threshold for emission, the spectrum is highly-multimode. The presence of the different modes is due to a combination of factors: distance between patterns (cavity length determining longitudinal modes), the width of the patterns and the width of the pump spot (defining the lateral modes), as well as the finite length of the pattern inducing 'parasitic' reflections and any scattering defects.

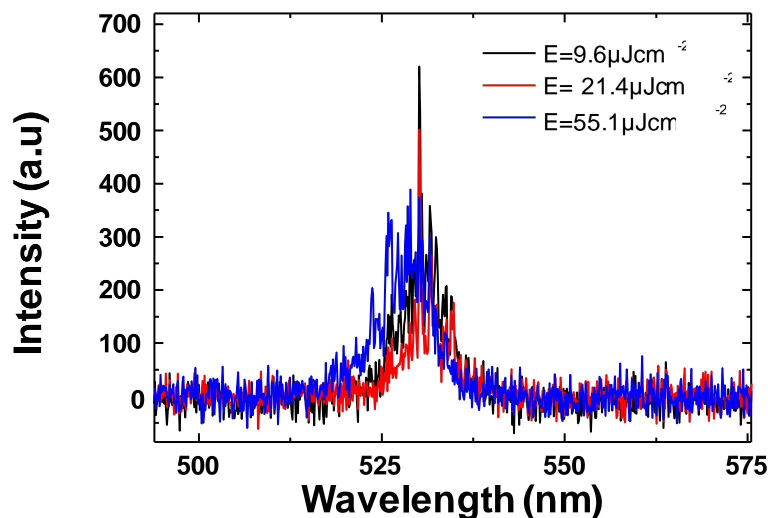

Figure 5.4.5 Normalised spectra of P1 pumped under varying energies.

While the spectrum is still complex, it is possible to recover some physical sense from it by taking the Fourier transform. The result shows if there is any dominating spatial frequency that can be linked to the physical characteristics of the DBR cavity structures. Figure 5.4.6 shows the averaged Fourier Transform of the spectra from figure 5.4.5 showing the presence of a

spatial frequency of ~0.23 nm^{-1}, corresponding to a free spectral range of 4.34nm. Such a free spectral range can be linked to a cavity length of ~21.1 μm which is close to matching the 15 μm separation between DBR mirror and the calculated field penetration depth for each mirror, 3 μm.

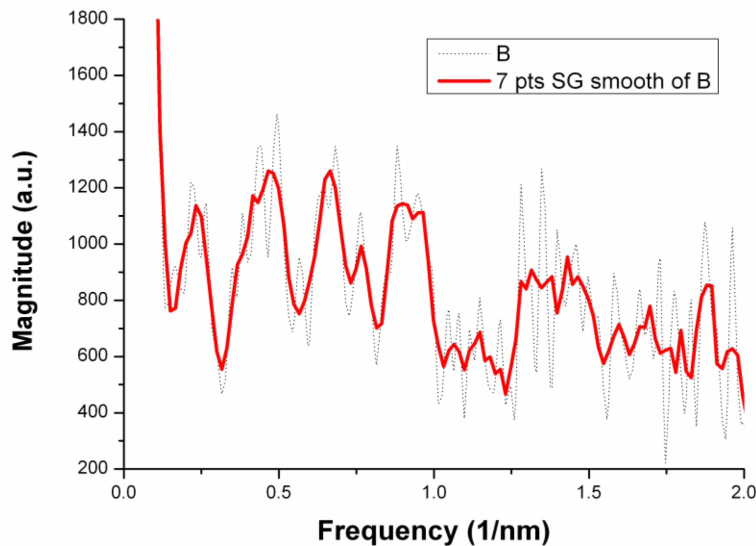

Figure 5.4.6 Fourier Transform of the overlain spectra of figure 5.4.5. A spatial frequency of ~0.23 nm^{-1} is observed.

5.5 Conclusions

This chapter covered the work done using dip pen nanolithography (DPN) to create "negative patterns" in soft materials. Different DPN tip geometries were explored in the attempt to create nanoscale imprint patterns and both 1D and 2D grating structures were fabricated. A tip obtained from Team Nanotec with a 10° half-cone angle was used in the creation of distributed Bragg reflectors (DBRs) made of 2D gratings, with a pitch of 700 nm and features of 50nm modulation depth and a FWHM of 205 nm, imprinted into a spin coated green-emitting π-conjugated polymer (poly[2,5-bis(2',5"-bis(2"-ethylhexyloxy)phenyl)-p-pheylene vinylene])

film. The DBR structures were coupled together to form planar optical cavities of length 15 μm and 100 μm, respectively. These active cavities were optically pumped with a 355nm Q-switched laser and the threshold for amplified spontaneous emission (ASE) tested. It was found that gain was achieved in a structure with 10-period DBRs separated by 15 μm. The ASE threshold pump energy was 0.4 μJ for this structure. It has been demonstrated that DPN has the capability of negatively patterning polymer films with sub-micron structures. Periodic structures realised in both a classical photoresist material as well as a light-emitting polymer have been demonstrated with feature sizes down to 160nm FWHM and 40nm of modulation depth. This is to our knowledge, at the time of writing, the smallest negatively pattern features obtained by DPN; moreover this was obtained in a sensitive light-emitting material. Structures designed and implemented have been shown to successfully act as reflectors in the light-emitting polymer by increasing feedback and in turn decreasing the onset of ASE. The ability for the DPN to vary pattern design means that the technique has full customisation for prototyping and the construction of more exotic grating combinations; for example Fibonacci sequences, quasi-random periodicity, combination 1D and 2D structures could be fabricated based on the individual nanosize features. With the ability to pattern photoresist material there is also the capability of use in semiconductor device fabrication.

5.6 References

1. T. Balla, S Mark Spearing, A. Monk, "An assessment of the process capabilities of nanoimprint lithography", J. Phys. D, Volume 41, Issue 17 (2008).
2. S. Dhuey, C. Peroz, D. Olynick, G. Calafiore, S. Cabrini, "Obtaining nanoimprint template gratings with 10 nm half-pitch by atomic layer deposition enabled spacer double patterning", Nanotechnology Volume 24, Issue 10 (2013).
3. T. Buß, J. Teisseire, S. Mazoyer, C. Smith, M. Mikkelsen, A. Kristensen, and E. Søndergård, "Controlled angular redirection of light via nanoimprinted disordered gratings", Applied Optics. Volume 52, Issue 4 (2013).
4. M. Heyde, K. Rademann, B. Cappella, M. Geuss, H. Sturm, T. Spangenberg, and H. Niehus, "Dynamic plowing nanolithography on polymethylmethacrylate using an atomic force microscope", Rev. Sci. Instrum. 72, 136 (2001).
5. B. Vasić, M. Kratzer, A. Matković, A. Nevosad, U. Ralević, D. Jovanović, C. Ganser, C. Teichert, R. Gajić, "Atomic force microscopy based manipulation of graphene using dynamic plowing lithography", Nanotechnology, Vol 72, Issue 1 (2013).
6. L. Weng, L. Zhang, Y. Chen, L. P. Rokhinson, "Atomic force microscope local oxidation nanolithography of grapheme", Appl. Phys. Lett, Vol 93, Issue 9 (2008).
7. E. Mele, F. Di Benedetto, L. Persano, R. Cingolani, D. Pisignano, "Multilevel, room-temperature nanoimprint lithography for conjugated polymer-based photonics", Nano Letters, Vol 5, Issue 10 (2005).
8. Chenais Sebastien, Forget Sebastien, "Recent advances in solid-state organic lasers", Polymer international, Vol 61, Issue 3 (2013).
9. A. Rose, Z. Zhu, C. F. Madigan, T. M. Swager, V. Bulovic, "Sensitivity gains in chemosensing by lasing action in organic polymers", Nature, Vol 434, Issue 7035 (2005).
10. Y. Chen, J. Herrnsdorf, B. Guilhabert, Y. Zhang, IM. Watson, E Gu, N Laurand, MD Dawson, "Colloidal quantum dot random laser", Optics Express, Vol 19, Issue 4 (2011).
11. B. N. Shivakiran Bhaktha, Nicolas Bachelard, Xavier Noblin, and Patrick Sebbah, "Optofluidic random laser", Appl. Phys. Lett. Vol 101, Issue 15 (2012).

12. Y. Chen, Y. Zhang, N. Laurand, A. L. Kanibolotsky, E. Gu, P. J. Skabara, M. D. Dawson, "Organic polymer composite random laser operating underwater", Optics Letters, Vol 37, Issue 24 (2012).
13. Y. Wang, G. Tsiminis, A. L. Kanibolotsky, P. J. Skabara, I. D.W. Samuel, G. A. Turnbull, "Nanoimprinted polymer lasers with threshold below 100 W/cm2 using mixed-order distributed feedback resonators", Optics Express, Vol 21, No. 12 (2013).
14. L. Mahler, A. Tredicucci, F. Beltram, C. Walther, J. Faist, H. E. Beere, D. A. Ritchie, D. S. Wiersma, "Quasi-periodic distributed feedback laser", Nature Photonics, Vol 4, Issue 3 (2010).
15. J. Stehr, J. Crewett, F. Schindler, R. Sperling, G. von Plessen, U. Lemmer, J. M. Lupton, T. A. Klar, J. Feldmann, A. W. Holleitner, M. Forster, U. Scherf, "A low threshold polymer laser based on metallic nanoparticle gratings", Adv. Materials, Vol 15, Issue 20 (2003).
16. C. J. R. Sheppard, "Approximate calculation of the reflection coefficient from a stratified medium", Pure Appl. Opt, Vol 4, Issue 5 (1995).
17. T. Erdogan, "Fiber Grating Spectra", Journal of Lightwave Tech. Vol 15, Issue 8 (1997).
18. L. Qin, S. Ye, Y. Hu, N. Zhang, Y. Ning, Y. Liu, L. Wang, "Theoretical analysis of emission characteristics of second-order distributed feedback semiconductor lasers", SPIE Proceedings: Semiconductor Lasers and Applications IV, Vol 7844 (2010).
19. G. von Freymann, W. Koch, D.C Meisel, M. Wegener, M. Diem, A. Garcis-Martin, S. Pereira, K. Busch, J. Schilling, R.B Wehrspohn, U. Gosele, "Diffraction properties of two-dimensional photonic crystals", App. Phys. Lett. Vol 83, Issue 4 (2002).
20. Z. Yu, A. Raman, and S. Fan, "Fundamental limit of light trapping in grating structures", Opt. Express , Vol 18, Issue 19 (2010).
21. Y. Chen, J. Hernsdorf, B.Guilhabert, A. L. Kanibolotsky, A. R. Mackintosh, Y. Wang, R. A. Pethrick, E. Gu, G. A. Turnbull, P. J. Skabara, I. D. W. Samuel, N. Laurand, M. D. Dawson, "Laser action in a surface-structured free-standing membrane based on a p-conjugated polymer-composite", Organic Electronics, Volume 12, Issue 1, 62-9 (2011).
22. F. Lahoz, C. J. Oton, N. Capuj, M. Ferrer-Gonzalez, S. Cheylan, D. Navarro-Urrios, "Reduction of the amplified spontaneous emission threshold in semiconducting

polymer waveguides on porous silica", Optics Express, Volume 17, Issue 19, 16766-16755 (2009).

23. J. C. Ribierre, G. Tsiminis, S. Richardson, G. A. Turnbull, I. D. Samuel, H. S. Barcena, P. L. Burn, "Amplified spontaneous emission and lasing properties of bisfluorene-cored dendrimers", Applied Physics Letters , Volume 91, Issue 8 (2007).

Chapter 6

Conclusion and Perspective

6.0 Conclusion

The work presented in this thesis has concentrated on exploring and expanding the capabilities of the soft lithography techniques of inkjet printing and dip-pen nanolithography for photonics. Improvements have been demonstrated regarding the achievable patterning resolution, enabling novel applications and opening the field for rapid prototyping of photonic structures that was hitherto lacking. The results achieved in this work are helpful in understanding the potential role that the tools used have for micro- and nano-scale fabrication. They have also expanded the previously known capabilities and shown a drastic improvement whilst also demonstrating the ability to reduce wastage of material when compared to commercial procedures.

Chapter 1 provided an overview of lithographic techniques currently used in the fabrication of inorganic and organic structures. It was here that the niche for the tools and techniques used in this thesis were outlined and the motivation for this work was introduced. The role that lithography plays pertaining to the fabrication of photonic devices was described in this chapter. The ubiquitous nature of these devices in our daily lives is self-evident whether it is at home, work, or travelling with screens interactive devices taking a larger and larger position in our lifestyles. The motivation for this thesis recognised an area by which these devices can be improved and fabricated in a timely and cost efficient manner.

Chapter 2 examined the physics behind the technology to be examined, the light emission properties of inorganic LEDs as well as outlining a model for light emission in organic polymers. An overview of relevant semiconductor physics was given beginning with band theory and leading onto semiconductor doping and the p-n junction. A description of quantum wells and double-heterojunction devices was given as a lead into GaN LEDs, and basic fabrication details were given alongside several geometries and modes of operation. This led onto the designs of GaN LEDs that are used in this work, namely matrix-addressable GaN LED arrays, which form the base of the hybridisation work in chapter 3, and planar GaN LEDs which are used in chapter 4 in the fabrication of nano-LEDs. Polymers were introduced next as the next key component of the body of this thesis. A basic introduction to the structures that polymers can take led into an explanation of the guest-host system which is necessary for many patterning processes, in this case allowing the optically active polymer to be fixed within the matrix via UV polymerisation once deposited. A model for light emission in conjugated polymers was then discussed and the specific light emitting polymers used in this thesis were introduced. The chemical structures for the three LEPs used within the CHDV guest-host matrix were outlined and the optical features of the lasing polymer BBEHP-PPV were discussed.

From chapter 3 onwards the results achieved in this work were presented. A short background by the work that inkjet printing technology has been used for previously was followed on the specifics of using the Dimatix DMP 2800 inkjet system including the specifications for operation and a discussion of its control systems. Next the ink design was explored in the context of the tolerances that the DMP2800 can manage and the aim of achieving a multi-wavelength colour conversion hybrid organic-inorganic photonic device. The absorption and emission properties of the LEP-CHDV blended inks were investigated for suitability as UV

colour converters and the inks had peak emission wavelengths of 418nm, 545nm and 645nm for blue, green and red emission respectively. The next stage was to ensure that we could control the shape of features being deposited. Hydrophobic surface treatments were explored initially on glass and then on the surface of the matrix-addressable GaN LED to be used. It was discovered that smaller features could be created by the hydrophobic treatment using PFODCS. However, deposition limited solely on the top of the LEDs was hard to achieve. This was due to the surface topography of the matrix-addressable micro-LEDs meaning that the ink could run into the tracks between the emitters and would also spread beyond the emitting area when deposited in larger volumes. A new deposition method was therefore employed to counteract this whereby once one droplet of LEP ink had been deposited upon the LED it would be immediately photo-cured to ensure it did not spread. Micro-PL measurements were taken of the printed samples, both when spot-pumped by a 375nm diode laser and when illuminated by the underlying UV GaN LED. The efficiencies for colour conversion when integrated onto an LED were calculated for each of the inks and found to be 13.2%, 31.5% and 5% for the blue, green and red hybrid LEDs respectively. An investigation was conducted into the spectral evolution of the hybrid LEDs as the bias was increased on the LED and it was possible to determine at what point the illumination saturates the integrated ink's ability to colour convert. The LEPs used in this work were specially designed and synthesised by another group. Given the fact that there was a limited amount of the pure LEP available it was not possible to conduct a concentration study but given more access it is hoped that this would be possible to investigate the effects of increasing the number of chromophores on the efficiency of colour conversion. The inkjet printer was also used to realise a totally mask-free fabrication method for LEDs whereby a pattern for an LED structure can be defined by a UV-LED direct writing set up.. The common n-contact was then created by printing a conductive silver ink track to contact the n-GaN and individually bonding the LEDs to be addressed. Thermal annealing of the silver

track generated a change in conductivity from $3.42\text{x}10^{7}\mu\Omega\cdot\text{cm}$ to $15.4\mu\Omega\cdot\text{cm}$. The conductivity of bulk silver is $1.587\mu\Omega\cdot\text{cm}$ and thus it was seen that the conductive tracks deposited were only a factor of ten higher than that of the best achievable.

Chapter 4 introduced the first work strand of Dip-Pen Nanolithography working towards the fabrication of nano-LEDs. Investigations into two types of photo-curable resist material were made and it was found that the acrylate based NOA series worked best. Both NOA 63 and NOA 68T were tested from this range as they are both UV-curable, transparent in the visible spectrum, and when cured have Shore D hardnesses of 50 and 90, respectively. The main difference between the two materials is their viscosity prior to UV curing, NOA 63 has a viscosity of 2000 cps whereas NOA 68T has a viscosity ranging between 20,000 cps and 25,000 cps. The increased viscosity of the latter allowed for smaller features to be deposited by the dip-pen system and, coupled with a reduction in dwell time, nanoscale features were achieved. The dimensions of the features deposited on a SiO_2 substrate were 560nm and 840nm, respectively in the x and y directions which is a marked improvement on previously deposited photoresist structures. The ability to deposit photoresist on a nanoscale was combined with a plasma pacification process on planar LEDs in an attempt to fabricate nano-LEDs. Treatment of the planar LEDs with CHF_3 plasma has the effect of passivating the Mg-doped conductive layer which results in no current passing through the quantum well structures. In this way one can use a protective mask to prevent the plasma treatment passivation of a pre-determined area thus defining the active device. It was found that due to the surface structure and the resultant surface tension with the deposited NOA 68T that it was not possible to achieve the same size as was demonstrated on an SiO_2 substrate. Definition of micro-emitters was achieved and the smallest emitter achieved with this method which had a 3 μm-sized emission profile at full-width half-maximum. As with the inkjet printing the additive lithography offered by the dip-

pen has been explored which readily offered the ability to deposit features of varying sizes in a swift manner and using miniscule amounts of material that ensures minimal waste during the process.

The potential of additive lithography using the dip pen system has been explored to negatively pattern materials, as reported in chapter 5. The tips provided with the NLP 2000 series dip-pen nanolithography tool were used to scribe tracks on a spin coated film of green-emitting π-conjugated polymer (poly[2,5-bis(2',5"-bis(2"-ethylhexyloxy)phenyl)-p-pheylene vinylene]). Write speed and tip pressure was varied whilst making 1D grating structures with a moderate degree of success. A key issue for this was found to be integral to the process itself - that of material displacement. Whilst writing, the material would either build up on the tip or be pushed aside. This caused large variations in the periodic structures being produced which would lead to large losses in any optically active structure. The next process attempted was to define 2D gratings where the tips were pressed into the surface to create a periodic structure of dot arrays. Initial results were successful but the desired resolution could not be achieved with the provided tips. Thus a new tip was purchased from Team Nanotec with a half-cone angle of 10° and radius of 10 nm at the tip to try to achieve higher resolution. The utilisation of a finer tipped tool enabled creation of DBR structures with a periodicity of 700 nm and a modulation depth of 50 nm. These were used in lasing structures varying the number of periods in the DBRs and width of the laser cavity penetration. It was found that with the addition of these DBR structures onto a spin-coated film of the green emitting polymer that the threshold optical pump energy necessary for gain was reduced from 5.5 μJ to 0.4 μJ. Again a highly flexible technique was demonstrated that lead to the fabrication of photonic devices that allowed for rapid prototyping for various designs within a reasonable time-frame and without requirements for new materials, masks, or imprint stamps.

6.1 Future work and Perspectives

There are many avenues that can be explored to further the work done in this thesis. One is improvement of the placement fidelity for the inkjet printer deposition into a well structure for definite confinement. This would allow for enhanced positioning and a form of correction for any minor placement misalignments. In addition there are many more organic light emitting polymers than can be explored in conjunction with the printer that may yield higher colour conversion efficiencies. To ensure that all of the underlying UV light is converted, an investigation into higher concentrations of colour converters in the ink could be conducted. The dip pen technique can also be examined for improvements; investigating different tip geometries that might allow for finer structures with a larger modulation that would produce better and/or more broadly applicable photonic structures. Design of the photonic structures can be investigated in various avenues; combination 1D and 2D structures, fractal structures, etc. The ability to scribe nano-scale troughs could be useful in the realm of microfluidics, designing the channels on a flexible substrate. Different mask materials can be utilised for the fabrication of nano-LEDs which are less permeable to the plasma treatment and thus maintain the structure, coupled with current super hydrophobic coatings the size of resist deposition could be greatly reduced to give nano dots of material.

The techniques developed here have a broad range of potential uses and can be combined with many other technologies to give a potent tool kit in the design and development of micro- and nano- fabricated devices. The dip-pen system has subsequently been used to demonstrate transfer printing of inorganic LEDs which can easily be combined with the work covered in this thesis in the production of advanced hybrid materials [1,2]. The probe holder for the DPN was adapted to take an elastomeric stamp. The elastomeric stamp picks up suspended LED

devices and can be re-bonded to a separate substrate via capillary action and Van der Waals bonding. This allows devices to be grown on a GaN wafer then transferred to a diamond substrate for enhanced thermal dissipation properties. Coupling the drop-on-demand nature of the inkjet printer, the placement capabilities of transfer printing, and the nano patterning of the dip pen highly customisable inorganic-organic hybrid materials and devices can be fabricated. Placing large area inorganic structures, placing nano-patterned structures upon the surface via the dip pen, and deposition of light-emitting organics with the drop-on-demand inkjet printer that enables fully hybrid inorganic-organic optical devices in a flexible manner whose emission properties can be sculpted by not only selection of organic material but by the modulation of nano-patterning it is placed upon.

The field of optogenetics also benefited from the work completed in this thesis, whereby the use of light-sensitive proteins can be stimulated with LED probes to control neural activity. A probe was designed with a view for testing the thermal and optical characteristics of such a probe *in vivo*. The community holds a commonly held concern that as LEDs are employed there would be thermal damage to the surrounding tissue as the device heats up. It was found not to be the case for these custom probes but a key stage in their fabrication was laser dicing and thinning to remove them from the substrate. Initially it was found that the edges of the probes were damaged during the laser lift-off process. As a protective step the injet printer was used to deposit a photo-resist layer onto the LED tip. It was successful and the probes fabricated with this step functioned correctly. Given the flexibility of the inkjet printing process it would allow further customisation of the probes to no impediment for the inkjet protection step.

Visible light communications (VLC) is one research avenue that greatly benefits from the capabilities that this thesis has highlighted. The need for rapid data transfer is only growing with our reliance on electronic media; to keep up with increasing amounts of data streaming

new systems must be developed. VLC serves this purpose by several means and when visible wavelengths of light are used data can be encoded in light sources currently employed serving dual purposes. Imagine the situation in a meeting room where a presentation is being made, the lights in the ceiling can be pulsed at a rate the human eye cannot detect but that a semiconductor photo-detector can. The presentation can automatically be transferred to any laptop or tablet wirelessly by the very light illuminating the room. Enhanced security is also possible here as only those devices with access to the light source would receive the data; the wireless transmission is blocked by optically opaque materials.

Transmitters for such a purpose need to have a rapid response time to ensure fidelity of signal at higher bit rates. Thus patterning of fast response photonic organics is essential when coupled with the inorganic LED's capability for short pulse lengths. A device design that incorporates all the aspects of this thesis is shown in figure 6.1.1. Enhancing the potential of the inkjet printing for the purposes of VLC requires an increase in the ability to place the organic colour converter on the LED emissive area. Introduction of a well mask on the LED design would achieve this function and permit a thicker membrane of colour converter to be placed. To enhance the light extraction of the hybrid device the patterning technique of the dip-pen can be used prior to organic deposition to create optically- active structures and once the fast-response organics have been placed the inkjet can deposit an optically clear material to form a lens. All this creates one emitter that can be used for data transfer, however the capability to deposit different organic inks allows for wavelength multiplexing with three different inks transmitting different data streams. The fact that these are part of an individually addressable LED array means that the power to each LED can be varied to generate white light, assuming RGB LEDs are fabricated.

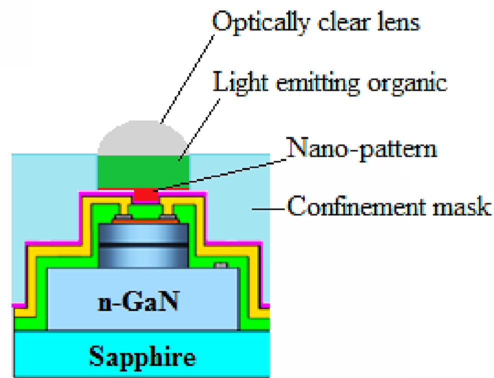

Figure 6.1.1 Illustration of a fusion of the techniques developed in our work to achieve a high efficiency hybrid LED.

In the case where these micro-LED arrays are used to transmit data along polymer optical fibres they gain a further advantage in the bit rates possible. Each "pixel" consists of 3 LEDs which can stream separate data by wavelength multiplexing. In addition, as the LEDs are part of a 64 x 64 array, several such pixels can be operated together and spacial multiplexing is achievable as another dimension for encoding data.

6.2 References

1. A. J. Trindade , B. Guilhabert, D. Massoubre, D. Zhu, N. Laurand, E. Gu, I. M. Watson, C. J. Humphreys and M. D. Dawson, "Nanoscale-accuracy transfer printing of ultra-thin AlInGaN light-emitting diodes onto mechanically flexible substrates", Applied Physics Letters, 103, (253302) 201, 2013.
2. A. J. Trindade , B. Guilhabert, E. Y. Xie, R. Ferreira, J. J. D. McKendry, D. Zhu, N. Laurand, E. Gu, I. M. Watson, C. J. Humphreys and M. D. Dawson, "Heterogeneous integration of gallium nitride light-emitting diodes on diamond and silica by transfer printing", Optics Express, Vol. 23, Issue 7, 2015.

Publications

Papers

Drafted/ Submitted

1. E. Richardson, A.J.C. Kuehne, Z. Gong, B. Guilhabert, E.Y. Xie, A.R. Mackintosh, E. Gu and M.D. Dawson. "Hybrid organic-inorganic micro-LED arrays of inkjet printed novel red, green and blue light emitting polymers".

Accepted/Published

2. N. McAlinden, D. Massoubre, E. Richardson, E. Gu, S. Sakata, M.D. Dawson and K. Mathieson, "Thermal and optical characterization of micro-LED probes for in vivo optogenetic neural stimulation", Optics Letters, Volume 38, Issue 6, Pages 992-4 (2013).
3. B Guilhabert, D. Massoubre, E. Richardson, J.J.D. McKendry, G. Valentine, R.K. Henderson, I.M. Watson, E. Gu and M.D. Dawson, "Sub-micron lithography using InGaN micro-LEDs: Mask-Free Fabrication of LED Arrays", IEEE Photonics Technology Letters, Volume 24, Issue 24, Pages 2221-4 (2012).
4. M. Wu, Z. Gong, D. Massoubre, Y. Zhang, E. Richardson, E. Gu, M. D. Dawson, "Inkjet-printed silver nanoparticle electrodes on GaN-based micro-structured light-emitting diodes", Applied Physics A, Volume 104, Issue 4, 1003-9, (2011).
5. D. Elfstrom, B. Guilhabert, J. McKendry, S. Poland, Z. Gong, D. Massoubre, E. Richardson, B.R. Rae, G. Valentine, G. Blanco-Gomez, E. Gu, J.M. Cooper, R.K. Henderson and M.D. Dawson, "Mask-less ultraviolet photolithography based on CMOS-driven micro-pixel light emitting diodes", Optics Express, Volume 17, Issue 26, Pages 23522-29 (2009).

Conferences

6. D. Massoubre, P.R. Edwards, E.Y. Xie, E. Richardson, I.M. Watson, E.Gu, R.W. Martin and M.D. Dawson. "Individually-addressed planar nanoscale InGaN-based light emitters". *In Proceedings of IEEE Photonics 2012 Conference*, 754 (2012).
7. B. Guilhabert, E. Richardson, D. Massoubre, E. Gu, I.M. Watson and M.D. Dawson, "maskless fabrication of GaN-Based Light-Emitting Diodes", *2010 23rd Annual meeting of the IEEE Photonics Society*, 649-650 (2010).

Hybrid GaN red, green and blue micro-LED arrays with inkjet-printed and absorption-engineered light-emitting polymers

E Richardson[1], A J C Kuehne[2], Z Gong[1], B Guilhabert[1], E Xie[1], A R Mackintosh[3], E Gu[1], N Laurand and M D Dawson[1]
1 Institute of Photonics, University of Strathclyde, 106 Rottenrow, Glasgow G4 0NW, UK
2 Interactive Materials Research – DWI at RWTH Aachen University, 52056 Aachen, Germany
3 Department of Pure and Applied Chemistry, WestChem, University of Strathclyde, Glasgow G1 1XL, UK

E-Mail:elliot.richardson@strath.ac.uk

Abstract A hybrid organic-inorganic micro-light-emitting-diode (micro-LED) array fabricated via inkjet printing of tailored red, green and blue light-emitting-polymers (LEPs) is reported. Composite inks consisting of a transparent encapsulation matrix loaded with LEPs having absorption optimised for 370 nm and peak emissions at 413nm blue, 535nm green and 610nm red, respectively, were integrated onto a 50μm pitch micro-LED array emitting at 368 nm. A layer-by-layer ink-jet deposition method is proposed and demonstrated in order to achieve precise control over the spatial structures of the colour-converting materials. The resulting colour conversion efficiency is found to be up to 31.5% for 20 layers of 1pl droplets of 20mg/mL LEP-ink solution individually integrated onto pixels of the array.

I. Introduction

The hybridisation of Gallium-Nitride (GaN) light-emitting diodes (LEDs) with chromophores for colour-conversion is a growing technological topic that aims to efficiently extend the emission spectrum of a monochromatic LED across the visible, to generate white light by colour-mixing and in some cases to deliver multi-colour light emission from a single LED array chip. Colour-converting materials are typically deposited or integrated on top of bare LEDs in order to absorb LED light and re-emit photons at longer wavelengths [1-4]. Applications for such hybrid GaN LEDs are varied and include solid-state lighting [5], scientific instrumentation and visible light communications (VLC)[6-7]. For all these applications, the light sources hybrid format is critical because, despite undeniable progress, the efficiency performance of the GaN LED technology is optimum in the blue-violet part of the spectrum and significantly degrades at longer wavelengths.

While broad-area LEDs, with typical emitting area sizes of 300μm x 300μm and above, are the most common, there exists another LED format: the so-called micron-size LED (micro-LED). Micro-LEDs have a designed emitting area spanning the range from 100 μm x 100 μm down to a couple of μm^2. Their micro-size provides them with unique characteristics: they can be driven at higher current density than their broad area counterparts and can also be modulated at higher frequencies [9]. Furthermore, thousands of these micro-emitters can be combined onto a 1 mm^2 chip. In this way, arrays of individually-addressable micro-LEDs can be made and possibly integrated with CMOS electronics [8], paving the way for truly smart micro-displays with both spatial and temporal control (pulses down to few hundreds of picoseconds in duration have been reported[9]). This makes micro-LED chips particularly well-suited to scientific instrumentation[10] and VLC applications[11]. Their functionality can be further extended through hybridization with appropriate colour-converters, adding spectral flexibility to the spatial and temporal capabilities.

Important characteristics for a LED colour-converter are processability, conversion efficiency and, for certain applications, excited state lifetime. The latter basically dictates how fast a colour-converter responds to a time-varying signal while shifting it to longer wavelengths. Current commercial white LEDs use colour-mixing with inorganic rare-earth phosphors as converters, which

are efficient but have excited state lifetime of the order of a few µs up to the ms regime [12]. Such an excited state lifetime is definitely too long for applications requiring nanosecond-pulses or fast modulated visible signals (again e.g. instrumentation and VLC). For faster responses, other types of luminescent converters such as organic chromophores and colloidal quantum dots can be considered [13,14]. These colour-converters are also relevant for illumination as the sustainability of rare-earth materials is not ensured due to limited supplies [15]. Of these two types of colour-converters, organic chromophores have the shortest excited state lifetimes with values of 1 to 5 ns typical for emission in the visible. However, organic colour-converters have often limited spectral absorption bandwidth, which necessitates a careful choice of the material for matching the emission wavelength of LEDs and can in turn complicate the fabrication of multi-colour hybrid LED chips. Thus, there is a need for organic colour-converters having different emission wavelengths but sharing the same absorption profile. In principle, such absorption-engineered materials could then be processed and directly deposited onto an LED array for hybrid integration in order to obtain, in a simple manner, multi-colour emission from a single LED chip.

In this work, we combine a 368 nm GaN-based micro-LED array with three light-emitting-polymers (LEPs) that, crucially, share the same peak absorption wavelength of ~370 nm[16] while emitting respectively in the blue, green and red region of the visible spectrum. This common excitation wavelength makes it possible for one UV LED array overcoated with these LEPs to yield red, green and blue emission, thereby facilitating fabrication of multi-colour micro-displays. The chosen hybrid integration approach utilises drop-on-demand inkjet printing technology to deposit composite inks based on the LEPs directly onto the desired pixels [17]. A layer-by-layer method for the ink deposition is developed in order to obtain optimum combined control of conversion efficiency and spatial coverage. The LED device used in these experiments is a 64x64 matrix array of individually addressable pixels; each pixel has a 16-µm diameter emission area and the pitch (separation between emitters) is 50 µm. The device emits in a top-emitting format i.e. through the p-doped GaN layer [9].

In the following, in section II, we present the design structures of the LEP materials as well as the preparation steps of the related inks. In section III, we describe the deposition process for the colour-converting inks and in particular the layer-by-layer optimisation. Finally, we present the results of fully integrated hybrid devices in section IV.

II. Ink Preparation and Characterisation

The LEP materials used are co-polymers based on a polyfluorene backbone, facilitating an identic UV-blue absorption spectrum peaking at 370 nm. The emission characteristics however are tuned by selecting different emissive monomer units as shown in figure 1. These are respectively 2,7-dibromo-9,9-(dihexyl)fluorene for the blue-emitter P1, 4,7-dibromo-2,1,3-benzothiadiazole for the green-emitter P2, and 4,7-bis(5-bromo-2-thienyl)-2,1,3-benzothiadiazole for the red emitter P3. Following excitation of these materials at 370 nm, resonant energy transfer 'funnels' the energy rapidly along the conjugated polymer backbone from the absorbing donor fluorene unit to the acceptor emissive unit (P1, P2 or P3). Reported characterisation for these materials gives internal photo-luminescence quantum yield (PLQY) efficiencies of 63%, 45% and 31% for the blue, green and red materials, respectively, when excited at 370nm in toluene solution [16]. The decrease in PLQY with increasing emission wavelength is due to a reduced spectral overlap between the emission of the polyfluorene backbone and the absorption of the emissive unit [18]. The conjugated polymers are functionalized with divinyl ether moieties to allow them to be incorporated into vinyl ether and glycidyl ether photoresist matrices (see fig. 1). This increases the processability of the resulting materials. The LEPs are then incorporated into a solvent-less photocurable matrix suited for ink-jet printing.

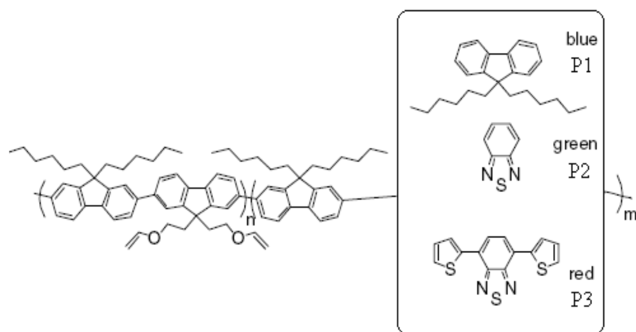

Fig 1. Chemical structures of the three LEPs used in this work. Each LEP is a statistical copolymer with a common conjugated polyfluorene backbone. The functionalisation units, dictating the emission colour of the molecules, are also shown in the box on the right.

The following procedure is used to formulate photocurable composite inks from the LEPs. LEP powder is combined with 1,4-cyclohexanoldivinyl ether monomers solution (CHDV), the encapsulation matrix material[19], and 4–octyloxy-diphenyliodonium hexafluoroantimonate, a photo-acid generator (PAG), to carry on polymerisation. The CHDV matrix is optically transparent at 370 nm[20] and throughout the visible spectrum [19], and thus can transmit both the direct micro-LED and LEP emission. Upon exposure to UV light the PAG dissociates to form an acid, which initiates a cationic polymerization, causing cross-linking of the CHDV monomer alongside the LEP divinyl ether. This allows immobilization of the LEP into a solid CHDV-polymer matrix. Specifically, the composite inks is made by measuring out 30 mg of LEP powder using a high precision scale and then dissolving it in 200 µL of chloroform. This solution is then added to 1.5 mL of the CHDV monomer and 3 mg of the PAG, which is adequate to ensure rapid polymerisation. The initial dissolution of LEP into a solvent aids the complete mixing of the LEP material within the CHDV monomer solution. The resulting solution undergoes vacuum treatment for 30 s to fully evaporate remaining chloroform solvent and is passed through a 0.2-µm-pore size PTFE filter to remove any large particulates.

We prepare film-on-glass samples using the LEP-inks to check for absorption and photoluminescence (PL) characteristics and confirm that the respective spectral peak positions remain unchanged once the LEPs are incorporated into the

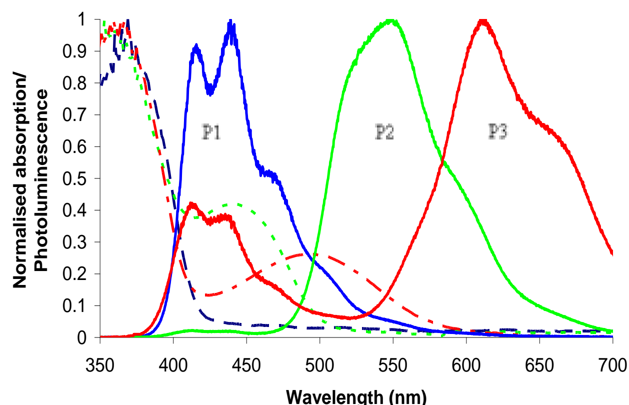

Fig 2. Normalised absorption and photoluminescence spectra for films of LEP in CHDV. Absorption spectra: P1, dashed line; P2, dotted line; P3, dot-dashed line. Photoluminescence spectra are represented by solid lines.

CHDV matrix. This is important to ensure the absorption peak of each of the different LEP-ink materials remains optimal for the UV LED emission wavelength. Absorption measurements are taken using a UV-VIS Cary spectrophotometer and the PL is measured with a fibre-coupled grating CCD spectrometer under 375nm laser excitation of the sample. The solid films of LEP inks are created via spin coating, using 100 µL of ink solution onto cleaned glass cover slides by spin coating at 2000 rpm for 60s. Films are subsequently photo-cured under 370 nm illumination for 60 s for a total exposure dose of 2.5 J.cm^{-2}. Figure 2 shows the absorption and emission spectra of the different inks. The absorption profiles peak at ~370 nm for each polymer ink. Secondary absorption peaks in samples with P2 and P3-based LEPs are caused by absorption of the different emissive units. Figure 2 also shows that upon photo-pumping at 375 nm emission in the visible spectrum is obtained. The three materials in question have vibronic emission peaks or shoulders at 413 nm, 437 nm and 460 nm; 545 nm; and 610 nm and 660 nm for P1, P2 and P3 emission, respectively [16].

III. Ink-jet Deposition for Integration

The printer used for integration of the composite inks with the micro-LEDs is a Dimatix DMP2800 printer, with drop-on-demand technology using a piezo-controlled microelectromechanical membrane within the print cartridge[20,21], delivering droplets

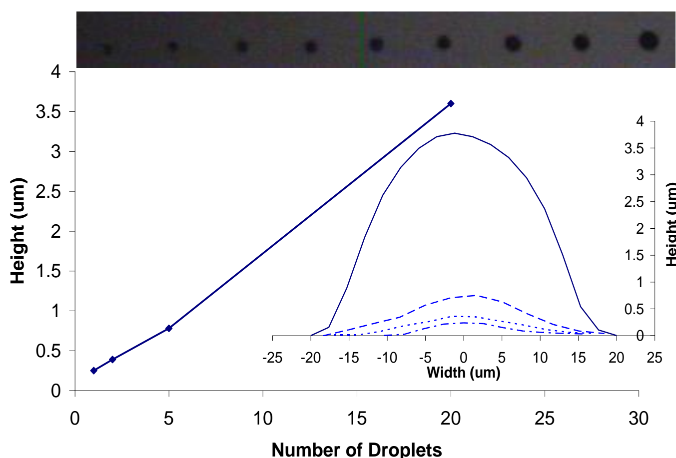

Fig 3. Evolution of the height of ink-jet structures with the number of deposited layers (each 1pL). Insert, top: optical micrograph of deposited droplets prior to dektak measurements, 100 µm centre to centre pitch. Insert, right: stylus profilometre measurements of structures composed of 1 (dash-dotted line), 2 (dotted line), 5 (dashed line) and 20 (solid line) printed layers of 1pL droplet.

volume down to 1 pL. The available printing area of the system is 200 mm × 300 mm with a positioning repeatability of +/-5 µm. A fiducial camera is available for substrate alignment. The DMP2800 cartridges impose some restrictions on the fluid to be jetted. The controlled deposition of an ink depends on its properties when ejected and on those of the substrate the droplet is deposited onto. A large surface tension causes the fluid to resist jetting, as does a high viscosity. The viscosity at the point of ejection has to be between 10 and 40 centipoises and the surface tension with the jetting nozzles around 30 dynes/cm. After deposition, surface tension between the ink droplet and the substrate determines the feature shape obtained, dictating the thickness and width of features on top of the LED. A hydrophilic surface provides a low surface tension and a low contact angle, resulting in wide, shallow features. Conversely a hydrophobic surface yields smaller but taller features as the jetted volume stays constant [22,23](1pL here).

The printability of the three LEP inks is assessed by depositing the materials on cleaned and surface-treated silica substrates. Protocol for cleaning and treatment of the SiO_2 substrate is first to submerge it in acetone and then in methanol for 5 minutes each whilst in an ultrasonic cleaner. To deposit the surface treatment the substrate is air dried and left in an enclosed chamber with a saturated atmosphere of tridecafluoro1,1,2,2tetra-hydro-octyl(1)dimethylchlorosilane. Condensation occurs on the glass substrates where the silanisation treatment adheres to loose oxygen bonds of the SiO_2 surface. The surface energy of the substrate surface is altered after this treatment, which results in an increase of the hydrophobicity and in turn reduces spreading of printed ink droplets. This effect is critical for the precise deposition of colour-converting materials onto each micro-LED individually. For full hybrid devices, deposition of the silane surface treatment onto the micro-LED device is done by leaving it within the aforementioned chamber for 60 minutes as well. The LED device has a SiO_2 surface layer so the treatment adheres in the same way as for the glass substrates.

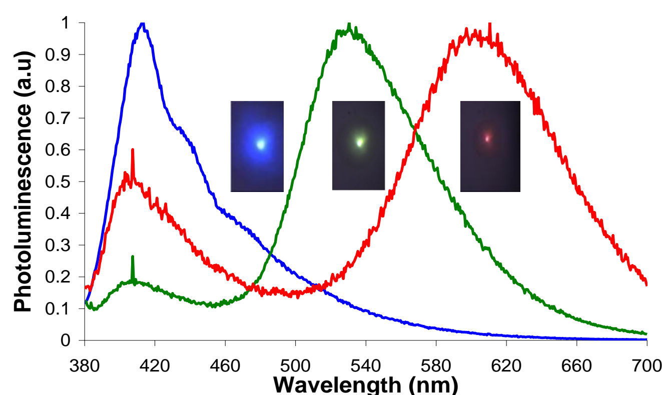

Fig 4. Normalised micro-photoluminescence spectra and optical micrographs of 5 layers of 1pL printed pumped with a 375-nm laser.

The micro-LED array is fully cleaned during manufacture so no additional ultrasonic cleaning is necessary beforehand.

Test printing of red, green and blue LEP-ink arrays is conducted on silane-treated glass substrates with droplet separation of 50 µm. A layer-by-layer approach for ink deposition and photopolymerisation is taken in order to build-up and control the feature thickness, which is desirable for light conversion, while minimising space coverage. This approach is advantageous in this context compared to the more standard route of full material deposition before photo-polymerisation (see discussion and comparison further). Stylus profilometre measurements is taken to assess the evolution of the feature morphology and height with the number of printed layers. Each deposited droplets (1 pL) is photo-cured at 370 nm for 60 seconds, giving an exposure dose of 2.5 $J.cm^{-2}$,

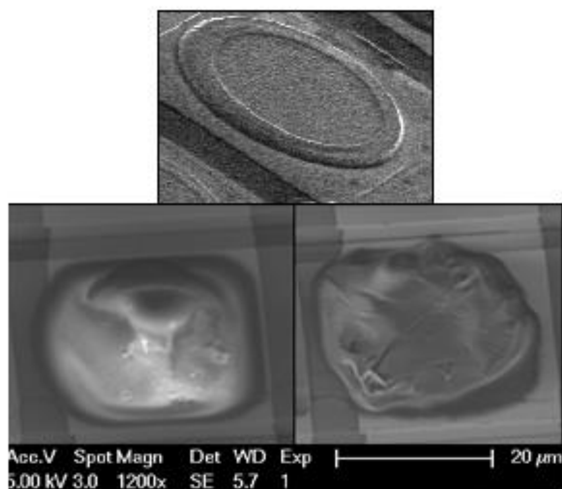

Fig 5. SEM images of a bare micro-LED pixel (top) and of two pixels integrated with CHDV (bottom). The SEM image of the bare pixel was taken under 10 kV acceleration voltage and 1500x spot magnification. The SEM images of the two pixels integrated with CHDV were taken under 5 kV acceleration voltage and 1200x spot magnification. The bottom left pixel was deposited with 20 layers of 1 pL then cured. The pixel on the bottom right was printed using the layer-by-layer technique.

before a subsequent droplet can be printed to form an additional layer. Figure 3 shows the height evolution of the printed features. The final profile of a 20-layer printed structure using this technique is shown in inset of figure 3. The dome-shape feature is 4 µm in height for a diameter of 30 µm at full width half maximum.

Micro-photoluminescence spectra are measured on 5-layer printed structures pumped with a 375 nm-emitting laser diode at an optical power density of 187 W/cm^2; the corresponding emission profiles are displayed in figure 4. The main peaks for P1 remain consistent with the spectra obtained for the LEP films; the PL spectrum exhibits vibronic peaks at 412 nm, 435 nm and 465 nm. The spectra for P2 and P3 however have shifted maxima at 530 nm and at 600 nm for, respectively, P2 and P3. Additionally the shoulder previously observed (see fig. 2) for P3 at 660 nm is non-evident. The difference in spectral shape with the PL measurements done on films and in particular the dominance of the lower wavelength emission peaks is attributed to less self-absorption in these thinner printed structures. For both P2 and P3 materials, in both films (fig. 2) and printed structures, a residual emission centred at 410 nm is measured, corresponding to the photoluminescence from the copolymers backbone (the polyfluorene absorbing units). This is due to incomplete energy transfer between donors and acceptors.

For full hybrid devices, two approaches of ink deposition is tried and compared: the ‘layer-by-layer with photo-curing steps’ approach described previously and a ‘full printing before polymerisation’ method, referred to as the standard method hereafter. The standard technique consists in depositing 20 1 pL droplet of liquid in a row followed by photo-curing only after the full 20 pL has been deposited. The layer-by-layer technique, as explained before, consists in printing 20 layers of 1 pL droplets with intermediate photo-curing steps between each droplet deposition. SEM images of hybrid micro-LED pixels fabricated with these two

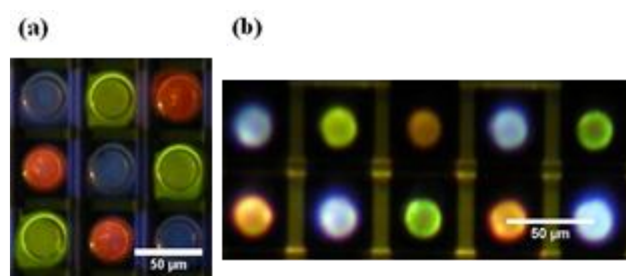

Fig 6. Red, green and blue arrays printed onto LED device and illuminated with a 370 nm lamp (a). Tri-colour arrays printed onto a packaged 370 nm emitting 64x64 matrix addressable micro-LED array, illuminated by each underlying UV pixel (b)

approaches are shown in figure 5. An SEM image of a bare micro-LED pixel, i.e. with no deposited ink, is also shown for information (top). The structure printed with the standard method (bottom left) exhibits a larger degree of spreading compared to the layer-by-layer method (bottom right). This effect is undesirable for generating small diameter, high thickness colour-converting structures. On the other hand, while an extended UV exposure can lead to some shrinkage of the CHDV matrix, the layer-by-layer printing approach gives overall better control on the thickness of the colour converter, allowing optimisation of the conversion efficiency. The layer-by-layer technique is thus well-suited for printing onto a micro-LED as each deposited droplet is immobilised on top of the emissive area, permitting the successive formation of layers and the build-up of printed converting structures without wasting material that could otherwise spread between micro-pixels.

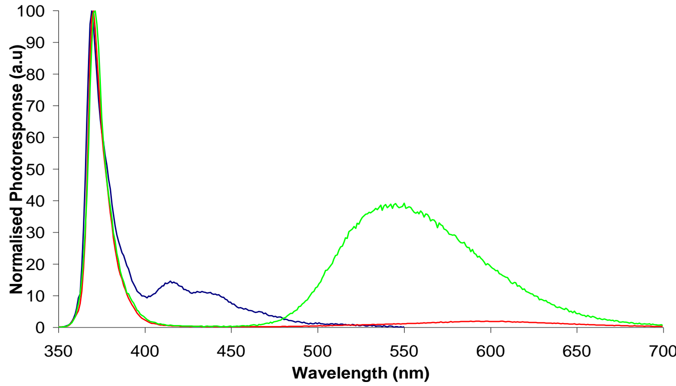

Fig 7. Emission spectra of hybridised micro-LED pixels. The PL peak at 370 nm is unconverted UV light from the underlying pixel and longer wavelength peaks at 413 nm, 532 nm and 610 nm are down-converted light from the blue, green and red LEP inks respectively.

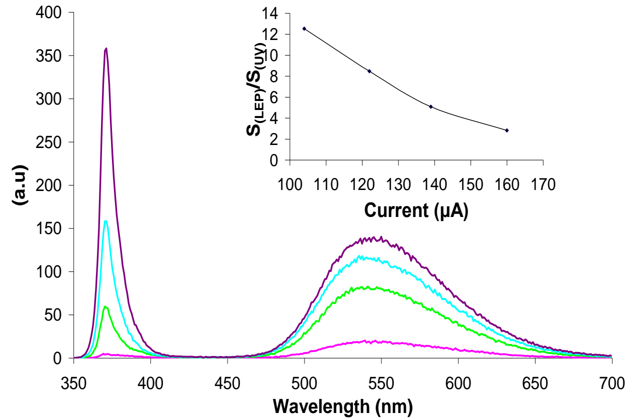

Fig 8. Evolution of the emission profile for the green composite ink with increasing bias applied to the micro-pixel (b). Insert showing the change in ratio of the UV and converted peaks with increasing current.

IV. Hybrid Device Characterisation

Successful integration of the three LEP inks onto a 368-nm-emitting matrix addressable micro-LED array is achieved. For this, 20 layers of the relevant ink are deposited onto each pixel (micro-LED) of the array using the layer-by-layer approach. Optical micrographs of the resulting tri-colour micro-LED array with the underlying UV micro-LEDs switched on are shown in figure 6. A clear RGB array using a single LED chip with a centre-to-centre spacing of 50 μm is thus demonstrated. Figure 7 shows the emission spectra of the hybridized devices. The peak at 368 nm is caused by unabsorbed light from the underlying GaN micro-LEDs; longer-wavelength peaks are caused by the colour-converted emission from the integrated LEP structures. Peak emissions at 413 nm, with a 435 nm shoulder, for P1-based LEP ink, 545 nm for P2-based LEP ink and 600 nm for P3-based LEP ink are obtained as could be expected from initial PL measurements of non-integrated structures (see section III).

The effect of the shape of the printed structure on the spatial emission profile and on the light extraction from the device is also investigated. Optical power measurements are made with a Coherent Fieldmax Top power meter for a bare pixel and repeated with the same pixel overcoated with 10 layers of pure CHDV matrix (i.e. with no LEP). In addition, the emission profile is determined by combination of a JVC TKC721EG charge-coupled device (CCD) camera and an Aerotech BM75 goniometer. The results show negligible changes in both the power and emission profile of the LED, implying there is no significant change in the extraction efficiency of LED light due to lensing of the polymer deposited on the micro-LED.

The colour-conversion efficiency of the hybrid micro-pixels is assessed. The LED light absorbed by the ink-structure is calculated by taking the difference between the forward emission of a reference LED, which is hybridised with a CHDV matrix dome containing no LEP material, and that of an LED integrated with a similar structure but made of the full LEP ink colour converter. Having determined the proportion of light absorbed by the LEP, the ratio of the converted light to the amount of absorbed light yields the forward UV-to-visible power efficiency for the integrated LEP structure. Forward power efficiencies of 13.2%, 31.5% and 5% for the integrated structures of P1-based ink, P2-based ink and P3-based ink, respectively, are obtained. The value for the P1-based device is underestimated because of some overlap of its emission with the micro-LED (see figure 7). The lower efficiency found for the red device is attributed to the reduced quantum efficiency as mentioned in section II as well as possible polymer degradation over time. For future improvements the issue of reduced quantum efficiency could be addressed in the future by copolymerizing benzothiadiazole moieties into the P3 polymer, which would facilitate an improved energy cascade

transfer into the red emitter. The polymer degradation could be addressed by reducing the time between synthesis and integration into the encapsulation material.

Finally, an examination of how the light conversion changes with increasing applied current is conducted. Figure 8 shows results for a green pixel. Initially, the converted light dominates over the UV emission but this ratio of converted to unconverted light changes as the applied current is increased to the point where the unabsorbed UV signal dominates over the LEP emission. This is due to the saturation of the LEP absorption, where the LEP structure converts as much UV as possible given the LEP efficiency and concentration. The effect is characterised by a change in the slope of the ratio of converted light to that unabsorbed light (S_{LEP}/S_{LED}) with applied current, shown in the inset of figure 7. By looking at the evolution of S_{LEP}/S_{LED} versus applied current it can be seen that the hybrid device enters the saturation regime above 140µA of applied current. Increasing the LEP concentration and/or the LEP-ink structure thickness should increase this value of current at saturation.

V. Conclusion

The hybridisation of a micro-LED array emitting in the near UV with red, green and blue-emitting polymers was reported using a drop-on-demand ink-jet printing technique. The LEPs were engineered for maximum absorption at 370 nm and were further functionalised with divinyl ether to facilitate their incorporation into a host matrix in order to form colour-converting inks. These colour-converting inks were successfully integrated onto a 368-nm-emitting, 64x64 matrix-addressable micro-LED array with a 50-µm pixel-to-pixel pitch by utilising a layer-by-layer deposition approach. This layer-by-layer deposition enables a better spatial control over the colour-converting features. Single pixel colour-conversion efficiencies from UV micro-LED emission to red, green and blue are measured to be 5%, 31.5% and 13.2%, respectively, for 20 layers of 1 pL droplets. This work demonstrates an attractive way to fabricate multi-coloured pixelated micro-LED devices with control at design of each individual emitter spectrum.

References

1. M. Achermann, M. A. Petruska, D. D. Koleske, M. H. Crawford and V. I. Klimov, ―Nanocrystal-Based Light-Emitting Diodes Utilizing High-Efficiency Nonradiative Energy Transfer for Color Conversion,‖ NANOLETTERS 6, 7, 1396-1400 (2006).
2. S. Chanyawadee, P. G. Lagoudakis, R. T. Harley, M. D. B. Charlton, D. V. Talapin, H. W. Huang, and C-H. Lin, ―Increased Color-Conversion Efficiency in Hybrid Light-Emitting Diodes utilizing Non-Radiative Energy Transfer,‖ Adv. Mater. 22, 602–606 (2010).
3. S. Nizamoglu and H. V. Demir, ―Förster resonance energy transfer enhanced color-conversion using colloidal semiconductor quantum dots for solid state lighting,‖ Applied Physics Letters 95, 151111 (2009).
4. G. Heliotis, G. Itskos, R. Murray, M. D. Dawson, I. M. Watson and D. D. C. Bradley, ―Hybrid Inorganic/Organic Semiconductor Heterostructures with Efficient Non-Radiative Energy Transfer, Adv. Mater. 18, 334-338 (2006).
5. S. Nizamoglu, E, Sari, J.H. Baek, I.H Lee, H.V. Demir, ―White light generation by resonant nonradiative energy transfer from epitaxial InGaN/GaN quantum wells to colloidal CdSe/ZnS core/shell quantum dots New J. Phys. 10, 12300 (2008)
6. F. Zhang, L.-P. Wang, M. Brauner, J. F. Liewald, K. Kay, N. Watzke, P. G. Wood, E. Bamberg,, G. Nagel, A. Gottschalk and K. Deisseroth, ―Multimodal fast optical interrogation of neural circuitry, Nature 446, 633-639 (2007).
7. B. R. Rae, K. R. Muir, Z. Gong, J. McKendry, J. M. Girkin, E. Gu, D. Renshaw, M. D. Dawson and R. K. Henderson, ―A CMOS Time-Resolved Fluorescence Lifetime Analysis Micro-System, Sensors 9, 9255-9274 (2009).
8. H. Zhang, D. Massoubre, J. McKendry, Z. Gong, B. Guilhabert, C. Griffin, E. Gu, P. Jessop, J. Girkin, and M. Dawson, ― Individually-addressable flip-chip AlInGaN micropixelated light emitting diode arrays with high continuous and nanosecond output power, Opt. Express 16, 9918-9926 (2008).
9. Z. Gong, H. X. Zhang, E. Gu, C. Griffin, M.D. Dawson, V. Poher, G. Kennedy, P.M.W. French, M.A.A. Neil, ― Matrix-addressable micropixellated InGaN light-emitting diodes with uniform emission and increased light output" , IEEE Transactions on Electron Devices **54** , 2650-2658 (2007)
10. A. Zarowna-Dabrowska, S. L. Neale, D. Massoubre, J. McKendry, B. R. Rae, R. K. Henderson, M. J. Rose, H. Yin, J. M. Cooper, E. Gu, and M. D. Dawson,― Miniaturized optoelectronic tweezers controlled by GaN micro-pixel light emitting diode arrays, Optics Express **19**, 3, 2720-2728 (2011)
11. J. McKendry, R. P. Green, A. E. Kelly, Z. Gong, B. Guilhabert, D. Massoubre, E. Gu and M. D. Dawson, ―High Speed Visible Light Communications Using Individual Pixels in a Micro Light-Emitting Diode Array, IEEE Photonics Technology Letters **22**, 18, 1346-1348 (2010).
12. B. Kang, J. Seo, S. Jeong, J. Lee, C. Han, D. Kim, K. Kim, S. Yeom, D. Kwon, H. Kim, and S. Kang, ― Highly efficient hybrid light-emitting device using complex of CdSe/ZnS quantum dots embedded in co-polymer as an active layer, Opt. Express 18, 18303-18311 (2010).
13. J. Herrnsdorf, B. Guilhabert, J.D. McKendry, Z. Gong, D. Massoubre, S. Zhang, S. Watson, A. E. Kelly, E. Gu, N. Laurand, and M. D. Dawson,― Hybrid organic/GaN photonic crystal light-emitting diode, Appl. Phys. Lett. 101, 141122 (2012)
14. B. Guilhabert, D. Elfström, A. Kuehne, D. Massoubre, H. X. Zhang, S. R. Jin, A. R. Mackintosh, E. Gu, R. Pethrick, and M. D. Dawson, ―Integration by self-aligned writing of nanocrystal/epoxy composites on InGaN micro-pixelated light-emitting diodes,‖ Opt. Express 16, 23, 18933-18941 (2008).

15. T. Erdem and H. V. Demir, — Semiconductor nanocrystals as rare-earth alternatives, Nature Photonics 5, 126 (2011)

16. A. J. C. Kuehne, A. R. Mackintosh, R.A. Pethrick, B. Tieke,— Novel vinyl ether functionalized fluorene polymers for active incorporation into common photoresist matrices, Tetrahedron Letters **49**, 32, 4722-4724 (2008)

17. M. Wu, Z. Gong, A. Kuehne, A. Kanibolotsky, Y. Chen, I. Perepichka, A. Mackintosh, E. Gu, P. Skabara, R. Pethrick, and M. Dawson, — Hybrid GaN/organic microstructured light-emitting devices via ink-jet printing, Opt. Express 17, 16436-16443 (2009).

18. Feron K, Belcher WJ, Fell CJ, Dastoor PC. Organic Solar Cells: Understanding the Role of Förster Resonance Energy Transfer. *International Journal of Molecular Sciences*. 2012

19. A. J. C. Kuehne, D Elfström, A. R. Mackintosh, A. L. Kanibolotsky, B Guilhabert, E Gu, I. F. Perepichka, P. J. Skabara, M. D. Dawson, R. A. Pethrick, — Direct Laser Writing of Nanosized Oligofluorene Truxenes in UV-Transparent Photoresist Microstructures, Advanced Materials **21**, 7, 781–785 (2009)

20. Dimatix DMP2800 system information- http://www.dimatix.com/files/DMP-2831-Datasheet.pdf

21. H. Dong, W. W. Carr, and J. F. Morris, — Visualization of drop-on-demand inkjet: Drop formation and deposition, Rev. Sci. Instrum. 77, 085101 (2006)

22. "Surface design: applications in bioscience and nanotechnology" By Renate Förch, Holger Schönherr, A. Tobias A. Jenkins

Thermal and optical characterization of micro-LED probes for *in vivo* optogenetic neural stimulation

Niall McAlinden,[1,†,*] David Massoubre,[1,†] Elliot Richardson,[1] Erdan Gu,[1] Shuzo Sakata,[2] Martin D. Dawson,[1] and Keith Mathieson[1]

[1]*Institute of Photonics, SUPA, University of Strathclyde, Glasgow G4 0NW, UK*

[2]*Strathclyde Institute of Pharmacy and Biomedical Sciences, University of Strathclyde, Glasgow G4 0RE, UK*

**Corresponding author: niall.mcalinden@strath.ac.uk*

Received December 6, 2012; revised February 6, 2013; accepted February 10, 2013; posted February 12, 2013 (Doc. ID 181141); published March 15, 2013

Within optogenetics there is a need for compact light sources that are capable of delivering light with excellent spatial, temporal, and spectral resolution to deep brain structures. Here, we demonstrate a custom GaN-based LED probe for such applications and the electrical, optical, and thermal properties are analyzed. The output power density and emission spectrum were found to be suitable for stimulating channelrhodopsin-2, one of the most common light-sensitive proteins currently used in optogenetics. The LED device produced high light intensities, far in excess of those required to stimulate the light-sensitive proteins within the neurons. Thermal performance was also investigated, illustrating that a broad range of operating regimes in pulsed mode are accessible while keeping a minimum increase in temperature for the brain (0.5°C). This type of custom device represents a significant step forward for the optogenetics community, allowing multiple bright excitation sites along the length of a minimally invasive neural probe. © 2013 Optical Society of America

OCIS codes: 170.0170, 130.3120, 170.2945, 230.3670.

Optogenetics is a technique that uses light-sensitive proteins to control neural activity [1]. The most commonly used protein is channelrhodopsin-2 (ChR2), which is activated by light at 460 nm and initiates action potentials in mammalian neurons with millisecond temporal resolution. However, a key problem limiting the development of this field is getting multiple compact light sources at high spatial, temporal, and spectral resolution to deep brain regions. The need for multiple optical sources stems from the desire to probe neighboring neurons, neural circuits, and cell types. Neurons are often arranged in laminar structures within morphologically distinct regions of the brain, such as the neocortex. A neural probe with multiple optical sites would be able to sequentially activate these layers while recording probes monitor the resultant neural activity. This would provide a valuable tool to further the understanding of how neural function maps to behavior. Most *in vivo* studies use a single tapered optical fiber to couple light into these regions [2]. Electrodes can be routinely inserted with the fiber to record the resultant electrical activity [3,4]. This method, while certainly providing adequate light intensity, only gives a single target region. If stimulation in several sites is required, several fibers must be inserted, greatly increasing the surgical complexity and the damage to delicate neural tissue. Further to this problem, each fiber requires its own light source which must remain connected to the fiber during the course of the experiment, meaning the subject is not free to move about unhindered. Several different solutions to address these problems have been suggested, including fiber bundles [3], waveguide devices [5,6], LED coupled to waveguide devices [4], and millimeter-sized LEDs within a glass pipette [7].

In this Letter, a new approach is introduced, a probe with integrated micrometer-sized LEDs. The main reasons that these LED probe devices have not been pursued before is due to the significant technical challenges involved and a commonly held belief that heat dissipation could damage local brain tissue. Here we examine the optical and thermal properties of LED probe devices, measured under the pulsed regimes required for optogenetic studies, and show that these devices provide sufficient power, with excellent spatial, spectral, and temporal resolution, while not increasing the temperature of local brain tissue by more than 0.5°C. Since the optical sites are integrated onto the probe and electrically activated, the device could potentially be extended to allow a freely moving subject through wireless communication. The integration of more LEDs onto the probe is only limited by the width of the metallic tracks, which can be as narrow as a few hundred nanometers. This gives the possibility of having 10 s of LEDs on a probe without having a probe width that will damage the neural tissue.

The LED probe was fabricated from a commercial GaN 450 nm LED wafer (SuperNovaOpto). The probe is designed to have a total length of 7 mm [Fig. 1(a)]. The tip is 1.3 mm long and 80 μm wide and was designed to minimize tissue damage during insertion [Fig. 1(c)]. Each tip contains five LEDs with a pitch of 250 μm

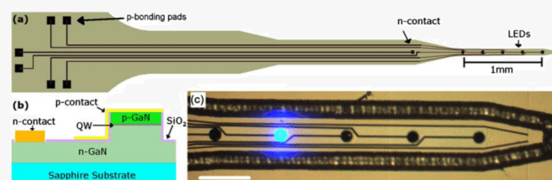

Fig. 1. (Color online) (a) Layout of LED probe, showing the single n-contact and bonding pads linked with tracks to the p-contacts for each LED. (b) Schematic cross section of the fabricated devices, showing the quantum well (QW) LED structure. (c) Tip of the five-site LED probe, before final thinning, with a single LED switched on, emission is through the sapphire substrate. Scale bar is 200 μm.

0146-9592/13/060992-03$15.00/0 © 2013 Optical Society of America

and a diameter of 40 μm. The other end of the probe contains bonding pads allowing each LED to be individually addressed. The following process flow was used to manufacture the probes as adapted from Zhang *et al.* [8]. After a deoxidation step, 30 nm of palladium was deposited by electron beam evaporation, followed by a rapid thermal annealing at 300°C for 120 s in a pure nitrogen ambient. This forms a semi-transparent ohmic contact with the p-doped GaN layer. A 30 nm/100 nm Ti/Au bilayer was then sputter-deposited to form the mirror/anode. This was followed by plasma-enhanced chemical vapor deposition (PECVD) of a 500 nm thick SiO_2 layer. The SiO_2 layer was then patterned by reactive-ion etching (RIE) and the resulting hard mask was used to create mesa structures down to the n-GaN, using further RIE and inductively coupled etching steps. This multistep dry etching approach allows the formation of LEDs with self-aligned mirrors using only one photolithography step. The SiO_2 hard mask was removed and a new SiO_2 layer deposited by PECVD to serve as a passivation layer. It was then patterned to get access to the mesa structures. Ti(30 nm)/Al(250 nm)/Ti(30 nm)/Au(100 nm) layers were sputter-deposited and patterned by a standard lift-off process to connect the LEDs to wire bonding sites [Fig. 1(b)]. Laser dicing was used to form 100 μm deep trenches around the probe. Each probe can be released by mechanically thinning (to 100 μm) from the back sapphire substrate and then bonded on a custom printed circuit board (PCB), the probe is wire bonded to allow each LED to be individually addressed. The whole device including PCB is electrically isolated by a 1 μm thick transparent parylene layer, this layer is biocompatible and protects the device from degradation. Due to the high pulse currents required for the LED, good electrical shielding will be required to negate any electrical artefacts in neighboring recording probes.

Each LED was characterized electrically and optically. They can deliver a maximum of 1 mW of light, at an efficiency of ~2%. The average switch on voltage for the LEDs was 2.6 ± 0.2 V (SD, $N = 23$), while the average differential resistance was $680 \pm 0.2\Omega$ (SD, $N = 23$). Figure 2(a) shows the output power density—current relationship with 2(b) showing a typical spectrum from one of the LEDs. It has a peak emission at 446 nm, shifting to 443 nm at higher current densities, with the FWHM increasing from 17 to 21 nm. The emission spectrum overlaps well with the absorption spectrum for ChR2. Finally, the light intensity expected at various depths away from the probe was calculated using the model described in Bernstein *et al.* [7] [Figs. 2(c) and 2(d)]. This model was supplemented with experimental data where the absorption through different thicknesses of brain slices was measured, the data was convolved with a Lambertian distribution to account for the source-detector distance remaining constant [Fig. 2(d)]. Brains were extracted from deeply anesthetized wild-type mice and sliced into coronal sections with a sliding microtome. All animal procedures were performed under license from the UK Home Office. Figure 2(d) demonstrates the usefulness of this light source for both small and larger volume stimulation through irradiance modulation.

Temperature increases adversely affect the neuronal activity, meaning that it is important to fully characterize the thermal properties of the device. Measurements were

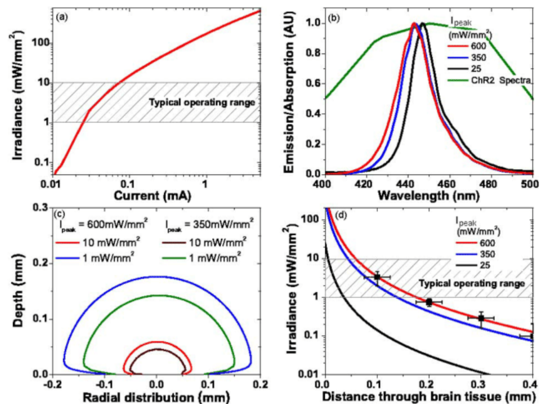

Fig. 2. (Color online) (a) Irradiance-current response for an LED. (b) Emission spectra of the LED at various light irradiances showing overlap with the absorption spectrum of ChR2. (c), (d) The calculated light intensity at differing depths within the brain for various device irradiances. The data points in (d) are from transmission experiments through varying thicknesses of brain slices (error is SD). Optogenetic constructs require 1–10 mW/mm^2 [1].

made using a thermal imaging camera (FLIR SC7000), with a close-up lens giving a spatial resolution of ~5 μm. The camera outputs a voltage for each pixel and this voltage can be related to temperature through the materials emissivity. Due to the variety of materials used in the probe devices, some of which have poorly defined emissivity, a calibration measurement was performed. The device was allowed to reach thermal equilibrium at a series of temperatures and the voltage was recorded for each material at each temperature. This calibration allowed accurate measurement of the device temperature.

A conservative limit on the allowable temperature rise in brain tissue adjacent to the device was chosen to be 0.5° C, based on the work of Andersen *et al.* who conclude that brain function should not be perturbed by a temperature rise of less than 1°C [9]. However, for a single pulse, higher temperature rises were manageable due to heat spreading through the device and not into the brain. By using finite-element analysis, the heat spreading from an LED during the on-phase was modeled. In particular, the maximum rise of temperature recorded in brain tissue adjacent to the probe was estimated. The finite-element model is approximating a solution to the heat equation $(\partial u/\partial t) = (k/c_p\rho)\nabla^2 u$. Here, u is heat, t is time, k is thermal conductivity, c_p is specific heat, and ρ is density. The specific heat and thermal conductivity of brain tissue were assumed to be 3650 J kg$^{-1°}$ C^{-1} and 0.5 W m$^{-1°}$ C^{-1}, respectively [10]. While the specific heat and thermal conductivity of the probe were assumed to be dominated by the relatively thick sapphire substrate, 756 J kg$^{-1°}$ C^{-1} and 23 W m$^{-1°}$ C^{-1}, respectively.

Thermal modeling shows that heat is preferentially spread along the sapphire probe. This is due to the significantly higher thermal conductivity of sapphire compared to brain tissue. The large heat capacity of brain tissue also prevents its temperature rising significantly. From this modeling it was predicted that a 2°C rise in

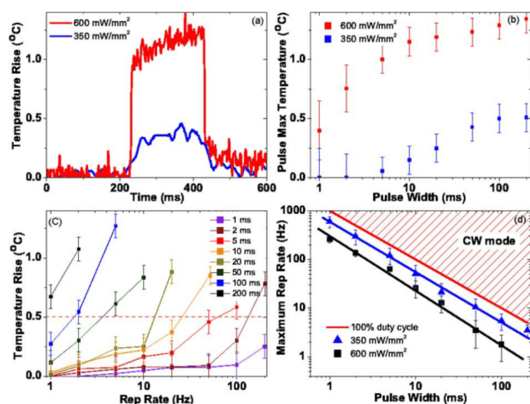

Fig. 3. (Color online) (a) Measured temperature profile for a single 200 ms pulse at 350 mW/mm^2 and 600 mW/mm^2. (b) Measured peak temperature of a single pulse for various pulse widths. (c) Measured average temperature rise versus repetition rate for an LED operating at 600 mW/mm^2 with various pulse widths. (d) The maximum repetition rate that the device can be operated at and not rise 0.5°C above ambient for two irradiances. Also shown is the maximum frequency for a given pulse. At lower irradiances the temperature rise was insufficient to be accurately recorded with the thermal camera.

temperature in the probe during a pulse, would lead to a 0.5°C increase in the neighboring brain tissue.

The measured temperature rise on the surface of the LED for a single 200 ms pulse is shown in Fig. 3(a) for two injection currents, 2 and 5 mA (350 mW/mm^2 and 600 mW/mm^2, respectively). A single pulse, even at these durations, does not result in the 2°C limit being exceeded. The maximum temperature from a single pulse of different durations is shown in Fig. 3(b).

Optogenetic applications require multiple pulses and heat will accumulate in the LED under these conditions. Figure 3(c) plots the average temperature rise at the surface of the LED (measured using the thermal camera) as a function of pulse repetition rate for multiple pulse widths driven at 5 mA. Heat accumulates from the multiple pulses and the probe and brain will eventually reach thermal equilibrium, it is the average temperature that is important. This average temperature should not increase by more than 0.5°C. A similar experiment was also preformed to measure the temperature within a 400 μm brain slice using a thermocouple. The temperature rise measured was within experimental error of that in Fig. 3(c). An example operating scenario would be to require 10 ms pulses with an irradiance of 2 mW/mm^2 at around 100 μm from the surface of the LED. This would require a current of 2 mA giving 350 mW/mm^2 at the LED surface [Fig. 2(d)] and places a 50 Hz limit on the pulse repetition rate [Fig. 3(d)]. It should be noted that 1 ms pulse widths at 200 Hz is at the upper extremes for neuronal firing and 10 ms pulses at a repetition rate of 20 Hz is typical in optogenetic studies.

In conclusion, the optical and thermal characteristics of a GaN on sapphire LED probe have been explored and found appropriate for the field of optogenetics. This allows spatiotemporal activation of optogenetically targeted neurons with multiple optical sites in a compact integrated system without the need for expensive laser sources and complex optics.

The authors were supported by SU2P pilot project and EPSRC grants EP/D078555/1 and EP/F05999X/1.

†Niall McAlinden and David Massoubre should be considered joint first authors.

References

1. K. Deisseroth, Nat. Methods **8**, 26 (2010).
2. X. Liu, S. Ramirez, P. T. Pang, C. B. Puryear, A. Govindarajan, K. Deisseroth, and S. Tonegawa, Nature **484**, 381 (2012).
3. Y. Hayashi, Y. Tagawa, S. Yawata, S. Nakanishi, and K. Funabiki, Eur. J. Neurosci. **36**, 2722 (2012).
4. E. Stark, T. Koos, and G. Buzsaki, J. Neurophysiol. **108**, 349 (2012).
5. A. N. Zorzos, J. Scholvin, E. S. Boyden, and C. G. Fonstad, Opt. Lett. **37**, 4841 (2012).
6. M. Im, I.-J. Cho, F. Wu, K. Wise, and E. Yoon, in *International Conference of the IEEE Engineering in Medicine and Biology Society* (IEEE, 2011), p. 5480.
7. J. G. Bernstein, X. Han, M. A. Henninger, E. Y. Ko, X. Qian, G. Talei Franzesi, J. P. McConnell, P. Stern, R. Desimone, and E. S. Boyden, Proc. SPIE **6854**, 68540H (2008).
8. H. X. Zhang, D. Massoubre, J. McKendry, Z. Gong, B. Guilhabert, C. Griffin, E. Gu, P. E. Jessop, J. M. Girkin, and M. D. Dawson, Opt. Express **16**, 9918 (2008).
9. P. Andersen and E. I. Moser, Hippocampus **5**, 491 (1995).
10. M. M. Elwassif, Q. Kong, M. Vazguez, and M. Bikson, J. Neural Eng. **3**, 306 (2006).

Sub-Micron Lithography Using InGaN Micro-LEDs: Mask-Free Fabrication of LED Arrays

Benoit Guilhabert, David Massoubre, Elliot Richardson, Jonathan J. D. McKendry, Gareth Valentine, Robert K. Henderson, Ian M. Watson, E. Gu, and Martin D. Dawson, *Fellow, IEEE*

***Abstract*— The fabrication of gallium-nitride (GaN)-based light-emitting diode (LED) arrays by a direct writing technique, itself using micron-sized LEDs (micro-LEDs), is reported. CMOS-driven ultraviolet GaN-based micro-LED arrays are used to pattern photoresist layers with feature sizes as small as 500 nm. Checkerboard-type square LED array devices are then fabricated using such photoresist patterns based on either single pixel or multipixel direct writing, and implemented as part of a completely mask-less process flow. These exemplar arrays are composed of either 450-nm-emitting 199 × 199 μm^2 pixels on a 200-μm pitch or 520-nm-emitting 21 × 18 μm^2 pixels on a 23-μm pitch. Fill factors of 99% and 71.5% are achieved with optical output power densities per pixel of 5 and 20 W/cm^2 at 90- and 6-mA dc-injected currents, respectively.**

***Index Terms*— Gallium nitride, micro light-emitting diodes (micro-LEDs), nanolithography, semiconductor device manufacture.**

I. Introduction

STANDARD manufacture of semiconductor devices requires multiple fabrication steps which involve patterning of photoresist (PR) by ultraviolet (UV) light exposure through a series of customized quartz-based photomasks. Consequently, each change in design requires the production of one or more new and expensive photomasks. As an alternative, mask-less fabrication approaches have attracted much attention as they offer flexibility and significant reduction of fabrication cost. Several mask-less methods have been developed including laser direct writing, 2-photon writing, interference lithography and inkjet printing, and these techniques have already been used for the fabrication of optoelectronic devices [1]–[3]. III-nitride semiconductor technology can already provide efficient LEDs with peak emission wavelengths around 365 nm and 405 nm, corresponding respectively to the i-line and h-line emissions from mercury discharge lamps used in mature photolithography. However, related III-nitride LEDs are also being developed offering emission into the deep UV, compatible with the majority of photo-acid generators and more advanced optical lithography [4]. In addition, III-nitride LEDs offer many advantages compared to mercury lamps, including compactness, low power consumption and no content of toxic material. Furthermore, the output power of these LEDs and their emission mode (pulsed and dc) can be easily changed via an integrated electronic driver circuit. Several proof-of-concept demonstrations of micro-patterning by LED direct writing have already been made using either conventional broad-area devices or micro-LEDs (we consider an LED as "micro" when one of its dimensions is below 100 μm) [5]–[7]. Feature sizes as small as 20 μm were obtained by using proximity exposure with micro-LEDs, while similar feature sizes have also been obtained using a broad-area LED source coupled to a microscope objective [5], [6]. The use of micro-LEDs brings the primary advantages of offering a large density of emitters on a small-scale chip, and a higher power density per pixel than broad-area LEDs [8].

We report here on the use of 8 × 8 micro-LED arrays with pixel sizes as small as 14 μm-diameter in an imaging optical setup (similar to the setup in ref. [9] but with a 10:1 demagnification) to pattern PR with features down to 500 nm-width in order to process GaN-based LED heterostructures [9], [10]. First, a single pixel was used to pattern a sacrificial PR mask for a "checkerboard-type" array with individually addressable LEDs emitting at 450 nm [11]. The checkerboard device was designed with a targeted 1 μm gap between adjacent pixels, resulting in a 99% filling factor arrays in a suitable configuration for subsequent flip-chip bonding to custom complementary metal-oxide-semiconductor (CMOS) [10], [12]. Typical measured optical output powers here were 2 mW (5 W/cm^2) per pixel at a driving current of 90 mA. Parallel direct writing is then implemented using 2 micro-pixels each of 24 μm diameter to create a 32 × 32 checkerboard design emitting at 520 nm. This had 21 × 18 μm^2 pixels on a 23 μm pitch, each delivering 77 μW (20 W/cm^2) at 6 mA injection current. These arrays were fabricated in a suitable

Manuscript received August 17, 2012; revised October 11, 2012; accepted October 11, 2012. Date of publication October 18, 2012; date of current version November 28, 2012. This work was supported in part by the Engineering and Physical Sciences Research Council under Grant EP/D078555/1 and Grant EP/F05999X/1. B. Guilhabert and D. Massoubre contributed equally to this work.

B. Guilhabert, D. Massoubre, E. Richardson, J. J. D. McKendry, I. M. Watson, E. Gu, and M. D. Dawson are with the Institute of Photonics, University of Strathclyde, Glasgow G4 0NW, U.K. (e-mail: benoit.guilhabert@strath.ac.uk; david.massoubre@strath.ac.uk; elliot.richardson@strath.ac.uk; jonathan.mckendry@strath.ac.uk; i.m.watson@strath.ac.uk; erdan.gu@strath.ac.uk; m.dawson@strath.ac.uk).

G. Valentine was with the Institute of Photonics, Glasgow G1 1XN, U.K. He is now with mLED Ltd., Glasgow G1 1XN, U.K. (e-mail: gareth.valentine@strath.ac.uk).

R. K. Henderson is with the Joint Research Institute for Integrated Systems, Institute for Micro and Nano Systems, School of Engineering, The University of Edinburgh, Edinburgh EH93JL, U.K. (e-mail: robert.henderson@ed.ac.uk).

Color versions of one or more of the figures in this letter are available online at http://ieeexplore.ieee.org.

Digital Object Identifier 10.1109/LPT.2012.2225612

1041–1135/$31.00 © 2012 IEEE

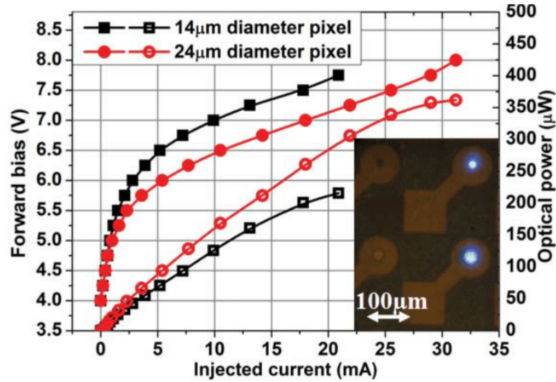

Fig. 1. Voltage and optical output power versus injected current of two representative pixels of 14 and 24 μm in diameter emitting at 370 nm. Optical micrograph of representative pixels of 14- and 24-μm diameters individually addressed from the 8 × 8 micro-LED arrays.

configuration for applications including lab-on-chip sensors, micro-displays, time-resolved spectroscopy and optoelectronic tweezing [13], [12], and provide demanding demonstrations of the capabilities of micro-LED direct writing in the rapid and accurate fabrication of active optoelectronic devices.

II. Micro-LED Mask-Free Lithography

This letter used micro-LED arrays emitting at a wavelength of 370 nm, flip-chip bonded onto a CMOS silicon backplane [10], [12]. The micro-LED device is an 8 × 8 array of micro-disk pixels on a 200 μm pitch with diameters progressing from 84 μm to 14 μm in 10 μm steps. The pixels are arranged in rows with fixed pixel diameters. All the pixels share a common negative electrode (n-contact) and are individually addressed through their respective positive contact (p-contact). Each pixel is provided with a 92 × 92 μm^2 separate bonding pad, connected to the pixel with a metal track to complete the positive connection (inset Fig. 1). This method of off-pixel bonding facilitates contacting of small-sized pixels to enable the highest direct writing resolution. CMOS driving offers the capability of individual dc and pulsed operation of the micro-LEDs down to few hundreds of picoseconds through a computer-controlled interface as well as projection of programmable patterns [10]. The forward bias voltage versus current of representative CMOS-bonded 14 μm and 24 μm-diameter pixels is shown in Fig. 1. Turn-on voltages estimated with the tangent method are about 6 V and 5.5 V respectively, and currents of 20 mA are reached for bias voltages of 7.6 V and 7.1 V, respectively. The CMOS chip design allows a maximum forward bias of 8 V. Typical optical output powers were measured with a large-area Si photodetector placed in near contact above the device, so as to collect all of the front-emitted optical power. Typical optical output powers as a function of injected current are plotted in Fig. 1. At 20 mA, optical power of 210 μW (14 μm device) and 275 μW (24 μm device) were measured.

In the following direct writing experiments, micro-LEDs are imaged using an optical setup as in [9], using a 4X

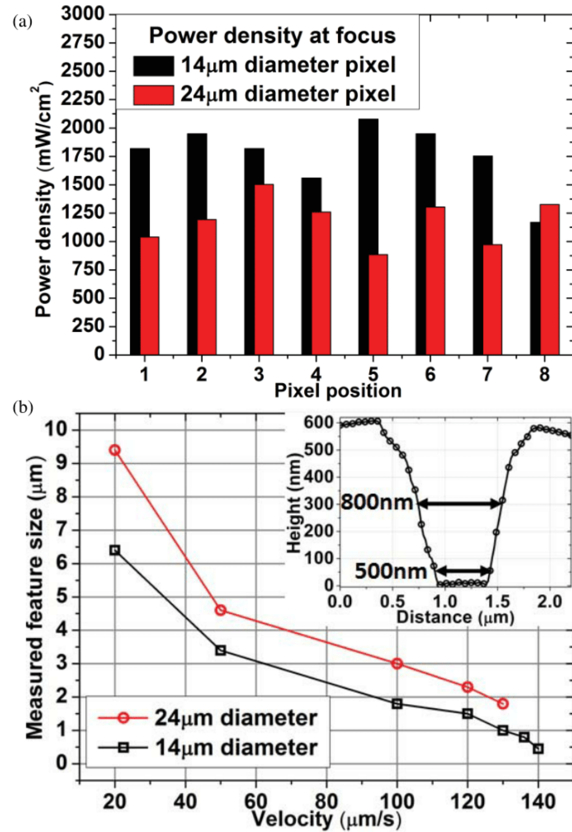

Fig. 2. (a) Optical power densities evaluated at focus for pixels diameter of 14 and 24 μm (1.4- and 2.4-μm diameter at focus, respectively) for a drive voltage of 5 V. (b) S1805 PR feature sizes (trench bottom) exposed by representative pixels of each diameter upon increased stages velocity. Inset: AFM scan profile of a S1805 trench written at 140 $\mu m/s^{-1}$.

and 40X microscope objectives for collection and projection, respectively, and demagnifying the pixels by a factor 10. The sample covered with PR is placed on an X-Y translation stage and positioned at the focus using the high-resolution z-stage supporting the 40X projection microscope objective [9]. The writing process itself is entirely automated through a computer interface. For the first demonstration, single micro-LEDs were used to evaluate the writing performance of the setup. The CMOS was configured to drive in dc mode at a voltage of 5 V and the power densities were measured at focus in this configuration for all the pixels of diameters 14 μm and 24 μm [Fig. 2(a)]. The projected spot sizes were about 2.4 μm and 1.4 μm at focus, respectively, as estimated from an intensity profile analysis from a calibrated image taken by a CCD camera. Average optical power densities of 1.7 W/cm^2 and 1.2 W/cm^2 with variances of 0.3 W/cm^2 and 0.2 W/cm^2 are calculated from these sets of results. The velocities of the X-Y stages are controlled to deliver the appropriate exposure dose and to adjust the feature size written into the PR. Typical writing speeds range from 20 μm/s to 140 μm/s leading to average exposure doses at focus of

280 mJ/cm^2 down to 40 mJ/cm^2 for the 14 μm-diameter pixel and from 360 mJ/cm^2 to 51 mJ/cm^2 for the 24 μm-diameter [9]. Feature sizes written at different velocities by both pixels were investigated by atomic force microscopy (AFM) over an area of 5 × 5 μm^2 of the patterned region. Trenches were written in resist S1805 (600 nm thick) which requires an exposure dose at 370 nm of 40 mJ/cm^2 (value from manufacturer's datasheet). Fig. 2(b) summarizes the measured trench bottom widths for these writing experiments ranging from 9 μm down to 2 μm and 6 μm down to 0.5 μm for the 24 μm and 14 μm-diameter pixels, respectively. The inset of Fig. 2 shows a 500 nm base-width trench realized with the 14 μm-diameter pixel at a writing speed of 140 μm/s. The profile shows a significant non-verticality of the trench sidewalls, resulting from the intrinsic exposure profile of the PR film, but not posing limitations for the microfabrication applications envisaged.

III. Device Fabrication and Characterization

First, a checkerboard-type LED design with an 8 × 8 array of 200 μm-pitch, 199 × 199 μm^2 LEDs was chosen as a demonstrator device, as each pixel can be easily individually wire bonded. Also it is directly compatible with the CMOS-backplane technology which has been developed to bond and drive our custom LED array devices [10]. The checkerboard GaN-based LED array was fabricated as in [8]. A 600 nm-thick PR film was spin-coated and soft-baked according to the vendor's datasheet in preparation for the micro-LED pattern writing. The mask-less patterning to define the LED mesa was performed at a linear translation speed of 140 μm/s using a single 14 μm pixel under 10X demagnification. The velocity was then reduced to 10 μm/s in order to write a large frame around the emission area for access to the n-doped GaN [see Fig. 3(a)]. The PR was then developed using a standard solution providing minimum features of about 560 nm in width on average, forming the 8 × 8 array and a surrounding frame of about 35 μm width around the array. This pattern was then transferred to the SiO_2 layer by reactive ion etching and a multi-step process combining wet and inductively coupled plasma etching was used to etch the metal stack and the GaN-based layers down to the n-GaN layer, resulting in an 8 × 8 n-shared mesa array. Finally the residual SiO_2 layer was stripped off the sample by wet etching. An optical micrograph of the checkerboard device's p-contact side after processing is shown in Fig. 3(a), left. Each trench is well defined with an average width close to the targeted value of 1 μm [Fig. 3(a), right]. The final gaps between pixels are larger than the PR feature defined by the mask-less lithography (560 nm) owing to the finite isotropic component of the various dry etch steps acting on the sidewalls.

An inkjet printing step of silver (Ag) nanoparticles defined metal tracks to connect the shared n-GaN in order to demonstrate a full mask-less fabrication process. The Ag nanoparticles (Silver-jet DGP, 40% w/w) were printed with a Dimatix DMP-2800 system as in [14]. Each pixel was finally individually wire bonded to a printed circuit board for characterization purposes. The inset of Fig. 3(b) shows an optical micrograph of the checkerboard-LED array with representative pixels turned on, demonstrating the individually-addressable capabilities of the device. The electrical and optical performance of the array was assessed. Typical injection current versus forward bias voltage (I-V) and optical output power versus injection current (L-I) characteristics of a representative pixel are shown in Fig. 3(b). The directed optical output was measured from the back side of the device (through the transparent sapphire substrate) using a power meter and a calibrated Si photodetector placed in close proximity. The device shows good electrical and optical performance with a maximum output optical power of 2 mW (5 W/cm^2) at an injected current of 90 mA (750 μW – 2 W/cm^2 at 20 mA injected current). A typical voltage of 4.3 V at 20 mA is measured, which is somewhat higher than a typical GaN-based LED (usually around 3 V). This is likely due to the lower conductivity of the nanoparticle Ag ink and the higher potential barrier at the Ag/n-GaN interface compared with a more standard n-metal contact such as Ti/Au, but is illustrative of the potential for a fully mask-less LED fabrication process flow.

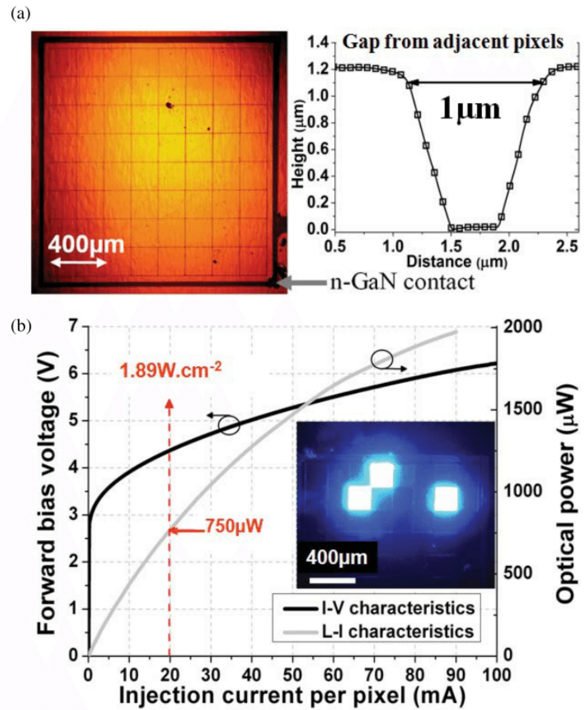

Fig. 3. (a) Optical micrograph of the entire 450-nm emitting 8 × 8 array (left) and AFM scan profile of a representative gap between adjacent pixels of the array (right). (b) $I - V$ and $L - I$ characteristics of a typical pixel of the 8 × 8 array with, inset, an optical micrograph of several pixels individually addressed.

The parallel writing capability of our setup was then demonstrated with 2 adjacent 24 μm-diameter pixels [namely pixels 7 and 8 from Fig. 2(a)] driven at the same forward bias voltage, 7.5 V (25.5 mA typical dc injected current). The pixels were

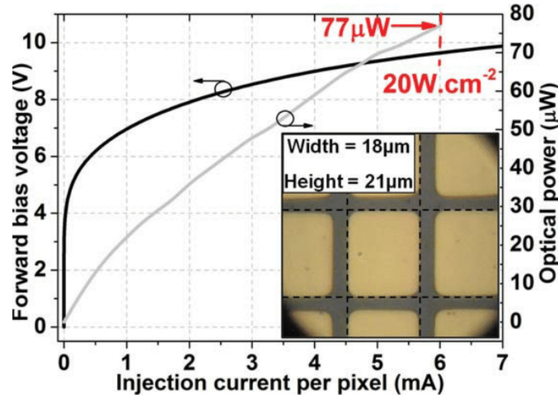

Fig. 4. $I-V$ and $L-I$ characteristics of a typical pixel of 520-nm-emitting 32 × 32 elements array. Inset: optical micrograph centered on a pixel from the array.

both placed within the field of view of the collection microscope objective so that their emission was collected altogether. In this configuration and driven individually, the two pixels deliver a different optical power at focus of 0.163 μW (3.6 W/cm^2) and 0.17 μW (3.75 W/cm^2), respectively, due to variation in pixel-to-pixel performance as shown in Fig. 2(a). However, due to the characteristics of the CMOS design, the current flowing through the chip when several LEDs are driven simultaneously induces a voltage drop at the LED electrodes due to the ground bounce effect [15]. Consequently, when driven simultaneously, the optical power projected is not the sum of the individual optical powers, instead a total optical power at focus of 0.131 μW (2.9 W/cm^2) is estimated per driven pixel. The checkerboard-design was again chosen to illustrate the lithographic capability in this case for high density micro-LED arrays emitting at 520 nm. An array of 32 × 32 elements with a 23-μm pitch was thus coded for a 2 pixel writing experiment. In the vertical direction (direction according to inset of Fig. 4.) each trench is exposed using a single pixel while, in the horizontal direction, both pixels were used consecutively. The writing speed was fixed to 100 μm/s in vertical giving a typical exposure dose of 69 mJ/cm^2, and 200 μm/s in the horizontal direction to take into account the overlapping exposure path from the two pixels. After PR patterning, the same etching process was applied as described previously resulting in an array of individually-addressable rectangular pixels. In this case the resulting fill-factor is reduced to 71.5% with 21 × 18 μm^2 pixels as shown in the optical micrograph inset of Fig. 4. Probes were used here to electrically and optically characterize the device. Fig. 4 summarizes the typical I-V and L-I curves for a pixel of the array. The pixel delivers an optical power of 77 μW at an injection current of 6 mA, giving an optical power density of 20 W/cm^2 with current density of 1.6 kA/cm^2.

IV. Conclusion

A custom-made 370-nm emitting micro-LED array bonded on CMOS backplane was used as a mask-less photolithography tool to fabricate complex and tailored optoelectronic devices through the use of an optical demagnifying setup and computer control. This direct writing technique was first used to pattern PR layers giving features as narrow as 500 nm at 140 μm/s writing velocities. In combination with wet and dry etching and inkjet printing, custom designed 450 nm emitting, 99% fill-factor, 8 × 8 broad-LED array and 520 nm-emitting 32 × 32 micro-LED array were fabricated by single and two-pixels parallel writing respectively. Typical optical output powers emitted by a single element were measured to be up to 5 W/cm^2 and 20 mW/cm^2, respectively, at injected current of 90 mA and 6 mA. These results demonstrate the advantages of micro-LED mask-less lithography, including re-configurable written patterns with sub-micron feature sizes and multi-beam parallel writing and implementation as part of a mask-less process flow, to address the easy fabrication of complex optoelectronic and photonic devices such as, but not limited to, GaN-based LED arrays.

References

[1] C. Rensch, S. Hell, M. Schickfus, and S. Hunklinger, "Laser scanner for direct writing lithography," *Appl. Opt.*, vol. 28, no. 17, pp. 3754–3758, 1989.

[2] J. Serbin, *et al.*, "Femtosecond laser-induced two-photon polymerization of inorganic organic hybrid materials for applications in photonics," *Opt. Lett.*, vol. 28, no. 5, pp. 301–303, 2003.

[3] I. Byun and J. Kim, "Cost-effective laser interference lithography using a 405 nm AlInGaN semiconductor laser," *J. Micromech. Microeng.*, vol. 20, no. 5, pp. 055024-1–055024-6, 2010.

[4] M. Asif-Kahn, K. Balakrishnan, and T. Katona, "Ultraviolet light-emitting diodes based on group three nitrides," *Nature Photon.*, vol. 2, pp. 77–84, Feb. 2008.

[5] C.-W. Jeon, E. Gu, and M. D. Dawson, "Mask-free photolithographic exposure using a matrix-addressable micropixellated AlInGaN ultraviolet light-emitting diode," *Appl. Phys. Lett.*, vol. 86, no. 22, pp. 221105-1–221105-3, 2005.

[6] R. M. Guijt and M. C. Breadmore, "Maskless photolithography using UV LEDs," *Lab-Chip*, vol. 8, pp. 1402–1404, May 2008.

[7] S. Suzuk and Y. Matsumoto, "Lithography with UV LED array for curved surface structure," *Microsyst. Technol.*, vol. 14, nos. 9–11, pp. 1291–1297, 2008

[8] H. X. Zhang, *et al.*, "Individually-addressable flip-chip AlInGaN micropixelated light emitting diode arrays with high continuous and nanosecond output power," *Opt. Express*, vol. 16, no. 13, pp. 9918–9926, 2008.

[9] D. Elfstrom, *et al.*, "Mask-less ultraviolet photolithography based on CMOS-driven micro-pixel light emitting diodes," *Opt. Express*, vol. 17, no. 26, pp. 23522–23529, 2009.

[10] J. J. D. McKendry, *et al.*, "Individually addressable AlInGaN micro-LED arrays with CMOS control and subnanosecond output pulses," *IEEE Photon. Technol. Lett.*, vol. 21, no. 12, pp. 811–813, Jun. 15, 2009.

[11] Z. J. Liu, K. M. Wong, C. W. Keung, C. W. Tang, and K. M. Lau, "Monolithic LED microdisplay on active matrix substrate using flip-chip technology," *IEEE J. Sel. Topics Quantum Electron.*, vol. 15, no. 4, pp. 1298–1302, Jul./Aug. 2009.

[12] A. Zarowna-Dabrowska, *et al.*, "Miniaturized optoelectronic tweezers controlled by GaN micro-pixel light emitting diode arrays," *Opt. Express*, vol. 19, no. 3, pp. 2720–2728, 2011.

[13] B. R. Rae, *et al.*, "CMOS driven micro-pixel LEDs integrated with single photon avalanche diodes for time resolved fluorescence measurements," *J. Phys. D, Appl. Phys.*, vol. 41, no. 9, pp. 094011-1–094011-6, 2008.

[14] M. Wu, *et al.*, "Ink-jet printed silver nanoparticles electrodes on GaN-based micro-structured light-emitting diodes," *Appl. Phys. A*, vol. 104, no. 4, pp. 1003–1009, 2011.

[15] R. J. Baker, *CMOS, Circuit Design, Layout and Simulation*, 2nd ed. Piscataway, NJ: IEEE Press, 2005, pp. 72–73.

Appl Phys A (2011) 104:1003–1009
DOI 10.1007/s00339-011-6506-x

Applied Physics A
Materials Science & Processing

RAPID COMMUNICATION

Inkjet-printed silver nanoparticle electrodes on GaN-based micro-structured light-emitting diodes

Min Wu · Zheng Gong · David Massoubre · Yanfeng Zhang · Elliot Richardson · Erdan Gu · Martin D. Dawson

Received: 14 March 2011 / Accepted: 8 June 2011 / Published online: 1 July 2011
© Springer-Verlag 2011

Abstract Silver nanoparticle ink has been inkjet printed onto inorganic GaN-based micro-structured light-emitting diodes to form narrow conductive tracks with a width down to ~30 µm and a resistivity value approximating that of a conventional sputtered metal (Ti/Au) track. These silver tracks serve as 'active' electrodes with comparable performance to the deposited metal tracks, demonstrating a new, simple and cost-effective route for the electrode fabrication of GaN-based LED devices.

1 Introduction

Traditional electrode fabrication in electronic and optoelectronic devices requires high-vacuum and complicated photolithographic procedures, which results in high production cost and low production efficiency. During the last decade, the inkjet-printing technique, especially in the form of drop-on-demand (DOD) inkjet printing, has been intensively investigated as this 'add-on' direct writing method can greatly simplify the process, reducing the material cost and contamination. The DOD system has also extended its applications as a rapid manufacturing tool for electronic devices such as thin-film transistors [1, 2], polymer capacitors [3], radio frequency identification (RFID) tags [4] and solar cells [5].

Common conductive inks used in inkjet-printed electronic devices include metallic nanoparticle suspensions and conductive polymers. The former are becoming more popular because of better conductivity performance. For instance, silver nanoparticle ink has been studied extensively for printed electronics in fabricating interconnections and solders [6], electrodes on polymeric substrates [7], circuit boards [8] and solar cells [9]. In previous work, silver nanoparticle ink printed electrodes have been studied mostly on organic substrates, due to advantages in conductivity and flexibility compared to conventional electrodes such as indium tin oxide (ITO) for the organic devices [10]. However, the electrical properties of these electrodes were barely studied or assessed for current injection during the device operation. Furthermore, to the best of our knowledge, printed conductive micro-structures have not been applied to inorganic optoelectronic micro-devices such as GaN-based micro-light-emitting diodes (micro-LEDs).

The specific GaN LED devices we use here as demonstrators of the capability of electrode printing are in the form of micro-pixellated arrays. These GaN 'micro-LEDs' have found numerous applications in such areas as micro-displays, mask-free photolithography, highly parallel on-chip fluorescence detection and 'optogenetic' neuron stimulation [11]. Unlike 'conventional chip' broad-area GaN LEDs (devices of several hundreds of microns dimension), micro-LEDs have typical pixel diameters of ten to a few tens of microns. Given the small size, specially designed metal tracks of high conductivity are generally required for externally addressing the respective emitters, in arrays that can contain up to a few thousand pixels. These metal tracks are commonly formed by optical lithography and subsequent metal deposition via sputtering or evaporation, which involves complicated procedures and relatively high cost.

In this work, we demonstrate a simpler route to integrate micro-electrode tracks onto the inorganic GaN-based micro-LEDs via inkjet printing. The electrical performance of these printed micro-tracks has been characterized in detail and compared with the traditional metal tracks (Ti/Au) which are fabricated by photolithography. By using a 21.5-

M. Wu · Z. Gong · D. Massoubre · Y. Zhang · E. Richardson · E. Gu (✉) · M.D. Dawson
Institute of Photonics, University of Strathclyde, SUPA, Glasgow G4 0NW, UK
e-mail: erdan.gu@strath.ac.uk

μm-diameter inkjet nozzle aperture, the printed silver micro-tracks on a reference silicon substrate have a width down to 31 μm, which is much narrower than those (>100 μm) reported previously, and a resistivity value (1.54 μΩ cm) comparable with Ti/Au tracks (1.21 μΩ cm) deposited on the same substrate. We further demonstrate that these inkjet-printed silver tracks are capable of performing as 'active' electrodes for current injection in GaN-based LED devices. This method can greatly simplify the device fabrication and packaging processes without compromising the device performance.

2 Experimental methods

The inkjet-printing process was carried out by a commercial inkjet printer (Dimatix DMP-2800). This is equipped with a piezo-driven cartridge delivering 10-pL droplets from a 21.5-μm-diameter nozzle, a fiducial camera for alignment and a flat platen which can be heated to 60°C. The drop spacing for printing the silver ink on different substrates was optimized at 35 μm for glass, 30 μm for silicon and 50 μm for GaN. The trigger electrical pulse length was 11.52 μs and the frequency was 5 kHz, while the drive voltage applied on the nozzle was adjusted to keep the droplet flying speed constant at ~4 m/s for the best performance. The platen was heated to 60°C during the printing process to stimulate the solvent evaporation and minimize the spreading of the printed track. All the silver tracks in this work were printed as a single layer on the substrate.

The silver nanoparticle ink used in this work was a commercial formulation (Advanced Nano Products Co., Ltd., Korea). The silver nanoparticles are dispersed in a polar solvent triethylene glycol monoethyl ether (TGME) with a solid metal content of 35.4 wt%. The average size of the silver nanoparticles was ~7 nm, which is sufficiently small compared to the nozzle diameter to avoid clogging. The viscosity and the surface tension of the silver ink are 15.5 cP and 37.1 mN/m, respectively, compatible with the requirements for printing. The sintering temperature for the ink is comparatively low, at 200°C according to the supplier.

The devices used in this work were GaN-based flip-chip (i.e. back-contacted, with light extraction through the polished sapphire epitaxial substrate) and what we term 'planar' micro-LEDs (see below). The fabrication and characterization of the flip-chip micro-LEDs have been reported previously [12]. Figure 1a shows the schematic cross-sectional structure of a flip-chip micro-LED pixel and the inkjet-printing process for connecting the LED pixels for matrix addressing. The LED pixel was defined by plasma etching and the pixel diameter and pitch of the flip-chip micro-LED arrays are 30 μm and 50 μm, respectively. Each pixel has a 10-nm-thick Ni/Au layer for current spreading and a 250-nm

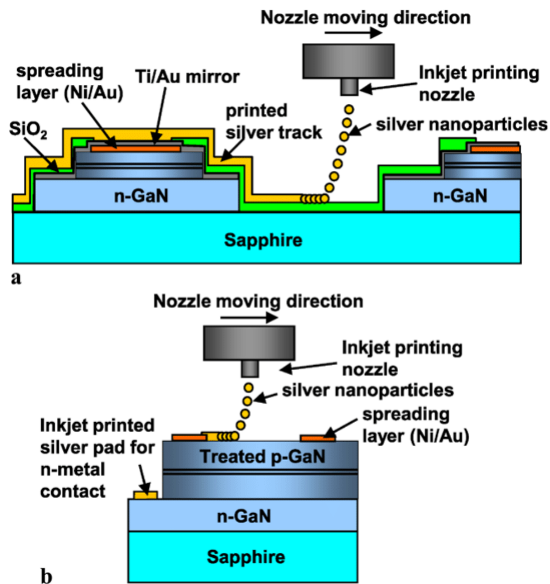

Fig. 1 Schematic printing process of the silver nanoparticle ink on the flip-chip (**a**) and the planar (**b**) micro-LED pixels, respectively

Ti/Au layer serving as a mirror electrical contact. The SiO_2 insulation layer on the LED array prevents the pixels from electrical cross-talk. The silver nanoparticle ink was printed directly on the top of each LED pixel and SiO_2 insulation layer to form conductive micro-tracks to connect the pixels.

For the planar micro-LEDs, on the other hand, in which light-emitting micro-pixels are defined by selective area electrical passivation using plasma treatment [13], the pixels are addressed by a Ni/Au current spreading pattern formed on the p-type GaN. Lacking the requirement for mesa etching (except for the n-contact) and dielectric deposition, this approach greatly simplifies the device fabrication process. A cross-sectional schematic of the planar LEDs and the associated printing process of silver nanoparticles is shown in Fig. 1b. In this case the printed electrode was formed on the treated p-type GaN surface rather than on a SiO_2 layer.

The printed silver track should have a width comparable to the pixel size and pitch of the micro-LEDs so as to interconnect a single row or column of the pixels. Both theoretical modelling and experimental results indicate that the width of inkjet-printed tracks decreases when the contact angle of printed droplets increases [14, 15]. Thus, in order to increase the contact angle for fabricating narrow silver nanoparticle tracks, we vapor deposited 1H,1H,2H,2H-perfluorooctyldimethylchlorosilane (PFODCS) (ABCR, Karlsruhe, Germany) [16] on glass, silicon and treated p-GaN substrates at room temperature. It was observed that the contact angle of the silver nanoparticle ink on these substrates was altered. The printed silver

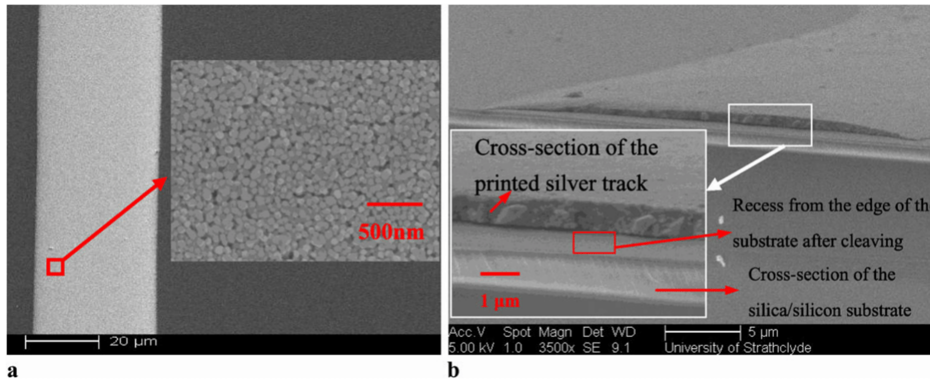

Fig. 2 Oblique SEM images of (**a**) plane-view of the inkjet-printed silver track on silicon substrate and close-by SEM image of the annealed silver nanoparticles in the track; (**b**) cross-section of the inkjet-printed silver track on silica/silicon substrate and close-by SEM image of the annealed silver nanoparticles in the track

tracks were afterwards sintered on a hotplate under ambient air. The electrical resistivity values of the printed silver tracks on different substrates after the sintering process were calculated from the equation below:

$$\rho = R\frac{S}{l}, \tag{1}$$

where ρ is the resistivity of the printed silver track; R is the track's resistance, which was extracted from the measured current–voltage curve by using a two-point method; S is the cross-sectional area of the printed silver track obtained by numerical integration of a measured profile by stylus profilometry; and l is the length of the printed silver track. In order to make a comparison between the printed silver track and a 'conventional' sputtered metal (Ti/Au) track which is normally used for connecting nitride-based LED pixels, the electrical resistance and resistivity values of a sputtered metal (Ti/Au) track on a silicon substrate were also measured and calculated from (1).

3 Results and discussion

3.1 The inkjet-printed silver tracks

Figure 2a is a scanning electron microscopy (SEM) image of an inkjet-printed silver track on a silicon substrate after sintering and the inset is a close-up SEM image showing the sintered silver nanoparticles constituting the track. The cross-sectional SEM image of the silver track printed on a silica/silicon substrate (a SiO_2 layer on top of a silicon substrate, same as the flip-chip micro-LED surface) is shown in Fig. 2b. It is observed that both the printed silver tracks are well defined spatially and have smooth surfaces and edges due to the substrate surface treatment. It is also shown that

Table 1 Contact angle after surface treatment, track width and resistivity values of the inkjet-printed silver track on glass, silicon and treated p-gallium nitride (GaN) substrate after 60-min sintering at 200°C, respectively

Substrate	Contact angle (°)	Line width (μm)	Resistivity (μΩ-cm)
Glass	∼44	∼33	∼1.1
Silicon	∼35	∼31	∼1.54
Treated p-GaN	∼31	∼54	∼3.76

the silver nanoparticles have been sintered together after the sintering process. Due to the size effect, the silver nanoparticles require a lower temperature to contact each other compared to the bulk material [17]. Under proper sintering temperature and duration, the dispersant (TGME in this case) in the suspension is removed, allowing the nanoparticles to contact each other and consequently reducing the electrical resistivity [18]. Electrical resistivity is a significant factor affecting the performance of the conductive track. Hence, the resistivity of the inkjet-printed silver tracks on different substrates was studied and compared with the resistivity value of sputtered metal (Ti/Au) reference tracks on a silicon substrate (∼1.21 μΩ cm). Table 1 lists the measured contact angle, track width and the calculated resistivity values of the inkjet-printed silver tracks on glass, silicon and treated p-GaN substrates, respectively, after sintering at 200°C for 60 min. In this work, all the silver tracks were sintered at 200°C for 60 min in order to obtain sufficient conductivity. The fact that well-defined silver micro-tracks can be successfully printed on treated p-GaN surfaces demonstrates the possibility of applying this technique to GaN-based optoelectronic devices. From the measured resistance, the resistivity of the silver tracks printed on the treated p-GaN surfaces is calculated to be 3.76 μΩ cm, which is not much

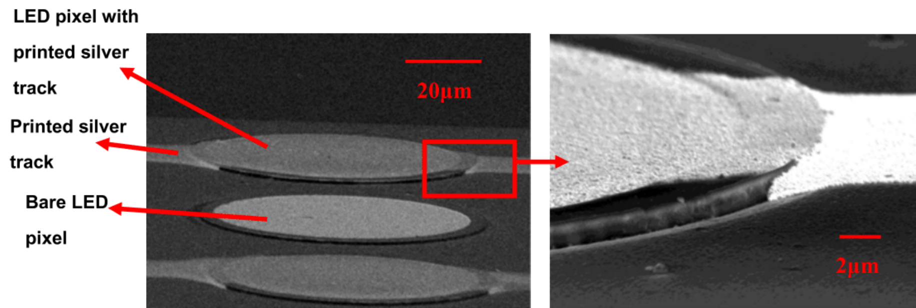

Fig. 3 Oblique SEM images of the inkjet-printed silver track on the flip-chip micro-LEDs

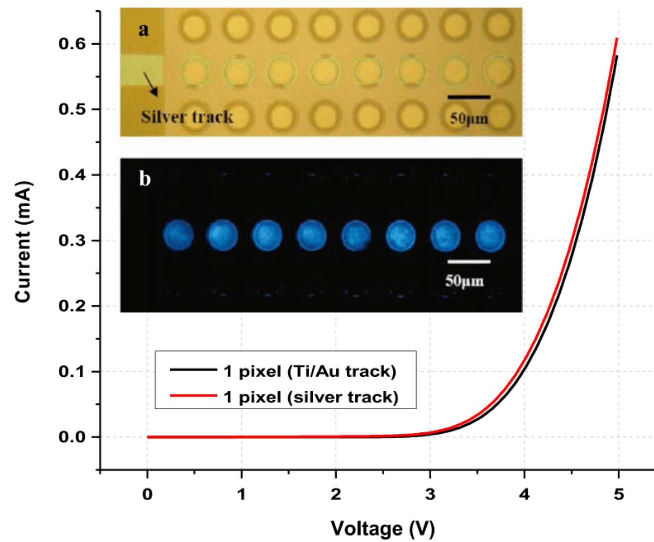

Fig. 4 Current–voltage curve comparison of the single pixel connected by the sputtered Ti/Au track and the inkjet-printed silver track on the flip-chip micro-LEDs; *insets* are optical microscope images of eight pixels interconnected by inkjet-printed silver track: (**a**) under normal white light illumination; (**b**) turned-on pixels

higher than that of the metal (Ti/Au) track. The following work shows that the printed silver tracks can serve well as electrodes for operating GaN-based LED devices. Furthermore, the practical cost of the silver metal track is much lower, since only a few droplets of the silver ink are required.

3.2 Applications of the inkjet-printed silver tracks on micro-LEDs

The inkjet-printed silver tracks were applied first to the flip-chip micro-LEDs. Figure 3 shows the SEM images of the printed silver tracks running over a representative flip-chip micro-LED pixel. The area between the pixels is covered with a deposited SiO_2 insulation layer, whose surface properties are similar to a glass substrate. Thus, the contact angle of the printed ink can be altered by PFODCS treatment [16]. However, there was no obvious contact angle alteration observed on the Au surface after the PFODCS treatment due to the different surface properties. It can be seen that the printed silver track has a smooth surface and a clean edge, while it spreads uniformly at the top of the pixel as the PFODCS barely has any effect on the Au surface. Besides, unlike the usual printed features on the flat surface of devices, here we demonstrate that it is possible to print the silver ink on uneven ridged surfaces. The pixel height in the flip-chip micro-LEDs is about 1 µm, which is determined by the plasma etching. Due to this height difference, the conventional thin metal track fabricated by metal deposition may break at the pixel side wall, resulting in pixel disconnection. The SEM image in Fig. 3 shows that the pixel side wall is sufficiently covered by the printed silver nanoparticles to ensure good electrical connection.

The inset (a) of Fig. 4 shows, as an example, that eight LED pixels are interconnected by the printed silver track. The turned-on device image (Fig. 4, inset (b)) demonstrates that the LED pixels have been electrically connected and the light emission from pixel to pixel is uniform. In order to characterize the performance of the printed silver nanopar-

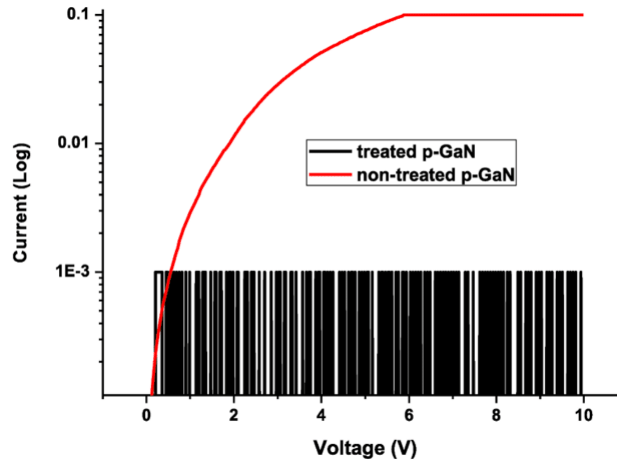

Fig. 6 Current leakage test of the printed silver track on plasma-treated and non-treated p-type GaN

ticle tracks, we have connected one LED pixel by a Ti/Au track formed by sputtering deposition and another pixel with a printed silver nanoparticle track on the same device. The measured current–voltage (I–V) curves of these LED pixels are shown in Fig. 4. It is clear that the I–V curves of the LED pixels connected by the silver track and the Ti/Au track are almost identical, indicating that the electrical performance of the printed silver track is comparable to the Ti/Au track fabricated by the conventional metal deposition and photolithography process. These results also confirm that the performance of the LED pixels is not influenced by the inkjet-printing and the sintering processes. For device applications, it is also crucial to study the maximum current the printed silver track can bear, as an overloaded current would break down the printed micro-tracks. We have connected nine pixels by a single printed silver track and our measurement shows that the silver track could sustain 100-mA current without breaking down. The corresponding current density is approximately 2×10^6 A/cm^2, which is much larger than the usual operating current density required for the nitride-based LED devices [12]. Thus, the inkjet-printed silver track is fully applicable as the electrodes for GaN LED devices.

The printed silver track approach has also been applied to the planar LED device for the replacement of the Ti/Au metal track and contact pads, further simplifying the fabrication process of the planar LED device. By printing the silver nanoparticle conductive ink, we fabricated not only conductive tracks for connecting the LED pixels but also conductive pads for wire bonding. Figure 5 is an optical image of a turned-on planar micro-LED pixel connected to a printed silver track. The printed silver pad was at the end of the track and, as shown in the image, metal wires have been successfully bonded to these pads. The key process in the fabrication of the planar device is the plasma treatment

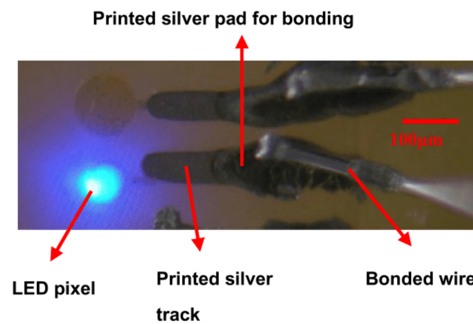

Fig. 5 Optical microscope image of a turned-on planar micro-LED pixel connected by a wire-bonded silver pad

of the top p-GaN layer, which passivates the p-GaN surface and thus prevents the current leakage from the p-GaN–metal interface. In order to demonstrate that the printed silver track and the sintering process do not compromise this electrical passivation of the treated p-GaN surface, silver tracks and pads were inkjet printed on both the plasma-treated and non-treated p-GaN surfaces and the n-GaN surface. The I–V curves were measured when the voltage was applied upon the p-GaN and n-GaN surfaces. Figure 6 shows that the I–V curves of the non-plasma-treated p-GaN surface present a typical diode characteristic, while the current is extremely low (at the measurement limit of the parameter analyzer) on the treated p-GaN surface.

In the planar device, circular LED pixels with different sizes varying from 2 μm to 100 μm in diameter have been fabricated. As the top Ni/Au current spreading layer which defines the planar LED pixel is very thin (10 nm), it is difficult to align the printed silver track with the small ($<$20 μm) LED pixels. By using the fiducial camera in the inkjet printer, however, we managed to print the silver track and align it successfully with the 20-μm and larger LED pix-

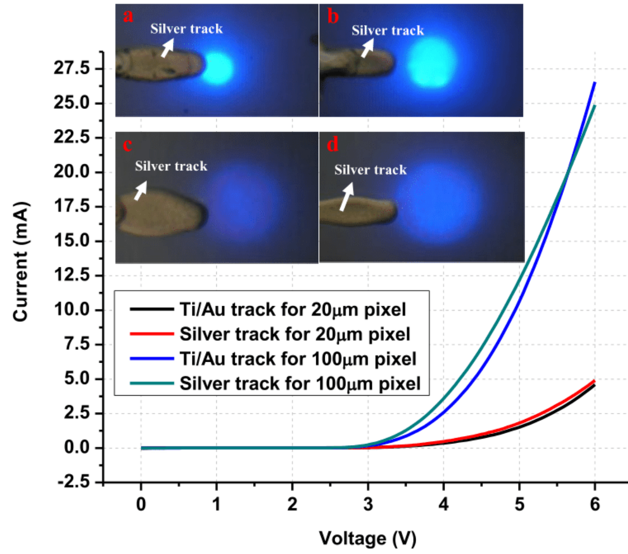

Fig. 7 Current–voltage curve comparison between the sputtered Ti/Au track and the inkjet-printed silver track connecting 20 μm and 100 μm size pixels of the planar micro-LEDs; *insets* are optical microscope images of the turned-on pixel connected by inkjet-printed silver track: (**a**) 30 μm; (**b**) 50 μm; (**c**) 70 μm; (**d**) 100 μm

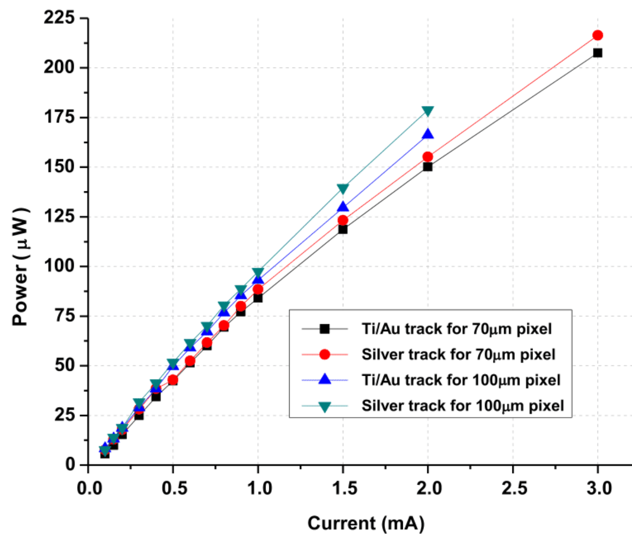

Fig. 8 Power comparison of 70 μm and 100 μm size pixels of the planar micro-LEDs connected by the sputtered Ti/Au track and the inkjet-printed silver track

els. The inset images (a) to (d) of Fig. 7 show several examples of different-sized pixels connected by the silver track, with all these pixels turned on. To make a proper comparison, we have fabricated a planar LED device chip, on which half of the LED pixels were connected by deposited Ti/Au tracks and the other half of the pixels were connected by the printed silver nanoparticle tracks. Figure 7 shows the I–V curve comparisons between these LED pixels. It can be seen that the I–V characteristics of all the silver track connected pixels of different sizes are similar to those connected by the Ti/Au track, which proves the performance of the printed silver track and demonstrates the feasibility of replacing the metal tracks with printed silver tracks.

The optical output powers of corresponding planar LED pixels connected by the printed silver track and the Ti/Au track have also been compared to further prove the capability of the silver track. As a demonstration, Fig. 8 plots the optical power versus the driving current of the LED pixels of 70 μm and 100 μm in diameter, respectively. It is clear that the optical power from the LED pixel connected by the printed silver track is close to that connected by the Ti/Au track. These results confirm that for the planar LED devices,

it is feasible to replace the deposited Ti/Au metal tracks with printed silver tracks for LED pixel connection.

4 Conclusion

In summary, the applications of silver conductive tracks inkjet printed from silver nanoparticle ink have been explored for inorganic GaN-based LEDs. As a specific illustration and challenge to the process, we chose to implement this contacting on a micro-pixellated form of GaN LED. The silver track is as narrow as ∼30 μm with a resistivity value of ∼1.1 μΩ cm when printed on a glass substrate. The operation performance of the micro-LED pixels connected by the inkjet-printed silver track has been characterized. The comparable results to those of pixels connected by the sputtered Ti/Au track prove that inkjet-printed conductive silver tracks are promising substitutes for simple and economical electrical connection fabrication on the micro-LEDs.

Acknowledgements This research work is supported by the Research Councils UK Basic Technology Research Programme and an EPSRC Science & Innovation Award on 'Molecular Nanometrology'. The authors thank Mark McGrady for helping with the contact angle measurements.

References

1. H. Sirringhaus, T. Kawase, R.H. Friend, T. Shimoda, M. Inbasekaran, W. Wu, E.P. Woo, Science **290**, 2123 (2000)
2. D. Kim, S. Jeong, S. Lee, B.K. Park, J. Moon, Thin Solid Films **515**, 7692 (2007)
3. Y. Liu, T. Cui, K. Varahramyan, Solid-State Electron. **47**, 1543 (2003)
4. D.C. Huang, F. Liao, S. Molesa, D. Redinger, V. Subramanian, J. Electrochem. Soc. **150**, G41 (2003)
5. C.N. Hoth, S.A. Choulis, P. Schilinsky, C.J. Brabec, Adv. Mater. **19**, 3973 (2007)
6. J.G. Bai, Z.Z. Zhang, J.N. Calata, G.Q. Lu, IEEE Trans. Compon. Packag. Technol. **29**, 589 (2006)
7. T.H.J. Van Osch, J. Perelaer, A.W.M. De Laat, U.S. Schubert, Adv. Mater. **20**, 343 (2008)
8. H.C. Jung, S.H. Cho, J.W. Joung, Y.S. Oh, J. Electron. Mater. **36**, 1211 (2007)
9. B.Y. Ahn, E.B. Duoss, M.J. Motala, X. Guo, S.-I. Park, Y. Xiong, J. Yoon, R.G. Nuzzo, J.A. Rogers, J.A. Lewis, Sci. Express Rep. 12 February, 1168375 (2009)
10. NanoMarkets, Market Rep. 'ITO replacement to impact OLED devices'
11. M.D. Dawson, M.A.A. Neil (Guest eds.), Cluster issue on 'Micro-pixellated LED's for science and instrumentation'. J. Phys. D: Appl. Phys. **41** 090301 (2008)
12. H.X. Zhang, D. Massoubre, J. McKendry, Z. Gong, B. Guilhabert, C. Griffin, E. Gu, P.E. Jessop, J.M. Girkin, M.D. Dawson, Opt. Express **16**, 9918 (2008)
13. D. Massoubre, J. McKendry, B. Guilhabert, Z. Gong, I.M. Watson, E. Gu, M.D. Dawson, in *Proc. IEEE LEOS*, paper MK2 (2009)
14. M. Ikegawa, H. Azuma, JSME Int. J. Ser. B **47**, 3 (2004)
15. S.H. Lee, K.Y. Shin, J.Y. Hwang, K.T. Kang, H.S. Kang, J. Micromech. Microeng. **18**, 075014 (2008)
16. A. Fuchs, F. Kanoufi, C. Combellas, M.E.R. Shanahan, Colloids Surf. A **307**, 7 (2007)
17. P. Buffand, J.-P. Borel, Phys. Rev. A **13**, 2287 (1976)
18. U. Caglar, K. Kaija, P. Mansikkamaki, in *IEEE Int. Nanoelectronics Conf* (2008), p. 851

Mask-less ultraviolet photolithography based on CMOS-driven micro-pixel light emitting diodes

D. Elfström[1], B. Guilhabert[1], J. McKendry[1], S. Poland[1], Z. Gong[1], D. Massoubre[1], E. Richardson[1], B. R. Rae[2], G. Valentine[1],G. Blanco-Gomez[3], E. Gu[1*], J.M. Cooper[3], R.K. Henderson[2], and M.D. Dawson[1]

[1]*Institute of Photonics, University of Strathclyde, Glasgow G4 0NW, UK*
[2]*Institute for Integrated Micro and Nano Systems, University of Edinburgh, Edinburgh EH9 3JL, UK*
[3]*Dept. of Electronics and Electrical Engineering, University of Glasgow, Glasgow G12 8LT, UK*
**erdan.gu@strath.ac.uk*

Abstract: We report on an approach to ultraviolet (UV) photolithography and direct writing where both the exposure pattern and dose are determined by a complementary metal oxide semiconductor (CMOS) controlled micro-pixellated light emitting diode array. The 370nm UV light from a demonstrator 8 x 8 gallium nitride micro-pixel LED is projected onto photoresist covered substrates using two back-to-back microscope objectives, allowing controlled demagnification. In the present setup, the system is capable of delivering up to 8.8W/cm^2 per imaged pixel in circular spots of diameter ~8µm. We show example structures written in positive as well as in negative photoresist.

© 2009 Optical Society of America

OCIS codes: (110.3960) Microlithography; (230.3670) Light-emitting diodes; (220.4000) Microstructure fabrication

References and links

1. S. P. A. Fodor, J. L. Read, M. C. Pirrung, L. Stryer, A. T. Lu, and D. Solas, "Light-directed, spatially addressable parallel chemical synthesis," Science **251**(4995), 767–773 (1991).
2. C. Rensch, S. Hell, M. Schickfus, and S. Hunklinger, "Laser scanner for direct writing lithography," Appl. Opt. **28**(17), 3754 (1989).
3. R. M. Guijt, and M. C. Breadmore, "Maskless photolithography using UV LEDs," Lab Chip **8**(8), 1402–1404 (2008).
4. T. Naiser, T. Mai, W. Michel, and A. Ott, "Versatile maskless microscope projection photolithography system and its application in light-directed fabrication of DNA microarrays," Rev. Sci. Instrum. **77**(6), 063711 (2006).
5. G. P. Watson, V. Aksyuk, M. E. Simon, D. M. Tennant, R. A. Cirelli, W. M. Mansfield, F. Pardo, D. O. Lopez, C. A. Bolle, A. R. Papazian, N. Basavanhally, J. Lee, R. Fullowan, F. Klemens, J. Miner, A. Kornblit, T. Sorsch, L. Fetter, M. Peabody, J. E. Bower, J. S. Weiner, and Y. L. Low, "Spatial light modulator for maskless optical projection lithography," J. Vac. Sci. Technol. B **24**(6), 2852 (2006).
6. C. W. Jeon, E. Gu, and M. D. Dawson, "Mask-free photolithographic exposure using a matrix-addressable micropixellated AlInGaN ultraviolet light-emitting diode," Appl. Phys. Lett. **86**(22), 221105 (2005).
7. H. X. Zhang, D. Massoubre, J. McKendry, Z. Gong, B. Guilhabert, C. Griffin, E. Gu, P. E. Jessop, J. M. Girkin, and M. D. Dawson, "Individually-addressable flip-chip AlInGaN micropixelated light emitting diode arrays with high continuous and nanosecond output power," Opt. Express **16**(13), 9918–9926 (2008).
8. J. McKendry, B. R. Rae, Z. Gong, K. R. Muir, B. Guilhabert, D. Massoubre, E. Gu, D. Renshaw, M. D. Dawson, and R. K. Henderson, "Individually-Addressable AlInGaN Micro-LED Arrays with CMOS Control and Sub-Nanosecond Output Pulses," IEEE Photon. Technol. Lett. **21**(12), 811–813 (2009).
9. A. Tan, K. Rodgers, J. P. Murrihy, C. O'Mathuna, and J. D. Glennon, "Rapid fabrication of microfluidic devices in poly(dimethylsiloxane) by photocopyingPresented at the 14th International Symposium on Microscale Separations and Analysis, Boston, January 13-18, 2001," Lab Chip **1**(1), 7 (2001).
10. W. K. T. Coltro, E. Piccin, J. A. Fracassi da Silva, C. Lucio do Lago, and E. Carrilho, "A toner-mediated lithographic technology for rapid prototyping of glass microchannels," Lab Chip **7**(7), 931–934 (2007).
11. M. H. Sorouraddin, M. Amjadi, and M. Safi-Shalamzari, "Simple and rapid methods for the fabrication of polymeric and glass chips for using in analytical chemistry," Anal. Chim. Acta **589**(1), 84–88 (2007).
12. G. M. Atkinson, F. P. Stratton, R. L. Kubena, and J. C. Wolfe, "30 nm resolution zero proximity lithography on high-Z substrates," J. Vac. Sci. Technol. B **10**(6), 3104–3108 (1992).
13. T. A. Savas, M. L. Schattenburg, J. M. Carter, and I. Henry, "Smith, "Large-area achromatic interferometric lithography for 100 nm period gratings and grids," J. Vac. Sci. Technol. B **14**(6), 4167–4170 (1996).
14. T. Sandstrom, A. Bleeker, J. Hintersteiner, K. Troost, J. Freyer, and K. van der Mast, "OML: optical maskless lithography for economic design prototyping and small-volume production," Proc. SPIE **5377**, 777 (2004).

#117704 - $15.00 USD Received 30 Sep 2009; accepted 31 Oct 2009; published 8 Dec 2009

15. N. Choksi, D. S. Pickard, M. McCord, R. F. W. Pease, Y. Shroff, Y. Chen, W. Oldham, and D. Markle, "Maskless extreme ultraviolet lithography," J. Vac. Sci. Technol. B **17**(6), 3047–3051 (1999).
16. D. Gil, R. Menon, and H. I. Smith, "The case for diffractive optics in maskless lithography," J. Vac. Sci. Technol. B **21**(6), 2810–2814 (2003).
17. X. Sun, D. Yin, H. Dai, J. Liu, R. Lu, and S. T. Wu, "Intermittent curing and its effect on pulsed laser-induced photopolymerization," Appl. Phys. B **92**(1), 93–98 (2008).
18. H. Xu, J. Zhang, K. M. Davitt, Y.-K. Song, and A. V. Nurmikko, "Applications of blue-green and ultraviolet micro-LEDs to biological imaging and detection," J. Phys. D Appl. Phys. **41**(9), 094013 (2008).

1. Introduction

Photolithography is the preferred method of micro-patterning, not only in electronics manufacturing but also in such emerging areas as micro-electromechanical systems (MEMS), micro-fluidics and 'digital optical chemistry' [1]. The process normally requires a custom-produced hard photo-mask to be manufactured, which is expensive, time consuming, and often limits flexibility. Much research has therefore gone into developing mask-less photolithographic methods for rapid prototyping, e.g. laser direct writing [2] which is now a commercial technique. Other mask-less approaches also under development include projection writing using a single spatially filtered light emitting diode (LED) [3], and various spatial light modulator (SLM) and digital light projector (DLP) based methods [4,5].

Micro-pixelated gallium nitride LED's ('micro-LEDs'), consisting of arrays of individually addressable micrometer-sized light emitting pixels, are being investigated by several groups for applications in areas including micro-displays, bioscience and instrumentation. These devices offer spatio-temporal control of the emission pattern, and also spectrally selective excitation because the emission bandwidth is typically narrow (~15nm full-width at half maximum (FWHM)), with the central wavelength being defined by the semiconductor epitaxy of the light-emitting quantum wells. Indeed, in a preliminary demonstration [6] we were able to show some simple micrometer-sized exposure patterns in photoresist achieved by a 'first generation' array designed to operate at an approximately *i*-line photolithography wavelength (365nm). More recently, the technology has advanced to the point where much higher powers are available per pixel through flip-chip bonding of the devices [7] and independent element addressing by custom CMOS control circuitry is possible [8].

Here we explore the implications for mask-free photolithography and other forms of optical direct-write patterning engendered by these recent developments. A CMOS-controlled 8 x 8 flip-chip 370nm gallium nitride-based micro-LED array demonstrator is de-magnified through various combinations of back-to-back microscope objectives. The CMOS is shown to be capable not only of controlling the emission pattern, but also the exposure dose. We show example structures written in positive as well as in negative photoresist. The system can be used to directly reproduce the pattern on the micro-LED array and/or lines can be written by moving the sample while one or several LED pixels are turned on. Our system can be considered to bridge the gap between low cost, but low resolution, mask-less prototyping techniques, such as the use of a photocopier [9], toner mediated lithography [10], or etching through a mask made using a cutter plotter [11] (feature size limited to over 200μm) and high cost methods competing with traditional optical projection lithography (OPL) in terms of resolution, such as scanning electron-beam lithography (SEBL), focused ion-beam (FIB) lithography [12], interference lithography (IL) [13], maskless optical-projection lithography (MOPL) [14,15], and zone-plate-array lithography (ZPAL) [16].

2. CMOS-bonded flip-chip micro-LED array

The AlInGaN quantum well micro-LED devices are based on 370nm-emitting epitaxial wafers and are designed for flip-chip bonding. They consist of a 16 x 16 array of individually-addressable micro-disk pixels, each 72μm in diameter on a 100μm center-to-center pitch. The sapphire (epitaxial substrate) side was polished and the substrate was diced into individual device chips of approximately 3x3mm^2, of which the active area is 1.6x1.6mm^2. A bump bonding process was used to electrically and physically contact these chips to a custom-

#117704 - $15.00 USD Received 30 Sep 2009; accepted 31 Oct 2009; published 8 Dec 2009
(C) 2009 OSA

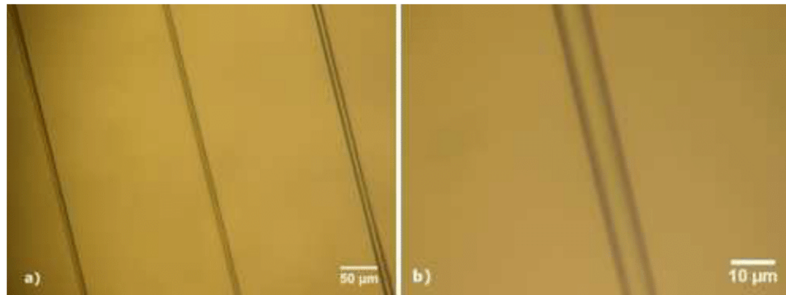

Fig. 5. (a) Three lines in NOA81 written in, respectively, CW mode, with 50ns pulses and with 40ns pulses at a velocity of 5µm/s. Widths are 11µm, 8µm and 8µm respectively. (b) Close up on the middle line showing good uniformity of the line width.

Further curing experiments in NOA81 were performed under pulsed operation of the LED device. By varying the pulse width from 5ns to 40ns, and hence the exposure dose from 16.4J/cm^2 to 120J/cm^2, spot-sizes ranging from 11µm to 24µm diameter were written with an exposure time of 40s. A selection of these written dots is shown as insets in Fig. 4. Lines in NOA81 were also written under pulsed operation, as well as in CW. The lines shown in Fig. 5(a) were exposed with a maximum dose, in the middle of the line, of 14.7J/cm^2, 6.0J/cm^2, and 5.4J/cm^2 going from right to left, corresponding to line widths of 11µm, 8µm, and 8µm respectively. The height of the lines was determined to be 1.7µm (i.e. curing the full thickness of the film), 0.9µm, and 0.9µm, by a stylus (Dektak) profilometer. The uniformity of the cured lines is good and shows no bulging or other variations.

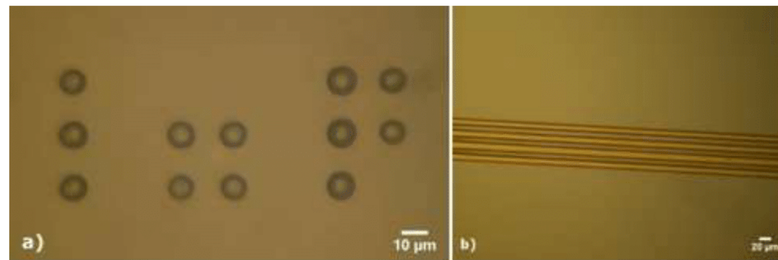

Fig. 6. (a)'IoP' (Institute of Photonics) pattern in NOA81. The exposed dots are 8-9µm in diameter. (b) Four parallel channels written in Microposit S1805 photoresist at a velocity of 100µm/s. Lines are 9-11µm wide. The two different patterns were chosen to show the static and dynamic writing capability of the system.

For the positive photoresist features as shown in Fig. 6(b), a standard photoresist, Microposit S1805 from Shipley, was used. It is optimized for *g*-line (436nm) exposure, but works well for exposure wavelengths down to 350nm. Recommended exposure dose at the *g*-line is 150mJ/cm^2. Silicon substrates were cleaned thoroughly in an ultrasonic bath with acetone and subsequently methanol. They were then rinsed in DI water and dried on a hotplate at 110°C for at least 20 minutes. The photoresist was spun at 2000 rpm for 30s. The substrate with the 0.7µm thick film was then placed on a hotplate at 120°C for 1 minute to soft-bake the photoresist prior to being exposed. After the exposure, development was completed using a micro-developer solution (Microposit 1:1 volume ratio with deionised water). The substrate was immersed and gently moved around in the solution for a duration of 1 minute. Residue developer was washed off with DI water. The four "channels" seen in Fig. 6(b) are written by turning on four individual pixels (each delivering an optical power of ~2.5µW to the sample) in one column of the micro-LED array while moving the sample at a

#117704 - $15.00 USD Received 30 Sep 2009; accepted 31 Oct 2009; published 8 Dec 2009
(C) 2009 OSA

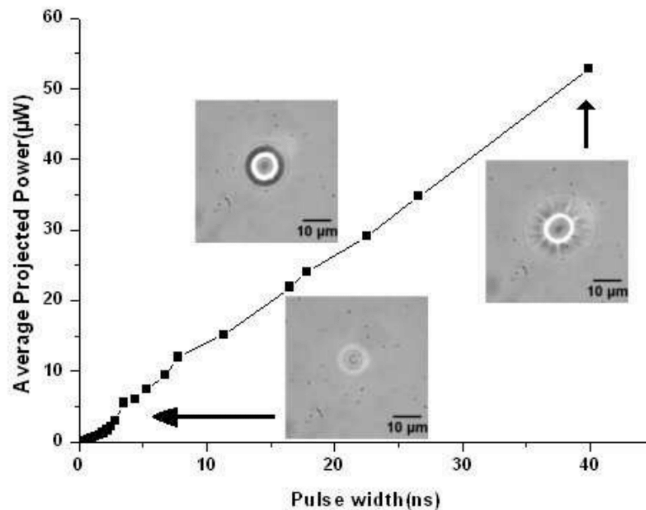

Fig. 4. The relationship between average projected power and pulse width is linear for long enough pulses. Repetition rate = 9.75 MHz throughout. The insets are optical micrographs of exposed dots in NOA81 negative photoresist on glass substrates exposed for 40s at 5ns, 20ns and 40ns pulse width. The spot diameters are 11µm, 17µm and 24µm, respectively.

5. Patterning experiments

To test the micro-lithography system, a number of different 'demonstrator' patterns were produced in positive as well as in negative photoresist. An optical adhesive from Norland (NOA81) was chosen for the negative type photoresist because of its excellent adhesion to glass and relatively low viscosity, allowing thin films to be spun on substrates and hence offering the possibility of feature a few µm in size. The optical adhesive has a spectral peak sensitivity at 365nm and the manufacturer's recommended dose for full cure is $2J/cm^2$. In preparation, substrates of borosilicate glass were cleaned thoroughly in an ultrasonic bath with acetone and subsequently methanol. They were then rinsed in deionised (DI) water and dried on a hotplate at 110°C for at least 20 minutes. NOA81 was then spin-coated at 8000 rpm for 40s, resulting in a film thickness of 1.7µm as measured by a stylus (DekTak) profilometer on cured structures. The substrate with the Norland film was placed on the XY stage and then exposed by the UV light from the micro-LED device projected through the setup. Directly after the exposure, the development was done by immersing the substrate in acetone for 1 minute. The substrate was cleaned of acetone and polymer residue in running methanol and subsequently in running DI water. The 'IoP' logo in Fig. 6(a) is used as a demonstrator pattern. The 'I' and the 'P' were exposed with square wave addressing for 8s while the 'o' was exposed for 4s, giving an average exposure dose of $10J/cm^2$ for each dot. This variation is due to the collection efficiency decreasing as the distance from the centre of the imaging area increases, which we note can be corrected for directly by the CMOS control. Small variations in exposure dose exist because pixel to pixel uniformity is not perfect. These issues can also, however, in principle be compensated for by adjusting the CMOS control duty cycle for each individual pixel.

#117704 - $15.00 USD Received 30 Sep 2009; accepted 31 Oct 2009; published 8 Dec 2009
(C) 2009 OSA

feature, although unintended, is actually beneficial when exposing photoresist as it gives better defined feature edges compared to the case with a Gaussian intensity profile.

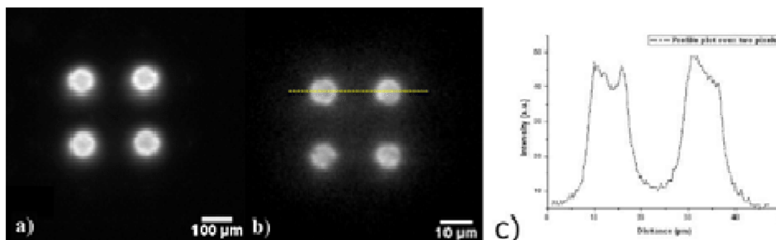

Fig. 3. Four LED pixels turned on., (a) on the device itself and (b) reflection off a mirror at the sample position, showing the focal spot size at the applications plane. The dashed line corresponds to the trace of the intensity profile plotted in (c).

By combining the spot-size measurements with the power measurements for various combinations of objectives, the intensity values presented in Table 1 were obtained. The maximum power density value of 8.8W/cm^2 permits the required exposure dose for most photoresist types to be reached in fractions of a second (e.g. 46ms for an exposure dose of 400mJ/cm^2).

Table 1. Intensities delivered by different collection and projection objectives. Image plane spot sizes measured in FWHM are in parentheses. Spot sizes have also been established by measurements in exposed photoresist and the errors in the measurements below are determined to be less than ± 10% throughout.

Collection objective\ Projection objective	4X	10X	20X	40X
4X	88mW/cm^2 (80µm)	0.51W/cm^2 (33µm)	1.7W/cm^2 (18µm)	8.8W/cm^2 (8.0µm)
40X	25mW/cm^2 (850µm)	0.16W/cm^2 (330µm)	0.61W/cm^2 (170µm)	3.3W/cm^2 (73µm)

The 4X collection objective has a larger field of view (~4mm), but it also has a lower N.A. which means it has a lower collection angle. This allows for the whole micro-LED device (1.6x1.6mm^2) to be imaged at once, but with the trade-off of lower light collection. Despite this, the highest optical power density is achieved using the 4X collection/40X projection objective combination. When calculating the power densities, all power was assumed to be uniformly distributed within the spot diameter [c.f. 'flat top' beam profiles in Fig. 3(c)]. Dosage energy is given by multiplying the optical power by the exposure time. When the sample is moving the dosage curve is given by

$$E = \frac{2P}{\pi R^2 v}\sqrt{R^2 - y^2},$$

where P is the total power, R the pixel radius, v the velocity, and y (≤R) the coordinate perpendicular to the velocity, i.e. a half-circular dosage curve.

The measurements presented above are all made under CW (DC driven) operation, however the CMOS driver provides the capability to use pulses for exposure. By adjusting the length of each pulse at a given repetition rate, effectively changing the duty cycle to the LED pixel, the projected optical output can be accurately controlled. Figure 4 shows how the average projected optical power varies with pulse duration from 0.5ns to 40ns at an example fixed repetition rate of 9.75MHz. The power scales linearly, but the pulsed driving of the LED allows us to explore the intermittent curing behaviour of photoresists [17]. This feature of the CMOS driver can also, in principle, be used to correct differences in output power between pixels and to compensate for collection efficiency variations over the field of view.

#117704 - $15.00 USD Received 30 Sep 2009; accepted 31 Oct 2009; published 8 Dec 2009
(C) 2009 OSA

on the orientation of the beam-splitter. Infinity-corrected objectives give collimated (or parallel) output beams of the object in the focal plane, hence when the camera objective is set to focus at infinity, the image displayed on the camera is optically conjugate to the focal plane of each objective.

A piezo-driven stage (PI P-725.4CD) for the Z-translation of the projection microscope objective gives a very accurate (100nm resolution with current driver and feedback measuring system) control of the focus on the sample. The sample is placed on an XY stage (2 x PI M-112.1DG) allowing for large areas (up to 25x25mm^2) to be patterned. The computer control allows for movement of the sample in any pre-defined pattern at a maximum velocity of 1.5mm/s and with a repeatability of ~1µm.

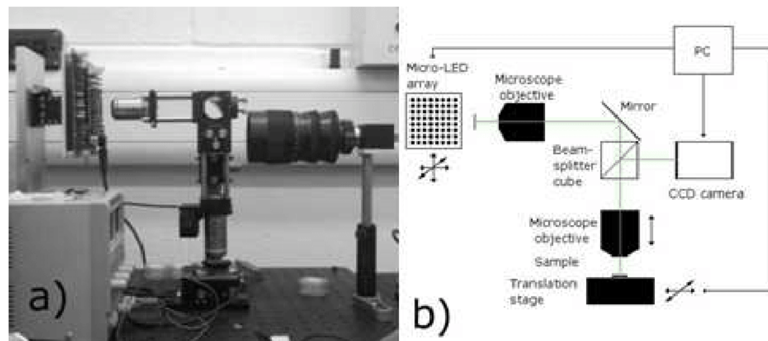

Fig. 2. A photograph of the micro-projection setup (a) and schematic of the same (b).

The two objectives can be changed to give the capability of magnifying or de-magnifying the projected spots from the LED pixels. A range of microscope objectives with magnifications from 4X to 40X gives theoretical spot-sizes from 7.2µm (4X collection objective and 40X projection objective) to 720µm (40X collection objective and 4X projection objective) when projecting the 72µm diameter pixels of the micro-LED device. In Fig. 3, four pixels can be seen through the 4X collection objective [Fig. 3(a)] and reflected off a mirror placed at the sample position through the 40X collection objective [Fig. 3(b)], showing how the system can demagnify the illuminated spot.

4. Characterization of the system

To characterize the performance of the system, the optical power *per pixel* delivered at the sample was measured by placing a calibrated UV optical power meter (Coherent FieldMax Top) at the sample position. The total projected power was measured to be 140µW with the 40X collection objective and 4.4µW with the 4X collection objective, all obtained at a CMOS drive current of ~27mA. The projected powers are independent of the projection objective as the transmission losses are low and very similar for this type of objective. The measurements also indicate that there are only small transmission losses in the overall system (approximately less than 4%), except for the beam-splitter where ~50% of the power is lost.

Projected spot-sizes are determined by imaging a reflection off a mirror placed at the sample position. By using the high precision Z-translation stage the projection objective was translated to match the focal plane to the reflective surface of the mirror. From the thus acquired images, intensity profiles were taken of the projected spots and the FWHM values were measured of the profiles. An example image, of the reflection from a mirror at the sample position, is shown in Fig. 3(b). The intensity profile through the centre of the two top spots in Fig. 3(b), is shown in Fig. 3(c). In this particular case, the 4X collection objective and the 40X projection objective were used, giving spot sizes of approximately 8µm FWHM. The form of the intensity profile is determined by the emission pattern from the light emitting pixel and typically has brighter edges, attributed to sidewall scatter in the emitting pixels. This

#117704 - $15.00 USD Received 30 Sep 2009; accepted 31 Oct 2009; published 8 Dec 2009
(C) 2009 OSA

designed CMOS control device in the manner reported recently [8], such that alternate pixels were operable, thus giving a light-emitting 8 x 8 array [Fig. 1(a)]. This was done due to the bump bonding process, which currently limits the pixel to pixel pitch to ~200μm.

The CMOS device permits continuous wave (CW) operation of the individual micro-pixels, square wave and pulsed operation [8]. In CW operation, we measured a single bare pixel to deliver an optical power of up to 604μW at a driving current of 80.0mA (340μW at 20mA) at 370nm. The frequency of the square wave (the repetition rate in pulsed mode) can be set by the on-chip voltage-controlled oscillator (VCO) from 6MHz to 800MHz. With the external clock facility any frequency can be chosen. In pulsed mode the duration of the pulses can be controlled, ranging from 300ps to 40ns.

The spectral characteristic in CW operation at 27mA, measured after the imaging, confirms that it is close to Hg *i*-line operation (peak at 370nm with a FWHM of 15nm).

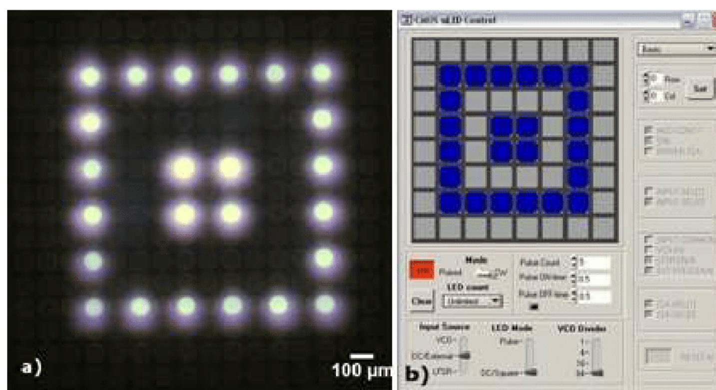

Fig. 1. (a) CMOS driven micro-LED device with pixels turned on to show a representative double square pattern, and (b) the computer control interface as the pattern in (a) is addressed.

The CMOS control device was attached to a printed circuit board (PCB), which is computer controlled via a field programmable gate array (FPGA) board (XEM3010-1000 from Opal Kelly). In the custom-made software interface, shown in Fig. 1(b), the mode of operation of the CMOS chip can be set to linear feedback shift register (LFSR, not used in this work), DC/External (if no external clock is present this is CW operation), or VCO. The LED mode can be set to either DC/Square (CW operation or a square wave clocked to the external or VCO frequency) or Pulse (pulse at a controllable duration with the repetition rate set by external or VCO frequency). The VCO divider sets a value (1, 4, 16, or 64) with which the VCO frequency is divided before it is used. A pixel or a pattern consisting of a set of pixels can be chosen either by setting the row and column [upper right corner in Fig. 1 (b)] or by highlighting the desired pixels in the grid pattern of the software interface. With the timing control the LED on-time can be set accurately down to ~100ms

3. The setup

A photographic image and a corresponding schematic of the setup for mask-less photolithography can be seen in Fig. 2. The setup consists of the CMOS driven computer controlled micro-LED device mounted vertically on a manual XYZ stage, a horizontally-mounted infinity-corrected microscope objective (Nikon CFI Plan Fluor Series) for light collection (collection objective), a mirror to direct the light downwards, a 50-50 UV beam-splitter cube, and a second (vertical) infinity-corrected microscope objective (projection objective), mounted on a Z-translation stage, to project the LED array image onto the sample. A CCD camera (Prosilica EC650C) with zoom lens attachment (Navitar, 11-110mm) adjusted to focus at infinity is used to monitor the position of the sample or the LED array depending

#117704 - $15.00 USD Received 30 Sep 2009; accepted 31 Oct 2009; published 8 Dec 2009
(C) 2009 OSA

velocity of 100µm/s. This corresponds to a maximum exposure dose, in the middle of each channel, of ~400mJ/cm^2.

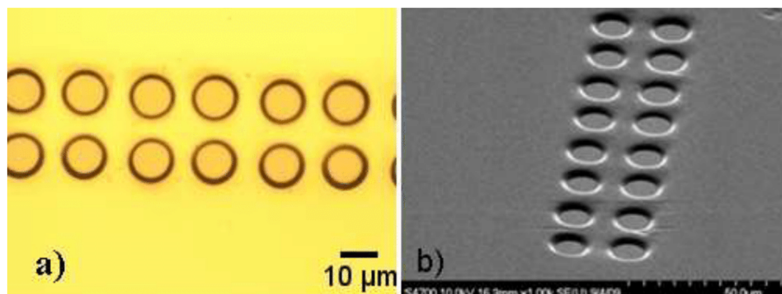

Fig. 7. (a) Micrograph showing an array of exposed dots in S1818, each with a diameter of ~9µm. (b) Oblique SEM image of the same array, showing well defined sidewalls and good dot to dot uniformity.

As a further demonstration patterns were written in a thicker positive type photoresist, Microposit S1818 from Shipley. Glass substrates were cleaned in a similar manner to previous samples and were subsequently covered with a ~2.0µm thick layer photoresist by spincoating. The samples were then exposed simultaneously by four pixels for the duration of 2s in pulsed mode, giving an exposure dose of 1.1J/cm^2. The sample was then translated 40µm and an other exposure was performed. This was repeated four times and followed by a development step as described above. The resulting pattern is shown in Fig. 7. The scanning electron microscope (SEM) image in Fig. 7(b) was taken by a Hitachi S4700 in ultra high resolution mode and confirms that we have well defined patterns with close to vertical sidewalls.

6. Conclusion

By combining novel CMOS driven micro-LED arrays with a projection system, we have built a versatile computer-controlled micro-photolithography tool capable of writing features down to ~8µm in positive and negative photoresist. It is capable of simultaneously exposing multiple spots and has, through the CMOS driving mechanism, facility to precisely control the dose delivered during a determined period of time as well as capability to correct for non-uniform exposure across the field of view. This type of system offers attractive prospects for many areas of direct write photo-patterning and patterned photo-stimulation, including polymer microstructuring, mask-less photolithography, digital optical chemistry, microfluidic systems and optogenetics [18]. Our demonstrator establishes a baseline capability, but offers considerable scope for further scaling and refinement. Wavelengths from deep ultraviolet to violet can readily be chosen for spectrally selective excitation and we have developed flip-chip devices of pixel diameter 5-10µm, where there is a separate bond-pad for each pixel for "off-pixel" bump bonding to CMOS. When incorporated into the system at 10:1 de-magnification, we anticipate being able to create 8 x 8 arrays capable of writing features down to ~1um. There is the prospect of further scaling of the number of CMOS controlled pixels.

Acknowledgements

We acknowledge support under an EPSRC Science and Innovation programme on "Molecular Nanometrology", the EPSRC "HYPIX" programme, from the EU (PHOTOLYSIS - LSHM-CT-2007-037765) and the Scottish Consortium in Integrated Microphotonic Systems.

Appendix A- NLP 200 Datasheet

DATASHEET

NLP 2000 System

NLP 2000 System

desktop nanolithography platform

The NLP 2000 System is a versatile desktop nanolithography platform designed for patterning a variety of materials using the proven technique of Dip Pen Nanolithography® (DPN®). An extensive catalog of materials including biological molecules, nanoparticles, and small molecules such as SAM forming thiols may be deposited on many different kinds of substrates. Arrays of nanoscale and microscale lines and dots can be rapidly generated inside the environmentally controlled work area with the simple and intuitive software interface. Multiplexed arrays are easily created using NanoInk's inkwells that bridge macroscale dispensing with micro- and nanoscale patterning.

5 Axis Nano Positioning Stage with High Resolution Optical Encoders

The NLP 2000 employs a 5 axis stage system to achieve nanometer XYZ precision printing with NanoInk's multi-pen arrays. The assembly is comprised of three piezo-driven linear stages (X, Y, Z) and 2 goniometer stages (T_x and T_y) all with optical encoders.

- XY Stage Travel Range: 40 mm x 40 mm
- Z Travel Range: 10 mm
- X- and Y-axis Resolution: +/- 25 nm
- Z-axis Resolution: +/- 75 nm
- T_x and T_y Goniometer Stages: +/- 5°
- T_x and T_y Goniometer Resolution: +/- 0.00025°
- Substrate Holder: Capable of accommodating microscope slides, petri dishes, and samples up to 4 inches in diameter
- Pen Holder: For NanoInk multi-pen arrays

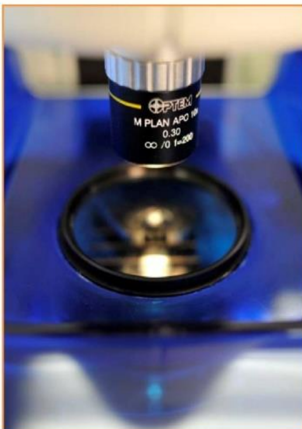

NLP 2000 Optical System

The NLP 2000 features integrated high resolution optical imaging for simultaneous visualization of pens and substrate.

- 10x Objective M Plan APO
  - 33.5 mm working distance
  - 0.30 numerical aperture
- Optical Resolution: < 1 µm
- Motorized Digitally Controlled 6x Zoom
- Digitally Controlled Halogen Illumination System
- High Resolution CCD Camera
  - 1.4 Megapixel Sensor
- Field of View
  - 0% Zoom: 844 µm x 629 µm
  - 100% Zoom: 143 µm x 110 µm
- Video Magnification : (280x -1700x)

Localized Environmental Chamber

User control of temperature and humidity within the printing environment.

- Software Controlled Temperature & Humidity
- Heating Temperature Range: (Ambient + 20°C)
- Cooling Temperature Range: (Ambient – 2°C)
- Temperature Stability: +/- 0.5 °C
- Humidity Range: (10-90% RH)
- Humidity Stability: +/- 5% RH

NLP 2000 Getting Started Kit

The NLP 2000 comes complete with all of the tools you need to create micro- and nanostructures using DPN. The Getting Started Kit includes everything needed for DPN experimentation.

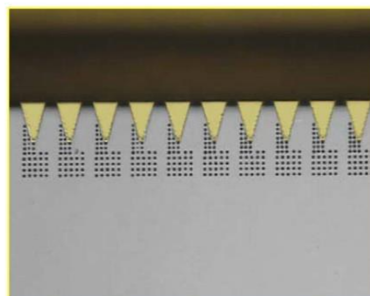

- Pens, Type-M Multi-Pen Arrays, qty 20
- Pens, Type-F Multi-Pen Arrays, qty 10
- Inkwell Arrays: Universal, M-6MW, M-12MW, qty 10 each
- Substrates, SiO_2 Pre-marked Substrates, qty 10
- Substrates, Gold Pre-marked Substrates, qty 4
- Printing Solution, Bio-A and Bio-B, 1 vial each
- Biological Printing Solution User Manual
- Printing Solution, MHA-Octanol, 1 vial
- Micropipette and Tips, 0.1-2.0 µL

DPN Multi-Pen Arrays

NanoInk's multi-pen arrays allow for deposition of a variety of materials. Features include:

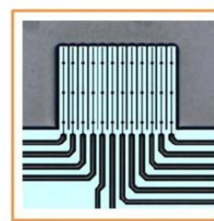

- Silicon nitride pens
- Large-area coverage and/or multi-ink patterning
- A-frame or diving board shaped cantilevers

Inkwells

NanoInk's inkwells are specifically designed to deliver a solvent-based ink to one or several tips among a pen array without cross-contamination.

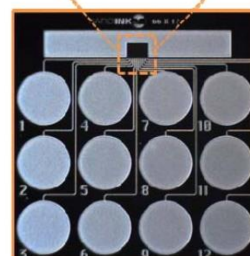

- With inkwells, an ink/solvent solution is delivered to one of the inkwell reservoirs via a micropipette
- Up to twelve unique molecular inks are possible on each inkwell chip
- Ink is guided through microchannels to the microwell, where the tip will dip and be coated with ink

System Options

2D nano PrintArray™ Kit

The 2D nano PrintArray Chip provides a high-throughput solution to flexibly pattern nanoscale features. The 2D nano PrintArray retains the direct write, high resolution, ambient deposition, and chemical and material flexible attributes of DPN, while multiplying the desired pattern 55,000 times across a 1 cm^2 area.

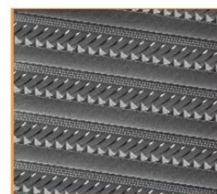

Extended Service Package

Receive an additional 1 year of service and warranty beyond the standard 1 year.

NLP 2000 System

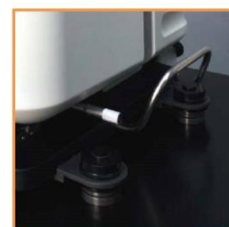

Vibration Isolation

The NLP 2000 has an integrated passive vibration isolation system.

- Vistek bearings isolate horizontal and vertical vibration components
- No external air source required
- System Footprint: 30” (76 cm) L x 22” (56 cm) W

NLP 2000 Controller

- Digital Closed Loop XYZ Stage Motion Control
- Digital Control Electronics for Optical system and Environmental Chamber
- Dimensions: 24” (61 cm) L x 13” (33 cm) W x 25” (64 cm) H

PC Workstation

- Dell® Computer Workstation with Pentium® 4 Processor
- 2 GB RAM
- 160 GB HDD
- 24“ Widescreen LCD Monitor

Warranty & Support

- On-site System Installation
- 2 Days User Training
- NLP Getting Started Guide & CD
- Full Access to DPNForum.com
- 1 Year Warranty Parts & Labor

Learn more about NanoInk products and services at www.nanoink.net. Or call us at 847-679-NANO (6266).

© 2010 NanoInk, Inc. All rights reserved. NanoInk, the NanoInk logo, Dip Pen Nanolithography, DPN, NSCRIPTOR, and 2D nano PrintArray are trademarks or registered trademarks of NanoInk, Inc.

Appendix B- Reflectivity calculation of a fourth-order in-plane grating

---

This programme calculates the reflectivities of a DBR made by patterns in the surface of a thin-film of organic semiconductor (BBEHP-PPV here although parameters can be changed if considering other materials). The effect is that of a mode interacting with a one-dimensional grating but even 2D problems can often be reduced/ approximated to such an equivalent 1D pattern. The reflectivity calculated is for the TE0 mode of the equivalent slab-waveguide, made by the thin film of organic on glass, propagating perpendicularly to the grating (i.e. within the film). A typical value for the effective refractive index, $n_{eff,}$ for the TE0 mode at a wavelength of 530 nm (that can be determined by a slab-waveguide analysis) for a BBEHP-PPV film of 200nm is considered.

The DBR in the experiment is made by a modulation of the thickness of the film obtained by indentation at the film surface. The equivalent grating thus considered is at the interface of the organic and air. It has a given depth, 'dg', which is smaller than the film thickness. This problem is reduced to a 'complete' multilayer DBR structure with parameters obtained through a couple mode analysis.

The reflectivity is computed using a matrix approach. A single, basic matrix represents the effect of the grating on the mode over one period. It encompasses the effects of, respectively, an interface, T, and a propagation matrix P (propagation in a medium of index n_{eff} over a distance equal to one period of the 'grating', Λ). The reflectivity matrix T is obtained through a couple-mode analysis (see below) and takes into account the effect of the air-organic interfaces weighted by the overlap of the field with the modulation structure (i.e. depending on the mode spatial profile and the grating depth dg).

The grating considered here is a 4th order for the wavelength. The diffraction orders +/-1, +/-2 and +/-3 are assimilated to loss (diffraction out of the organic film) and is incorporated as a loss term, α , in

the matrix T. α represents the loss over one period. The diffraction order -4 is considered as the feedback or reflectivity, r, experienced by the mode over one period and, as said before, this effect is also incorporated in the interface matrix T. These loss and reflectivity terms are obtained from a determination of the coupling coefficients κ corresponding to the different diffraction orders. Some approximations were made but it is still based on the actual characteristics of the structures fabricated by dip-pen (more details below).

The optical gain in the organic material (which can be triggered by optical pumping) is also taken into account by incorporating a gain term, g. This term g represents the distributed gain and is therefore incorporated in the propagation matrix P. The spectral dependency of this gain is assumed to have a Lorentzian shape with characteristic homogeneous and inhomogeneous linewidths as parameters. Note that the coupling coefficients are also wavelength dependent, however the refractive index dispersion of the organic is not taken into account. The model is therefore the most precise close to the central wavelength λc.

The matrix of a single period of the grating is given by the matrix product M= T P. The overall matrix M_T of the structure is the product of this matrix by itself (N times M if N is the number of periods). The reflectivity of the mode is deduced from the elements of M_T. The programme also includes the possibility to induce 'disorder' in the grating structure. This is done by considering an additional random phase term in the P matrix.

Programme - Reflectivity calculation of a fourth-order in-plane grating - Model of surface-patterned light-emitting slab-waveguide -

Use for dip-pen patterned organic laser material

PARAMETERS

Overlap of the TE0 field mode with 'grating'

$\Gamma := 0.16$

Effective refractive index of the mode in the patterned film (this is separately calculated for the structure using an equivalent slab waveguide analysis)

$neff := 1.56$

Grating/modulation period (recovered from the Fourier transform of the AFM profile)

$\Lambda := 676 \cdot nm$

Refractive index contrast between BBEHP-PPV and air

$\Delta n := 1.75 - 1$

Duty cycle of the grating/nanostructure (average obtained by AFM measurements of nanopatterns)

$b := 0.3 \cdot \Lambda$

Grating/modulation depth

$dg := 40 \cdot nm$

Coupling coefficients - calculated with couple-mode theory

The modulation is approximated to be sinusoidal for simplification

References

Kazarinov and Henry, IEEE J. Quant. Electron., 21, 2, p 144 (1985)

Chuang, 'Physics of photonic devices, second edition, Wiley (2009)

Streifer et al., IEEE J. Quant. Electron., 13, 4, p 134 (1977)

$$\kappa ref(\lambda) := \frac{-\Delta n \cdot \Gamma}{\lambda} \cdot \sin\left(2 \cdot \pi \cdot \frac{b}{\Lambda}\right)$$

$$\kappa(m,\lambda) := -\frac{2\Delta n \cdot \Gamma}{m \cdot \lambda} \cdot \sin\left(m \cdot \pi \cdot \frac{b}{\Lambda}\right)$$

$$\kappa L(N,\lambda) := 2 \cdot \frac{\Delta n \cdot dg}{\lambda} \cdot \tan\left(\pi \cdot \frac{b}{\Lambda}\right) \cdot \kappa ref(\lambda) \cdot \left(\frac{\frac{\sin\left(\pi \cdot N \cdot \frac{b}{\Lambda}\right)}{\pi \cdot N}}{\frac{\sin\left(\pi \cdot 1 \cdot \frac{b}{\Lambda}\right)}{\pi \cdot 1}}\right)^2$$

Loss and reflection parameters for the matrix determination

$$\alpha(\lambda) := 2\cdot(\kappa L(1,\lambda) + \kappa L(2,\lambda) + \kappa L(3,\lambda))\cdot\Lambda$$

$$r(\lambda) := \kappa(4,\lambda)\cdot\Lambda$$

Wavevector

$$k(neff,\lambda) := \frac{2\pi}{\lambda}\cdot neff$$

Gain definition

$$gnet := 40\cdot cm^{-1}$$

$\lambda c := 535\cdot nm$ $\quad\Delta\lambda := 50\cdot nm$ $\quad\Delta\lambda in := 5\cdot nm$

$$Lorentz(\lambda,\lambda c,\Delta\lambda) := \left[\frac{\Delta\lambda^2}{(\lambda - \lambda c)^2 + \Delta\lambda^2}\right] \qquad Inhomogeneous(x,\Delta\lambda in) := \exp\left[\frac{-2\cdot(x - \lambda c)^2}{\Delta\lambda in^2}\right]$$

$$gt(\lambda,\Delta\lambda,\Delta\lambda in) := \frac{\sum_{x=-100}^{100}(Lorentz(\lambda,\lambda c,\Delta\lambda)\cdot Inhomogeneous(x\cdot nm + \lambda c,\Delta\lambda in))}{1}$$

$$g(\lambda) := gnet\cdot Lorentz(\lambda,\lambda c,\Delta\lambda)$$

$$\lambda := 500\cdot nm, 500.1\cdot nm .. 880\cdot nm$$

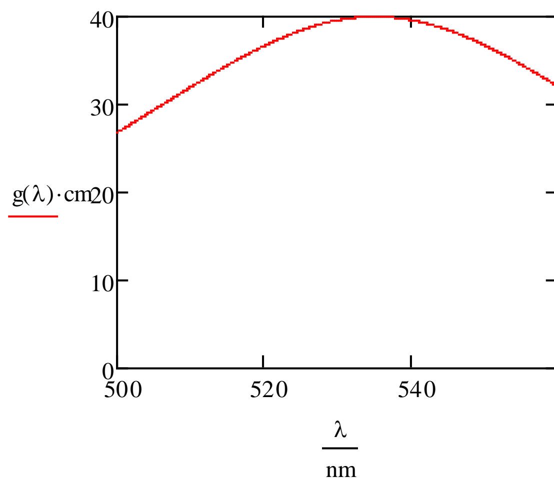

Random number generation for inclusion in a disorder term (as a random phase, see further)

$f(x) := x$

$Rvals := (\text{"X"} \quad 0 \quad 0.)$ $\qquad$ $Rvals2 := (\text{"Y"} \quad 0 \quad 0.0)$

$n := 100$ $\qquad$ $n2 := 100$

$M := \text{montecarlo}(f, n, Rvals)$

$M2 := \text{montecarlo}(f, n2, Rvals2)$

MATRICES

$$T(\lambda) := \frac{1}{\sqrt{1 - r(\lambda)^2 - \alpha(\lambda)^2}} \cdot \begin{pmatrix} 1 & r(\lambda) \\ r(\lambda) & 1 \end{pmatrix}$$

$$P(\lambda, X) := \begin{bmatrix} \exp\left[i\cdot(k(neff,\lambda) - i\cdot g(\lambda))\left(\Lambda + M2_{X,0}\cdot\Lambda\right) + i\cdot\left(M_{X,0}\cdot 2\cdot\pi\right)\right] & 0 \\ 0 & \exp\left[-i\cdot(k(neff,\lambda) - i\cdot g(\lambda))\left(\Lambda + M2_{X,0}\cdot\Lambda\right) + i\cdot\left(M_{X,0}\cdot 2\cdot\pi\right)\right] \end{bmatrix}$$

$$M(\lambda, X) := P(\lambda, X)\cdot T(\lambda)$$

$$MT(\lambda, N) := \prod_{X=1}^{N} M(\lambda, X)$$

Reflection of DBR

$$rDBR(\lambda, N) := \frac{MT(\lambda,N)_{1,0}}{MT(\lambda,N)_{1,1}} \qquad tDBR(\lambda, N) := \frac{1}{MT(\lambda,N)_{1,1}}$$

$$R(\lambda, N) := \left(\left|\frac{MT(\lambda,N)_{1,0}}{MT(\lambda,N)_{1,1}}\right|\right)^2 \qquad \phi(\lambda, N) := \arg\left(\frac{MT(\lambda,N)_{1,0}}{MT(\lambda,N)_{1,1}}\right)$$

SPECTRAL REFLECTIVITY

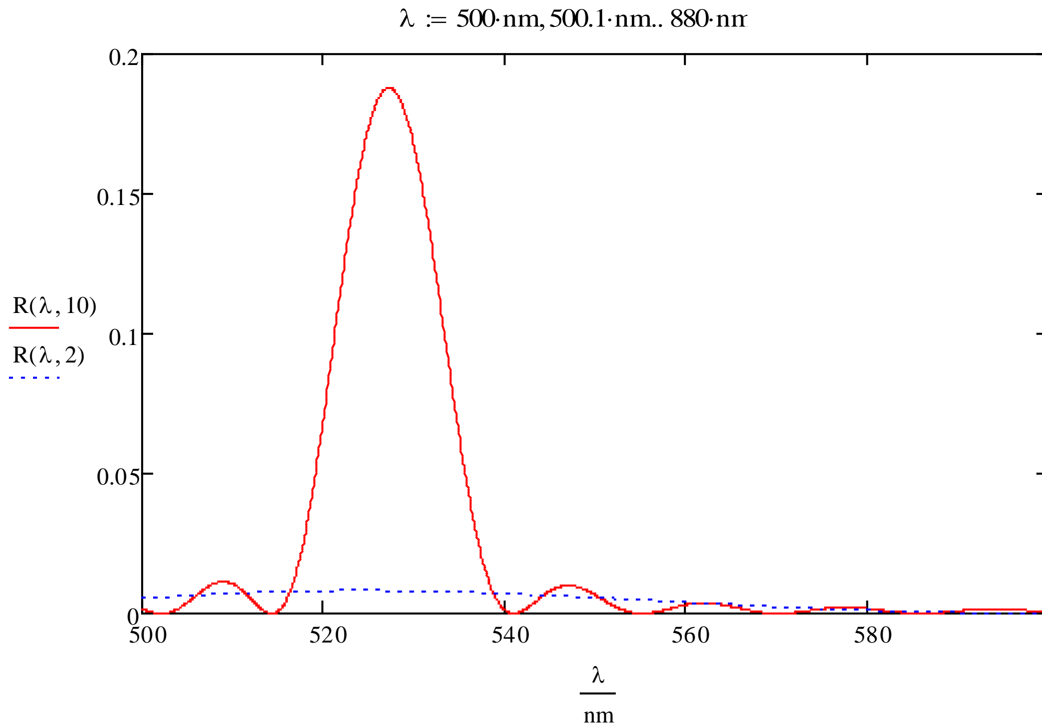

PHASE AND PENETRATION DEPTH

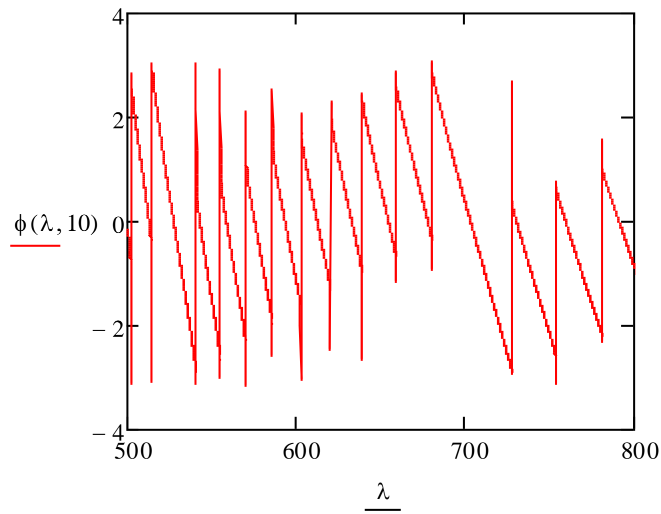

$$delay(\lambda, N) := -\frac{\phi(\lambda + 0.1 \cdot nm, N) - \phi(\lambda - 0.1 \cdot nm, N)}{0.2 \cdot nm} \cdot \frac{\lambda^2}{2 \cdot \pi \, c}$$

$$Lpen(\lambda, N) := c \cdot \frac{delay(\lambda, N)}{2 \cdot neff}$$

$$Lpen(\lambda c, 10) = 3.143 \times 10^{-6} m$$

Reflectivity of DBR laser structure (i.e. 2 mirrors and the separation gap made of unpatterned region)

$$Pgap(\lambda) := \begin{bmatrix} \exp[i \cdot (k(neff, \lambda) - i \cdot g(\lambda))(15 \cdot \mu m)] & 0 \\ 0 & \exp[-i \cdot (k(neff, \lambda) - i \cdot g(\lambda))(15 \cdot \mu m)] \end{bmatrix}$$

$$rint := 0\%$$

$$Tint := \frac{1}{\sqrt{1 - rint^2}} \cdot \begin{pmatrix} 1 & rint \\ rint & 1 \end{pmatrix}$$

$$Mlaser(\lambda, N1, N2) := Tint \cdot MT(\lambda, N1) \cdot Pgap(\lambda) \cdot MT(\lambda, N2) \cdot Tint$$

$$rDBR(\lambda, N1, N2) := \frac{Mlaser(\lambda, N1, N2)_{1,0}}{Mlaser(\lambda, N1, N2)_{1,1}} \qquad R(\lambda, N1, N2) := \left(\left| \frac{Mlaser(\lambda, N1, N2)_{1,0}}{Mlaser(\lambda, N1, N2)_{1,1}} \right| \right)^2$$